

Dynamics of Ultra-short Laser Pulse Interaction with Solids at the Origin of Nanoscale Surface Modification

**Von der Fakultät für Mathematik,
Naturwissenschaften und Informatik
der Brandenburgischen Technischen Universität Cottbus**

zur Erlangung des akademischen Grades

**Doktor der Naturwissenschaften
(Dr. rer. nat.)**

genehmigte Dissertation

vorgelegt von

Dipl.- Phys.

Florența Adriana Costache

geboren am 16.11.1971 in Berca, Rumänien

Cottbus 2006

Gutachter

Prof. Dr. Jürgen Reif

Gutachter

Prof. Dr. Wolfgang Kautek

Gutachter

Dr. Philippe Martin

Datum der Einreichung:

12.12.2006

Datum der mündlichen Prüfung:

30.03.2007

ABSTRACT

This *thesis* addresses fundamental physical processes which take place at the surface region of a target during and after the interaction with ultra-short laser pulses. The general goal is to bring together different phenomena and discuss the non-equilibrium nature of the interaction of femtosecond laser pulses ($\tau_p < 100$ fs) with various materials, in particular dielectrics and semiconductors.

Different experiments, using various techniques, are designed to explore the basic mechanisms of laser ionization, defect creation, electron-lattice energetic transfer, charged particles desorption, optical breakdown, phase transformations and surface morphological changes. Such processes are shown to depend strongly on the laser intensity. Thus, they are analyzed for intensities over four orders of magnitude (10^{11} - 10^{14} W/cm²), around the surface optical breakdown (damage) threshold intensity.

First, experimental studies using time-of-flight mass spectrometry indicate that non-resonant intense ultra-short laser pulses can efficiently ionize a dielectric (semiconducting) material leading to emission of electrons as well as charged particles, i.e. atomic ions and large clusters, and neutral particles. Under these irradiation conditions, the ionization processes can be at best described by multiphoton ionization and ionization at defects sites. The structural defects provide the means for an increased positive ion desorption rate. A multiple pulse incubation effect in the ion yield can be well related with the reduction of the multi-pulse damage threshold with increasing intensity.

Following the initial electron excitation and emission, positive ions are released from the surface in a substantial amount with high ion velocities indicative of a localized microscopic electrostatic expulsion. With increasing intensity, the amount of ions gets larger and larger and their velocity distribution exhibits a bimodal structure. Also, in these conditions, negative ions are detected. The ion desorption can arise from a combination of a localized electrostatic repulsion (macroscopic Coulomb explosion) and a thermal ‘explosive’ mechanism. The later becomes more important with increasing intensity.

The very fast energy input and particle emission result in a transient perturbation and deformation of the target lattice. Using pump-probe experiments the temporal evolution of lattice dynamics can be analyzed upon single-pulse excitation for many different target materials. This deformation is indicated to be a material characteristic. It is associated with the generation of transient defects in dielectrics or fast phase transitions in semiconductors and metals. Therefore, it could well give estimates of lifetime of transient defect states or electron-phonon relaxation times.

At last the surface morphology after ablation is analyzed, with emphasis on the laser-induced surface periodic patterns (ripples). The patterns observed appear to be very different from the ‘classical’ ripples formed after long pulse ablation. They can have periods much smaller than the incident wavelength and are rather insensitive to the variation of the laser wavelength and angle of incidence. We show that control factors are laser beam polarization and the irradiation dose. Additionally, the patterns exhibit features pointing toward a chaotic origin. Their possible formation mechanism is likely linked with the non-equilibrium nature of the interaction.

ZUSAMMENFASSUNG

Diese Dissertation befasst sich mit den grundlegenden physikalischen Prozessen, die im Oberflächenbereich eines Materials während und nach der Wechselwirkung mit ultrakurzen Laser Pulsen stattfinden. Es ist das wesentliche Ziel der Arbeit unterschiedliche Phänomene zu vereinen und zu zeigen, dass die Wechselwirkung von Femtosekunden-Laserpulsen ($\tau_p < 100$ fs) mit unterschiedlichen Materialien, insbesondere Dielektrika und Halbleiter, fern vom thermischen Gleichgewicht stattfindet.

Verschiedene Experimente, die unterschiedliche Techniken nutzen, werden entwickelt um die grundlegenden Mechanismen für Laserionisation, Defekterzeugung, Elektron-Gitter Energieaustausch, die Desorption von geladenen Teilchen, den optischen Durchbruch, Phasen-Transformationen und Änderungen der Oberflächenmorphologie zu untersuchen. Es wird gezeigt, dass solche Prozesse sehr stark von der Laserintensität abhängen. Daher werden sie in einem Intensitätsbereich von vier Größenordnungen (10^{11} - 10^{14} W/cm²) um die Schwelle für den optischen Durchbruch an der Oberfläche (Zerstörungsschwelle) studiert.

Experimente mit Flugzeit-Massenspektrometrie zeigen, dass nichtresonante, intensive ultra-kurze Laserpulse ein Dielektrikum (Halbleiter) sehr effizient ionisieren können. Neben Elektronen werden auch schwere geladene Teilchen emittiert, d.h. atomare Ionen und große Clusterionen, sowie Neutralteilchen. Der Ionisationsprozess kann hier am besten beschrieben werden als Mehrphotonen-Ionisation und Ionisation von Defekten. Strukturdefekte bewirken eine erhöhte Desorption von positiven Ionen. Daher gibt es einen Effekt der Multi-Puls Inkubation für die Ionenausbeute, der auf einer Reduzierung der Zerstörungsschwelle beruht und stark von der Intensität abhängt.

Als Folge der Anregung und Emission von Elektronen verlassen positive Ionen in beträchtlicher Zahl mit hoher Geschwindigkeit der Oberfläche. Dies deutet auf eine lokale mikroskopische elektrostatische Abstoßung hin. Mit zunehmender Intensität wächst die Zahl der Ionen stark an, und ihre Geschwindigkeits-Verteilung entwickelt eine bimodale Struktur. Jetzt können auch negative Ionen nachgewiesen werden. Die Ionen-Desorption kann hier auf einer Kombination von einer lokalen elektrostatischen Abstoßung (Coulomb Explosion) und einem thermischen Explosions-Mechanismus beruhen. Dieser wird mit wachsender Intensität zunehmend wichtiger.

Da der Energie-Eintrag und die Teilchen-Emission sehr schnell erfolgen, entsteht eine transiente Störung und Deformation des Gitters der Probe. Mit Pump-Probe Experimenten kann die zeitliche Entwicklung der Gitterdynamik nach Einzelpuls-Anregung für viele unterschiedliche Materialien untersucht werden. Die Gitterdeformation ist offensichtlich Material-spezifisch. Sie ist verknüpft mit der Erzeugung von transienten Defekten in Dielektrika oder schnellen Phasenübergängen in Halbleitern und Metallen. Daher können solche Experimente eine gute Abschätzung liefern für die Lebensdauer von transienten Defektzuständen oder für Elektron-Phonon-Relaxationszeiten.

Schließlich wird die Oberflächenmorphologie der Probe nach der Ablation studiert, insbesondere werden Laser-Induzierte Periodische Strukturen (Ripples) beobachtet, die offensichtlich sehr verschieden sind von ‚klassischen‘ Ripples nach der Ablation mit langen Pulsen. Ihre Periodizität ist viel kleiner als die einfallende Wellenlänge, und es wird kein großer Einfluss von Wellenlänge und Einfallswinkel beobachtet. Wir zeigen, dass eher Laserpolarisation und Bestrahlungsdosis wichtig sind. Außerdem zeigen die Muster Eigenschaften, die auf eine Selbstorganisation hindeuten.

TABLE OF CONTENTS

Introduction	I
1. Ultra-short laser-pulse interaction with solids: Electronic transport and material removal	1
1.1. Non-linear absorption of ultra-short laser pulses in non-metallic solids.....	2
1.1.1. Photo-ionization/Free electron generation	3
1.1.2. Electron-lattice coupling.....	7
1.2. Models for material removal mechanisms.....	16
1.2.1. Ion desorption driven by electronic transitions	16
1.2.2. Thermodynamical processes in laser ablation	20
2. Instrumentation	25
2.1. Laser system	26
2.2. Laser desorption analysis	29
2.2.1. ToF mass spectrometer	29
2.2.2. Ion desorption analysis: experimental set-up	29
2.3.3. Kinetic energy measurements	35
3. Laser-induced particle emission from non-metallic surfaces	39
3.1. Charged particle desorption from dielectric surfaces.....	40
3.1.1. Laser-desorbed positive ions	40
3.1.2. The explosive character of charged particle emission	45
3.1.3. Factors enhancing the ion desorption	49
3.1.3.1. Incubation: the role of laser induced defects.....	49
3.1.3.2. Incubation influence on damage threshold.....	52
3.1.3.3. The nature of defects: Laser induced fluorescence	60
3.1.4. Particle emission kinetics	64
3.1.4.1. Negative ion detection.....	64
3.1.4.2. Effects due to laser intensity variation.....	68
3.1.5. Particle desorption (ablation) mechanism.....	77
3.2. Extension of ablation mechanisms to silicon.....	82
3.2.1. Charged particle desorption from silicon surfaces.....	82
3.2.2. Ion desorption from silicon: Coulomb explosion?.....	85
3.3. Conclusions.....	87
4. Dynamics of particle emission from solid surfaces	89
4.1. Pump-probe experiments using desorption products.....	91

4.1.1. Experimental details.....	91
4.1.2. Dynamics of ion desorption from a dielectric surface	93
4.1.3. Dynamics of ion desorption from silicon and aluminum	100
4.2. Discussion on characteristic times for ion desorption	104
4.2.1. Transient states of matter	105
4.2.1.1. Probing transient surface states	105
4.2.1.2. Probing electron-lattice coupling dynamics	110
4.3. Conclusions	115
5. Surface patterning upon fs laser pulse ablation	117
5.1. LIPSS – Early experimental results and models.....	118
5.2. Femtosecond LIPSS on dielectrics	121
5.2.1. Scattered-surface waves.....	122
5.2.2. Periodic surface structures	124
5.2.2.1. Ripples generated by multiple pulse ablation	124
5.2.2.2. Effects of single pulse interaction	132
5.2.2.3. Control factors for ripple generation.....	136
5.2.3. Two-beam experiment.....	141
5.3. Surface modification upon laser ablation of silicon.....	148
5.3.1. From regular to irregular surface patterns.....	148
5.3.2. Phase transformations	156
5.4. Ripples formation from instabilities.....	161
5.5. Conclusions	169
6. General conclusions and outlook	171
Appendix A	175
References	177
Acknowledgements	

LIST OF PUBLICATIONS

Part of this work is published in:

1. J. Reif, F. Costache, and M. Henyk, *Subpicosecond ion emission from transparent dielectrics*, Proc. SPIE Int. Soc. Opt. Eng. 4426, 82 (2002).
2. F. Costache, M. Henyk, and J. Reif, *Modification of Dielectric Surfaces with Ultra-Short Laser Pulses*; Appl. Surf. Sci. 186, 352 (2002).
3. M. Henyk, F. Costache, J. Reif, *Femtosecond Laser Ablation from Sodium Chloride and Barium Fluoride*, Appl. Surf. Sci. 186, 381 (2002).
4. J. Reif, F. Costache, M. Henyk, and S. Pandelov, *Surface morphology after femtosecond laser ablation of insulators*, Proc. SPIE Int. Soc. Opt. Eng. 4760 (2002) 980.
5. M. Henyk, F. Costache, and J. Reif, *Ultra short laser pulse ablation from sodium chloride - the role of laser induced color centers*, Appl. Surf. Sci. 197-198, 90 (2002).
6. J. Reif, F. Costache, M. Henyk, and S.V. Pandelov, *Ripples Revisited: Non-Classical Morphology at the Bottom of Femtosecond Laser Ablation Craters in Transparent Dielectrics*, Appl. Surf. Sci. 197-198, 891 (2002).
7. F. Costache, M. Henyk, and J. Reif, *Surface patterning on insulators upon femtosecond laser ablation*, Appl. Surf. Sci. 208-209, 486 (2003).
8. J. Reif, F. Costache, and M. Henyk, *Explosive ion emission from ionic crystals induced by ultra-short laser pulses: influence on surface morphology*, Proc. SPIE Int. Soc. Opt. Eng. 4948, 380 (2003).
9. F. Costache and J. Reif, *Femtosecond laser-induced Coulomb explosion from calcium fluoride*, *Thin Solid Films*, 453-454, 334 (2004).
10. F. Costache, S. Kouteva-Arguirova, and J. Reif, *Sub-damage-threshold femtosecond laser ablation from crystalline silicon: surface nanostructures and phase transformation*, Appl. Phys. A 79, 1429 (2004).
11. J. Reif, F. Costache, S. Eckert, and M. Henyk, *Mechanisms of ultra-short laser pulse ablation from ionic crystals*, Appl. Phys A 79, 1229 (2004).
12. F. Costache, S. Kouteva-Arguirova, and J. Reif, *Self-Assembled Surface Patterning and Structural Modification upon Femtosecond Laser Processing of Crystalline Silicon*, *Solid State Phenomena* 95-96, 635 (2004).
13. J. Reif, F. Costache, S. Eckert, S. Kouteva-Arguirova, M. Bestehorn, I. Georgescu, A. Semerok, P. Martin, O. Gobert, and W. Seifert, *Formation of self-organized regular nanostructures upon femtosecond laser ablation*, Proc. SPIE Int. Soc. Opt. Eng. 5662, 737 (2004).

-
14. J. Reif, F. Costache, and S. Kouteva-Arguirova, *Femtosecond laser-induced nanostructuring and phase transformation of crystalline silicon*, Proc. SPIE Int. Soc. Opt. Eng. 5448, 756 (2004).
 15. F. Costache, M. Ratzke, D. Wolfframm, and J. Reif, *Femtosecond laser ionization mass spectrometric analysis of layers grown by pulsed laser deposition*, Appl. Surf. Sci. 247, 249 (2005).
 16. F. Costache, S. Eckert, and J. Reif, *Dynamics of laser induced desorption from dielectric surfaces on a sub-picosecond timescale*, Appl. Surf. Sci. 252, 4416 (2006).
 17. O. Varlamova, F. Costache, J. Reif and, M. Bestehorn, *Self-organized pattern formation upon femtosecond laser ablation by circular polarized light*, Appl. Surf. Sci. 252, 4702 (2006).
 18. J. Reif, F. Costache, and S. Eckert, *The role of energy and phase relaxation (T_1 and T_2) in ultra-fast laser ablation*, J. Phys.: Conference Series, ISSN 1742-6588/65.
 19. J. Reif and F. Costache, 'Self-organized surface nano-structuring by femtosecond laser processing', in Recent Advances in Laser Processing of Materials, eds. J. Perrière, E. Millon, and E. Fogarassy, Elsevier, Oxford, 2006.
 20. J. Reif and F. Costache, 'Femtosecond Laser Interaction with Solid Surfaces: Explosive Ablation and Self-Assembly of Ordered Nanostructures', in *Advances in Atomic, molecular and optical physics*, eds: J. Rempe and M.O. Scully, Elsevier Inc. Vol. 53, 228 (2006).
 21. F. Costache, S. Eckert, and J. Reif, 'On ultra-short laser induced instabilities at the surface of non-metallic solids', Proc. SPIE Int. Soc. Opt. Eng., 6261, 2006, doi: 10.1117/12.673618.
 22. F. Costache, S. Eckert, and J. Reif, 'Dynamics of femtosecond laser interaction with solids: from energy coupling to surface relaxation', Appl. Surf. Sci. submitted.
 23. O. Varlamova, F. Costache, M. Ratzke and J. Reif, *Control parameters in surface patterning upon femtosecond laser ablation*, Appl. Surf. Sci. submitted.
 24. J. Reif, M. Ratzke, O. Varlamova, and F. Costache, *Electrical properties of laser-ablation initiated self-organized nanostructures on silicon surface*, Mat. Sci. and Eng. B, in press, Available online 6 September 2006.
 25. J. Reif, F. Costache, O Varlamova, and S. Eckert, *Femtosecond laser-induced instabilities resulting in self-organized structures*, Advanced Laser Technologies, SPIE Proc., in print.

INTRODUCTION

The laser discovery by Maiman in 1960 successfully launched a large number of laser applications in materials processing, optoelectronics and medicine. Later on, with the development of mode-locking techniques, the advent of short ($\tau_p < 10$ ps) and ultra-short laser pulses ($\tau_p < 1$ ps), immensely broadened the range of laser usage. The highly intense electric fields generated in such short timescales found applications from testing ultra-fast semiconductor devices to precise materials processing and micromachining, from triggering or testing chemical reactions to key applications in microsurgery or ophthalmology [SiI95, LFG98, HuK97]. Ultra-short laser pulses have given the researchers access to timescales never-attained before. Thus, it is possible to follow experimentally ultra-fast relaxation processes often encountered in atomic physics and chemistry. Ultra-short laser pulses can act as fast probes, hence they are used to study and control atomic, molecular or electronic dynamics, or in multiphoton microscopy and micromachining [Gen03, KAE00]. The interaction of matter with radiation of unprecedented intensity gives rise to novel nonlinear optics regimes [BrK00].

With the laser techniques available today, wave packets of only few optical cycles (few oscillations of the electric and magnetic fields) can be generated in beams focusable to spot sizes comparable to the radiation wavelength. The possibility of extreme temporal and spatial radiation confinement implies that moderate pulse energies ($E_p \cong 1\mu\text{J}$) can result in peak intensities higher than 10^{16} W/cm². The amplitude of the electric field E_0 of a linearly polarized plane wave is related to its intensity I_0 by: $E_0 = (\mu_0/\varepsilon_0)^{1/4} (2I_0)^{1/2}$, where μ_0 and ε_0 are the magnetic permeability respectively the electric permittivity in vacuum. Thus, for an intensity of 10^{16} W/cm² the amplitude of the electric field is about 10^9 V/cm. This field strength exceeds the Coulomb field experienced by the valence electrons in a typical atom.

Already for several orders of magnitude lower intensity, the field strength is significantly high. Accordingly, the intense electric fields generated by the laser pulse are large enough to allow a non-linear relation with the material response, i.e. polarization.

The extreme conditions in which light and matter are forced to coexist during their interaction have posed a continual challenge both to the experimentalists and theorists.

The intrinsic mechanisms leading to material removal are strongly dependent on the material, photon energy, pulse duration and intensity range applied. Thus, in laser ablation with long pulses ($\tau_p > 10$ ps), the rapid heat conduction increases the area and the depth of the ablated region. Intense ultra-short laser pulses can efficiently ionize very different materials. The laser pulse ends before the excitation energy is transferred to the lattice and much faster than any formation and expansion of a plasma plume. The consequences are a sharper fluence threshold, ionization closer to the near-surface region and a smaller spot size.

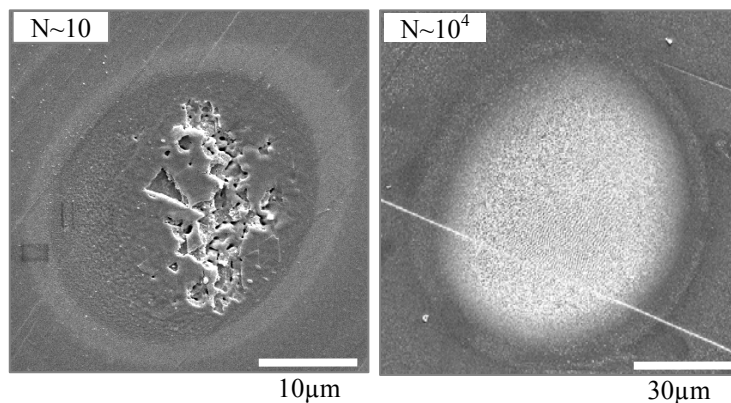


Figure I.1. Images of laser ablated spots on CaF_2 target irradiated with 10 pulses at 50 TW/cm^2 (left) and 10^4 pulses at 5 TW/cm^2 (right).

Femtosecond laser irradiation on metals, semiconductors, or dielectrics yields a considerable amount of charged particles, i.e. atomic ions and large clusters, and neutral particles. The kinetics of particle emission is correlated with the damage induced by the laser, both depending strongly on the intensity. Under low irradiation conditions, as an effect of an outward emission of energetic charged particles from the target, only a few mono-layers per pulse can be removed. The ablation rate increases dramatically with the laser intensity. For intensities where the surface optical breakdown occurs, together with plasma formation and high pressure conditions, a brittle material will be easily broken apart. Figure I.1 illustrates the difference in morphology of a surface irradiated at low intensities and thousands of pulses and intensities around the threshold and only a few pulses.

This thesis describes intensity dependent phenomena occurring at the interaction of femtosecond laser pulses with different target materials.

The objectives of this work are: to analyze the non-linear processes taking place at the interaction of femtosecond laser pulses with dielectric/semiconducting surfaces; to study the kinetics of particle emission; to learn about non-equilibrium, ultra-fast processes occurring during or after the interaction and their timescales; to identify their role in surface modification; to understand the basic mechanisms of surface patterning.

The materials investigated are well-characterized single fluoride crystals, silicon and aluminum.

This thesis is structured as follows:

The first chapter introduces fundamental processes occurring at the ultra-short laser pulse interaction with wide band-gap materials, addressing the influence of pulse duration, photon energy, and laser fluence. The objective is to present the recent progress in understanding of phenomena related to the laser-matter interaction, in particular for the excitation conditions to be achieved in this work.

The second chapter presents the main experimental set-up for studies of laser-induced desorption of particles from solid surfaces.

In the third chapter, we describe experimental results concerning the kinetics of charged particle emission from dielectric and silicon surfaces. Here, the analysis of the electron and ion yield with increasing intensity reveals a transition from a simple desorption of particles from localized sites to a more complex, macroscopic damage. An incubation effect in the ion yield is modeled as an effect of an increased contribution from defects to the free electron density.

The fourth chapter addresses ultra-fast dynamics of the laser-matter interaction. Pump-probe experiments, monitoring the ion yield, indicate that primary lattice deformation could happen already during the pulse or much later. For very different materials, the measurements reveal fast transient phases, which appear to reflect the electron-lattice coupling dynamics. Phenomena such as transient defect generation (in dielectrics) and fast phase transitions (in silicon and aluminum) are here used to explain these phases.

Chapter 5 deals with surface modification upon laser interaction. Among the many morphological features induced by the femtosecond laser pulse on the dielectric and silicon surfaces, periodic pattern formation are the most intriguing ones. This is enhanced by our observation on ripples of periods much smaller than the incident wavelength. The examination of different patterns indicates that the possible origin mechanism is likely linked with the non-equilibrium nature of the interaction.

In the final section, we present general conclusions and a possible outlook of this work.

CHAPTER 1

ULTRA-SHORT LASER PULSE INTERACTION WITH SOLIDS: ELECTRONIC TRANSPORT AND MATERIAL REMOVAL

Fundamental processes involved in ultra-short laser pulse-induced particle desorption from solids, in particular from wide band-gap materials are addressed here. The different channels for radiation absorption and energy redistribution leading to material removal are presented in the frame of existing models.

The dynamics of laser-matter interaction are shown to depend on the electronic excitation and recombination mechanisms. The fast energy transfer between the excited electrons and lattice can lead to carrier removal and surface effects such as surface charging and structural defects, phase transitions and heat dissipation.

The mechanisms of laser-induced particle desorption from dielectric surfaces can be driven both by electronic transitions and thermal processes.

The energy transport in ultra-short laser pulse ablation is twofold: (i) absorption of laser radiation inside the surface and bulk by bound and free electrons, (ii) energy transfer to the lattice, bond breaking and material removal. The various microscopic processes with effect on a macroscopic (mesoscopic) scale depend greatly on the strength of the incident laser electric field and laser wavelength.

An initial stage in laser ablation of any material is free electron generation and formation of electron-hole pairs. For dielectric (semiconducting) targets interacting with ultra-short laser pulses, the major part of the energy imparted to electronic excitation is first converted in kinetic energy of electrons. The energetic electrons can undergo further excitation or lose their energy by interaction with phonons, charged carrier removal, electron-hole recombination or bulk carrier diffusion.

This chapter will address these fundamental processes occurring at the laser-matter interaction and also important consequences such as: electron-lattice interaction, surface optical breakdown, electron trapping at defect sites and permanent defects, surface charging and charged particle emission and phase transitions, which are studied experimentally in the following chapters.

1.1. NON-LINEAR ABSORPTION OF ULTRA-SHORT LASER PULSES IN NON-METALLIC SOLIDS

The ultra-short laser pulse energy is deposited onto the solid targets through non-linear absorption processes. While in metals the free electron density can be considered constant during the interaction, in semiconductors and wide band-gap insulators the free electron density could change due to interband transitions.

The interaction of intense laser radiation with matter is described by a nonlinear relationship between the induced polarization \mathbf{P} and the electric field \mathbf{E} of the electromagnetic radiation [Blo74]. The induced polarization can be regarded as a superposition of linear and nonlinear material responses:

$$\mathbf{P} = \varepsilon_0 \cdot \chi^{(1)} : \mathbf{E} + \mathbf{P}_{\text{NL}} = \varepsilon_0 \cdot \chi^{(1)} : \mathbf{E} + \varepsilon_0 \cdot \chi^{(2)} : \mathbf{E}\mathbf{E} + \varepsilon_0 \cdot \chi^{(3)} : \mathbf{E}\mathbf{E}\mathbf{E} + \dots \quad (1.1)$$

where $\mathbf{P}_L = \epsilon_0 \cdot \chi^{(1)} \cdot \mathbf{E}$ is the linear term in \mathbf{E} , \mathbf{P}_{NL} is the nonlinear term in \mathbf{E} with $\chi^{(k)}$ the k^{th} order susceptibility. The induced polarization follows instantly the change of the electric field even on the femtosecond timescale.

In the conditions of non-resonant excitation and for an interacting electromagnetic field weaker than the static atomic Coulomb field, the atomic energy levels undergo a small perturbation, resulting in a displacement depending on the amplitude of the field. Nonlinear interactions taking place under these conditions can be described by a perturbative approach. If the electric field strength becomes comparable to the Coulomb field experienced by the outer-shell electrons in an atom, the electron escape probability increases and it is detached from the atom before the laser field reverses its sign. This is the strong-field regime of nonlinear optics.

1.1.1. Photo-ionization / free electron generation

To determine the probability for different ionization regimes of *atoms* in intense laser fields, Keldysh expressed a scale (adiabatic) parameter long ago [Kel65]:

$$\gamma = \frac{2\pi\nu \cdot (m_{re} E_i)^{1/2}}{e \cdot E} \quad (1.2)$$

where ν is the laser frequency, E is the laser electric field, e is electron charge, E_i is the ionization energy, and $1/m_{re} = 1/m_e^* + 1/m_v^*$ is the electron reduced effective mass, with m_e^* and m_v^* the effective mass of the electrons in the conduction band and valence band, respectively.

Keldysh's ionization probabilities calculations indicate that, depending on the laser intensity and frequency, photo-ionization could occur either through tunneling ionization or multiphoton ionization or both. Generally, when the scale parameter γ is smaller respectively larger than unity, either tunneling or multiphoton ionization can occur.

Tunneling ionization (optical field ionization) occurs for very strong laser fields (~ 200 MV/cm), which are easily obtained with ultra-short laser pulses and low laser frequencies [Kel65]. By applying such an intense laser field, the binding Coulomb potential in atoms is suppressed, this temporarily enhancing the non-linear atomic polarization. The superposition of the Coulomb field of the nucleus and the laser electric

field results in an oscillating finite potential barrier. Bound electrons can tunnel the narrow barrier and become free in a time shorter than one laser period, i.e. one optical cycle (Figure 1.1 (a)).

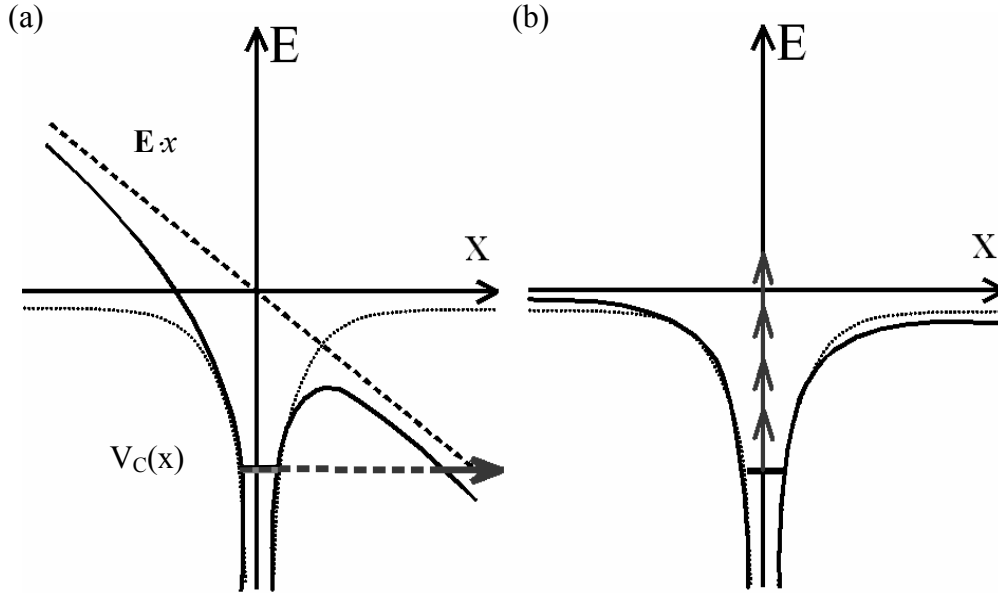


Figure 1.1. Photo-ionization processes. The intense laser field \mathbf{E} perturbs the Coulomb potential in the atom $V_C(x)$ either (a) strongly, when subjected to high laser field strengths (bound electrons can tunnel the resultant narrow Coulomb barrier), or (b) only slightly, at low incident intensities, where the electron is freed by multiphoton ionization.

As the free electron oscillates in the laser electric field, the effective ionization potential becomes:

$$E_{eff} = E_i + \varepsilon_{osc} = E_i + \frac{e^2 E_L^2}{16m_{re}\pi^2\nu^2} \quad (1.3)$$

where ε_{osc} is the mean kinetic (ponderomotive) energy of the electron in the laser field [Kel65]. The Keldysh parameter can be re-expressed as $1/\gamma^2 = 2\varepsilon_{osc}/E_i$. This implies that for $\gamma < 1$, the external electric field dominates over the static Coulomb field as $\varepsilon_{osc} > E_i/2$. Hence, the free electron is removed from its position and acquires a high kinetic energy in a laser period. Strong field regime phenomena include above-threshold ionization [AFM79, FMB86, CBB89], high order harmonic generation [HLM92, Cor93, SKB98], or

relativistic effects such as self-channeling [PuM96] and non-linear Thompson scattering [CMU98].

Figure 1.2 illustrates, for 1.55 eV incident photons, the ponderomotive energy dependence on the laser intensity (using Eq. 1.3 and taking the reduced mass equal to the free electron mass). This is compared to the band-gap energy of a dielectric (CaF_2) to distinguish the intensity ranges where different ionization regimes can occur. In this case, the strong field regime becomes important for laser intensities greater than 10^{14} W/cm^2 .

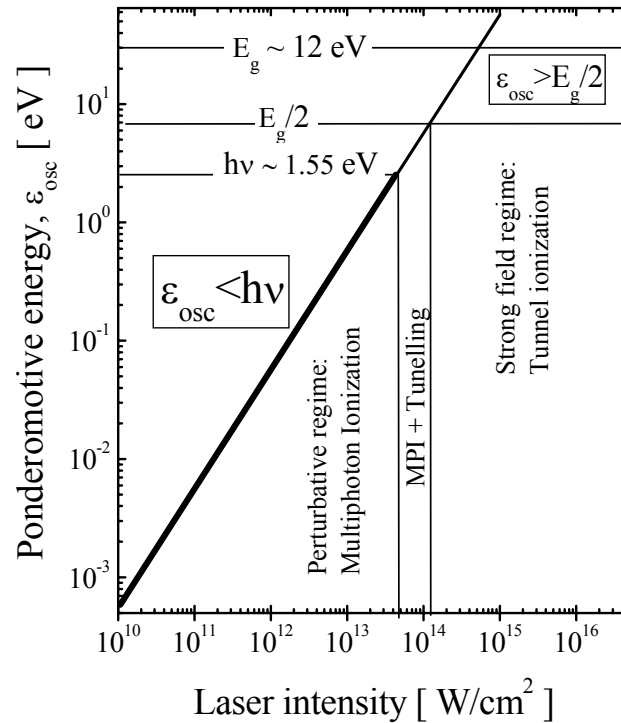


Figure 1.2. The ponderomotive energy of an electron versus laser intensity (from Eq. 1.3). The tunneling and multiphoton ionization regimes are delimited for the case of CaF_2 ($\sim 12 \text{ eV}$ band-gap) irradiated with photons of 1.55 eV energy (800 nm).

If the laser electric field is lower or comparable with the Coulomb static field (Figure 1.1 (b)) and for $\gamma > 1$, respectively $\epsilon_{osc} < h\nu < E_i/2$ (Figure 1.2), the electron is freed by *multiphoton ionization*.

The multiphoton ionization can be treated using high order perturbation theory. Generally, for a transition across n -states, the transition probability between an initial and a

final state depends on the $n-1$ intermediate states [Sch55]. As the coupling between the atom and the electromagnetic field is proportional to the amplitude of the laser electric field, the transition probability depends on the field and therefore, on the laser intensity by $P^{(n)} = \sigma_n E^{2n} = \sigma_n I^n$, where σ_n is the absorption cross-section for n photons. The ionization cross-section has been shown to depend on the order of the ionization process, as follows [AgP88]:

$$\sigma_n = 10^{16} \cdot 10^{-(32 \pm 1)n} (cm^2 s^{n-1}) \quad (1.4)$$

If we address now the case of a *solid* which is much more complex than an atom, by *multiphoton ionization*, valence electrons are promoted in the conduction band by simultaneous absorption of several photons, their added energy being equal or greater than the band-gap energy.

In a solid, the conduction band electrons collectively oscillate in the laser field and also undergo collisions with their surroundings.

Providing that there is a sufficient number of free ('seed') electrons in the conduction band of a dielectric, *avalanche ionization processes* can also occur. Thus, free electrons can further absorb photons and acquire high average kinetic energies, much higher than the minimum of the conduction band (Figure 1.3 (I)). Here, the energy and momentum conservation requires absorption or emission of a phonon. The free electron excess energy can go above the minimum of the conduction band by a value equal or greater than the bandgap energy. In this case, the excess energy can be used to ionize a valence electron upon impact with the free electron. The end result is two electrons at the edge of the conduction band (Figure 1.3 (II)).

The 'seed' electrons required for the avalanche ionization are provided by thermally excited carriers, ionized impurities, and defect states or by direct ionization of free carriers through photo-ionization, the so-called *multiphoton-mediated electron avalanche*.

Impact ionization takes place if the colliding free electron has a minimum kinetic energy needed to fulfill the energy and momentum conservation, which is given by [KRV00]:

$$E_{crt} = \frac{1+2\mu}{1+\mu} \cdot (E_g + \varepsilon_{osc}) \quad (1.5)$$

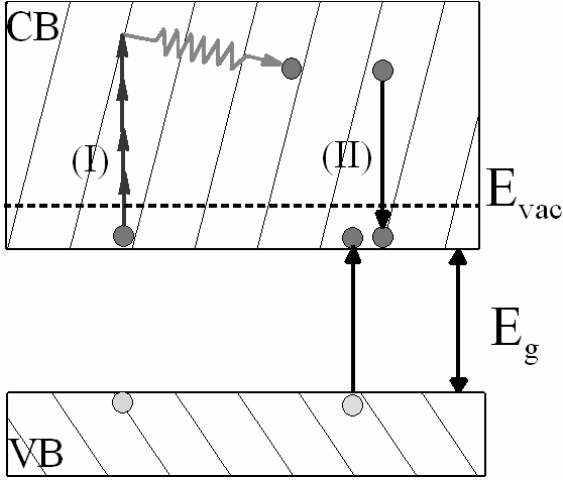


Figure 1.3. Free carrier absorption (I) and impact ionization (II) involved in avalanche ionization in a schematic valence band (VB) and conduction band (CB). A free electron absorbs several photons (I) then impact ionizes another electron (II).

where $\mu = m_e^*/m_v^*$. For $\mu \sim 1$, m_e^* and m_v^* both being equal with the free electron mass, the critical energy is higher than an effective band-gap energy by $E_{crit} \sim 1.5 \cdot (E_g + \epsilon_{osc})$.

Taking into consideration momentum conservation, Kaiser et al. [KRV00] calculated the contribution of impact ionization to the free electron density in a dielectric. They found that, depending on the intensity and only for laser pulses longer than 100 fs, the contribution to the free electron density from impact ionization and avalanche processes may become important.

The contribution of different ionization processes to the free electron density will be further addressed in subsection 1.1.2.3.

1.1.2. Electron-lattice coupling

The system is brought back to thermal equilibrium by recombination processes which can result from electron-electron and electron-phonon scattering (i.e. electrons can couple with lattice vibrations). The electron-phonon interaction makes the description of electronic excitation much more complicated in a solid than at atomic level.

The strength of the electron-lattice interaction is characterized by a coupling constant g [Kit56], given by the ratio between average deformation energy and average phonon energy:

$$g = \frac{\text{deformation energy}}{\hbar \omega_{LO}} = \frac{1}{2} \left(\frac{1}{\epsilon_\infty} - \frac{1}{\epsilon_0} \right) \frac{e^2}{r_p} \frac{1}{\hbar \omega_{LO}} \quad (1.6)$$

where ϵ_0 is the static dielectric constant of the crystal, ϵ_∞ is the dielectric constant at (high) optical frequencies and ω_{LO} is the frequency of the longitudinal optical phonon. In an insulator, the combination of an electron and the polarized field created by the excitation

itself in the lattice gives rise to a polaron. Its radius is defined by $r_p^2 = (\hbar^2 / 2m_p^*)(\hbar\omega_{LO})$ with m_p^* the effective mass of a polaron.

Thus, the coupling constant g gives a measure for the number of phonons accompanying an electron moving in a polarizable lattice created by the laser field (i.e. it is a measure of the electron-optical phonon interaction). Also it gives a measure for the ionicity of the atomic bonds, being large in ionic crystals, smaller in materials with covalent binding and almost vanishing for metals [Kit56, AsM76]. In ionic crystals and for low excitation density, the laser energy could be localized on a single atom or groups of atoms [HaK92], while in metals the energy could be localized only at defects [HON92].

The laser-induced defects in dielectrics and consequences of energy transfer from electron to the lattice are further addressed in this section.

1.1.2.1. Radiation-induced defects in dielectric materials

The effect of energy localization in ionic crystals is the creation of defects, which can play

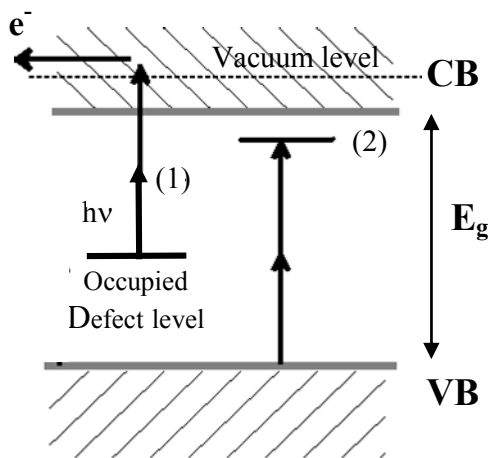


Figure 1.4. Energy level for a wide band-gap insulator with the schematic of defect-mediated ionization (1) and defect state creation by multiphoton ionization (2).

a major role in particles desorption from the surface.

Figure 1.4 shows a schematic diagram of energy levels of an insulator. Photons of energy $h\nu < E_g$ can be absorbed at an occupied defect state within the band-gap (Figure 1.4 (1)). Thus, by single or multiphoton absorption, these defect states can couple with free electron states in the conduction band or even above the vacuum level and lead to electron ejection from the surface. Such defect states can be excitonic states.

Excitons are excited electronic states of the lattice determined by coupled electron-hole pairs. They can be formed by an inelastic scattering that could slow down the free electron [VFM99] or by resonant absorption of multiple photons (Figure 1.4 (2)).

The migration of the electronic excitation (electrons, holes or excitons) through the lattice (i.e. polaron formation) is associated in solids with local atomic distortions that

deepen the potential well in which the carrier resides. This is called self-trapping. Thermal fluctuations can provide enough energy for at least one particular lattice site to undergo instantaneous deformation for the self-trapping to begin [TaO80]. An excitonic self-trapped state has a longer lifetime than the free electron. Self-trapped excitons (STE) formed through the interaction between the free electron and the lattice can relax through photon emission (luminescence) or non-radiative transitions to more stable or permanent defect configurations [ItT86]. Materials that undergo self-trapping are predominantly insulators with wide band-gap, such as alkali halide and SiO_2 . In alkali halides, free electrons and excitons can likely relax to a self-trapped state, thus the electronic energy is highly localized. Different possible STE configurations are sketched in Figure 1.5.

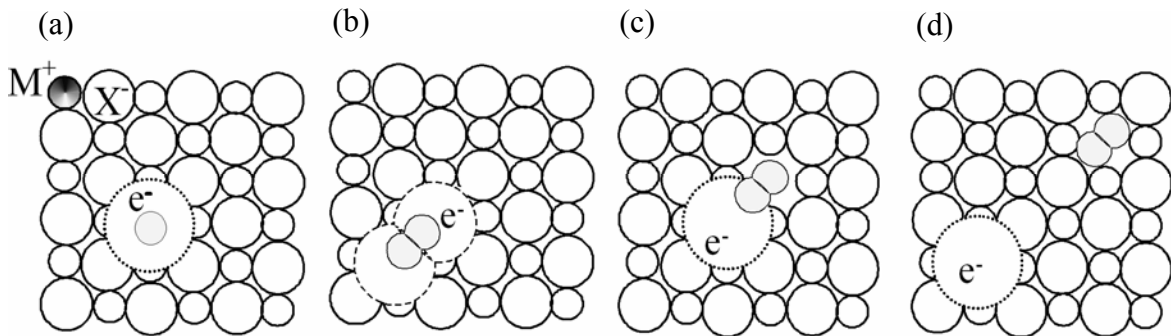


Figure 1.5. Configurations of self-trapped excitons in alkali halides as proposed by [ItT86]: (a) atomic STE; (b) molecular STE; (c) STE with strong electron-hole interaction (d) Frenkel pair with separated F - and H -centers (the light gray filled circles represent neutral halogen atoms).

It is generally accepted ([WSF86, Ito95] and references therein), that in alkali halides a photo-generated hole can undergo self-trapping. By electron capture, this can lead to the formation of a self-trapped exciton (Figure 1.5 (a)).

From an STE, the lattice relaxation gives rise to the formation of Frenkel (pair) defects. Here, the electron and hole are converted into spatially separated defects (Figure 1.5 (d)): an F -center (electron trapped at an anion vacancy) and an H -center (relaxed neutral interstitial halogen). The decay of Frenkel pairs and F -center diffusion to the surface may lead to energetic *neutral halogen* desorption [HaK92].

1.1.2.2. Electron-lattice energy transfer

Generally, the femtosecond laser pulse provokes fast non-equilibrium processes at the surface region of the target.

Upon irradiation with long pulses, both electrons and lattice are heated simultaneously and are at thermal equilibrium, characterized by a common temperature. In contrast, upon ultra-short laser pulse irradiation, the electrons are heated during the pulse and only much later the energy is transferred to the lattice and thermal diffusion takes place [AKP74]. The electron and lattice subsystems could be regarded as fully decoupled during the interaction with femtosecond pulses. In the transient phase, the electron temperature can be many orders of magnitude higher than the lattice temperature. Consequently, fast and ultra-fast phenomena dependent on the electronic temperature could be strongly amplified by making use of femtosecond laser pulses. For instance, pump-probe techniques are used to measure *electron-phonon relaxation times* (see Chapter 4).

The spatial and temporal evolution of the electron and lattice are described by a *two-temperature* diffusion model [AKP74, GiG95, NMJ97]. In this model, one describes the material as two coupled subsystems, one for electrons and one for phonons (lattice or ionic system). Each subsystem is in a local equilibrium, so that the electrons are in a Fermi-Dirac distribution of temperature T_e and the phonons in a Bose-Einstein distribution of temperature T_i . Their interaction, via the electron-phonon coupling, gives rise to an energy exchange at a rate proportional to $(T_e - T_i)$. For the direction z perpendicular to the target surface, the time evolution of the energy in the two subsystems is governed by the following equations,:

$$\begin{aligned} C_e \frac{\partial T_e}{\partial t} &= \frac{\partial}{\partial z} \kappa(T_e) \frac{\partial T_e}{\partial z} - g \cdot (T_e - T_i) + S(z, t) \\ C_i \frac{\partial T_i}{\partial t} &= g \cdot (T_e - T_i) \end{aligned} \quad (1.7)$$

where $S(t, z)$ is a source term describing laser heating with a laser intensity $I(t)$, C_e and C_i are the electron, respectively lattice (ionic) heat capacities (per unit volume), g is the electron-lattice coupling constant and κ is the thermal conductivity of the electronic subsystem.

The electron-phonon coupling intervenes simply as a phenomenological parameter, this being a characteristic of the energy exchange between the two subsystems. This model works well for metals [WHG99]. However, with the right choice of the *source term*, e.g. the assumption that laser-excited metals and strongly ionized semiconductors and dielectrics could be regarded as dense plasmas [KRV00, BSR04], this model could be used for energy balance description in metals, semiconductors or dielectrics. This model will be invoked in the discussion of ultrafast dynamics of aluminum in Chapter 4.

In the following, we address the influence of electronic excitation on the lattice optical properties and surface optical breakdown.

1.1.2.3. Surface optical breakdown

When the density of the conduction band electrons reaches a critical density (plasma critical density – or just below it [SCP02]), the material becomes strongly absorbent. Avalanche processes, the main cause for optical breakdown and plasma plume formation in metals, do not occur in wide band-gap materials, except for very high fluences, due to their low free electron density.

For long laser pulse ablation ($\tau_p > 10$ ps), a generally accepted picture of the interaction considers heating of the ‘seed’ electrons and transfer of their energy to the lattice during the laser pulse. When the control factor of the damage process is the thermal conduction, then a damage fluence threshold dependence on the pulse duration should scale with $\sqrt{\tau_p}$ [DLK94, Nie95]. There are statistical fluctuations in the number of ‘seed’ electrons (provided by e.g. impurities) required for avalanche processes, because of the low free electron density $n_0 \sim 10^8$ cm⁻³ in dielectric materials [Blo74]. This implies important fluctuations which are indeed observed in the damage fluence threshold for dielectric materials irradiated with long pulses. For instance, a laser beam focused to a spot of 10 μ m in diameter, and a ~ 75 μ m Rayleigh range, corresponds to a 10⁻⁸ cm³ focal volume, this resulting in an average of only one impurity per focal volume.

On the other hand, for the high electric fields provided by short pulses ($\tau_p < 10$ ps), the multi-photon ionization probability increases significantly therefore a change from the $\sqrt{\tau_p}$ scaling has been predicted. For intensities greater than 10¹³ W/cm², multiphoton ionization can provide enough free electrons, thus there is no more need of an

avalanche process and implicitly ‘seed’ electrons. A deviation from the $\sqrt{\tau_p}$ scaling was observed first by Soileau et al. [TeS81] and later by Du et al. [DLK94] and others [SFR95, TBK99] for pulses shorter than 10-60 ps. A deviation from $\sqrt{\tau_p}$ scaling has been suggested to arise because avalanche processes cause the electron density to increase exponentially in time, while the multiphoton ionization causes it to increase linearly in time [SFR95].

The ionization processes in dielectrics irradiated with ultra-short laser pulses are described with models based on solving a Boltzmann transport equation [ACD92] or a kinetic equation [SFR95]. These models indicate multiphoton ionization as the main free electron generation channel. It is postulated that the ablation starts when the electron density reaches the plasma critical density ($n_c \sim 10^{21} \text{ cm}^{-3}$ at 800 nm). Just below n_c , the material is highly absorbent and abruptly becomes reflective above n_c due to plasma formation. Here, the highly ionized dielectric material exhibits metallic behavior. If the plasma oscillation frequency is given by:

$$\omega_p = \left(\frac{ne^2}{\epsilon_0 m_e} \right)^{1/2} \quad (1.8)$$

where n is the electron density and m_e is the electron mass, then the optical breakdown occurs when the laser electric field ω equals the plasma oscillation frequency ω_p . This occurs for a critical electron density given by:

$$n_c = \frac{\omega^2 m_e \epsilon_0}{e^2} \quad (1.9)$$

The Drude model for free electron gas and plasma of metals and doped semiconductors can be applied to highly ionized dielectrics.

Stuart et al. provided the description of the temporal evolution of the electron density in femtosecond laser irradiated dielectrics by developing a model based on a kinetic approach in a flux doubling approximation¹ [HoF74, ACD92].

¹ This model assumes that an electron of high energy impact ionizes a valence electron, thus at the end the two electrons would have just enough energy to be at the edge of the conduction band (see Figure 1.3). Thus, the current at the bottom of the conduction band is twice the current at the top of the energy range.

The kinetic equation of a Fokker-Planck type, improves upon the earlier flux-doubling model by including sources of electrons (Joule heating rate) and sinks of electrons (electron-phonon inelastic scattering and electron energy diffusion). This predicts the temporal evolution of the free electron density, as a function of the pulse duration and intensity level applied [SFR95, SHF96]. The kinetic equation has been refined in [ApH00, VaN02] by including recombination terms.

Stuart et al. suggested a linear increase of the avalanche rate with the laser intensity and transformed the kinetic equation into a simple rate equation, as follows:

$$\frac{dn(t)}{dt} = \alpha_i \cdot I(t) \cdot n(t) + \sigma_m \cdot n(t) \cdot [I(t)]^m \quad (1.10)$$

where $\beta = \alpha_i \cdot I(t)$ is the avalanche (impact ionization) rate with α_i the avalanche coefficient and $I(t)$ laser intensity and $P_m(I) = \sigma_m \cdot n(t) \cdot [I(t)]^m$ is the photo-ionization rate of an m -photon process. The avalanche process was considered to start at the laser peak intensity.

A Gaussian temporal profile of the laser pulse of τ_p duration is given by:

$$I(t) = I_0 \exp\left(-4 \ln 2 \frac{t^2}{\tau_p}\right) \quad (1.11)$$

with the peak intensity at $I_0 = \frac{2F}{\sqrt{\pi/\ln 2} \tau_p}$, with F being the pulse fluence.

The solution of Eq. (1.11) gives the temporal evolution of electron density as follows:

$$n(t) \approx n_0 \cdot \exp\left[\int_0^\infty (\alpha I) dt\right] \approx n_0 \cdot \exp\left[\frac{\alpha I_0 \tau_p}{4} \left(\frac{\pi}{\ln 2}\right)^{1/2}\right] \quad (1.12)$$

where $n_0 = \int_0^{\tau_p} (PI) dt \approx \sigma_m N_s \left(\frac{I_0}{h\nu}\right)^m \left(\frac{\pi}{\ln 2}\right)^{1/2} \frac{\tau_p}{4}$ is the electron density due to multiphoton ionization. The multiphoton ionization cross-section and avalanche constant are typically obtained from the ionization probabilities provided by Keldysh's theory [Kel65], or experimentally, evaluating the surface damage threshold dependence on the pulse duration and then using Eq. 1.10 as a fit function [LKS98].

As indicated in [SFR96], we apply Eq. 1.10 to obtain the temporal evolution of the electron density for fused silica SiO_2 , when excited with 2.37 eV photons delivered in 1.2 ps pulses of 12 TW/cm^2 intensity. The photoionization process implies a simultaneous absorption of 4 photons. Here, we use a 4-photon ionization cross-section of $\sigma_4 = 2 \times 10^{-141} \text{ cm}^8 \text{ ps}^{-3}$ obtained by using Eq. 1.4 and an avalanche coefficient for SiO_2 of $\alpha = 11 \text{ cm}^2 \text{ J}^{-1}$ [SFH96, ApH00]. Figure 1.6 illustrates the temporal evolution of electron density for a combined contribution from multiphoton and avalanche ionization. The electron density produced by multiphoton ionization alone is also presented for comparison.

Later, an additional term was added to Eq. 1.10 to account for the recombination processes, such as self-trapping of excitons, as indicated by experiments of Li et al. [LMN99] and Petite et al. [PGM99]. The rate equation becomes:

$$\frac{dn}{dt} = \alpha I n + \sigma_m n I^m - \frac{n}{\tau_x} \quad (1.13)$$

with $R_{n_{STE}} = -\sigma_x n_{STE} I^x + \frac{t}{\tau_x}$ where $R_{n_{STE}}$ is the rate of free carrier losses through self-trapping and recombination, σ_x is the multiphoton cross-section of order x for STE formation and τ_x is the characteristic trapping time of the STE.

Considering that the STE in SiO_2 has a characteristic trapping time of $\tau_x = 0.15 \text{ ps}$ [PGM99] and including a decay term due to trapping in Eq 1.10, we obtain:

$$n(t) \approx n_0 \cdot \exp \left[\int_0^t \left(\alpha I - \frac{1}{\tau_x} \right) dt \right] \approx n_0 \cdot \exp \left[\frac{\alpha I_0 \tau_p}{4} \left(\frac{\pi}{\ln 2} \right)^{1/2} - \frac{t}{\tau_x} \right] \quad (1.14)$$

Figure 1.6 shows also the temporal evolution of electron density including the decay term due to recombination via electron trapping as given in Eq. 1.14. The result is a rapid decrease of the electron density at the end of the laser pulse.

Thus a simple rate equation including ionization and recombination at defect sites can be used to interpret experimental data.

Such a model will be used in Chapter 3 to explain experimental results on the dynamics of charged particle desorption and defect creation.

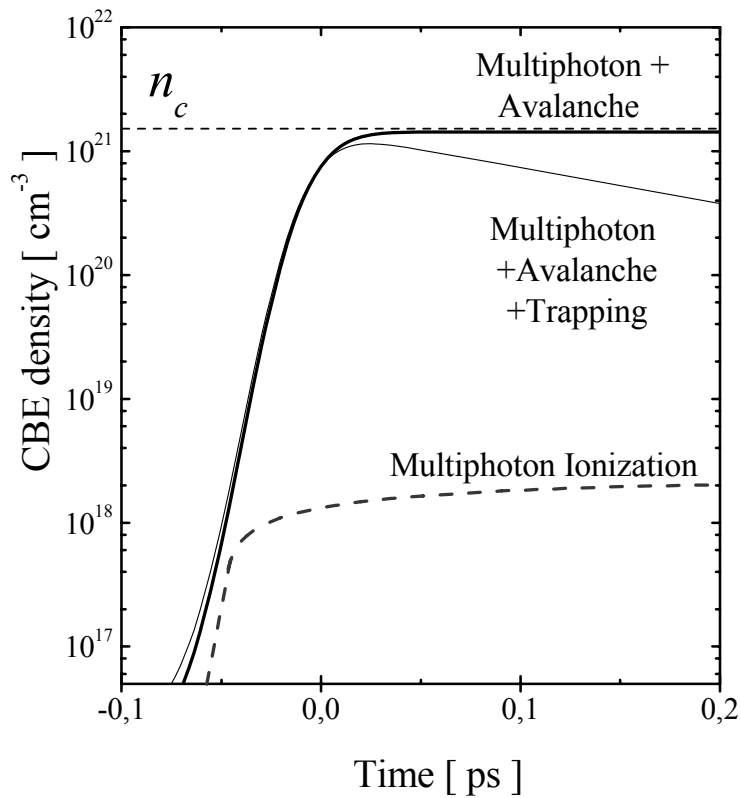


Figure 1.6. The evolution of free electron density due to multiphoton ionization only (dashed line); multiphoton and avalanche ionization (solid line); multiphoton, avalanche ionization and recombination by electron trapping (dotted line) in fused silica upon interaction with a 1.2 ps pulses of 2.37 eV photons (after [SFH96, LMN99]). The damage threshold defined for a critical electron density of $n_c = 1.74 \times 10^{21} \text{ cm}^{-3}$ [SFH96] is reached here for 12 TW/cm^2 .

1.2. MODELS FOR MATERIAL REMOVAL MECHANISMS

The laser pulse excitation can cause ionization of defect states or optically weaken and break up surface bonds. The results obtained from the molecular dynamics calculation by Jeschke et al. [JGB01, JGL02], clearly indicated that the initial excitation can cause lattice oscillations and bond breaking. The ultra-fast response of the lattice to ‘hot’ electrons involves the occurrence of *coherent phonons*, which can lose their coherence in time due to anharmonic, large amplitude distortions of atoms. For instance, in graphite these phonons are associated with motion or a change in the distance between different atomic planes [MJG00]. The coherent phonon dephasing may result also from electron-hole recombination.

The laser initial excitation is converted into driving energy for atomic motion, the result being also desorption of atoms, ions and molecules. The mechanisms of particle ejection are greatly dependent on the electronic structure of the material, photon energy, pulse duration and laser fluence range. Various models for particles desorption based on electronic transitions or processes described by thermodynamics have been previously proposed.

1.2.1. Ion desorption mechanisms driven by electronic transitions

1.2.1.1. Desorption at a molecular level

Earlier proposed models for ion desorption upon electron bombardment [ToL83] have been used to explain photon-induced ion desorption. As shown above, for wide band-gap insulators, self-trapping of excitons and possibly holes provides a means for energy localization and thus initiate electronic transitions to a lower energetic state.

In the semi-classical *Menzel-Gomer-Redhead* model [MeG64, Red64] for ions emitted by Electron Stimulated Desorption (ESD), the incident beam excites a bonding electron to an anti-bonding state via a Franck-Condon transition (Figure 1.7). The adsorbate subsequently evolves along the nuclear coordinate axis on the excited anti-bonding potential energy surface (PES). Thus potential energy is converted into kinetic energy $\Delta\varepsilon_k$, until the adsorbate is de-excited and returns to the ground state. Here the

excess energy is sufficient to overcome the effective potential between the surface atom and solid, and the atom desorbs.

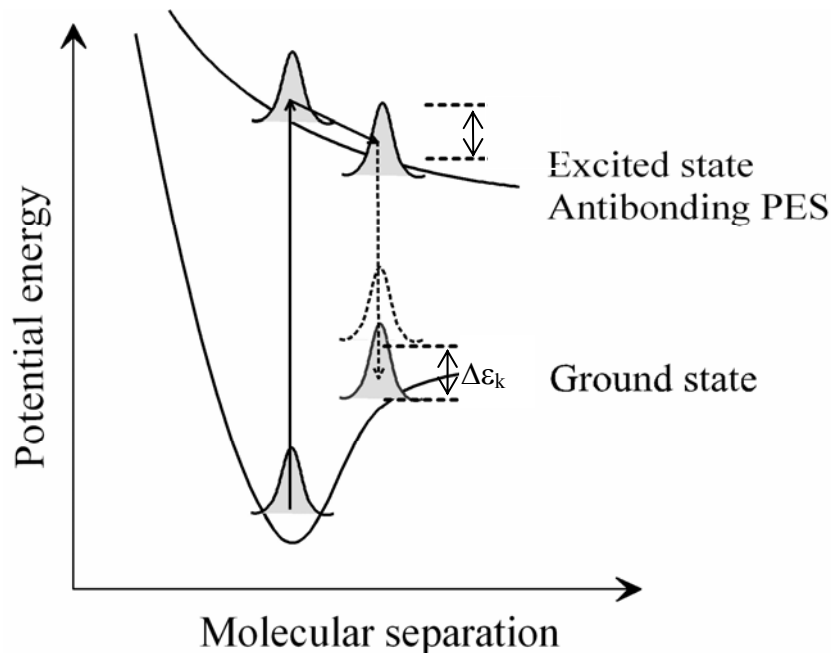


Figure 1.7. Menzer-Gomer-Redhead model: the system is excited directly to an anti-bonding potential energy surface (PES) by a Franck-Condon transition from the ground state. The wave packets jump between different states.

A desorption mechanism based on the MGR picture has been proposed to explain the neutral atom desorption in alkali halides [HaK92]. Figure 1.7 illustrates possible modes of configurational changes, represented by a configuration coordinate Q (translational motion and molecular separation), suffered by a self-trapped exciton en route to halogen atom emission. In this picture, the free exciton (an electron- X^0 pair) represents the bonding ground state. If self-trapped, the exciton is highly localized, hence it has a high binding energy (E). The STE can couple with the neighboring halide ion to form a halogen molecular ion X_2^- ($Q1$ configuration). The X_2^- can separate in F - and H -centers, which migrate easier inside the lattice ($Q2$). When reaching the surface, the neutral halogen atom (the ‘hole’) is repulsed by the neighboring alkali ions and desorbs ($Q3$). The energy variation related to translational motion and binding properties of the different configurations has the same nature as the anti-bonding PES in the MGR model.

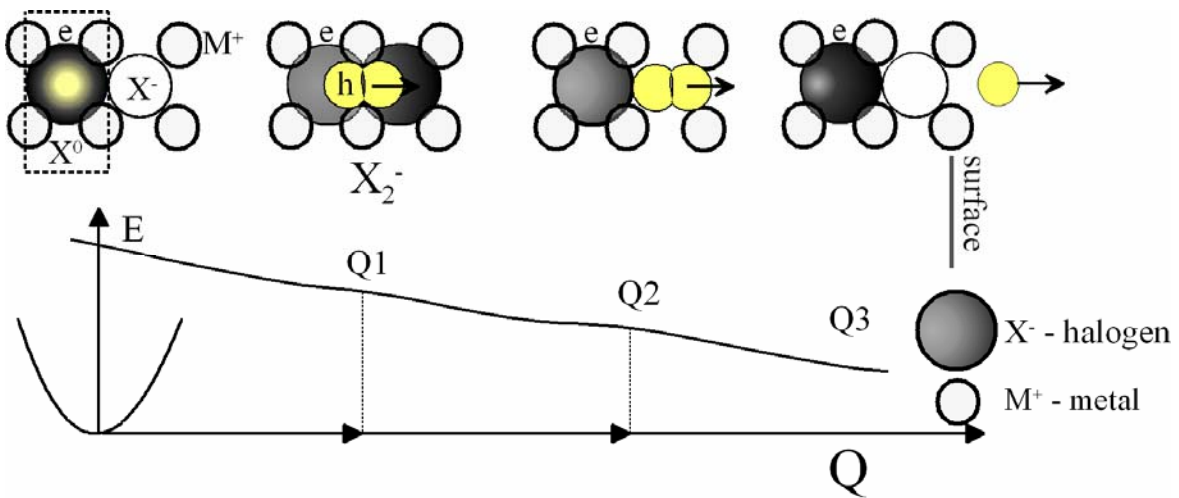


Figure 1.8. Configurational modes to describe the laser-induced desorption in alkali halides [HaK92]. The initial electron-hole pair undergoes self-trapping, halogen molecular ion X_2^- formation, separated F- and H- centers (Q2) and ultimately results in emission of a neutral halogen atom (Q3).

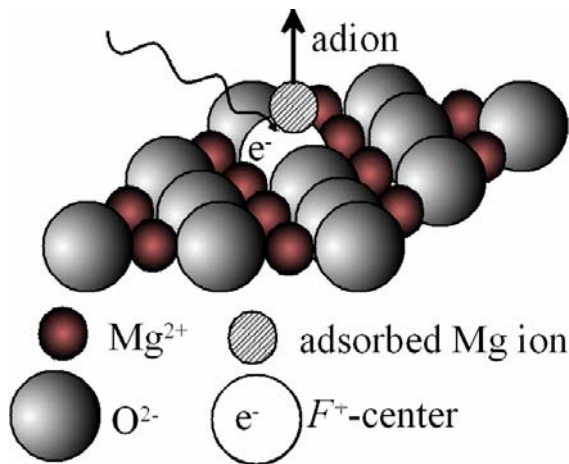


Figure 1.9. Positive ion emission mechanism involving an anion vacancy defect in MgO [DLS94].

For ionic crystals (e.g. BaF_2 and CaF_2), another desorption mechanism for laser desorption assumes an electrostatic interaction of localized paired holes, similar to the Knotek-Feibelman (KF) mechanism in ESD [KnF78, KJR79]. In the KF mechanism, the pair of holes results from an Auger decay of a core hole. Using a similar picture to explain laser desorption from CaF_2 , a possible mechanism suggests that an F^- can be double ionized and form a $Ca^{2+}F^+$ complex with the neighboring metal ion. At the surface, the repulsive

Coulomb force leads to desorption of F^+ ion [Rei89].

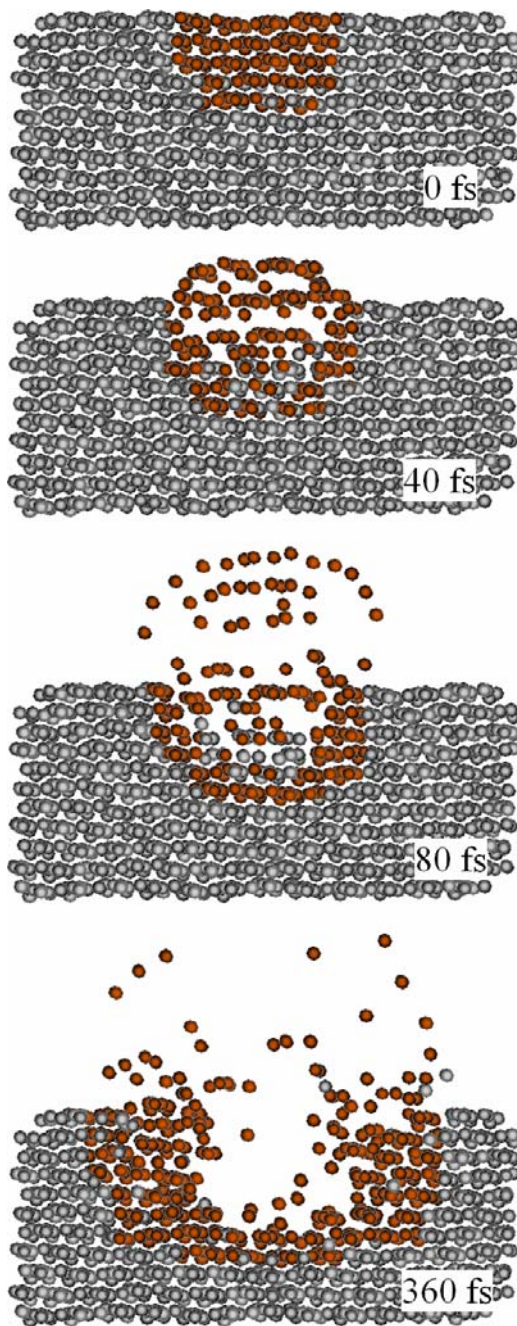
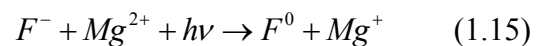


Figure 1.10. Snapshots of the temporal evolution of the irradiated surface in the Coulomb explosion model.

A Si(111) surface is irradiated with energetic ions. As a result, the surface region of the solid becomes ionized. (Here Si^+ ions (red) and Si atoms (grey)). A surface decomposition due to Coulomb repulsion between positive ions starts in 40 fs. In hundreds of femtoseconds, a massive amount of particles is removed (from [ChG97]).

Also Dickinson et al. [DLS94] proposed a mechanism similar to the KF process to explain laser-induced desorption of positive ions, except that their picture requires lattice defect sites acting as radiation absorption centers. They attested an agreement between experimental determination of the kinetic energy of Mg^+ and Mg^{2+} (emitted from a MgO sample) and a theoretical prediction based on Madelung binding energies calculations at surface defect sites. This picture suggests that certain defects, i.e. F -centers, if placed at the near surface region, imply a loss of charge, this reducing the binding of the nearby positive ions. The formation of Mg^+ ion could involve a photo-induced charge exchange as follows:



with F^- and F^0 the neutral (one electron at a vacancy site), respectively charged surface defects. Figure 1.9 illustrates a Mg^+ ion adsorbed on an oxygen vacancy site (F -center). The effect is the Coulomb repulsion of the weakly bound Mg^+ ion by the nearby positive metal ions.

1.2.1.2. Macroscopic Coulomb Explosion

The laser-induced processes driven by electronic transitions result usually in

structural modifications and removal of ions, clusters and neutral atoms. The emitted ions have high kinetic energies and narrow angular distribution oriented normal to the target surface.

The models described in the preceding section inspired the idea of a macroscopic picture for laser-induced material removal and crater formation: the Coulomb explosion mechanism.

The basic physical picture leading to surface breakdown by a Coulomb explosion assumes that both highly energetic ions [ChG97] and intense laser pulses [Rei89, HMW00, SAR00, CoR03], when incident on a surface, rapidly pull electrons out from the solid surface. If a large amount of electrons are removed sufficiently fast, the solid cannot replenish them immediately, hence positive charges accumulate in a localized surface region. The Coulomb forces within the localized charged region overcome the cohesive forces in the solid, leading to an explosive surface decomposition due to repulsion between adjacent ions. Figure 1.10 presents the molecular dynamics results obtained by Cheng et al. for a silicon (111) surface bombarded with energetic ions [ChG97]. The repulsive potential energy is spread into the surroundings or converted into kinetic energy for the ions emitted during the Coulomb explosion in about 40 fs. A crater is formed within less than a picosecond.

1.2.2. Thermodynamic processes in laser ablation

Laser-induced ablation from solids combines a whole range of optical, mechanical and thermodynamic processes. Their analysis becomes more complex as the laser pulses get shorter.

The loss of material could be described by thermodynamic processes such as vaporization, normal boiling and explosive boiling (homogeneous nucleation or phase explosion). These processes, associated with phase transitions, have been considered to occur mainly in long pulse ablation ([KMM98] and references therein).

‘Normal’ vaporization is called so to indicate vaporization in the sense of particle emission from the outer surface. It occurs by heating the material at normal pressure, which corresponds to a timescale much longer than 1 ns. The particle flux Φ per unit area and unit time is given by the Knudsen-Langmuir equation:

$$\Phi = \alpha_{vap} \cdot (p_{sv} - p_v) \cdot (2\pi mkT)^{-1/2} \quad (1.16)$$

here α_{vap} is the vaporization coefficient [Pou72], p_{sv} is the equilibrium vapor pressure, p_v is the vapor pressure of the ambient and m is the particle mass. On the other hand, ‘normal’ boiling involves heterogeneous nucleation of vapor bubbles².

1.2.2.1. Velocity distribution of laser-emitted particles

When the density of particles emitted per pulse is small enough, the particles are considered to leave the surface without interaction and a Maxwellian can describe the particle velocity distribution. This is appropriate for ‘normal’ vaporization and boiling. For a larger quantity of particles removed per unit time (e.g. a half a monolayer in a nanosecond [NLZ88]), then gas-phase collisions are assumed to occur. This happens within a Knudsen layer [KeM96], which is assumed to be a liquid layer formed at the surface region with a thickness of a few mean free paths ($\sim 10 \mu\text{m}$ for a $\sim 10 \text{ ns}$ pulse). In this layer, the non-equilibrium velocity distribution of particles is transformed into an equilibrium thermal distribution. Thus, through collisions, the ablated particles reach a Maxwell-Boltzmann equilibrium distribution. The subsequent three-dimensional expansion of the ablated plume could be analyzed using hydrodynamic models [SiN90].

If collisions occur, the initial center-of-mass velocity of the ejected particles must be approximately conserved and appear as a correction to the final particle velocity (v_z) in the direction normal to the target surface [KeM96, OSN92, OtG93, MiK99]. Thus, the Maxwell-Boltzmann velocity distribution function changes as follows:

$$dN(v, T_u, u) = \left(\frac{m}{2\pi k T_u} \right)^{3/2} \cdot \exp \left(- \frac{m [v_x^2 + v_y^2 + (v_z - u)^2]}{2k T_u} \right) dv_x dv_y dv_z \quad (1.17)$$

where k is the Boltzmann’s constant, v_x , v_y and v_z are the velocity components, u is the center-of-mass velocity and T_u is the temperature in the Knudsen layer. This distribution is taken from the theories of isentropic supersonic expansion of a molecular beam jet. It is successfully used to model the distribution of emitted particles upon laser sputtering [ZHS89].

² They originate from in-homogeneities within the liquid phase such as impurities, solid or gaseous, or defects, which tend to diffuse at a temperature near the boiling temperature.

Collisions in gas phase are assumed to be responsible for the narrowing of the angular distribution (Figure 1.11) and the increase of the effective temperature of the energy distribution ([EIL97] and references therein).

By performing large scale molecular dynamics simulation (the so-called breathing sphere model), for short pulses (10-150 ps), Zhigilei et al. observed that faster, larger, and more numerous clusters were produced in a regime with higher fluences or shorter pulses. The species ejected in this regime correspond to higher velocities with a stronger forward peaking angular distribution.

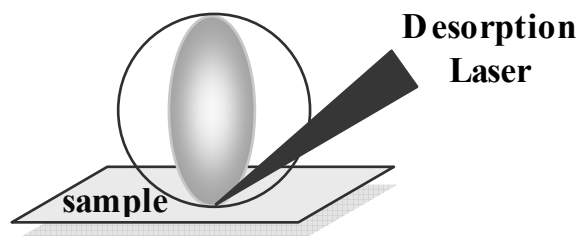


Figure 1.11. Typical geometry for laser ablation experiments.

The open circle describes a $\cos\theta$ distribution typical for an isotropic, low-density ablation, while the filled figure shows a forward-peaked, $\cos^p\theta$ distribution typical for high-density ablation plumes.

The angular distribution is commonly acknowledged as a $\cos^p(\theta)$ function, with θ the polar angle to the surface normal in respect with the ablation plume. Additionally, in the desorption regime (low particle yields) moderate peaking is observed as compared to the ablation regime (high particle yields), where the ejected products peak forwardly.

Experimental and theoretical works have shown that different materials

behave very similar when irradiated with femtosecond pulses, also below the threshold for plasma formation [CSB99, CSB98]. For ablation of metals and semiconductors, a fast phase transition (phase explosion) can be expected to take place.

1.2.2.2. Thermodynamic instabilities at the surface

By superheating the material near the thermodynamic critical temperature T_c , a homogeneous nucleation of gas bubbles (*phase explosion*) can take place. Subsequently, the hot, high pressure region near the surface can explode very fast into a mixture of gas phase and liquid droplets.

Phase explosion can be understood following the schematic van-der-Waals-like P - V diagram. Figure 1.12 illustrates the main regions: Here, BCD curve (spinodal) indicates the two-phase instability, i.e. the liquid-vapor (L-V) coexistence region. The region below

ACE curve (binodal) delimitates the homogeneous metastable region: ACB is the region of super-heated liquid and DCE the region of under-cooled gas. The binodal curve is the equilibrium curve for the liquid and vapor phases. Highly intense laser pulses can heat up the material very fast (in a few ps [SBC98]) and far above the critical point (Figure 1.12, path (a'-a-b)). The system can undergo a fast adiabatic expansion and terminates directly into the gas phase (Figure 1.12, path (b-c)).

If the material is irradiated at laser fluences near the threshold (e.g. $\sim 1.5F_{th}$ for silicon from [CSB99]) as illustrated in Figure 1.12 by the path (a'-a), the system evolves in a more complex manner. The resulting hot liquid can undergo an adiabatic cooling and cross the liquid-gas coexistence curve (ACE) into the metastable state (Figure 1.12, path (a-d)). Near the spinodal curve (BCD), the superheated liquid undergoes volume fluctuations leading to a sudden growth of vapor nuclei (bubbles). Here, the material can either cool along the equilibrium curve (d-d') or it enters the two-phase instability region as an inhomogeneous mixture of vapor and liquid phases. The area below BCD is unstable and therefore a 'jump' into the region DCE occurs (the so-called *phase explosion*). This is accompanied by a large increase of volume due to a rapid creation of vapor nuclei. Upon expansion up to a critical radius, the nuclei collapse producing a shock wave in the surrounding medium.

Martynyuk [Mar83] describes the rate of homogeneous nucleation by:

$$I_n \approx 1.5 \times 10^{32} \exp\left(\frac{\Delta G_n}{k_B T}\right) \times \exp\left(\frac{-\tau_{PE}}{t}\right) \quad (1.18)$$

where ΔG_n is the Gibbs energy for formation of a homogeneous nucleus and τ_{PE} is the phase explosion time constant. Martynyuk argues that the value of I_n becomes significant for $T \cong (0.8-0.9)T_c$ ($I_n < 1$). The I_n dependence on the reduced temperature T/T_c makes phase explosion to resemble a threshold process. In his calculations Martynyuk takes the relevant time parameter $\tau_{PE} > 1$ ns, which would imply that phase explosion is less relevant for materials irradiated with shorter pulses (τ_{PE} is taken as being less or equal to the pulse duration).

However, later experiments [CSB99] revealed typical phase explosion evidence (disruption of the surface in typical re-solidified liquid droplets) produced by irradiating a whole range of materials with much shorter pulse duration, down to hundred of

femtoseconds. Molecular dynamics simulations of Lorazo et al. [LLM03] have indicated that phase explosion can occur for a pulse duration <10 ps, which is the characteristic time for heat conduction.

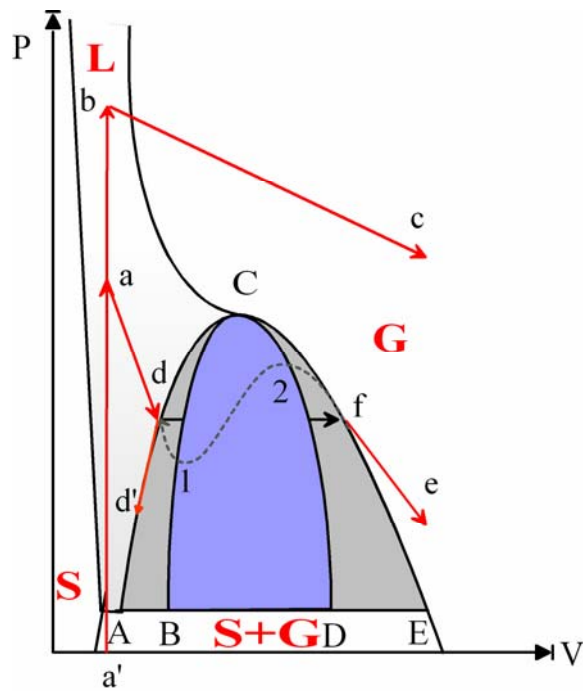


Figure 1.12. Schematic van der Waals-like PV diagram revealing the thermodynamic paths to ablation. Solid (S), liquid (L) and gas (G) phase ACE – binodal curve, BCD – spinodal curve, C critical point. Possible pathways to ablation are $a'-a-b-c$; $a'-a-d-d'$; $a'-a-d-f-e$. The 1-2 line represents the portion on isotherm passing the unstable region.

Spinodal decomposition has been also invoked to occur for femtosecond laser pulse ablation. Here the system is brought into the unstable region of the phase diagram, where it undergoes density fluctuations and phase separation [VJL01].

These processes are still controversial for ablation with ~ 100 fs laser pulses. In the following chapters, we will show that experimental results on kinetics of particle emission suggest the occurrence of fast non-equilibrium processes at the surface. Since the mechanisms triggered directly by electronic transitions cannot account for all the details of the observed kinetics, phase explosion can be considered an alternative mechanism.

CHAPTER 2

INSTRUMENTATION

Experiments of femtosecond laser induced ablation were carried out on different solid targets placed in an ultra-high vacuum chamber. This chapter presents the laser system and focusing conditions and, on the other hand, the surface analytical instruments.

A linear Time-of-Flight mass spectrometer could help to analyze the ablated charged particles. Here, we present the instrument performances and the methods used to estimate the kinetic energy distribution of charged particles.

The surface morphology after ablation was investigated by using different microscopes.

2.1. LASER SYSTEM

The ultra-short laser pulses used for the experiments described this work were provided by a titanium-doped sapphire (Ti:Sapphire) laser system. Ti:Sapphire has a broad absorption bandwidth in blue and green, thus the optical pumping can be supplied by standard solid-state continuous-wave (CW) lasers.

The femtosecond laser system is a commercial, ‘all solid-state’ Ti: Sapphire laser system (Spectra Physics) using the CPA technique³. Pulses of less than 80 fs duration and higher than 75 kW in peak power, corresponding to energies in the nano-Joule range, are provided by a mode-locked Ti: Sapphire laser (Tsunami, Model 3960, Spectra-Physics). The oscillator is pumped by the 532 nm radiation delivered by a CW Nd:YVO₄ laser⁴ (Millenia V, Spectra Physics).

The mode-locked Ti: Sapphire laser runs at a repetition rate of about 82 MHz, ensured at laser start-up and maintained for extended periods by an acousto-optical modulator. For achieving near transform-limited (*chirp* free) Gaussian pulses, two pairs of prisms are used. For a Gaussian pulse, the fundamental relation $\Delta\tau_p \times \Delta\nu > 0.441$ applies (here $\Delta\tau_p$ is the laser pulse width and $\Delta\nu$ is the spectral bandwidth). The spectral bandwidth $\Delta\nu$ of the 80-fs output pulse can be greater than 10 nm. By making use of optimized mirrors, a standard output wavelength range of 720-850 nm has been chosen for the experiments described in this work. As specified by Spectra-Physics, the output laser beam diameter is less than 2 mm (at $1/e^2$ from its intensity), with less than 0.6 mrad divergence (measured at full angle) and up to 5 % pulse-to-pulse stability.

³ As needed for many applications, the femtosecond pulse energy is increased by using the technique of Chirped Pulse Amplification (CPA). Here, additional energy is efficiently transferred to the femtosecond pulse in a regenerative amplifier (a laser active media inside a resonator with a long storage time). In addition, the CPA technique removes an important obstacle: A 1-mJ, 100-fs pulse focused to a 50- μ m spot-size delivers a power density of about 10^{12} W/cm². The damage threshold of most optical materials is only a few GW/cm², i.e. a thousand times lower. By stretching the pulse in time, the enormous peak power of the input pulse is decreased and secondary nonlinear effects are minimized, this preventing the damage of the amplifier’s optics.

⁴ The Millennia laser takes advantage of high-efficiency diode pumping and intracavity frequency-doubling and provides a high power output (greater than 5 W).

The femtosecond ‘seed’ pulses are injected into a Ti: Sapphire regenerative amplifier (Spectra Physics, Spitfire). A frequency-doubled, Nd: YLF laser (Merlin, Spectra-Physics) delivers the optical excitation at 532 nm to the Ti: Sapphire resonator, at a repetition rate of 1 KHz. In the amplifier, the input (seed) ultra-short laser pulse is stretched in time (*chirped*), using a single grating. The pulse amplification in the multi-pass Ti: Sapphire resonator and the subsequent recompression in the single grating compressor gives rise to an output of 1mJ energy and pulse duration of >120 fs at full width at half maximum (FWHM). The output beam is linear (horizontal) polarized with a Gaussian spatial intensity profile and 3% pulse-to pulse stability.

To measure the temporal and spectral intensity of the ultra-short pulse, standard pulse measurements for spectral bandwidth and pulse length were carried out. The pulse duration was extracted from the width of an autocorrelation trace given by a Single-Shot Autocorrelator (Model 409, Spectra Physics). Here a Gaussian temporal shape has been considered with a deconvolution factor of 0.65, this being the ratio between the real pulse width and the autocorrelation width of a Gaussian function.

For some of the experiments, we used a second Ti: Sapphire laser system⁵ delivering pulses of >50 fs duration, at 20 Hz and energy of ~200 mJ/pulse. Here the energy distribution in the near-field is Gaussian with a beam parameter M^2 of 3.6.

The laser energy could be varied using a combination of a half wave-plate and two dielectric thin film polarizers. They were placed in the femtosecond laser pulse amplifier before the pulse compressor in order to minimize the pulse distortion on optical components.

The intensity profile of the focused laser beam is nearly Gaussian as determined by using a CCD camera (Spiricon) placed in the focal plane (Figure 2.1). For a Gaussian distribution, the energy depends on fluence as follows:

$$\mathcal{E} = \iint_{x,y} F(x, y, z) \cdot dx \cdot dy = F_0 \left(\frac{\pi w^2}{2} \right) \quad (2.1)$$

The electric field propagation of a Gaussian beam can be described in a simple way by:

⁵ LUCA system from CEA, Saclay.

$$E(r) = E_0 \cdot \exp \left[-2 \left(\frac{r}{w} \right)^2 \right] \quad (2.2)$$

where w is the beam waist along the beam propagation direction. The radius w of a Gaussian beam and the wavefront radius of curvature R at a certain position on the propagation direction z are given by the fundamental relations:

$$w^2(z) = w_0^2 \left[1 + \left(\frac{\lambda z}{\pi w_0^2} \right)^2 \right] \quad (2.3)$$

$$R(z) = z \left[1 + \left(\frac{\pi w_0^2}{\lambda z} \right)^2 \right]$$

with w_0 the beam waist at $z = 0$. The minimal R occurs at $z = z_R$, where z_R is the characteristic Rayleigh length $z_R \propto \pi w_0^2 / \lambda$. Also $2z_R$ is an important quantity known as the confocal parameter, i.e. the size of the interval $(-z_R, z_R)$ or the so-called Rayleigh range.

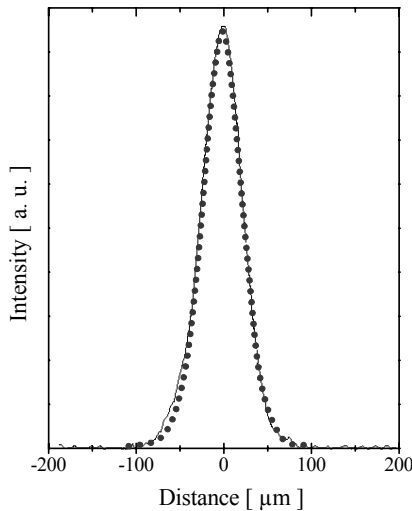


Figure 2.1. Intensity profile of a ~120-fs laser beam (800 nm) in the focus of a convergent +300 mm lens. The dotted line is a Gaussian fit to the signal recorded using a camera (Spiricon).

For $0 \leq z \leq z_R$, the beam waist varies between $w_0 \leq w \leq w_0 \sqrt{2}$. The half divergence angle in the focused beam is given by $\theta = \lambda / (\pi w_0)$.

As used in the following experimental set-up, a beam with a diameter of ~5mm focused by a convergent lens of +300 mm focal distance has a waist of about ~30 μm , with a confocal parameter $2z_R$ of 7.2 mm. By applying the fundamental relationship given by Eq. 2.3, a diffraction-limited beam within the Rayleigh range has a diameter of ~60-86 μm .

2.2. LASER-DESORPTION ANALYSIS

For analyzing the dynamics of laser ablation from solid surface, mass spectrometry is frequently used owing to its high detection sensitivity for low laser intensities.

2.2.1. Time-of-Flight mass spectrometer

A time-of-flight (ToF) mass spectrometer is an analytical instrument of choice for studying laser desorption from solid surfaces.

A single-stage extraction, linear ToF mass analyzer was used in the experiments described in this work.

A *single-stage extraction* ToF mass spectrometer has the advantage that, as long as the ions do not come across other electrical fields, such as reflectrons or other electrical sectors, the ion trajectories could be better controlled with effect on increasing ion transmission. On the other hand, in a *linear* ToF mass spectrometer, the (metastable) ion fragments produced in the extraction or drift region will arrive at the detector at the same time as their parent ions. Since we deal with relatively low molecular masses (up to a few thousands) and femtosecond laser ablation appears to yield low fragmentation, a linear ToF mass spectrometer is appropriate for these experiments.

2.2.2. Experimental setup

The laser desorbed electrons, negative and positive particles could be analyzed with the help of the linear ToF mass spectrometer (for a more detailed description see [Hen03]).

The schematic of the experimental setup is presented in Figure 2.2. A laser beam was focused onto the target placed in an ultra-high vacuum (UHV) chamber (Figure 2.2 (1)). The target position could be manipulated, with micrometer precision, in translation on x - y - z axes and rotation about the z -axes. A CCD camera (or a He-Ne laser beam) was used to visualize and position the target.

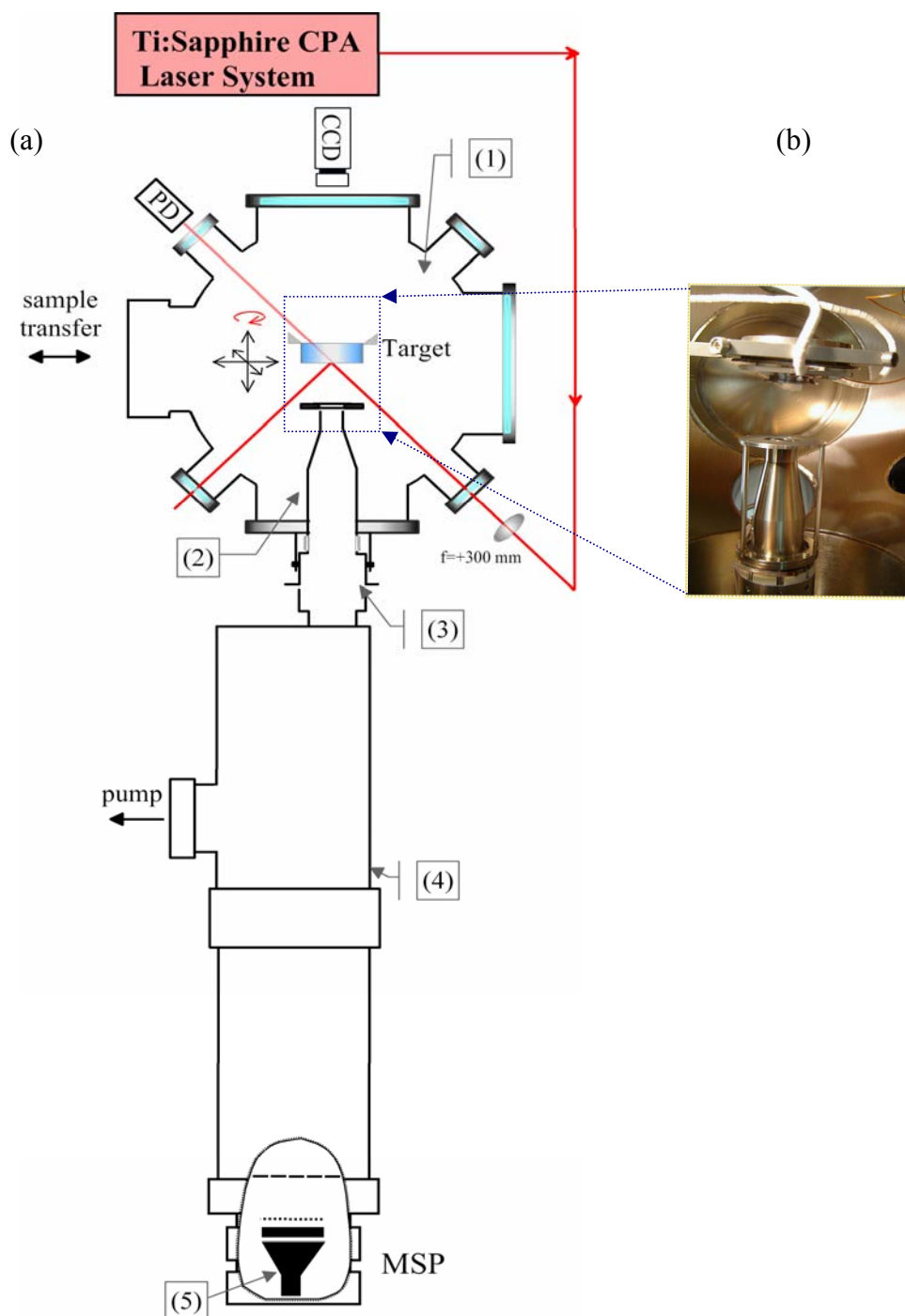


Figure 2.2. Schematic of the general experimental set-up. The laser beam is focused onto the target (e.g. a transparent crystal) positioned in a UHV chamber (1). The target can be manipulated in translation on x-y-z and in rotation about the z-axes. A CCD camera is used for target alignment. A linear ToF mass spectrometer is connected to the UHV chamber. The laser-desorbed ion beam is collected in a conical skimmer (2), stirred in the ion optics region (3), and transmitted through a free field (drift) tube (4) to the MSP detector (5); (b) Photograph of a transparent target sample aligned in front of the entrance aperture of the ToF mass spectrometer.

A linear ToF mass spectrometer is connected to the UHV chamber. This and the tube of the spectrometer are connected to pumps purging to a level of up to 10^{-10} mbar. An improved vacuum leads to elongated ion mean free path, thus a lower risk of collision within the ionization and drift regions which implies a lower metastable or post-source fragmentation. The ultrahigh vacuum is achieved by turbo-molecular pumps (260 l/s) with fore-pumping given by membrane pumps.

In the schematic from Figure 2.2, we represent the different sectors of the ToF mass spectrometer: the conical skimmer (Figure 2.2. (2)), the collimation optics consisting of two electrostatic lenses (Figure 2.2. (3)), the flight tube (Figure 2.2 (4)), and a micro-sphere plate (MSP) detector in a cross-section of the tube (Figure 2.2 (5)).

A schematic of laser-target interaction geometry and the electrostatic fields in the ToF mass spectrometer is given in Figure 2.3. In a short source ionization region ($s = 2.8$ cm) in Figure 2.3 (a), a high voltage of about $U \sim 2.5-3.5$ KV of the same sign as the ions needed to be analyzed, is applied on the repelling plate. Here, the metallic target holder plays the role of a repelling plate. The entrance aperture of the ToF mass spectrometer being grounded, a high and relatively homogeneous electric field ($E = U/s \sim 1000$ V/cm) is established in front of the target. The ions accelerated in this field are then directed into the field-free region (a drift tube of length $D = 1.42$ m), where they separate according to their m/Z ratio. Finally, they arrive at the MSP detector⁶ and the resulting signal, a complete mass spectrum, is visualized and processed using a fast oscilloscope⁷. Provided that the mass resolution is given by $m/\Delta m = t/2\Delta t$, the uncertainties in time for ion formation are minimized by using the long flight tube, which results in longer flight time t for the individual masses, while maintaining a relatively constant time difference Δt between ions of the same kind.

⁶ A double thickness Micro-Sphere Plate (MSP) detector is used for ion detection. This is a compact electron multiplier, which can be set for positive ion detection (in a grounded anode configuration) or negative ion detection (in a high voltage anode configuration) as specified by the producer (El-Mul Technologies). The microsphere plate is a thin porous plate of sintered 50 microns glass beads. It is placed between two plates ('front' and 'back'), which help applying a high electric field across it. The secondary emitted electrons are collected at a conical anode. The MSP detector is suitable for pulse counting applications and single particle detection. Current amplification exceeds 10^7 at the maximal operating voltage of 3.6 KV.

⁷ LeCroy, 400 MHz.

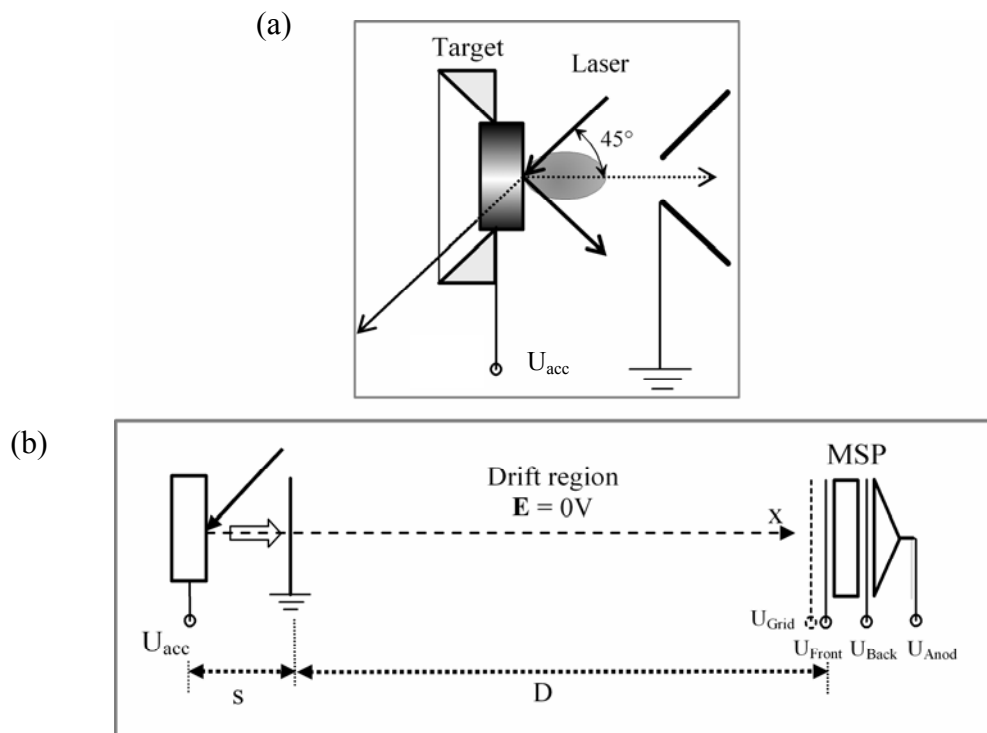


Figure 2.3. (a) The geometry of the laser beam incident at 45° on a transparent target, placed in a metallic target holder of cylindrical symmetry. A bunch of ions is removed from the target by the laser pulse and accelerated toward the entrance of the spectrometer; (b) Schematic of electrostatic fields in a single-stage extraction ToF mass spectrometer. The ejected ions are accelerated at U_{acc} on a short distance s (cf. (a)) and then fly freely to the detector.

This ToF spectrometer provides a mass resolution of about 300, which is sufficient for the purpose of our experiments.

The target sample is placed in a metallic target holder of a cylindrical geometry to ease the sample alignment (see Figure 2.3 (a)). For a minimal distortion of the initial temporal and spatial ion distribution, an equipotential extraction surface and a homogeneous extraction field are desired. However, since the target holder is here the repeller, the extraction field exhibits inhomogeneities⁸, in particular for insulating targets. The effect is a lower extraction field at the sample center of about 4% from U_{acc} as compared to the edges [Hen03]. This effect should be taken into consideration in the measurements of ion kinetic energy distribution (see next subsection).

⁸ As an effect of the cylindrical target holder (repeller plate) geometry, the extraction field lines will be slightly bent in the region of the hole.

To improve the detection sensitivity (increased ion transmission), the ToF mass spectrometer is equipped with collimation (ion) optics consisting of two Einzel lenses of rotational symmetry. Their geometry is presented in a simulation obtained by using a SIMION 6.0 program, in Figure 2.4.

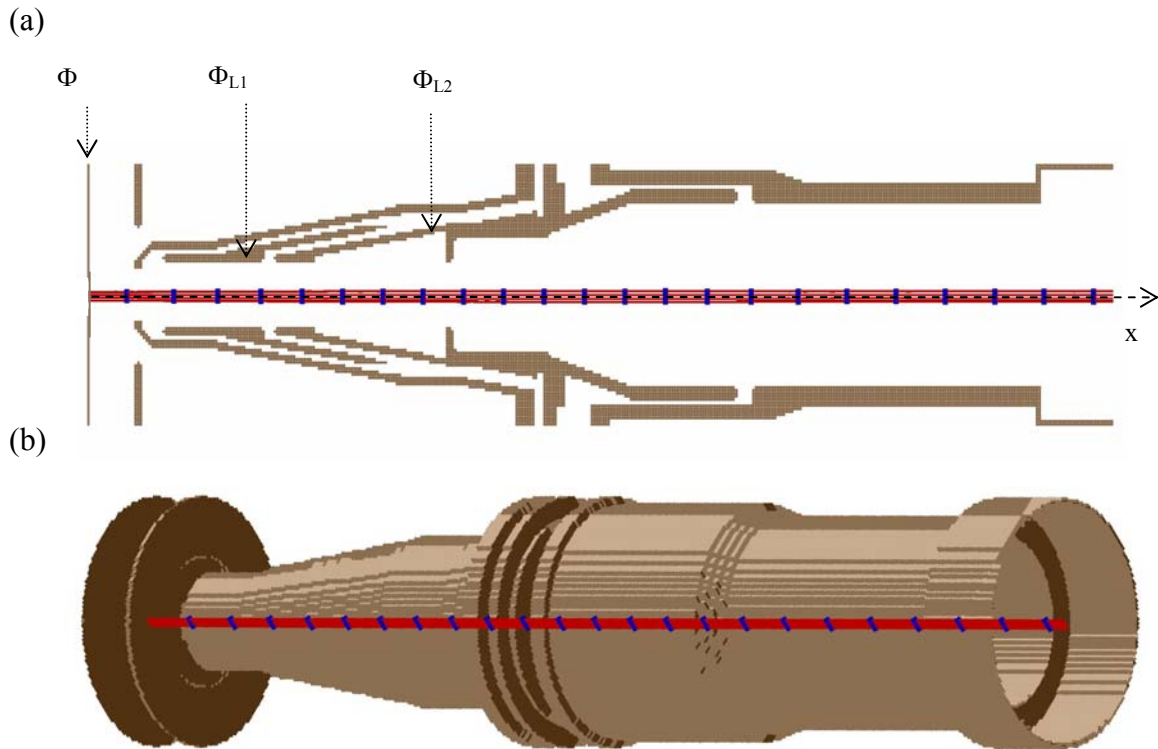


Figure 2.4. The ion extraction and ion optics segments of the ToF Mass spectrometer used in this work, in a 2D (a) and 3D (b) simulation of equipotential surfaces (using the SIMION 6 program). The picture from (a) shows a cross section of the simulated ion extraction region and ion optics, two electrostatic lenses of rotational symmetry.

The red lines represent the calculated trajectories of four $^{138}\text{Ba}^+$ ions of initial energy of 3 eV, flying at the same time from left to right toward the detector. They form at different locations in regard to the repelling potential surface. The flight path length on this image is 370 mm on the x-axes. The potentials at the different surfaces were set as following: $\Phi = + 2.5$ kV (repelling potential), $\Phi_{L1} = 2$ kV respectively $\Phi_{L2} = 0\text{V}$ (potential surfaces simulating the electrostatic lenses); marked with blue bullets are 3 μs -step instances in the ion trajectory. All the other surfaces are set at 0 potential.

In the 3D simulation (b), for better visibility, the ion trajectories are made observable by representing ‘transparent’ potential surfaces.

To indicate the geometry of the extraction region and ion optics, Figure 2.4 shows simulated equipotential surfaces representing the repelling plate (repelling potential at Φ) at 28 mm from the entrance aperture of the spectrometer and the electrostatic lenses as potential surfaces Φ_{L1} and Φ_{L2} . Ions of given initial conditions (i.e. formation time, space,

angle and kinetic energy), entering adjustable fields, are stirred axially toward the detector by choosing appropriate potentials. Figure 2.4 shows an example of calculated trajectories for four $^{138}\text{Ba}^+$ ions with initial energy of 3eV, flying at the same time and from different

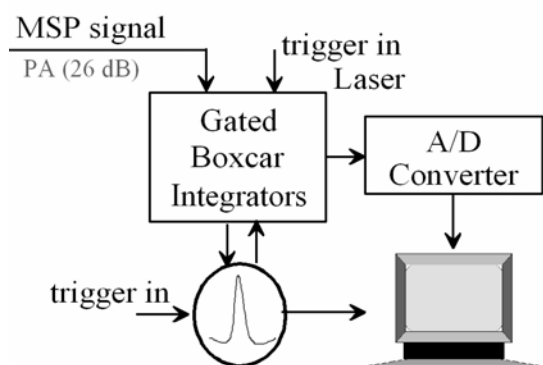


Figure 2.5. Schematic of the recording electronics setup. The MSP signal could be amplified (26dB preamplifier), gated, visualized and processed via integrators and a 400MHz oscilloscope.

locations along the repelling potential surface. The ion trajectory simulation assumes for the following potentials: $\Phi = +2.5$ kV (repelling potential), $\Phi_{L1} = 2$ kV respectively $\Phi_{L2} = 0$ V (potential surfaces simulating the electrostatic lenses). In this case, the simulation shows that the ions are flying on the trajectories indicated with a velocity of ~ 5.2 km/s.

The ions collected at the detector are recorded in a setup similar to that shown in Figure 2.5. The ToF spectra can be visualize on a fast oscilloscope, then recorded and processed.

In Figure 2.6, as an example, we present a segment from a ToF spectrum of positive ions obtained by laser desorption from a silicon target and the conversion to a mass-to-charge spectrum. Each spectrum is averaged over 1000 pulses and shows singly charged Si^+ , Si_2^+ and isotopes.

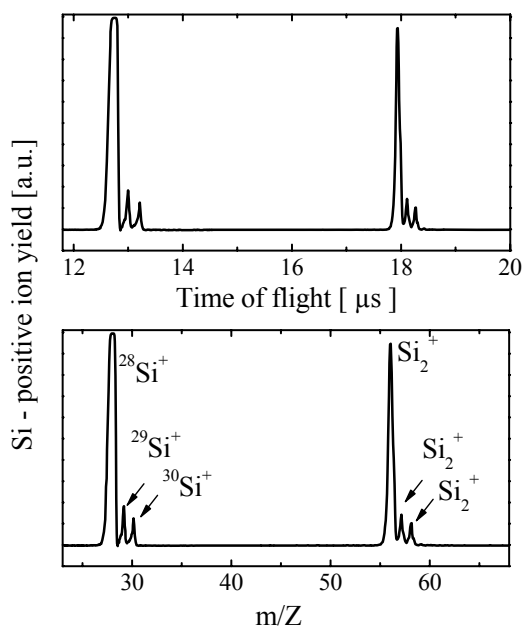


Figure 2.6. A typical ToF spectrum and the corresponding mass spectra revealing silicon ions and isotopes.

Signals within selected time-of-flight ranges can be recorded synchronously using gated integrators of nanosecond resolution.

2.2.3. Kinetic energy measurement methods

As shown before, once removed from the surface, the ions of mass m and charge $q = Ze$ are accelerated in a short extraction region s by a potential difference U and injected in the free drift region of length D . If the desorbed ions have an initial kinetic energy K_0 , the final kinetic energy after acceleration is $K = K_0 + qU$. The difference in flight times of an ion accelerated from rest with one having a non-zero initial kinetic energy gives the difference in arrival times (Δt) due to kinetic energy spread. It is simple to show that, for $s \ll D$, the mass resolution can be approximated by:

$$\frac{m}{\Delta m} = \frac{2t}{\Delta t} \cong \frac{eU}{K_0} \quad (2.4)$$

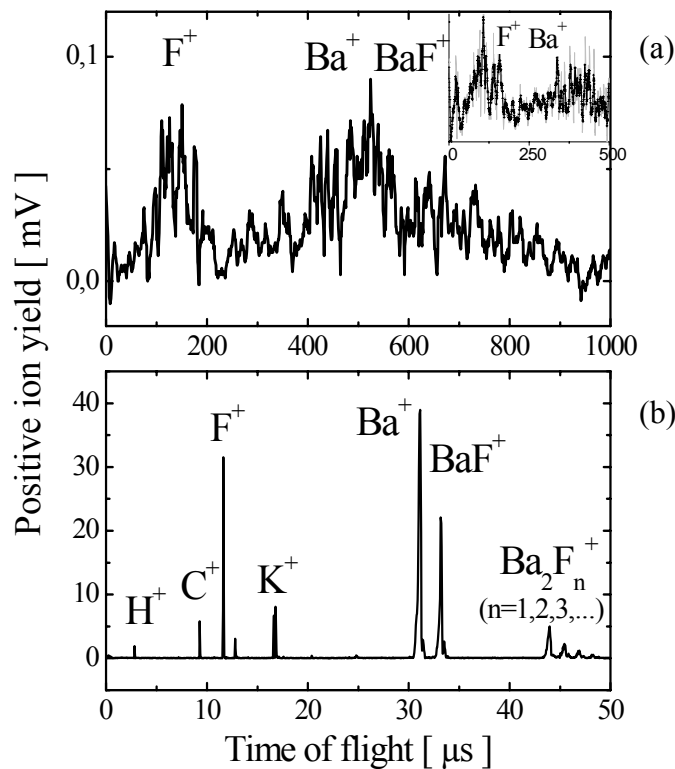


Figure 2.7. Positive ion ToF spectra from a BaF_2 target obtained by laser desorption (~ 120 -fs pulse duration, 800 nm , at $\sim 2 \text{ TW/cm}^2$) recorded in (a) ‘drift’ mode and (b) ‘acceleration’ mode with $U_{\text{acc}} = +2.9 \text{ kV}$. The inset in (b) shows a magnified segment of the drift spectrum. Evidently, the mass discrimination is much clearer in (b). It can also be used to perform a rough mass calibration of the ‘noisy’ spectrum from (a).

Ideally, an ion desorbed with an initial kinetic energy K_0 should not need any additional acceleration. In this case, it travels the distance $s + D \cong D$ in a time $t_d = D$

$(m/2K_0)^{1/2}$ (the so-called ‘drift’ mode). As a numerical example, if K_0 is at the order of tens of eV, then the time in which a Ca^+ ion travels the drift length of 1.5 m is at the order of hundreds of microns. Thus, the ion initial kinetic energy K_0 could be estimated by recording t_d . In the case of no additional acceleration, however, the ion flight time increases and so does the ion kinetic energy spread. Thus, the signal-to-noise ratio gets worse and the mass resolution can drop significantly.

Figure 2.7 shows comparatively ToF spectra of positive ions obtained by laser desorption in the same irradiation conditions, recorded in a ‘drift’ mode (Figure 2.7 (a)) and in an ‘acceleration’ mode where the ions were additionally accelerated at $U_{acc} = +2.9$ kV (Figure 2.7 (b)). The difference in mass resolution is significant. However, a mass discrimination can be also observed in the ‘drift’ ToF spectrum, indicating that the ion initial kinetic energy is important. Therefore in Chapter 3, we use ‘drift’ ToF spectra to analyze the kinetic energy of laser desorbed ions.

The ion kinetic energy can be estimated using the effect of a variable potential U_{RETARD} applied on a grid placed in front of the MSP detector (Figure 2.3 (b)). When recording mass spectra, U_{RETARD} is kept at zero. A variable U_{RETARD} gives rise to a retarding potential on a short distance in the free field before the detector. This could slow down or even stop ions of the same sign to come across it. The ion signal dependence on the retarding (stopping) voltage U_{RETARD} can be fit with a sigmoid curve given by:

$$y(K) = \frac{y_{\min} - y_{\max}}{1 + \exp\left(\frac{K - K_0}{dK}\right)} \quad (2.5)$$

where y_{\min} and y_{\max} are the minimum respectively the maximum of the sigmoid. The ion initial kinetic energy distribution can be derived from the function $y(K)$.

When using this method, the ion kinetic energy at the detector should be described by $K_{ion} = K_0 + qU_{eff}$, where K_0 is the actual birth ion energy and U_{eff} is given by:

$$U_{eff} = U_{acc} + \sum_i U_i^{add} \quad (2.6)$$

where the influence of additional electrostatic fields U_i^{add} must be taken into consideration. These additional fields are induced by inhomogeneities in the extraction field such as the

lens effect in the case of dielectric targets, which has been already pointed out, or further effects related to the ion beam deflection by the retarding field itself.

To deduce the actual ion kinetic energy distribution K_0 by using the retarding potential effect on selected peaks from the mass spectra obtained in ‘acceleration’ mode is therefore challenging. However, this method could be applied on ion peaks selected from ‘drift’ mass spectra⁹.

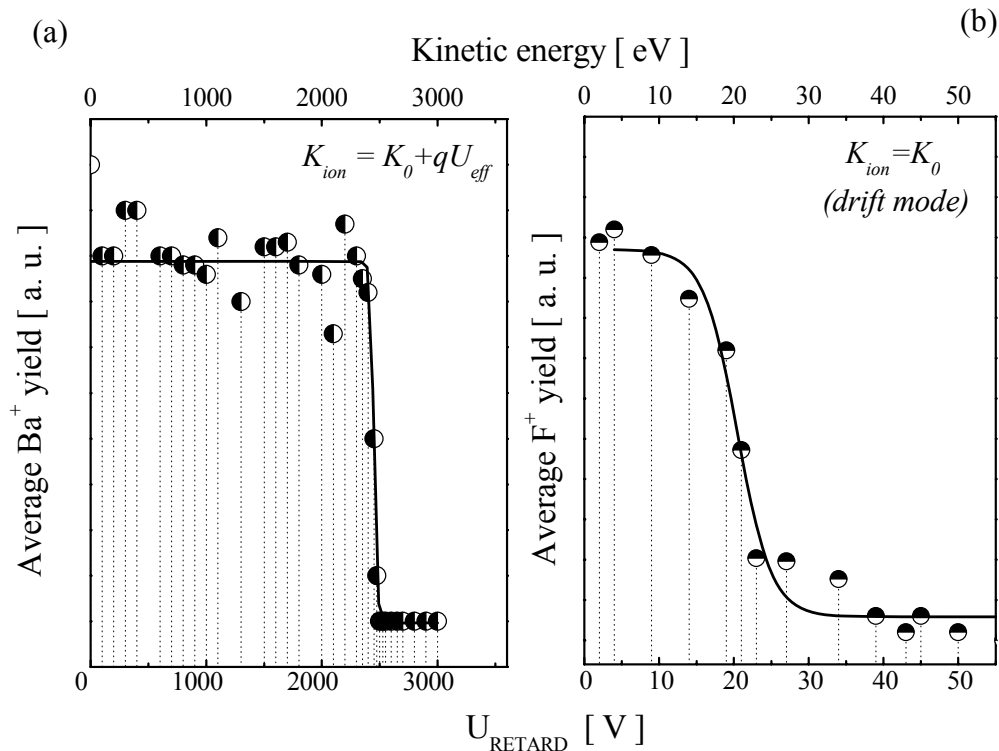


Figure 2.8. Ion yield as a function of retarding potential variation for: (a) a Ba^+ ion yield (BaF_2 target) selected from a mass spectrum obtained by using $U_{acc} = +2.9$ kV; (b) a F^+ ion (BaF_2 target) selected from a ‘drift’ spectrum.

Figure 2.8 shows for comparison the effect of retarding potential variation on an ion peak selected from a mass spectrum obtained in ‘acceleration’ mode and one selected from a ‘drift’ spectrum. The fit on the experimental data is a sigmoid function given by Eq. 2.9.

To obtain the kinetic energy of the ion using Figure 2.8 (a), we need to apply an important correction factor to account for positive velocities for the desorbed ions, as we

⁹ The kinetic energy evaluation using drift mass spectra can be altered by recombination processes between negative and positive ions in the drift tube as they are no more separated. In our experiments this situation is more probable to occur for high laser intensities.

believe these ions should have. Instead, for the F^+ from drift mass spectra, the data show ions of high kinetic energies K_0 .

Sample materials

The aim of this work is to understand basic physical aspects of laser matter interaction. Thus, we performed experiments on different target materials such as:

- Freshly cleaved single crystals of CaF_2 (111), BaF_2 (111), polished MgF_2 cut along c-axes, polished sapphire Al_2O_3 cut along c-axes;
- Low doped Si (100) wafers with a native oxide layer. In some cases the oxide layer was removed in the conventional way, i.e. by etching it in a solution of 25% HF.
- High purity aluminum foils.

The **dielectric targets** were acquired from Korth Kristalle and Mateck. The transmission ranges of the crystals are: BaF_2 : 0.11 - 7.5 μm ; CaF_2 : 0.2-11 μm ; MgF_2 : 0.11 μm - 9.5 μm ; Al_2O_3 : 0.2 μm – 5 μm .

Surface morphology analysis

The surface morphology investigation was performed by means of:

- Optical microscopy
- White-light interference microscopy
- Scanning electron microscope (Cambridge Stereoscan S360).
- Atomic force microscope in contact and non-contact mode (NT-MDT Smena).

CHAPTER 3

LASER-INDUCED PARTICLE EMISSION FROM NON-METALLIC SURFACES

The femtosecond laser pulse interacting with dielectric materials provokes the desorption of surface constituents. Experimental data demonstrate that, as an effect of initial excitation, electrons and energetic positive ions are released from the surface region of the target.

The excitation process and surface charging effect are greatly enhanced by pre-existing or laser-induced transient and permanent defects. We analyze the role of defects on surface decomposition from the dependence on the number of pulses of both the particle yield and damage threshold intensity.

The intrinsic mechanisms of ion desorption exhibit higher complexity with increasing intensity. Thus, positive ions with bimodal velocity distribution are detected. In addition, the negative ion ejection becomes more significant. The dynamics of negative and positive-ion yields indicate essential differences in the origin and desorption mechanisms.

The results are discussed in the frame of microscopic models for ion desorption, the Coulomb explosion of a charged surface and thermal processes.

Common mechanisms for particle desorption from non-metallic solids are identified by additionally exploring the impact of femtosecond laser pulses on silicon surfaces.

It has been previously indicated that upon interaction with femtosecond laser pulses, processes such as lattice destabilization and removal of surface constituents, both as charged and neutral particles, as well as plasma formation can be separated from the excitation processes.

The objective of this chapter is to give experimental support to the idea that femtosecond laser pulses interacting with solids give rise to a strong perturbation in the interaction volume, corresponding to a state of *non-equilibrium* with the surrounding dielectric (and semiconductor) material, by addressing details of the lattice deformation and decomposition after the initial excitation. These experimental findings will be used to explain the surface morphology after interaction in Chapter 5.

This chapter considers different aspects of the kinetics of charged particles desorbed from the surface of single crystal fluorides (BaF_2 and CaF_2) and silicon. The experiments were carried out at laser intensities *below and near* the surface optical breakdown, i.e. the single shot damage threshold and plasma onset, which is typically at the order of 10 TW/cm^2 for most insulating materials.

The linear ToF mass spectrometer described in the previous chapter helps to analyze the electron, positive and negative-ion yields. The following experiments deal with different issues such as: the excitation processes and origin of particle yields; surface charging effects; the nature and role of defects, which mediate the ionization process and desorption of ions; the explosive character of ion emission and different intensity-dependent aspects; different characteristics of ion ejection from silicon as compared to dielectrics.

3.1. CHARGED PARTICLE DESORPTION FROM DIELECTRIC SURFACES

3.1.1. Laser-desorbed positive ions

In these experiments, single ionic crystals of freshly cleaved BaF_2 (111) and CaF_2 (111) were used as target materials. Relative ion yield measurements were performed under a multi-shot mode *N-on-1*, i.e. applying *N* pulses of the same energy on a surface site.

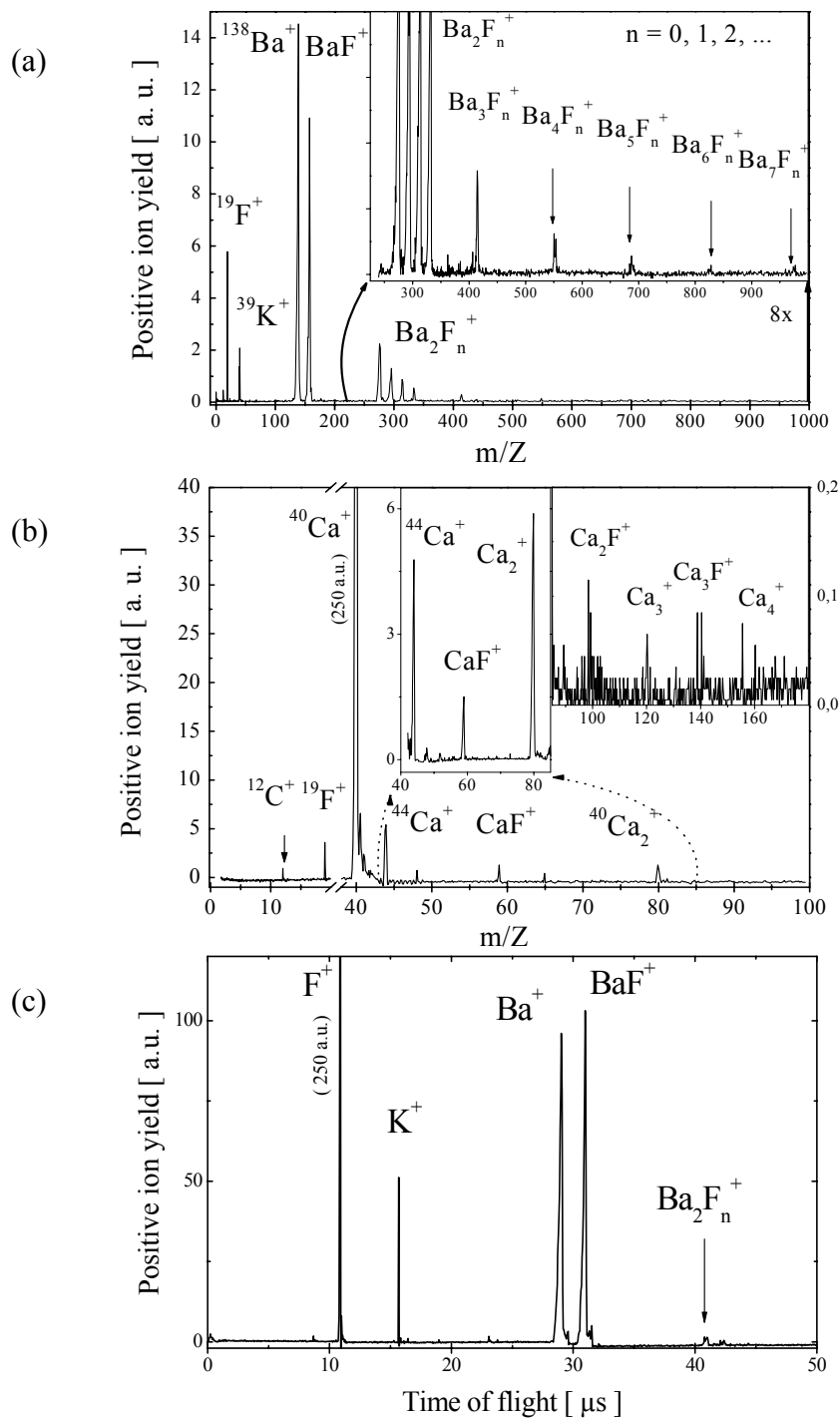


Figure 3.1. Positive ion mass spectra obtained from BaF_2 (a) and CaF_2 (b) upon femtosecond laser desorption (~ 120 -fs, $h\nu \sim 1.55$ eV at ~ 1 TW/cm² intensity). The insets represent magnified sections from the corresponding spectra. Note that only singly charged ions and clusters are desorbed. (c) ToF spectrum from a BaF_2 target revealing positive ions detected upon excitation with $h\nu \sim 3.1$ eV.

As shown in Figure 3.1, one result of the interaction of 120-fs laser pulses (800 nm, i.e. $h\nu \sim 1.55$ eV; p -polarization) with the target surface is the ejection of a substantial amount of positive ions. In our ToF mass spectrometer, positive ions could be detected for intensities above ~ 0.2 TW/cm² for BaF₂ and above ~ 0.5 TW/cm² for CaF₂. For both materials, the positive ion mass spectra are typically dominated by *singly charged* atomic ions and small clusters such as: ¹⁹F⁺, ¹³⁸Ba⁺ and BaF⁺ ions from a BaF₂ (111) target (Figure 3.1 (a)) and ¹⁹F⁺, ⁴⁰Ca⁺ and CaF⁺, respectively from a CaF₂ (111) target (Figure 3.1 (b)). Additional, less abundant positive species were detected for instance: (i) Ba⁺ isotopes, Ba_nF_m⁺, and Ba_n⁺ clusters (from a BaF₂ sample); (ii) Ca⁺ isotopes, Ca_nF_m⁺, and Ca_n⁺ clusters (from a CaF₂ sample) where $n, m = 1, 2, 3, \dots$. The ion yield increases with the incident intensity, both as amplitude and widths.

For different conditions of laser excitation, the general aspect of a positive ion mass spectrum does not notably change, however certain differences occur. For instance, upon excitation with ~ 120 -fs pulses at 400 nm ($h\nu \sim 3.1$ eV¹⁰), *the F⁺ peak can be the main desorption product*, as shown in Figure 3.1 (c) for a BaF₂ target. This suggests *a larger desorption cross-section for F⁺* at 3.1 eV excitation as compared to 1.55 eV excitation, for the same incident intensity.

Also, from surfaces irradiated with p -polarized beams, the recorded ion yields are higher than with s -polarized beams at the same intensity level. It is worth noting that a similar result is reported in [AWA00].

To understand the ion emission origin and desorption mechanism, it is very important to identify the corresponding excitation processes. Resuming from Chapter 1, Section 1.1.1, for femtosecond laser pulses at near IR wavelength and laser intensities below 1 TW/cm², multiphoton ionization (MPI) is expected to be the main source for free electron generation. The number of excitations per second is given by $N^{(n)} = \sigma_n (I/h\nu)^n$ for multi-photon excitation of order n , with the ionization cross-section σ_n . Thus, it appears feasible to identify the main ionization processes from the electron and ion yield dependence on the incident intensity.

¹⁰ The double frequency of 400 nm was obtained by placing a nonlinear crystal (LBO) at a phase matching angle in front of the laser beam.

Figure 3.2 displays log-log plots of the charged particle yields versus the incident intensity I , for electron, Ca^+ and F^+ yields from a CaF_2 target, in different excitation conditions. Linear fits on the experimental data show slopes greater than unity, which indicate a non-linear ionization processes. Upon 1.55 eV excitation, the dependence on laser intensity of the electron signal¹¹ exhibits a slope of $n \sim 8$ (Figure 3.2 (a)). This result indicates an 8-photon ionization process. Indeed, this would correspond to a band-to-band ionization process in CaF_2 , providing that the bandgap for the bulk CaF_2 is $E_g \sim 12$ eV [Rub72]. By giving just an overall indication of the MPI order, our result does not exclude a possible reduction (or increase) of the multiphoton ionization order to 7 (or 9). This is quite reasonable since due to pre-existing surface defects, the surface bandgap in CaF_2 can shrink to $E_g \sim 10$ eV [CCL05 and references therein¹²].

As shown in Figure 3.2 (a) for low intensities, the electron yield dependence on the intensity reduces its non-linear character to $n \sim 2$, signaling a lower order MPI process. Actually, a reduction of the MPI order could occur if the ionization process is mediated by resonances provide by defect states located within the bandgap. The nature of laser-induced defects in fluorides is analyzed in Section 3.1.3.3. For the moment, we note that, as concluded from photoemission experiments [KHM86], in CaF_2 a surface F -center lies about 8.3 eV above the valence band. The ionization of a surface F -center with 1.55 eV photons would imply a two-or three-photon process. This low order ionization process can occur with larger probability for low intensities.

For 1.55 eV excitation, the slope of the log-log plot of the Ca^+ yield increases with intensity as $n \sim 10$, indicating a power law of: $N_{\text{Ca}^+} \sim I^{10}$ (Figure 3.2 (b)). In addition, for 3.1 eV excitation, the non-linear effect appears of the form $N_{\text{Ca}^+} \sim I^8$ (Figure 3.2 (c)). An essential observation is that Ca^+ yield increases already *highly non-linearly* within the intensity range where the electron yield non-linearity is low. At this intensity range the suggested defect-mediated ionization process appears to be sufficient to produce an important hole density.

The F^+ yield increases also non-linearly with the incident intensity, following a power law of $N_{\text{F}^+} \sim I^6$ as illustrated in Figure 3.2 (b). For high intensities, the ion signal

¹¹ The electron yield is obtained by integrating the corresponding peak from a mass spectrum (see subsection 3.1.4.1).

¹² In this work, we used freshly cleaved samples of CaF_2 which, as compared to polished surfaces, should contain a relatively lower defect density [CCL05].

appears to ‘saturate’ in a threshold-like manner. The Ca^+ yield ‘saturation’ threshold intensity of $\sim 1.2 \text{ TW/cm}^2$ is marked in Figure 3.2 (b)¹³. It is evident that the ‘saturation’ threshold for Ca^+ nearly coincides to the detection threshold intensity for F^+ yield. Also the CaF^+ and larger clusters yields develop at this intensity level more clearly, suggesting an increased disruption of the surface.

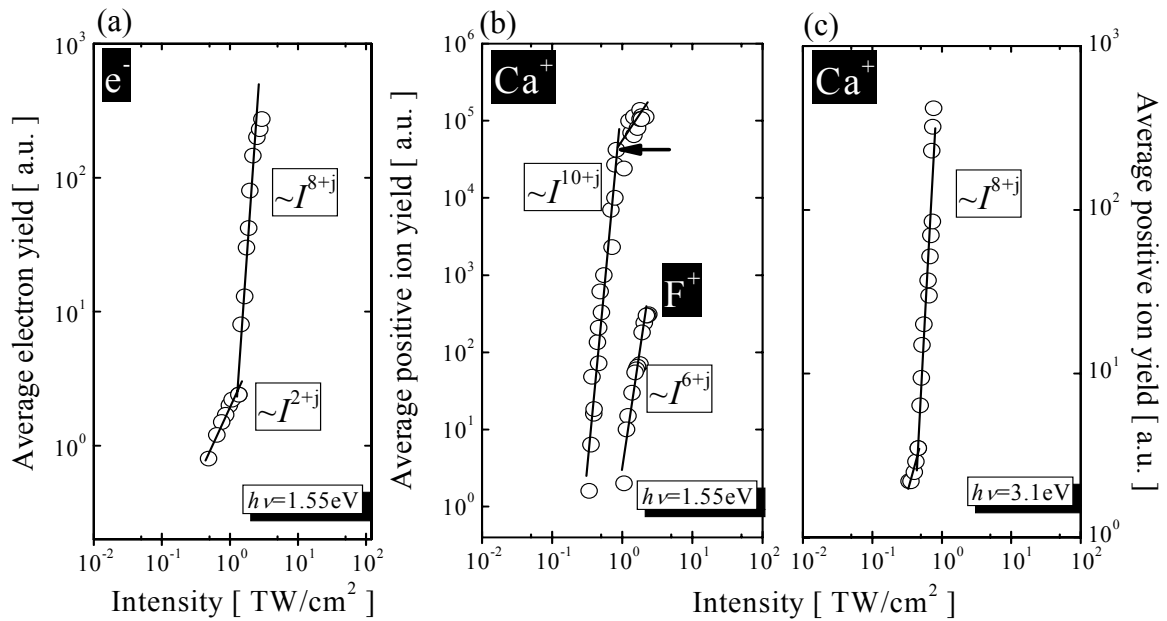


Figure 3.2. Log-log plots of electron yield (a) positive-ion yield (b, c) as a function of laser intensity after excitation with 1.55 eV (a, b) and 3.1-eV photon energy (c), respectively, from a CaF_2 target. The slopes suggest multiphoton ionization as the main laser excitation process¹⁴; the integer $j = \pm 1$ accounts for the uncertainty in the order of ionization.

Similar measurements, carried out for a BaF_2 target [HRW00, HCR02] under 1.55 eV excitation here indicated correspondingly: (i) a 6-7-photon process, which is likely the band-to-band ionization in BaF_2 ($E_g(\text{BaF}_2) > 9 \text{ eV}$); (ii) a highly nonlinear increase of the positive ions with intensity and a ‘saturation’ phase for above 0.5 TW/cm^2 .

¹³ As the ion yield still increases with the intensity in this ‘saturation’ phase, this does not appear to be the saturation of the detector.

¹⁴ While the ToF instrument is adequate for positive ion detection, it provides only a reduced transmission for the light electrons. Consequently, poorer electron detection sensitivity is expected.

3.1.2. The explosive character of charged particle emission

The kinetics of emitted charged particles help to better understand the basic desorption mechanisms. Hitherto, we have shown that as an effect of fs-laser excitation, multiple positive ions are detected. This happens even for incident intensities of several orders of magnitude below the damage threshold for a single pulse, when the surface is apparently unchanged.

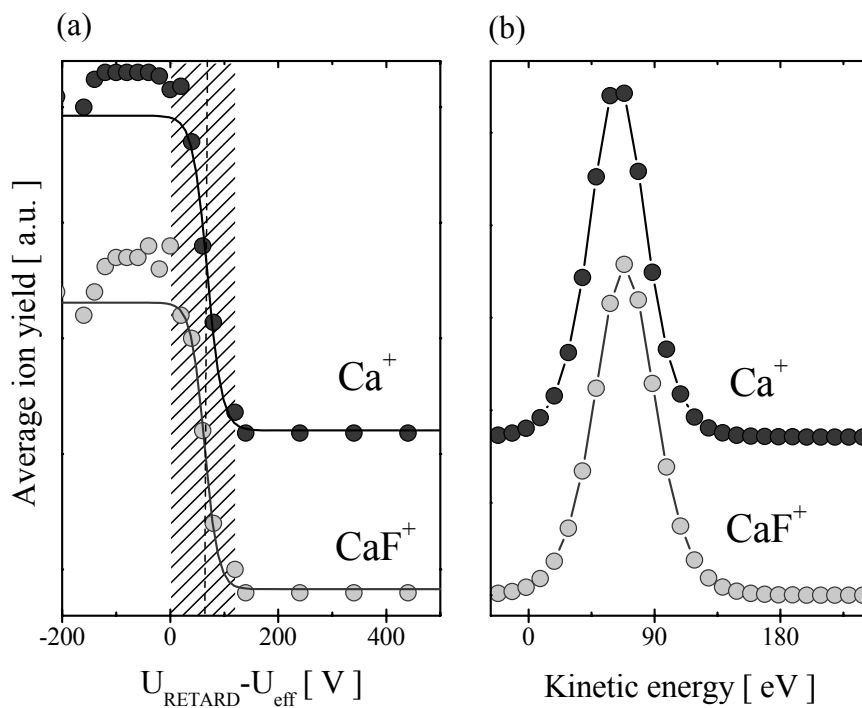


Figure 3.3. (a) The effect of the retarding potential variation¹⁵ on Ca^+ and CaF^+ yields at $2\text{TW}/\text{cm}^2$ intensity. The data points were obtained by integrating the corresponding peaks from positive ion ToF spectra – see also Figure 3.1, and averaging over 1000 pulses. (b) Ion kinetic energy distribution as extracted from the sigmoid fits on the two sets of data in (a).

To estimate the positive ion velocity distribution, we used the effect of a variable retarding (stopping) potential on the ion yield. As indicated in the previous chapter, an appropriate potential could stop the ions of the same sign and corresponding velocity from coming across and reaching the detector.

¹⁵ Here, the retarding voltage applied U_{RETARD} is already corrected by an effective acceleration voltage U_{eff} (see Chapter 2); thus the ion kinetic energy can be estimated from $K_{\text{ion}} (\text{eV}) = U_{\text{RETARD}} - U_{\text{eff}} (\text{V})$.

The retarding potential analysis on Ca^+ and CaF^+ yields, as selected from a mass spectrum is presented in Figure 3.3. The ion signals were recorded synchronously to permit a direct comparison.

Basically, both ion yields responded in the same way to the retarding potential variation. From a sigmoid fit on the experimental data, we can derive the ion kinetic energy distribution (see Chapter 2). The results show that these singly charged ions are emitted at *nearly equal kinetic energies*, independent on their mass. Also their mean translational kinetic energy is high of about ~ 60 eV (Ca^+) and ~ 68 eV (CaF^+).

Ion kinetic energy distribution obtained from ‘drift’ ToF spectra

The estimate of ion kinetic energy with a method described above requires a correct evaluation of the effective acceleration voltage, U_{eff} (with $U_{\text{eff}} = U_{\text{acc}} + U^{\text{ad}}$, see Chapter 2), needed to be extracted from the retarding voltage. Since this can be a difficult task, additional experimental data were obtained by applying the retarding potential to analyze positive-ion yields selected from ToF ‘drift’ spectra. Figures 3.4 and 3.5 present such data for a CaF_2 (111) and BaF_2 (111) surface, respectively. As indicated in the previous chapter, the ‘drift’ ToF spectra, although not providing a satisfactory mass resolution, permit a direct estimate of initial ion kinetic energies. The inset in Figure 3.4 (a) displays a ‘drift’ ToF spectrum, obtained for 2.5 TW/cm^2 , where the prominent peak is attributed to Ca^+ (a main product of fs-laser desorption from a CaF_2 surface). The effect of a variable retarding potential on the Ca^+ peak can be used to estimate the kinetic energy distribution as shown in Figure 3.4 (a). The resulting narrow velocity distribution is well described by a modified Maxwell-Boltzmann¹⁶, where the ejected particle velocity (v) is corrected by a center-of-mass (drift) velocity, u :

$$f(v) = C \cdot \exp\left[\frac{-m \cdot (v - u)^2}{2kT_u}\right] \quad (3.1)$$

with u and T_u (the distribution width, regarded as a temperature) taken as fit parameters.

¹⁶ Although, no visible crater appears to form at this intensity range, the ion flux may be still high. This reasons the use of a modified Maxwell-Boltzmann distribution.

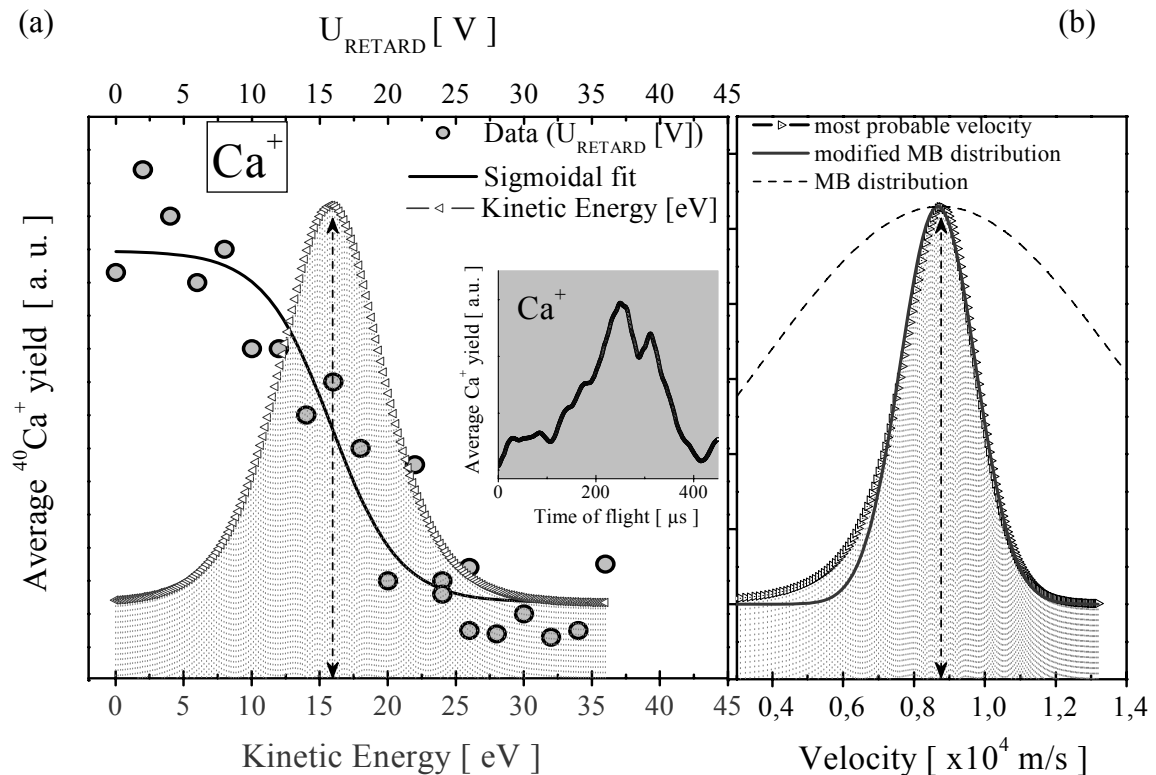


Figure 3.4. (a) The effect of retarding potential variation on the Ca^+ yield from a CaF_2 target (bullets). These data are obtained by integrating the Ca^+ peak selected from ‘drift’ ToF spectra with a typical example shown in the inset; they represent an average over 1000 laser pulses of intensity $I = 2.5 \text{ TW/cm}^2$. The energy distribution (scattered line) is derived from a sigmoid fit (solid line) to the experimental data.

(b) Ion velocities (scattered line) as derived from the kinetic energy distribution in (a). A modified Maxwell-Boltzmann (solid line) is used to fit the velocity distribution. The corresponding fit parameters are here: $u \cong 9 \times 10^3 \text{ m/s}$ (velocity shift: stream velocity) and $T_u \cong 5350 \text{ K}$ (distribution width).

For comparison, a thermal Maxwell-Boltzmann distribution yielding the same maximum velocity is represented by a dashed line.

Using Eq. 3.1 as a fit function, we obtain the ion velocity distribution here centered around $u_{\text{max}} = 9 \times 10^3 \text{ m/s}$ and a narrow width as compared to the corresponding thermal distribution, of about 0.6 eV (5350 K). The mean translational energy is here about 16 eV, clearly *smaller* than the result presented before in Figure 3.3 and obtained for nearly the same intensity but using the ‘acceleration’ mode of the ToF spectrometer. One reason for this difference can be the uncertainty in evaluation of the actual acceleration voltage.

Figure 3.5 presents, as another example, a similar measurement of the velocity distribution for the F^+ ion as desorbed from a BaF_2 target at nearly the same intensity of

about 3 TW/cm^2 intensity. The ion peak was selected from the corresponding positive ion ‘drift’ ToF spectra (inset in Figure 3.5 (a)). Here, the F^+ ion seems to be ejected from the target surface with a maximum velocity of $u_{max} = 15 \times 10^3 \text{ m/s}$. The width of the distribution is $T_u \sim 0.32 \text{ eV}$ (3800 K), while the corresponding mean translational energy is high at the order of 20 eV.

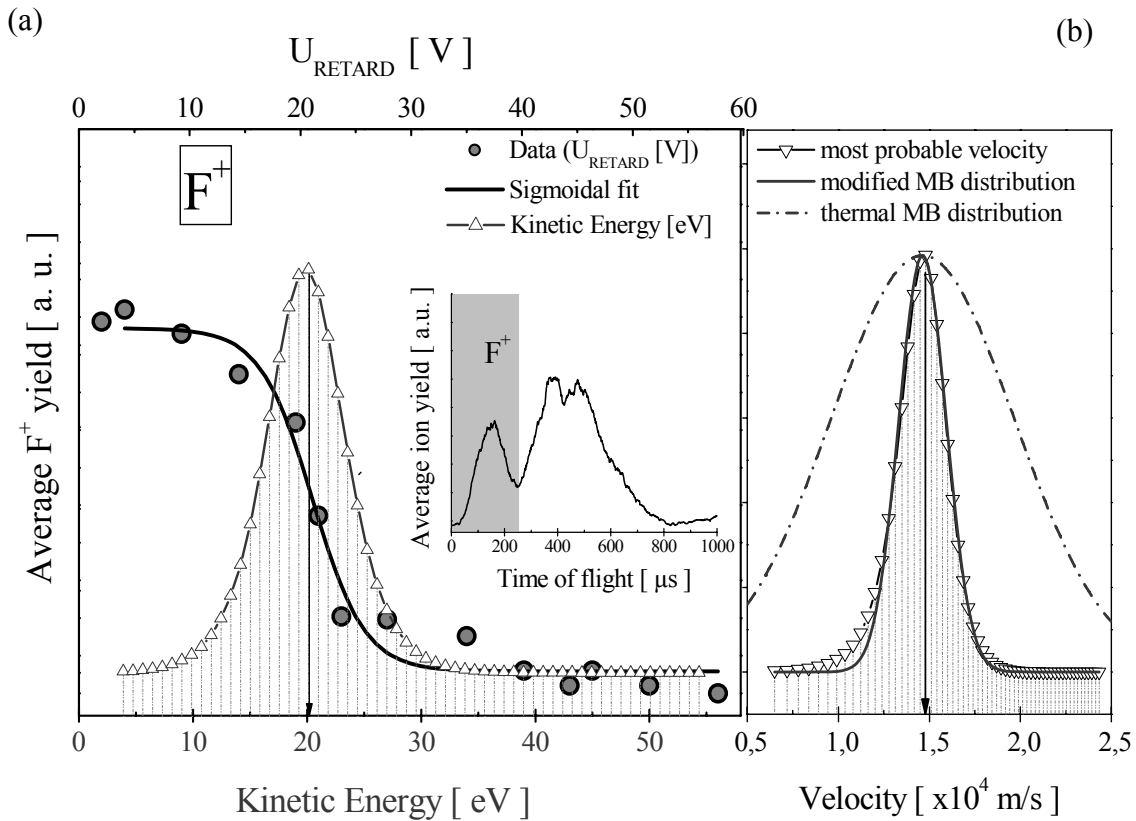


Figure 3.5. (a) The effect of retarding potential variation on the F^+ yield from a BaF_2 target (bullets). The data are obtained by integrating the corresponding F^+ peak selected from positive ion ‘drift’ ToF spectra as shown in the inset. These spectra were acquired by averaging over 1000 pulses at intensity $I = 3 \text{ TW/cm}^2$. The energy distribution (scattered line) is derived from a sigmoid fit (solid line) to the experimental data.

(b) Ion velocities (scattered line) as derived from the kinetic energy distribution in (a). A modified Maxwell-Boltzmann (solid line) is used to fit the velocity distribution. The corresponding fit parameters are here: $u \cong 15 \times 10^3 \text{ m/s}$ (velocity shift) and $T_u \cong 3800 \text{ K}$ (distribution width).

For comparison, a thermal Maxwell-Boltzmann distribution yielding the same maximum velocity is represented by a dashed-dotted line.

So far, the experiments have shown that femtosecond laser pulses interacting with fluoride targets give rise to the ejection of a large amount of *energetic* positive ions. This happens even for laser intensities of several orders of magnitude below any surface damage can be detected.

In the following sections, we will show that the dynamics of ion yields are strongly dependent on the irradiation conditions and surface preparation.

3.1.3. Factors enhancing ion desorption

Photo-absorption and generation of conduction band electrons are influenced by factors such as the pre-existing or radiation produced defects. This is well-known to affect surface optical breakdown and lower the damage fluence threshold for multiple laser pulse interaction [GGS87, ALR99, ASR00, GNA02].

3.1.3.1. Incubation: the role of laser-induced defects

The dramatic increase of the positive-ion yield with the number of laser pulses is known as ‘incubation’. This is an intensity-dependent effect, supposedly associated with an accumulation of defects on the surface region. For instance, in Figure 3.6 we show that Ba^+ and Ca^+ yields, respectively, from BaF_2 or CaF_2 targets irradiated at low laser intensities, increase with the number of laser pulses applied on the surface. For low incident intensities, the ion signal starts to develop in form of individual spikes only after applying a large number of pulses on a site (as in Figure 3.6 (a) for Ca^+ yield at 1.1 TW/cm^2). By further irradiation, the ion yield suddenly increases. Depending on the incident intensity and after a certain number of incubative pulses a quasi-steady ion yield in average is reached. When this quasi-steady regime is achieved at further irradiation no significant change is observed anymore, situation resembling a saturation effect¹⁷. This is shown in Figure 3.6, from measurements of Ba^+ and Ca^+ yields as a function of the number of pulses for different incident intensity.

¹⁷ Here, the ion yield is not in the saturation limit of the MSP detector.

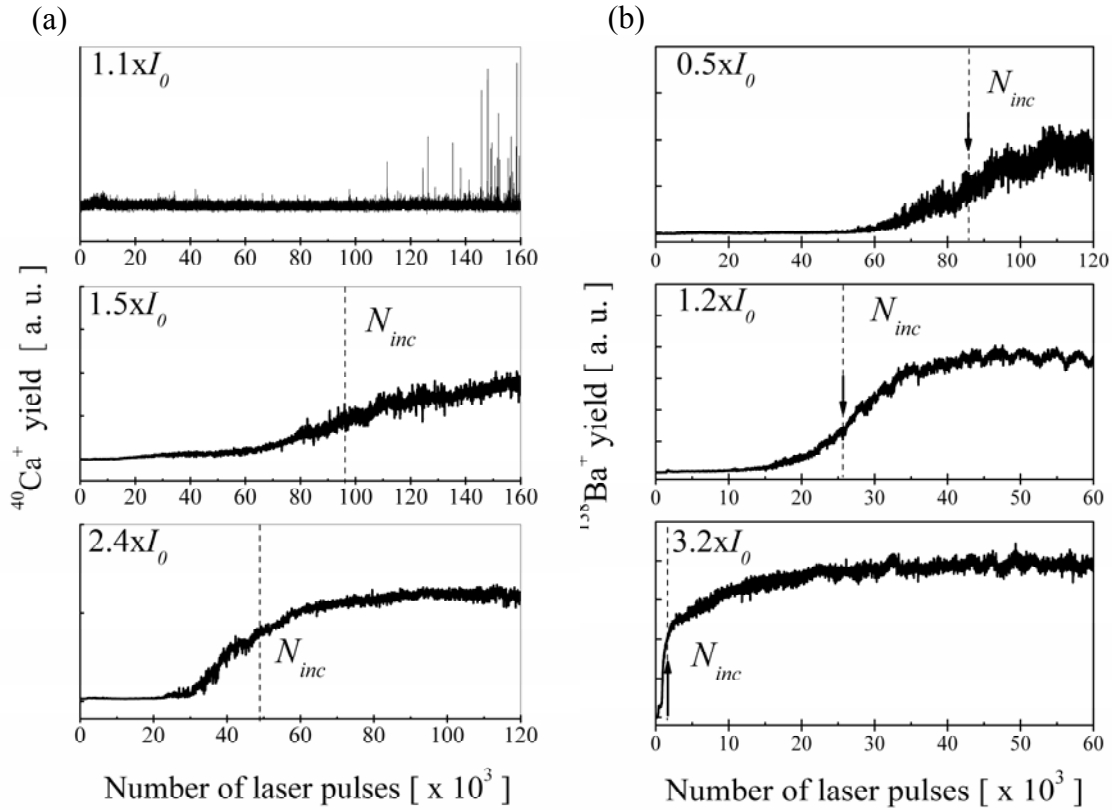


Figure 3.6. Incubation behavior of Ca^+ ions from a CaF_2 target (a) and Ba^+ ions from a BaF_2 target (b) at different laser intensities indicated in the panels ($I_0 = 1 \text{ TW/cm}^2$). Here, the ion peaks were selected from the ToF spectra and integrated pulse by pulse.

A number of incubative pulses N_{inc} , used to quantitatively describe the incubation, is set at a mean value between an averaged minimum and maximum ion yield, respectively.

A common interpretation for the incubation effect is that first laser pulses create defects on the surface, which increase in number at further irradiation until the defect density locally saturates. Here, the empirical observation is that ions desorb when a certain surface defect density is *locally* reached¹⁸. Simply, if the ion yield is proportional to the number of defects accumulated on the surface, the defect creation rate for N laser pulses depends on the number of existing defects as follows:

$$\frac{dn_d}{dN} = -k \cdot n_d \quad (3.2)$$

¹⁸ At this intensity, since no real crater can be detected, the ions seem to be desorbed only locally.

where k is a constant dependent on the incident intensity. Accordingly, the solution of Eq. 3.2 gives $n_d \sim n_{d0} \exp(-kN)$ with $k = k(I)$ and n_{d0} the initial defect concentration. If the number of defects increases with the laser intensity, it follows that $I(N) \sim n_d(N) \propto \exp(-aN)$, with a being a constant. On the other hand, if we assume a characteristic number N_{inc} as the mean value between the averaged minimum and maximum ion yield (see Figure 3.6), and represent the intensity $I(N_{inc})$ as a function of N_{inc} , we find such an exponential decay both for Ba^+ from a BaF_2 target and Ca^+ from a CaF_2 target (Figure 3.7)¹⁹.

Thus, we basically observe the usual effect of *reduction of damage threshold intensity* in dielectrics for multiple pulses irradiation. Several models explaining the incubation effect have been reported until now. However, to our knowledge, these models

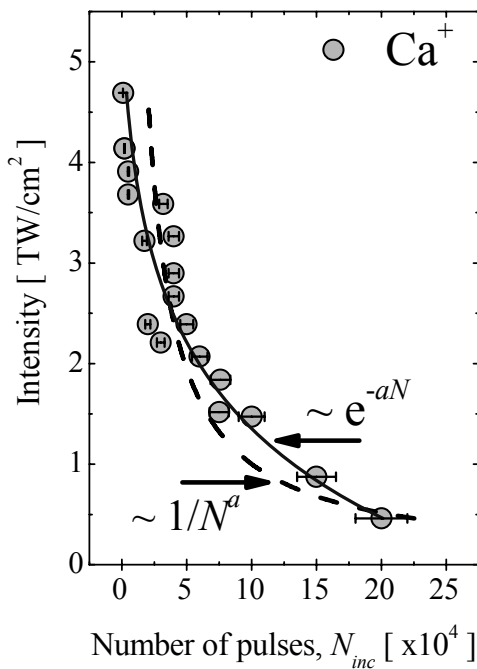


Figure 3.7. The intensity dependence on the number of incubative pulses in the Ca^+ yield fitted with an exponential decay and a power law.

provide limited insight into the microscopic processes of energy dissipation and defect creation. An exponential decay is included by [PER89] in a model taking into account a non-linear absorption mechanism, where the energy per absorber (defect) is considered to depend nonlinearly on the incident intensity. On the other hand, a power function is proposed in a statistical model developed in [JBW88] for ablation of metals. Accordingly, we also compare our data to a function of the form $I(N_{inc}) \propto 1/N_{inc}^a$ in Figure 3.7. A clear attempt to identify the microscopic processes was made by considering the volume expansion due to microscopical structural changes (defect

creation) and thermally generated stress in laser irradiated alkali halides [JBC89].

For a comparison, we examined the incubation effect from the point of view of *surface damage* induced after multiple pulses irradiation, which is presented in the

¹⁹ Also important variations in incubation data could occur from structural defects such as kinks and steps specific of a cleaved surface.

following section. Afterwards, we introduce a model to describe incubation as due to pulse-by-pulse accumulation of defects of lifetime longer than the period between pulses.

3.1.3.2. Influence on damage threshold intensity

As already stated, incubation is the effect of surface alteration provoked by a repetitive exposure to a number of laser pulses.

3.1.3.2.1. Multi-pulse damage threshold intensity

We measured the damage threshold intensity of fluoride samples for a single pulse (1-on-1) and multiple pulse (N -on-1) ablation.

To estimate the damage threshold intensity, we used a method similar to [MHL03]. Here, the damage (ablation) threshold is defined as the applied intensity which gives a minimal modification of the surface. If the Gaussian beam irradiance distribution in a plane perpendicular to the propagation direction Oz is given by:

$$I(r) = I_0 \cdot e^{-2\frac{r^2}{w_0^2}} \quad (3.3)$$

with w_0 is the beam waist, for a threshold intensity I_{th} , Eq. (3.3) transforms to:

$$I_{th} = I_0 \cdot e^{-2\frac{r_{th}^2}{w_0^2}} \quad (3.4)$$

where r_{th} is the radius of the minimal surface modification. Considering the spot diameter $D_{spot} = 2r_{th}$, Eq. 3.4 can be written as:

$$D^2 = 2w_0^2 \cdot \ln \frac{I_0}{I_{th}} \quad (3.5)$$

This implies that the damage threshold intensity can be obtained by extrapolating to zero a linear fit on the semi-logarithmic plot of the squared laser spot diameter with the incident intensity.

By using an AFM, we studied the morphology of the ablated crater, specifically the diameter of the ablated crater, after ~ 120 -fs single pulse irradiation at different laser intensities. From the resulting plots, we obtained a damage threshold intensity of ~ 36 TW/cm² for CaF₂ and ~ 29 TW/cm² for BaF₂, respectively. For more details on these measurements see also [Eck06].

Our damage threshold intensity estimates appear to be up to a factor of two higher than those reported in the literature for CaF_2 and BaF_2 for the same excitation conditions [AVR96, JCH06]. Although these experiments seem to be similar to ours, several important differences must be noticed. In this work, we used cleaved surfaces, which are known to include a lower density of defects [CCL05], as compared to the polished surfaces used for instance in [JXL03]. Consequently, at a cleaved surface the material bandgap can be wider, which means that the ionization would require higher intensities, i.e. a higher damage threshold intensity.

Moreover, the damage threshold has been estimated using different definition criteria and measurements methods. Thus, surface damage has been observed by employing

different methods such as: a Nomarski microscope [TBK99], an AFM and SEM [VAR96], or plasma emission [LMN99], which usually led to different results for the single-pulse damage threshold intensity.

On the other hand, some references estimate the damage threshold intensity after multiple laser pulse ablation [SFH96], which differ essentially from the damage threshold given by a single laser pulse [TBK99].

To increase the number of data describing the incubation effect, in this work, we measured the multi-shot damage threshold intensity for a BaF_2 target. Thus, we applied a number of known pulses on a site and analyzed the induced damage, ex-situ, using an AFM. Figure 3.8 shows semi-logarithmic plots of the estimated squared ablated crater

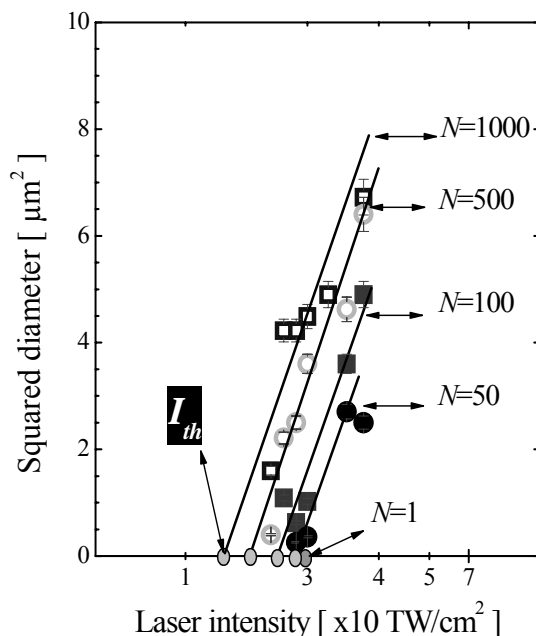


Figure 3.8. Semi-log plots of squared diameter of craters' area as a function of intensity (BaF_2 sample irradiated with multiple 120-fs laser pulses). The number of pulses applied N is 50, 100, 500 and 1000 pulses. The extrapolation to zero of the linear fits on the experimental data gives the multi-shot laser ablation threshold intensity. The single-shot ablation threshold obtained in a separate measurement (see also [Eck06]) is also indicated.

diameters as a function of intensity. From the extrapolation to zero of the linear fits, we obtained the damage threshold intensity. Taking $I_{th}(N)$ as the intensity to produce a minimal surface damage after irradiation with N laser pulses, then: $I_{th}(1000) < I_{th}(500) < I_{th}(100) < I_{th}(50) < I_{th}(1)$. This indicates the typical reduction of the threshold intensity with increasing the number of irradiating laser pulses.

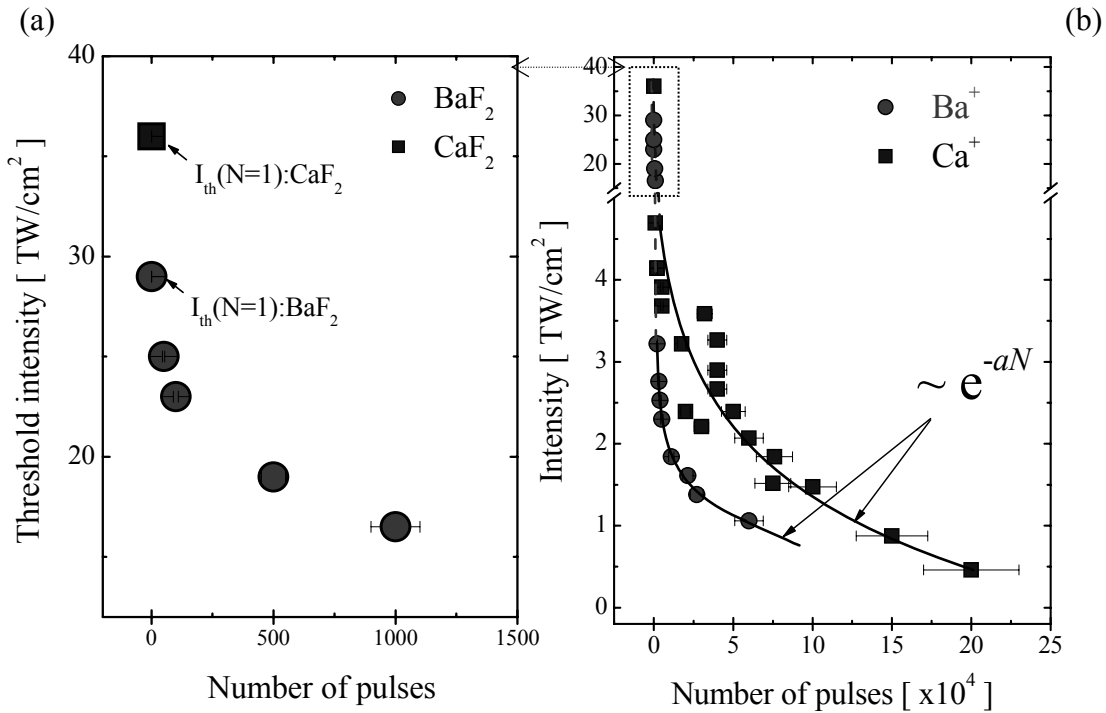


Figure 3.9. (a) The effect of damage threshold intensity reduction with the number of pulses for BaF₂ (see also Figure 3.8). The single pulse damage threshold intensity for CaF₂ is also presented.

(b) The data from (a) are plotted together with the ‘incubation’ data for the Ca⁺ and Ba⁺ yield, i.e. the intensity dependence on the number of ‘incubative’ pulses (for clarity see also Figures 3.6 and 3.7). The lines represent exponential decay fits on the experimental data.

In Figure 3.9, we compare: (a) *the damage threshold intensity* as a function of number of pulses, and (b) the intensity dependence on *the number of (incubative) pulses* necessary to bring the ion yield, Ca⁺ from a CaF₂ target and Ba⁺ from a BaF₂ target, respectively, in the quasi-steady regime of emission (see the previous subsection and Figure 3.7).

From Figure 3.9 we can extract two important aspects:

- These sets of data (from panel (a) and (b), respectively) describe the same incubation effect, thus both could be explained as due to defect accumulation on the surface;

- The damage threshold intensity is clearly lower for BaF₂ as compared to CaF₂, as is the ion detection threshold, already a well-known fact [PER89]. In addition, for a certain intensity level, from the incubation data we also find that a lower number of incubative pulses are required to reach the quasi-steady regime in the Ba⁺ yield as compared to the Ca⁺ yield.

3.1.3.2.2. *Incubation model*

The effect of cumulative exposure to many laser pulses can be discussed from different points of view such as: (i) for the electronic excitation, a pulse-to-pulse increase of the excited electron density might occur, if the relaxation process is accomplished via intrinsic defect states with an effective decay time comparable or longer than the inter-pulse time period (cf. our observation described in section 3.1.3.3); (ii) for the crystalline lattice, this would mean a more important structural deformation due to an increased number of permanent defects. This latter is generally considered in the statistical models for incubation.

Based on our experimental results, we attempt to describe incubation considering excitation and recombination processes. We assume that the conduction band electron (CBE) density builds up by band-to-band multiphoton ionization (MPI), MPI mediated by defect states located within the bandgap and avalanche processes. Indeed, earlier density of states calculations [WRM89] show the existence of unoccupied defect states within the wide bandgap of fluoride materials. We apply the formalism proposed in [SFH96, LMN99] and discussed in Chapter 1, where the conduction band electron (CBE) density can be described by a rate equation (Eq. 1.10). Here, we add a term describing the recombination rate at defect states. The next section will show that defect states in fluoride materials, under our irradiation conditions, can last more than 50 ms (cf. section 3.1.3.3.).

Thus, we hypothesize long life-time recombination processes at defect states and neglect possible fast recombination processes. Then, we describe the defect population as a source on CBEs and take into the rate equation only the generation and relaxation of these defects. We consider important long lifetime defect state such as that associated to the

surface F -center in CaF_2 . As before indicated, a surface F -center lays at 8.3 eV from the VB edge [KHM86]²⁰. Therefore in our excitation conditions, this defect can be created via a 6-photon process.

In CaF_2 of a bandgap of $E_g \sim 10 - 12$ eV, a 7-photon process is taken as the band-to-band photoionization process. Using Eq (1.4), for the 7-photon ionization cross-section, we obtain $\sigma_7 \sim 10^{-142} \text{ cm}^{-14} \text{ ps}^6$ and for a 6-photon ionization cross-section $\sigma_6 \sim 10^{-121} \text{ cm}^{12} \text{ ps}^5$. To express the growth rate of CBEs density, we combine a multiphoton ionization and an avalanche rate with a recombination rate at defect states. This is:

$$\frac{dn(t)}{dt} = \alpha \cdot I \cdot n(t) + PI - R_d \quad (3.6)$$

Here, $PI = \sigma_7 \cdot \left(\frac{I}{h\nu}\right)^7 \cdot N_s$ is the 7-photon ionization rate with N_s the solid atom density (for CaF_2 , this is around $N_s \sim 2.4 \times 10^{21} \text{ at/cm}^3$). R_d is taken as the recombination rate at defect states with $R_d = \frac{dn_d}{dt} = -PI_d + \frac{n_d}{\tau_d}$, where $PI_d = \sigma_6 \cdot \left(\frac{I}{h\nu}\right)^6 \cdot N_s$ is the 6-photon ionization rate for generation defect, and τ_d is the defect state decay time.

For a Gaussian pulse given by:

$$I = I_0 \exp\left(-4 \ln 2 \frac{t^2}{\tau_p^2}\right) \quad (3.7)$$

an approximate solution of Eq. 3.6 can be written as follows:

$$\begin{aligned} n(t) &\approx (n_0 + n_{0,d}) \cdot \exp\left[\int_0^\infty \left(\alpha I - \frac{1}{\tau_d}\right) dt\right] \approx \\ &\approx (n_0 + n_{0,d}) \cdot \exp\left[\frac{\alpha I_0 \tau_p}{4} \left(\frac{\pi}{\ln 2}\right)^{1/2} \text{erf}\left(2 \ln 2 \frac{t}{\tau_p}\right) - \frac{t}{\tau_d}\right] \end{aligned} \quad (3.8)$$

where $n_0 = \int_0^{\tau_p} (PI) dt \approx \sigma_7 N_s \left(\frac{I_0}{h\nu}\right)^7 \left(\frac{\pi}{\ln 2}\right)^{1/2} \frac{\tau_p}{4}$ is the electron density due to

²⁰ We base our assumption on results of time-resolved absorption spectroscopy experiments on surface F -center formation by UV irradiation, which indicated that surface F -center forms in CaF_2 via a 2-photon process [KHM86].

photoionization, respectively $n_{0,d} = \int_0^{\tau_p} (PI_d) dt \simeq \sigma_6 N_s \left(\frac{I_0}{h\nu} \right)^6 \left(\frac{\pi}{\ln 2} \right)^{1/2} \frac{\tau_p}{4}$ is the electron density due to creation of defects, and $erf(n) = (2/\sqrt{\pi}) \cdot \int_0^n \exp(-x^2) \cdot dx$ is the standard error function. The avalanche coefficient in CaF₂ was determined experimentally in [SBM01] to be $\sim 2\text{cm}^2/\text{J}$.

Since the evolution function of the defect density growth rate with the number of pulses is unknown, we consider here, for simplicity, a linear increase. Thus, the CBE density after a number of pulses N , follows from Eq. 3.9 as:

$$n(t, N) \approx [n_0 + N \cdot n_{0,d}] \cdot \exp \left[\frac{\alpha I_0 \tau_p}{4} \left(\frac{\pi}{\ln 2} \right)^{1/2} erf \left(2 \ln 2 \frac{t}{\tau_p} \right) - \frac{t}{\tau_d} \right] \quad (3.9)$$

Depending on τ_d , the incident intensity and the number of pulses, an additional defect population can be present at the beginning of each subsequent pulse to contribute to building-up the CBE density. Figure 3.10 shows the temporal evolution of the conduction band electron density using Eq. 3.9, assuming that $\tau_p = 120$ fs and $\tau_d = 100\mu\text{s}$, for different intensities and number of pulses.

On the other hand, the ion emission for a single pulse possibly occurs, as suggested in Figure 3.9, close to the damage threshold intensity. Following the assumption that the damage threshold (surface optical breakdown) occurs when the critical electron density for plasma is reached [SFH96], we also calculate the temporal evolution of the CBEs density for a single laser pulse to yield n_{cr} , where $n_{cr} \sim 1.7 \times 10^{21} \text{ cm}^{-3}$ at a laser wavelength of 800 nm (Figure 3.10 (a)). Note that the corresponding intensity is roughly the single-shot ablation threshold for CaF₂. Here, it is evident that such an accumulation effect could provide an additional CBE density at the beginning of the next pulse. In fact, following these assumptions, for any intensity the critical density can be reached after a sufficient number of pulses.

The CBE density dependence on the number of pulses (Eq. 3.9) is presented in Figure 3.10 (b), for intensities below or equal to the single-shot ablation threshold intensity, at a time T equal to the period between two successive pulses (for 1kHz repetition rate, we take $T = 1\text{ms}$). It follows that, if there defect states of longer decay times

are available, the resulting defect population contributing pulse by pulse to building-up the CBE density would be even higher, so that a critical density would be reached after a lower number of pulses.

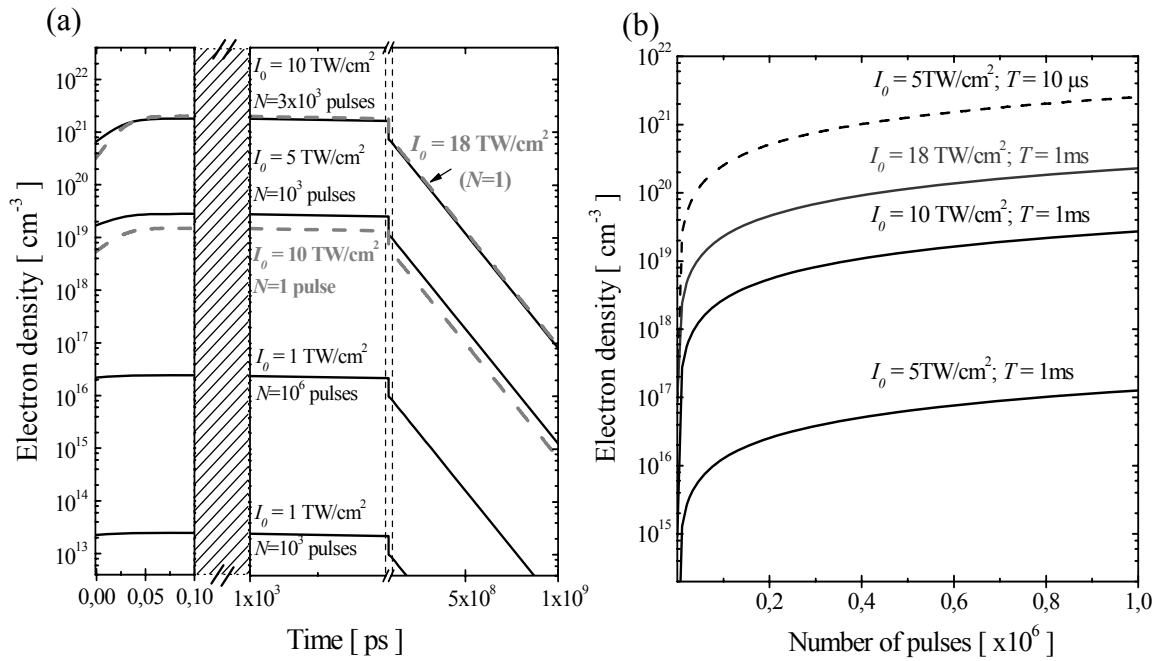


Figure 3.10. (a) The temporal evolution of the conduction band electron density at different incident intensities and number of laser pulses: $N = 10^3$ and 10^6 (solid lines). For 3×10^3 number of pulses of 10 TW/cm^2 the critical electron density is reached.

The temporal evolution of conduction band electron density for a single laser pulse, for two intensity levels, one corresponding to reaching the critical density of $n_{cr} \sim 1.7 \times 10^{21} \text{ cm}^{-3}$ (grey, dashed lines);

(b) Evolution of the electron density with the number of pulses for different intensities and time periods between successive pulses, T .

In conclusion, the electron and consequently ion yields appear to be enhanced via transient *defect states* located within the bandgap. If these defect states have a decay time longer than $> 0.1 \text{ ms}$, for our conditions, they can help to increase the density of the conduction band electrons by providing a residual defect population at the beginning of the next pulse. The defects accumulated after a certain number of pulses could ease the emission of ions out of the target until the occurrence of a significant damage (optical

breakdown). It is possible that transient defects can enhance pulse-by-pulse the surface perturbation. Long lifetime defects could be more important in producing a permanent damage.

The initial assumption is that ion desorption occurs when a certain surface charge density is reached at least locally. This can be discussed considering the excitation and recombination processes. We hypothesize that the conduction band electron density is built up (as described in Chapter 1) either via MPI only or MPI and avalanche processes and is depleted via recombination at defect states with a long relaxation time. In the conditions of a pulse repetition rate of 1 kHz, surface defects with lifetime longer than 1 ms, for instance STE, could survive between pulses. Thus, the number of created defects could accumulate pulse by pulse and so does the surface charging. Once a critical surface charge density is reached, ions desorb out of the target due to an electrostatic unbalance. By adding more pulses, the charge density continues to grow and the excess charge (ions) to be expelled. Finally, the emitted ions can attain a quasi-steady yield.

For low intensities, the charge is localized. The degree of delocalization (number of absorbent sites) increases with laser intensity and possibly reaches a maximum near the single shot ablation intensity threshold, where the incubation effect may reduce substantially.

3.1.3.3. The nature of defects: Laser-Induced Fluorescence

The model presented in the previous section has considered that defects are created by the laser pulse and contribute to the ionization process. So far, we have shown that the main contribution to building-up the CBE density in the laser irradiated dielectric is given by multiphoton ionization processes. The measurement of electron yield as a function of intensity presented in Section 3.1.1, indicated a reduction of the multiphoton ionization order for low incident intensity, where the band-to-band ionization probability can be still significantly low. This reduction is possibly determined by defects creation, which significantly ‘shrinks’ the bandgap by providing filled intermediate states.

The defect relaxation can be accompanied by fluorescence emission. In fact, strong arguments toward defect creation are: a blue fluorescence observable on the fluoride target long after the laser pulse stops, or, after repetitive laser irradiation, a darkening effect of thin channels in the bulk of fluoride targets. To characterize the transient defects induced in fluoride crystals by femtosecond laser pulses, we carried out laser-induced fluorescence (LIF) measurements.

The experimental set-up for detection of LIF from BaF_2 and CaF_2 is presented in Figure 3.11 (a). A Ti:Sapphire laser system of 800 nm and up to 1 mJ energy per pulse was used for excitation²¹. The pulse compressor could be adjusted to produce either ~50-fs or ~120-fs pulses. Single pulses were selected from a 20 Hz pulse train by means of an electronic shutter. LIF was detected at laser intensities near the single-pulse damage threshold, where the fluorescence intensity, its emission characteristics and lifetime could be easily measured. At this intensity, we also observed a plasma plume.

The gated signal from an ICCD camera of nanosecond resolution was collected at a controlled time delay with respect to the laser pulse, t_{LIF} . The integration time could be reduced to 10 ns. The LIF emission bands were analyzed by using a set of band-pass filters placed in front of the ICCD camera.

Figure 3.11 (b) shows a typical image of the fluoride target surface region: a single laser pulse hits the surface and generates a plasma plume and fluorescence in the interaction volume

²¹ LUCA system, CEA Saclay, France.

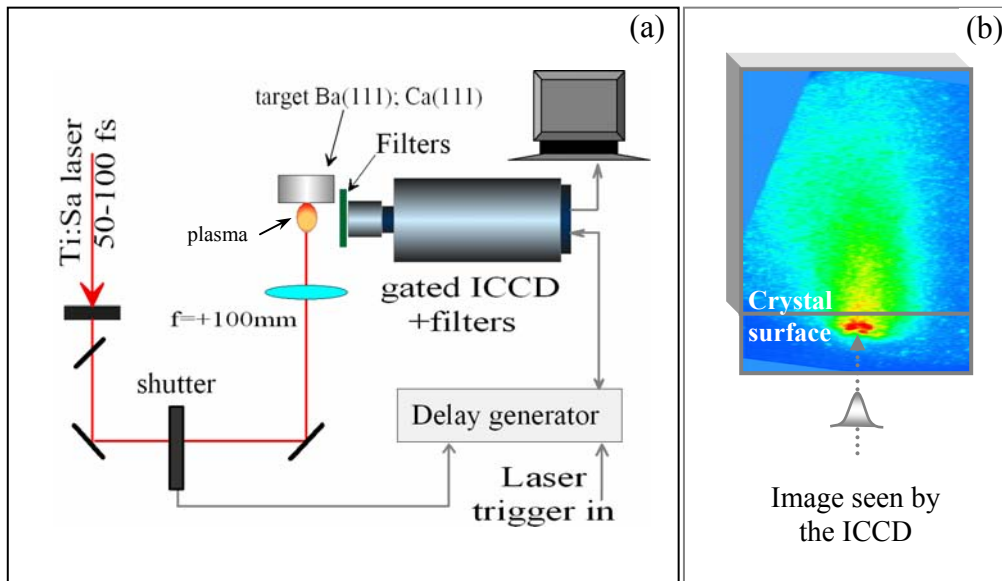


Figure 3.11. (a) Schematic of the experimental set-up for laser-induced fluorescence measurements; (b) Image seen by the ICCD camera, in a cross-section of a transparent crystal; the laser pulse hits the crystal surface at normal incidence giving rise to fluorescence emission in the interaction volume.

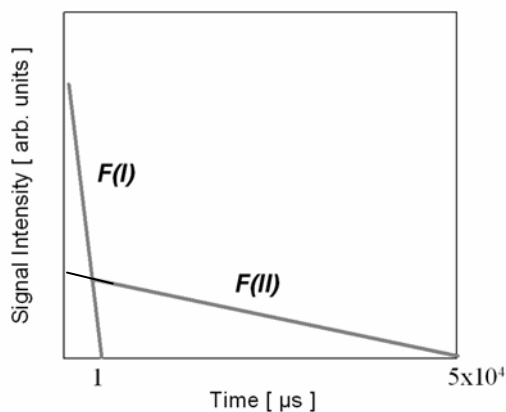


Figure 3.12. Relative intensity versus decay time of the laser-induced fluorescence in fluoride crystals.

The emission spectrum and detection time interval reveal two main fluorescence bands: a more intense, short-lifetime fluorescence band F(I) and a less intense fluorescence band F(II) of a longer lifetime (see the schematic in Figure 3.12). Images of a single 50-fs laser pulse induced plasma radiation and fluorescence emission in a BaF₂ (111) target, for various delay times with respect to the laser pulse, are presented in Figure 3.13.

The images show as follows: the plasma plume expansion after ~ 10 ns delay time to the laser pulse (Figure 3.13 (a)); images of F(I) fluorescence as detected and integrated for a time interval between 10 ns to 1 μ s (Figure 3.13 (b, c)); a F(II) fluorescence as detected and integrated in a time interval

between $1\mu\text{s}$ to 50ms (Figure 3.13 (d)). LIF images obtained with a $\sim 120\text{-fs}$ laser pulse showed nearly no difference.

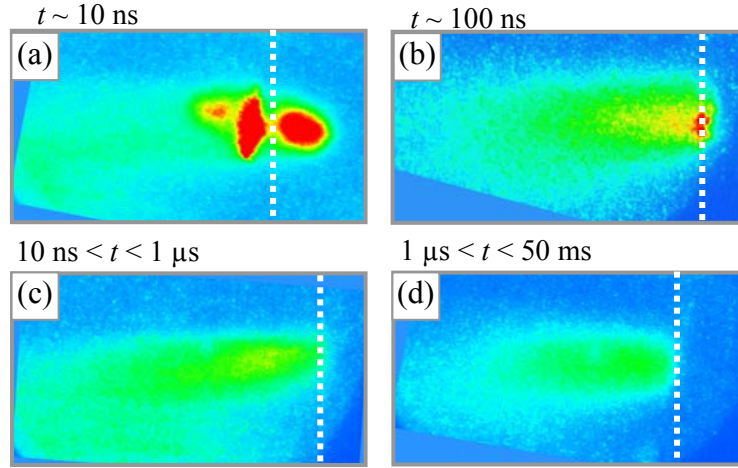


Figure 3.13. Images of plasma radiation and LIF emission in a BaF_2 (111) target irradiated with a single 50-fs laser pulse, at 800 nm and time delays as indicated: (a) plasma formation and expansion in 10 ns (b,c) F(I) fluorescence detected and integrated between 10ns to $1\mu\text{s}$ (d) F(II) fluorescence detected and integrated between $1\mu\text{s}$ to 50ms delay time to the laser pulse. The laser pulse came from the right side on the crystal surface represented by dotted lines. (Laser intensity: $1.1 \times 10^{15}\text{ W/cm}^2$).

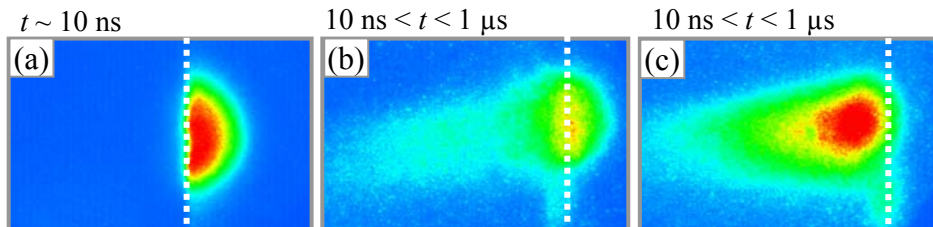


Figure 3.14. Images of plasma (a) and fluorescence F(I) (b, c) induced in a $\text{CaF}_2(111)$ target by irradiation with a single $\sim 120\text{-fs}$ pulse (800 nm). The time periods (intervals) where plasma and F(I) were detected and integrated are indicated. The laser intensity per pulse was $0.5 \times 10^{15}\text{ W/cm}^2$ (a, b) and $0.7 \times 10^{15}\text{ W/cm}^2$ in (c).

Both fluoride materials investigated provided similar LIF results. For instance, Figure 3.14 shows that both the plasma plume and fluorescence emission, as induced on a CaF_2 (111) surface by a single $\sim 120\text{-fs}$ pulses, were detected in time intervals just similar to the results for BaF_2 . In Table 3.1, we summarize the fluorescence emission bands and the corresponding detection time intervals.

As already shown in the previous sections, a pulse by pulse increase in the surface defect density can potentially enhance the free electron density, leading to photo-electron and ion emission. It is known that material dependent surface states, e.g. color centers (F -centers²²), are possible promoters of a resonant enhancement of radiation absorption [RWM88, Rei89, MTT03]. Femtosecond laser pulses can induce in fluoride materials transient defects. They can decay over several intermediate states, reaching an overall lifetime of $>1\mu\text{s}$ (for instance the self-trapped excitons, STE²³, are well-known to form in laser irradiated fluoride materials [Ito95, RHO98, Tan01]). The fluorescence band F(I) can indicate the decay of an STE, as it is known that this can involve a fluorescence around 278 nm with a lifetime of $\sim 1\mu\text{s}$ [TKI89, Tan01, LWR01].

Table 3.1. Laser-induced fluorescence from BaF_2 and CaF_2 target irradiated by single 50 fs-pulses at $5 \times 10^{14} \text{ W/cm}^2$ intensity: Emission bands and their detection time intervals

	Emission band (nm)	Fluorescence: detection time interval, t_{LIF}
BaF_2	F(I): 300-400 nm	1 μs
	F(II): 400-465 nm	50 ms
CaF_2	F(I): 300-400 nm	100 ns
	F(II): 500-600 nm	10-50 ms

On the other hand, the long lifetime F(II) fluorescence could indicate the formation of longer lifetime defect, for instance a surface F -center [RHO98, HRM97], used as a premise in the incubation model presented in the previous section.

In Chapter 4, the time-resolved studies of dynamics of the perturbed target will point again to the generation and relaxation of a defect state.

²² As discussed in Chapter 1, both laser and electron beam irradiation are known to create color centers at the surface region of a fluoride material. A repetitive laser irradiation produces point defects which can extend. On the other hand, crystal cleaving could induce dislocation loops, which, upon laser interaction, migrate at the surface or in the bulk [DJW93]. After electron bombardment and UV laser irradiation, CaF_2 shows at least two major optical absorption bands, in UV and visible. They have been associated with STE formation [TKI89, MTT03].

²³ An STE consists of a F_2^- molecular ion (where F denotes a fluorine atom) with a neighboring F -center oriented along the (111) direction [CHK75].

3.1.4. Particle emission kinetics

The preceding sections have shown that upon femtosecond laser pulse interaction a substantial amount of electrons and positive ions leave the surface, already for intensities well-below the damage threshold and plasma onset. In order to understand the desorption mechanisms, we present in the following different features of ion yield dependence on irradiation conditions. Indeed, the desorbed ion yields are strongly intensity dependent, i.e. they increase highly nonlinearly with the incident intensity. Examining again Figure 3.2 (a), we can notice that, at a certain higher intensity level, Ca^+ yield seems to saturate while F^+ yield becomes important. At about this intensity level also negative ions can be detected.

3.1.4.1. Negative ion detection

Negative ions are detected at intensities around $\sim 0.5 \text{ W/cm}^2$ (BaF_2) and $\sim 0.9 \text{ TW/cm}^2$ (CaF_2). With increasing intensity, first electrons and then negative ions occur in the mass spectra. Typical negative ion mass spectra, as detected, are shown in Figure 3.15 for two target materials.

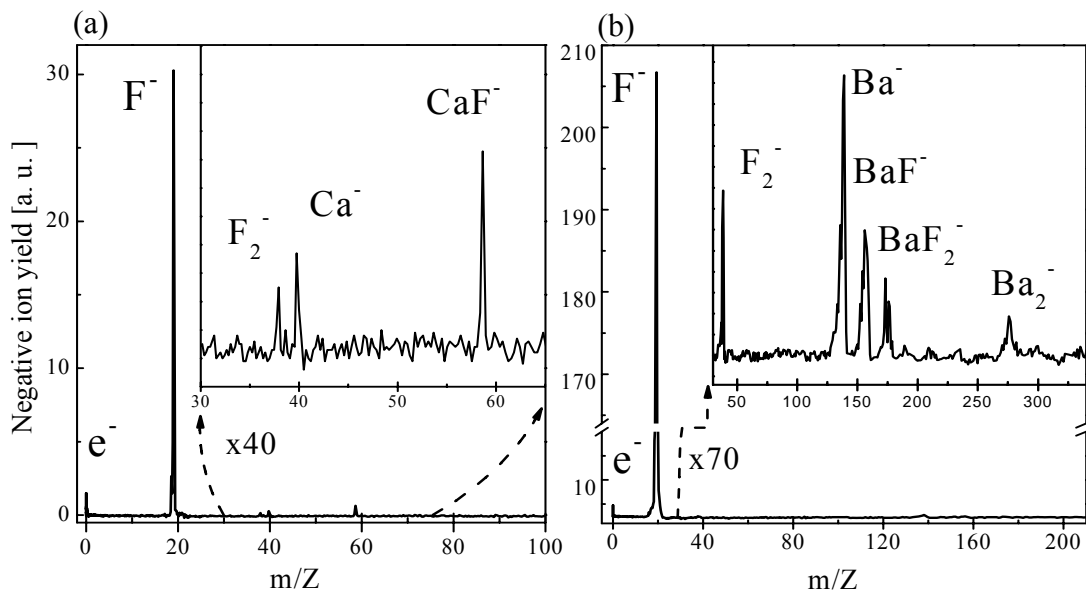


Figure 3.15. Negative ion mass spectra from (a) a CaF_2 and (b) a BaF_2 sample upon irradiation with 120-fs pulses of $\sim 1.2 \text{ TW/cm}^2$. The spectra were averaged over 1000 laser pulses.

For the same irradiation conditions, the number of negative ion species is *lower* compared to the positive ions. For both CaF_2 (111) and BaF_2 (111) samples, F^- is the main constituent of the negative ion spectrum. Less prominent are F_2^- , Ca^- , CaF^- from CaF_2 (Figure 3.15 (a)) and the F_2^- , Ba^- and larger clusters from BaF_2 , respectively (Figure 3.15 (b))²⁴. Similar to the positive ions, they exhibit a high non-linear increase with intensity (see also [HeR03]).

The detection intensity threshold for negative ions appears to be higher than for the positives. Moreover, we observed important *differences in arrival times* (at the detector) for the positive and negative ions of the same kind. In Figure 3.16, we compare the arrival times for F^+ and F^- , respectively, as extracted from ToF spectra recorded at nearly the same incident intensity (the ions are desorbed from a CaF_2 target). The negative F^- is by far the dominant negative ion product of desorption, whereas F^+ is only minor as compared to the other positive ions. It is evident that the positive ion arrives at the detector much earlier than the corresponding negative ion.

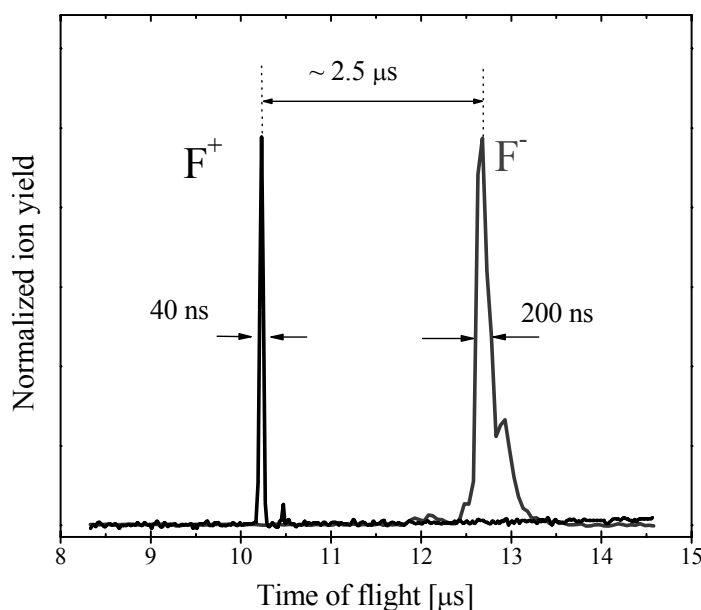


Figure 3.16. Normalized ToF spectra of the positive and negative fluorine ions from a CaF_2 sample, desorbed by 120-fs pulses at 2.3 TW/cm^2 . The ToF spectra were averaged over 1000 laser pulses. The extraction voltage applied was $+2.9 \text{ kV}$ for positive ions and, respectively, -2.9 kV for the negative ions. The electrostatic lenses were kept at 0 V .

²⁴ Following the mass-to-time-of-flight conversion, certain peaks should be attributed to Ca^- respectively Ba^- . The desorption of such negative ions remains to date not understood.

The *incubation* effect described above appears to affect the negative-ion yield more drastically than the positive one. Figure 3.17 displays, for comparison, typical incubation effects in the positive and negative-ion yields from a CaF_2 target. It is again evident that incubation is an intensity dependent effect. With increasing intensity, the ion yield reaches a quasi-steady regime for desorption after a lower number of pulses (Figure 3.17 (a, b) for F^- and Figure 3.17 (c, d) for F^+). Also, as compared to the positive F^+ , to obtain a significant F^- yield, more incubative pulses are needed, thus: $N_{inc}^{neg} > N_{inc}^{pos}$ (Figure 3.17 (a c)). In addition, Figure 3.17 (d) shows that the positive Ca^+ has the lowest threshold for a detectable signal.

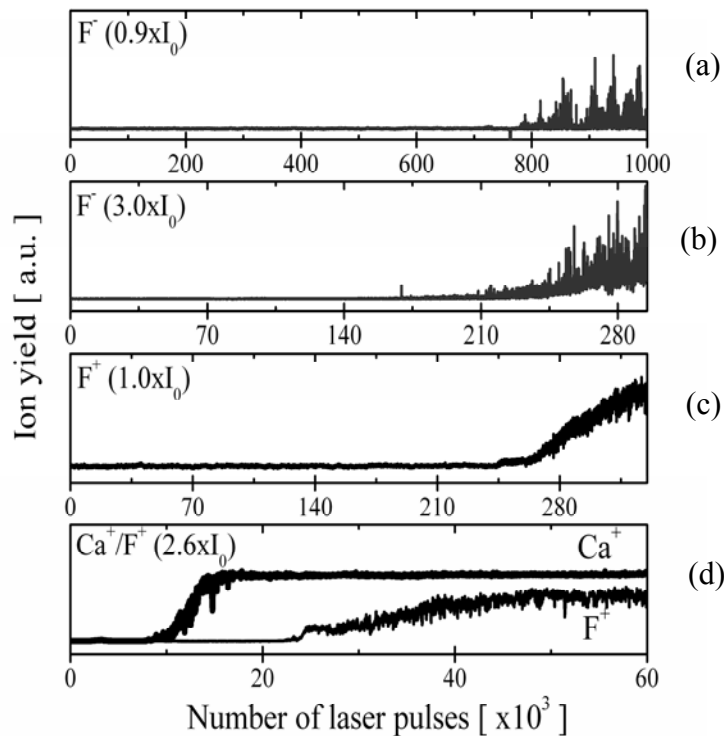


Figure 3.17. Incubation effects in the negative ion yields (a, b), respectively the positive ion yields (c, d), after irradiation with 120-fs pulses at intensities as indicated (CaF_2 target). Here, $I_0 = 1\text{TW}/\text{cm}^2$.

An important feature of negative ion emission is indicated by the ‘drift’ ToF spectra. In Figure 3.18, we present the positive and negative ion desorbed from a CaF_2 surface. The spectra are taken for two different incident intensities in the quasi-steady regime of desorption. For the lower intensity where the positive-ion yield is well discernable, the negative-ion yield is deficient. Increasing the laser intensity near the damage threshold, a

small negative ion signal is detected. Here, the corresponding positive ion signal already contains larger clusters (see also the next subsection).

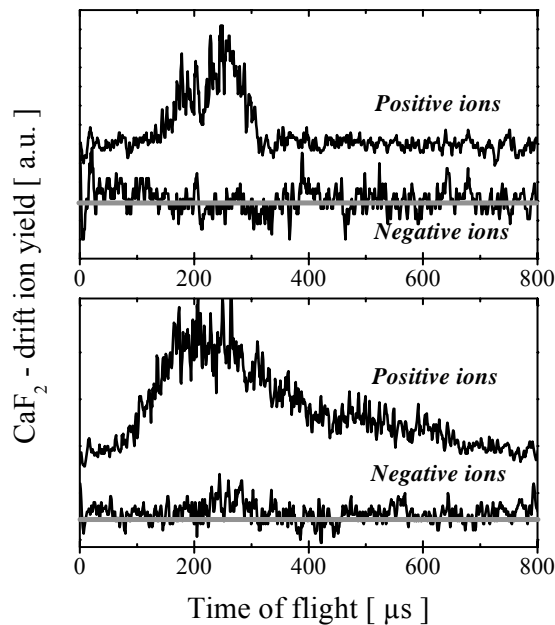


Figure 3.18. Comparison between positive and negative ion yields in CaF₂ as revealed by time-of-flight ('drift') spectra at two different incident intensities: 4TW/cm² (upper panel), 6.8TW/cm² (lower panel). The spectra were acquired by averaging the ion signal over 1000 pulses.

On the other hand, the 'acceleration' mode ToF spectra indicate negative ion emission for much lower laser intensities. This suggests that the negative ion angular distribution is rather broad, much broader than the corresponding positive ion angular distribution. As a comparison, the ToF spectra suggest that the positive ion emission is peaked forwardly with a narrow angular distribution around the surface normal (see also [HWR00]).

So far, the experiments show important differences in the ion yield characteristics for positive as compared to the negative ions, pointing to different desorption mechanisms for ions of different sign. As compared to the positive ions, the negative ion emission is characterized by: (i) detection at higher intensity threshold and larger number of laser pulses; (ii) longer times-of-flight (later arrival times); (iii) broader angular distribution.

A possible mechanism for negative ion desorption is discussed in the next section in the context of variation in the kinetics of positive ion emission with increasing intensity.

3.1.4.2. Effects due to laser intensity variation

When increasing the laser intensity or the number of pulses, the kinetics of positive ions emission appears to change significantly, as it can be seen from the ‘drift’ ToF spectra in Figure 3.19 and 3.20.

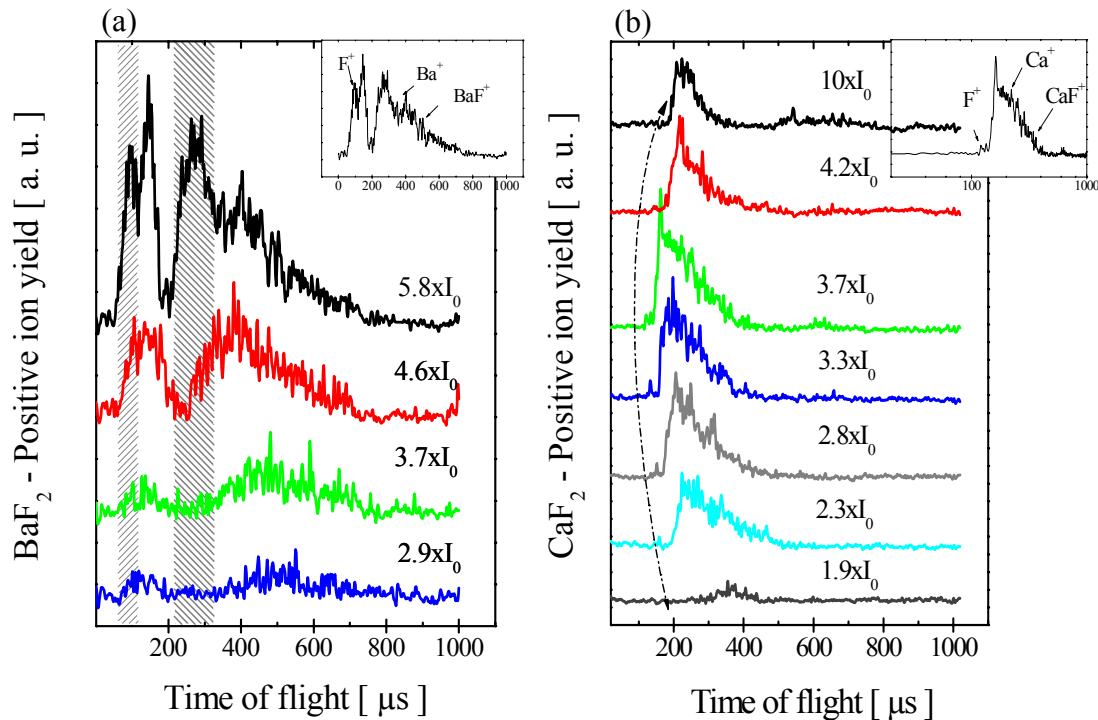


Figure 3.19. ‘Drift’ ToF spectra recorded at different laser intensities from (a) BaF₂; (b) CaF₂ samples ($I_0 = 1 \text{ TW/cm}^2$). The spectra were averaged over 1000 pulses. By increasing the incident intensity, we note: (a) A clear separation of fast ions as indicated in the grey areas; (b) Above $\sim 3.7 \text{ TW/cm}^2$, the fast peaks vanish at the expense of increasing contributions from clusters.

In the spectra from the insets in (a, b), the individual peaks are designated to the most probable desorption products.

From both the laser irradiated BaF₂ and CaF₂ targets, the ion yield increases significantly with the laser intensity. For higher intensities, higher molecular masses (clusters) are better distinguishable. Also, additional, faster ion contributions are detected (Figure 3.19, in the grey areas). Moreover, as shown in Figure 3.19 (b) from a laser irradiated CaF₂ target, there is a threshold intensity where a minimum ion time-of-flight is detected, i.e. a maximum ion velocity. By further increasing the intensity, the fast ions vanish at the expense of more important contributions from clusters

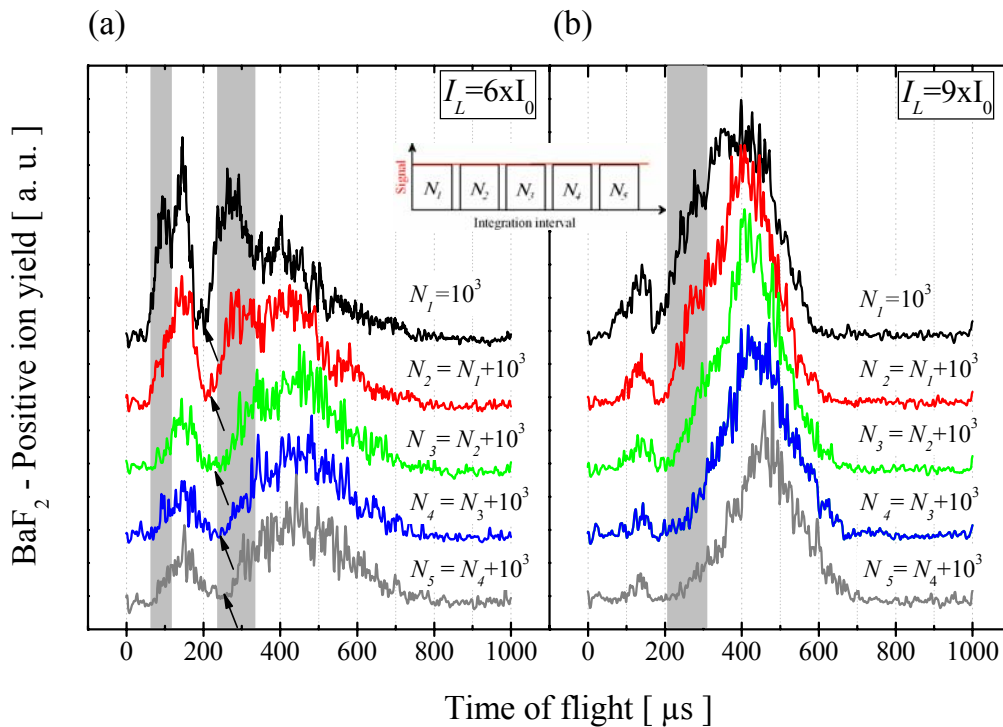


Figure 3.20. Positive ion ToF spectra from BaF_2 , recorded upon laser irradiation at different intensities I_L and number of laser pulses N as indicated in the panels ($I_0 = 1\text{TW}/\text{cm}^2$). These spectra were recorded from successive trains of 1000 pulses, upon continuous irradiation as shown in the inset (they are integrated over 1000 pulses).

The contributions of fast ions (in the grey areas) decrease with increasing N . The ion signal seems to reach a steady regime from a certain N . An ion (peak) arrival time is marked with arrows in (a) to emphasize its reduction with increasing N .

Rather similar effects are obtained with increasing the number of laser pulses on a site. For BaF_2 and two different intensities, Figure 3.20 shows the variation of the positive-ion yield with increasing the number of laser pulses. For both intensities, a higher number of pulses results in a reduction of the fast ions contributions. When increasing the number of pulses even more, the ion yield seems to have reached a steady regime (the spectra, as far as the number of peaks, their amplitudes and widths are concerned, do not seem to change significantly anymore).

The ion kinetic energy variation with intensity is analyzed with the retarding potential method. These measurements suggest again that the ions kinetic energy increases with the incident fluence, reaches a maximum at around $3\text{ TW}/\text{cm}^2$ and then falls back to

lower energies (Figure 3.21)²⁵. It appears that this threshold-like behavior likely indicates a change in the ion desorption mechanism.

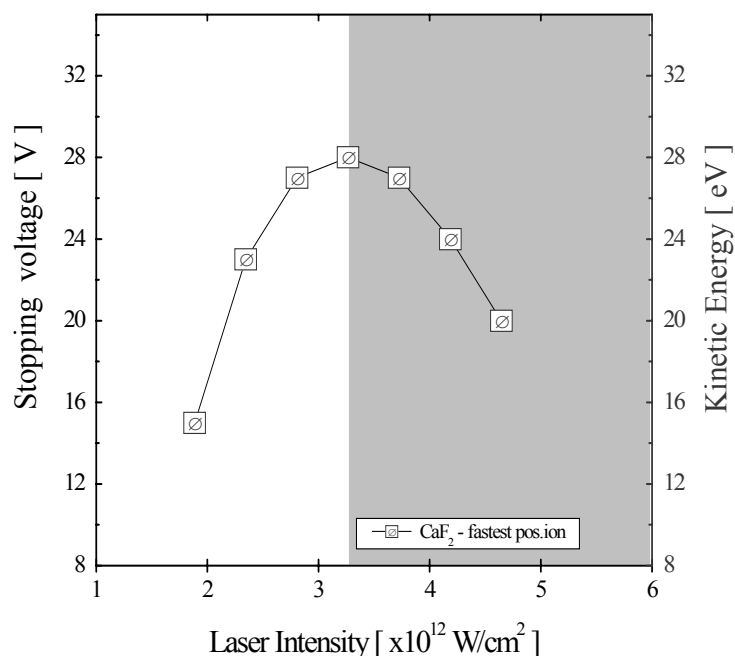


Figure 3.21. Voltage applied on the ‘drift’ ToF spectra in order to cancel the ion signal, this yielding the maximum ion kinetic energy (CaF₂ target). The grey area delimitates a region where the ion desorption mechanism appears to change.

More information on the kinetics of charged particle emission, i.e. on the ion kinetic energy, can be gathered examining the ‘drift’ ToF spectra. In the ‘drift’ ToF spectra, however, the discrimination between different ions (i.e. mass-to-charge ratio) is more difficult.

As mentioned in Chapter 2, in order to decide which mass-to-charge ratio can be attributed to different ToF peaks, an acceleration voltage is gradually applied on the target. Figure 3.22 presents a comparison between a ToF spectrum in ‘drift’ mode and two examples of spectra recorded for different acceleration voltages.

²⁵ A similar result was previously reported in [Hen03] for NaCl as a target material

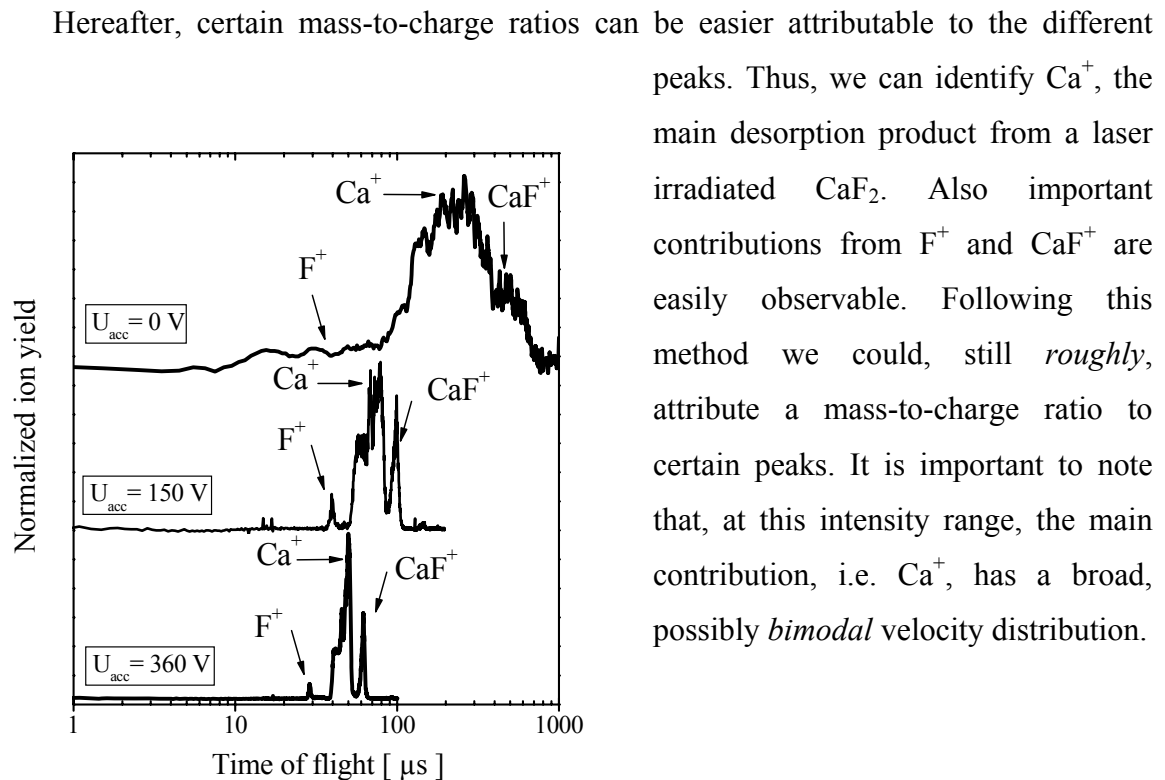


Figure 3.22. Positive ion ToF spectra at different extraction fields (acceleration voltages) applied on the target. Here, a CaF_2 target was irradiated by 120-fs laser pulses at 6.8 TW/cm^2 intensity. These spectra were averaged over 1000 pulses. The time-of-flight to mass-to-charge conversion for the ‘drift’ mode ToF spectrum is obtained upon a direct comparison with ‘acceleration’ mode spectra.

3.1.4.2.1. Kinetic energy distribution

As already indicated in Chapter 2, the ion kinetic energy distribution can be directly obtained from the ‘drift’ ToF spectra. Using the method indicated in Figure 3.22, we can analyze, in more detail, ToF ‘drift’ spectra recorded at different incident intensities (Figure 3.23).

The ‘conversion’ of the ion ‘drift’ ToF spectra to a ion kinetic energy distribution can be done by using an appropriate fit function. Since broad and asymmetric ion peaks suggest an addition of several masses, to analyze the data we used a sum of several distributions [DLS94] as follows:

$$f(t) = A/t^4 \cdot \sum_j \left[N_j \cdot \exp \left(-\frac{m_{ion} \cdot (D/t - u_j)^2}{2kT_j} \right) \right] \quad (3.10)$$

where $f(t)$, the new fit function, can be used to fit a j number of ion peaks. Here A and N_j are scaling factors, D is the drift length (~ 1.5 m in our experimental set-up), m_{ion} is the mass of a singly charged ion, k is the Boltzmann constant. The u_j and T_j , the velocity shift (stream velocity), respectively, distribution width of the j -th ion contribution are taken as fit parameters. Without claiming that the fit function given by Eq. 3.10 is the most suitable to describe our data description, we use it as a general basis for our kinetic energy distribution estimate.

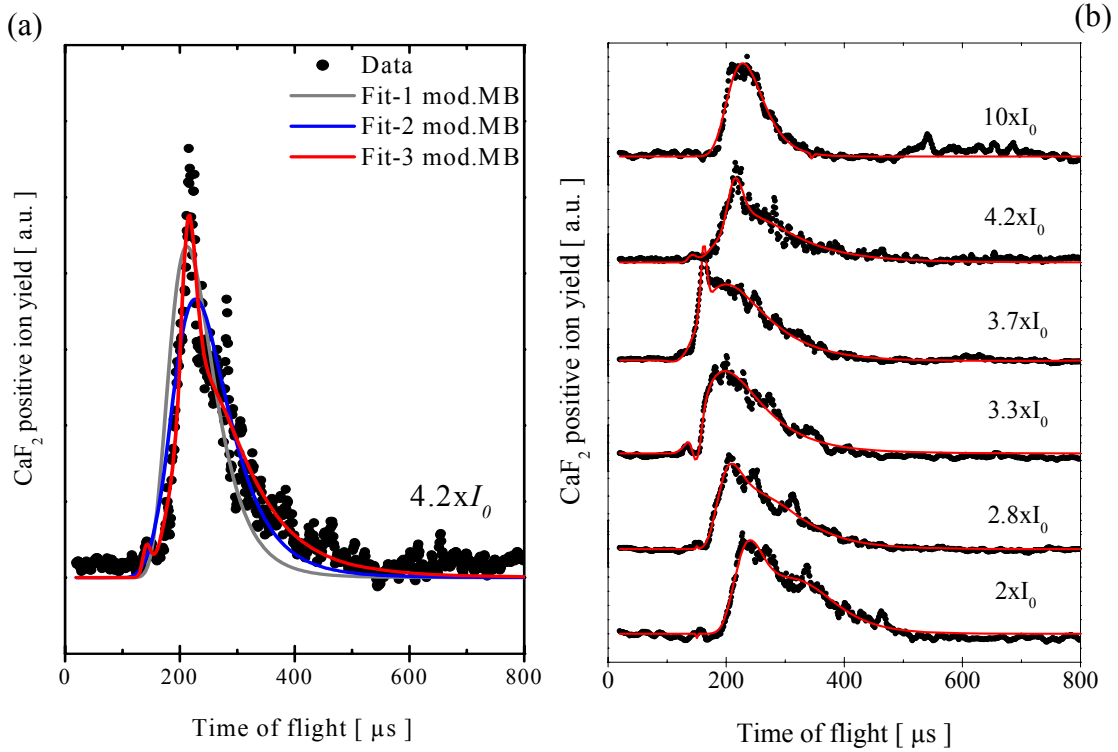


Figure 3.23. Positive ions ‘drift’ ToF spectra from a CaF₂ target (black dots) after irradiation at different laser intensities as indicated ($I_0 = 1$ TW/cm²).

(a) This spectrum is fitted with modified Maxwell-Boltzmann (MB) distributions assuming: a Ca⁺ ion (gray line); a sum of two modified MB distributions with contributions from F⁺ and Ca⁺ ions (blue line); a sum of three modified MB distributions, cf. Eq. 3.11, with a contribution from F⁺ and a fast and a slow contribution from Ca⁺ (red line).

(b) Each spectrum is fitted with a sum of three modified MB distributions cf. (a).

In all fit procedures, for each modified MB distribution, individual drift velocities and temperatures are taken as fit parameters. The results of the fits (stream velocities) from (b) are used in Figure 3.24.

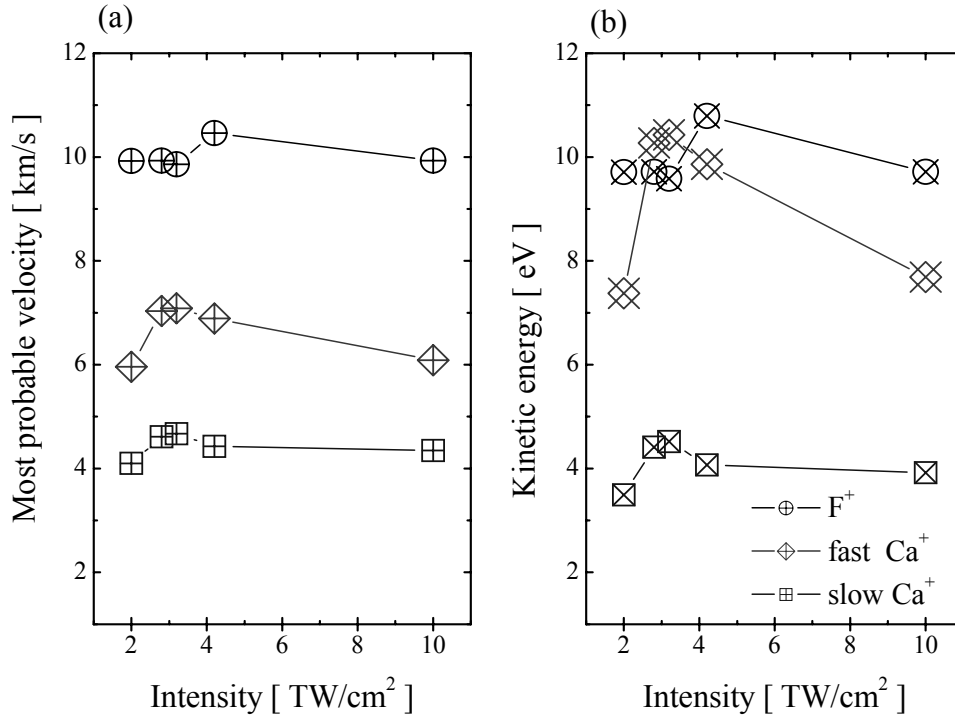


Figure 3.24. (a) Most probable velocities dependence on intensity for an F^+ , fast and slow Ca^+ ions as indicated. The velocities are results of fits using Eq. 3.12 on the ‘drift’ ToF spectra (u_1 , u_2 , u_3) in Figure 3.23. (b) Ion kinetic energy using the data from (a) as a function of intensity.

Using the method indicated in Figure 3.22, we can analyze more in detail ToF spectra recorded at different incident intensities (Figure 3.23). We assumed, for simplicity, only major contributions from F^+ and Ca^+ ²⁶. We tested different combinations for the fit function (Figure 3.23 (a)). The best fit function consisted of a sum of three modified MB distributions assuming an F^+ and a bimodal contribution of fast and slow Ca^+ , as follows:

$$f(t) = \frac{A}{t^4} \cdot \left[N_1 \cdot \exp\left(-\frac{m_F \cdot (D/t - u_1)^2}{2kT_1}\right) + N_2 \cdot \exp\left(-\frac{m_{Ca} \cdot (D/t - u_2)^2}{2kT_2}\right) + N_3 \cdot \exp\left(-\frac{m_{Ca} \cdot (D/t - u_3)^2}{2kT_3}\right) \right] \quad (3.11)$$

²⁶ Following the indication from Figure 3.22, a possible assumption would include also a CaF^+ ion. Our observation in the case of increasing intensity was that the ion velocity distribution does not change significantly. Since the separation of CaF^+ in the spectrum is not evident, we chose to limit the number of ions to F^+ and Ca^+ .

where u_1, u_2, u_3 , are the stream velocities and T_1, T_2, T_3 , are the widths of the distributions (red lines in Figure 3.23). This function fits our data well also expected from the large number of inter-dependent parameters.

The most probable velocities provided by these fits are presented in Figure 3.24. Consequently, femtosecond laser interaction with a CaF_2 target provokes an emission of positive ions with velocities of about 10 km/s corresponding to energies around 10 eV. Apparently, the ion kinetic energy increases with the incident laser intensities and appears to saturate. The distribution widths were taken here only as *free* fit parameters. It is evident that for low laser intensities F^+ and fast Ca^+ ions have about the same kinetic energy. This was also suggested in [Hen03] for other dielectric targets, e.g. NaCl. The ion kinetic energy estimated from ‘drift’ ToF spectra deviate but slightly from the energy evaluation with the retarding potential method.

So far, we presented the positive-ion yield dependence on the incident intensities from a CaF_2 target. Similar measurements of positive ion ‘drift’ ToF spectra from BaF_2 recorded at various laser intensities have been already presented in Figure 3.19 (a). Here, for low intensities the ToF spectra reveal single (or slower) peaks, while additional, faster components develop at higher intensities. Again, this could be a general feature, as it has been also observed for other dielectrics [Hen03].

Already discussed in Chapter 1, different variations of the modified MB distribution could give a physical interpretation for *mono-* or *bimodal* ion velocity distributions. For instance, Zhigilei et al. [ZhG97] proposed such a function to account for the geometry of the ejected plume with a distribution of ablated particles corresponding to different stream velocities and a common temperature (surface temperature). In the following, we show that by using certain assumptions we can better control the output of the fit function.

As compared to CaF_2 the bimodal velocity distribution for the positive ions is better distinguishable in the ‘drift’ ToF spectra from BaF_2 (indeed, F^+ and Ba^+ are much different as far as their atomic mass is concerned). Thus, in order to analyze the spectra from Figure 3.19 (a), we reduce the number of free parameters by considering the following hypothesis: (i) F^+ and Ba^+ are taken as the main desorption products from a laser-irradiated BaF_2

target²⁷; (ii) the two distinct peaks are attributed to F⁺ and Ba⁺ both of bimodal velocity distribution of slow and fast ion; (iii) the fast singly charged ions are considered to occur in the same process and be emitted at the same kinetic energy; a similar assumption is made for the slower ions; (iv) one common temperature T_u is considered for each process. The number of fit parameters is then reduced as follows: a stream velocity u_1 and a ‘surface’ temperature²⁸ T_1 corresponding to fast ions of equal energy, respectively, a stream velocity u_2 and a ‘surface’ temperature T_2 which correspond to slow ions of equal energy.

Thus, the positive ion ToF ‘drift’ spectra can be analyzed with a function $f(t) = f_{F^+}(t) + f_{Ba^+}(t)$, where the difference from Eq. 3.12 is given by the assumptions on the parameters:

$$f_{F^+}(t) = \frac{A}{t^4} \cdot \left[N_1 \cdot \exp\left(-\frac{m_F \cdot (D/t - u_1)^2}{2kT_1}\right) + N_2 \cdot \exp\left(-\frac{m_F \cdot (D/t - u_2)^2}{2kT_2}\right) \right] \quad (3.12)$$

$$f_{Ba^+}(t) = \frac{A}{t^4} \cdot \left[N_3 \cdot \exp\left(-\frac{m_{Ba} \cdot (D/t - u_1/c)^2}{2kT_1}\right) + N_4 \cdot \exp\left(-\frac{m_{Ba} \cdot (D/t - u_2/c)^2}{2kT_2}\right) \right] \quad (3.13)$$

where $c = \sqrt{m_{Ba}/m_F}$. The F⁺ and Ba⁺ peaks are fitted separately, sharing parameters as in Eq. 3.12 and Eq. 3.13, respectively. The results of these fits are presented in Figure 3.25 for ion ToF ‘drift’ spectra obtained at three different laser intensities. Indeed, the fit parameters (as listed in Table 3.2) suggest that positive ions are emitted out from the target at high velocities (high translational kinetic energies). The ion translational kinetic energy slightly increases with increasing the laser intensity. Moreover, the obtained ion velocity values are very close to those given by the retarding potential analysis. Also the parameters suggest high ‘surface’ temperatures at the order of 10^4 K for each process, which at higher intensities tend to equilibrate. These results are used in the following discussion on possible desorption mechanisms.

²⁷ For simplicity, we neglect here BaF⁺ and the larger clusters. Although, they likely occur in the tail of the slower peak at longer times-of-flight they are not clearly resolved.

²⁸ The results of the fits indicate that it is reasonable to consider the distribution widths T_1 and T_2 as ‘surface’ temperatures (this idea is also supported in the model proposed in [ZhG97]).

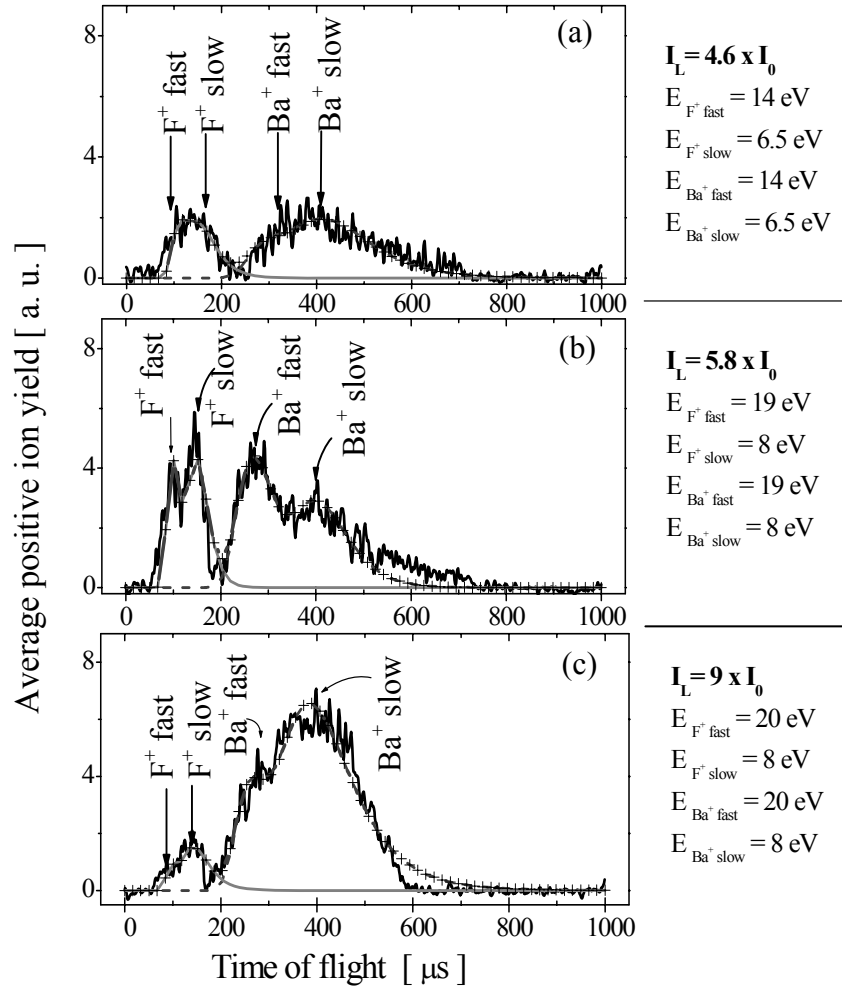


Figure 3.25. Positive ion ToF ‘drift’ spectra at various incident intensities ($I_0 = 1 \text{ TW/cm}^2$) from BaF_2 . The peaks attribution to F^+ and Ba^+ is indicated in each panel.

The data are fitted with a superposition of four modified Maxwell-Boltzmann distributions ($+$ symbols), which is a sum of functions as given by Eqs. 3.12 and 3.13. The fast and slow ion contributions are assumed to have the same kinetic energy independent of mass. Common temperatures T_1 , T_2 and common stream velocities u_1 , u_2 are taken as fit parameters (see text). Eq. 3.12 is used to fit the F^+ peak (solid grey lines) and Eq. 3.13 is used to fit the Ba^+ peak (dashed grey lines) with the fit parameters listed in Table 3.2. Estimates of the translational kinetic energies for these ion peaks are indicated in each panel.

Table 3.2. Parameters resulting from fitting the positive ion ‘drift’ ToF spectra from Figure 3.25 with Eqs. 3.12 - 3.13.

Intensity (TW/cm^2)	u_1 , km/s	u_2 , km/s	T_1 , 10^4 K	T_2 , 10^4 K
4.6	≈ 11.8	≈ 8.1	≈ 1.2	≈ 0.7
5.8	≈ 13.6	≈ 9.2	≈ 1.2	≈ 0.4
9	≈ 14.3	≈ 8.9	≈ 1	≈ 0.9

3.1.5. Particle desorption (ablation) mechanisms

Relying on experimental findings on the kinetics of charged particle desorption, so far, we have pointed out different processes induced by femtosecond laser pulses on dielectric (fluoride crystals) targets. In the following, we discuss possible mechanisms that lead to surface decomposition.

- *Photo-electron* emission occurs through a non-linear process of multi-photon absorption. Also, it appears likely that the photo-electron emission is enhanced by resonances within the bandgap provided by defect states. If there any avalanche processes act to increase the free electron density, their contribution may be quite minor under the irradiation conditions used in this work.

- *Positive singly charged atomic ions and large clusters* are emitted from the targets in a significant amount. Their yield increases highly nonlinearly with the incident intensity. Since no laser-plasma plume interaction takes place, the ions should be emitted directly from the target already at high kinetic energies and strongly forward around the normal on the target surface.

For both fluoride targets, the results suggest that, with increasing *intensity*, the density and translational kinetic energy of the desorbed atomic ions also increases.

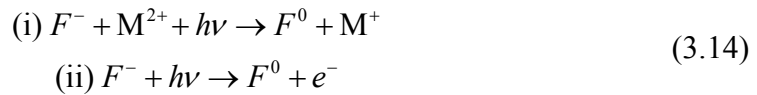
In addition, the ion yield increases with the *number of pulses*, signaling an incubation effect. Once incubated, upon further irradiation, the desorbed ions become slower, which is an indication of a possible desorption from regions deeper inside the solid (or localized micro-craters).

At intensities closer to the damage threshold, i.e. of above $\sim 5 \text{ TW/cm}^2$ for Ca^+ in CaF_2 and $\sim 4 \text{ TW/cm}^2$ for Ba^+ in BaF_2 , distinct faster and slower contributions from ions of the same kind are detected (i.e. bimodal ion velocity distribution). This result is consistent with similar observations in nanosecond [DLS94, HJB99, JHB02] and femtosecond laser desorption from semiconductors [CSB99] and metals [AWA00, YeG01]. Bimodal ion velocity distribution are often associated with different competing desorption mechanisms, both leading to surface instability and disintegration. These can be: (i) an impulsive ion desorption in locally enhanced electric fields as a result of charge unbalance; (ii) volume expansion due to bond breaking and phase transitions. Both could lead to the emission of energetic ions.

- *Negative ions* are detected at higher intensities and are either slower or emitted at a later time as compared to the positives. Hence, they likely originate from a different desorption process. Since their angular distribution appears to be broad, a thermal emission mechanism (see Chapter 1) is likely responsible for their formation.

Possible desorption mechanisms

As already detailed in Chapter 1, different microscopic models have been proposed to explain the laser-induced ion desorption. To understand the positive ion desorption mechanism, we rely on models suggested in [Rei89, DLS94], which require defects at the near surface region. Indeed, we have shown that defects such as (surface) F^- -centers (an electron trapped at fluorine vacancy F^-), can easily occur under these laser irradiation conditions. The formation of such defects would involve a loss of charge at the surface. From a laser irradiated MX_2 material, with M standing for the metal (here calcium or barium) and X for halogen (e.g. fluor), the metal ion M^+ desorption can occur from a region near a surface with localized F^- -centers. Several processes can take place such as: (i) a charge exchange between a surface F^- center and a doubly charged M^{2+} or (ii) ionization of surface defects, i.e. electron emission with formation of vacancies (F^0), as follows:



In fact, such processes can give rise to a local accumulation of positive ions. Thus, a Coulomb repulsion between adjacent surface positive ions (M^+ with the M^{2+} from its first vicinity) happens and positive ions desorb. An evidence for this is that positive ions are emitted at high kinetic energies. A simple estimate of the ion kinetic energies based on Coulomb electrostatic ejection from a nearest positive neighbor site (bond distance in CaF_2 : $a=5.45\text{\AA}$), gives approximately $e^2/4\pi\epsilon_0 a=5.8\text{eV}$. Our results show that positive ions can be emitted at even higher kinetic energies²⁹.

Such a microscopic mechanism of positive ion desorption from localized sites appears reasonable, since no macroscopic damage can be detected under these irradiation conditions. However, the extension of this picture from a microscopic to a macroscopic scale can explain a macroscopic material removal and the formation of a crater on

²⁹ Femtosecond laser-induced ion desorption from dielectric materials such as NaCl or Al_2O_3 have given similar results [HCJ02, Hen03].

dielectric surfaces interacting with femtosecond laser pulse of higher intensities. A somewhat speculative, suggestive model of macroscopic Coulomb explosion was proposed for intensities above 10 TW/cm^2 [SVR00, SAR00, SRA02, BSR04], but also for two orders of magnitude lower intensities [HRW00, HCR02]³⁰.

This is based on a model by Fleisher et al [FPW65] to explain ion explosion spikes and regions of intense damage (tracks). Fleisher's model invokes the condition that the Coulomb repulsive forces within the ionization region be sufficient to overcome the lattice binding energy.

Bringing together the experimental observations described so far in this chapter, a scenario for the macroscopic surface disintegration can be developed. Firstly, the fast ionization process gives rise to an instantaneous photo-electron emission. The surface region is a non-equilibrium transition region, since with increasing excitation density, the number of lost electrons cannot be compensated immediately by the slower ion emission. Thus, after electrons break away from the target, the surface region depleted of electrons becomes positively charged. In effect, an electric field is established as well as carrier density gradients. Thus, if the surface region contains a high density of positive surface charges, it decomposes due to Coulomb repulsion between positive ions. The crystal structure is destroyed as a result of an impulsive outward ejection of positive atomic ions and clusters from within the surface region of the crystal (cf. Figure 3.26).

Considering the photoelectron emission and charged carrier transport in and out of a dielectric target, Bulgakova et al. [BSR05] showed that this region could involve only a few atomic layers at the order of the electron escape depth, with a nearly exponential decrease toward the bulk.

Following a similar idea as in [SRA2] for BaF_2 , we can approximate the amount of surface ionization by estimating the number of emitted positive ions per pulse. From AFM measurements of the crater volume, the ablated volume per pulse is in average of about $0.5 \mu\text{m}^3$ at 10 TW/cm^2 . For a solid density of $1.6 \times 10^{21} \text{ at/cm}^3$ in BaF_2 , we can estimate about 10^{12} atoms removed per pulse at this intensity. Integrating the corresponding positive ion 'drift' ToF spectrum obtained upon axial detection, correcting for detection conditions and

³⁰ The experiments reported on these references are performed with a laser system similar to the one used in this work.

amplification ($\sim 10^6$) and for the loss in transmission due to angular distribution, we obtain an estimate of about 10^{11} ions removed by a single pulse of 10 TW/cm^2 . Thus at least 10 % of the emitted particles from the surface per pulse are positive ions, which is consistent with a model of Coulomb explosion induced by ion beam sputtering on the surface [ChG97], described in Chapter 1.

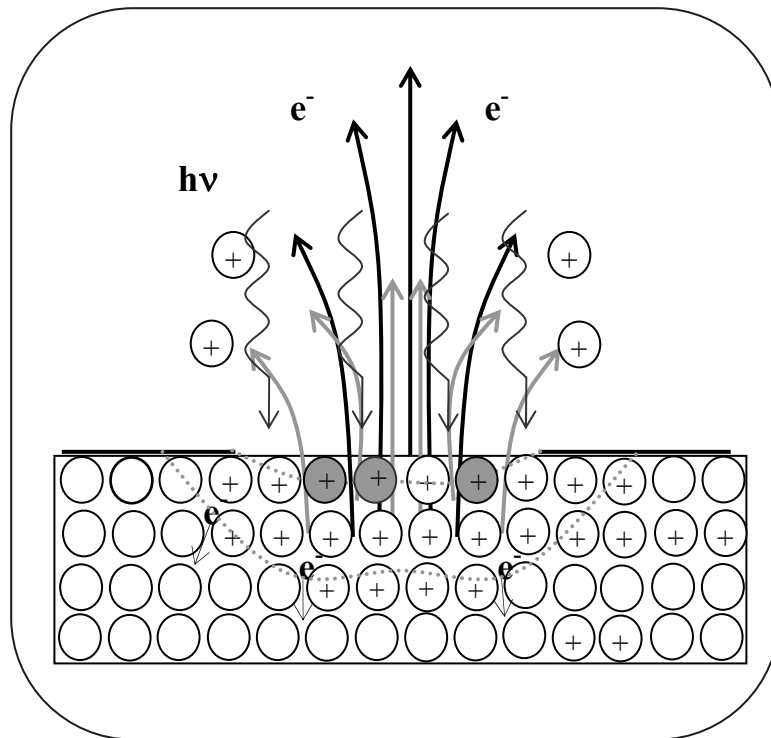


Figure 3.26. Principle of surface disintegration by outward positive ion emission. The laser excitation causes photoionization and emission of energetic electrons. Some electrons are trapped in the bulk. The remaining positive ions are ejected at a later time due to inner electrostatic repulsion.

It is important to add that also *doubly* and *triply* charged ion are detected for laser irradiated MgF_2 (cf. next chapter). To account for a possible formation mechanism of multi-charged ion fragments, we indicate that they are a typical signature of cluster decomposition in intense electric fields by Coulomb explosion [PoC98].

Furthermore, an increasing fraction of the generated electrons cannot leave the crystal, being held back (trapped in the bulk) by the positive space charge. These electrons can then be heated by free carrier absorption and impact processes to produce a hot

electron gas, which subsequently relaxes to the lattice by electron-phonon collisions. Since typical time constants for this process are in the sub-picosecond to picosecond range (see also next Chapter), the resulting heating of the sample surface region is still much faster than in thermal equilibrium.

However, at higher intensities, as before indicated [JCE04], also thermal mechanisms for desorption such as phase explosion can occur, where a superheated region near the surface undergoes a fast explosion into a mixture of gas and liquid phases. Our experiments at higher intensities reveal that the ion emission becomes almost constant, despite of an increased ablated volume. This can be explained by an increased amount of ionic clusters as well as neutral particle emission, the latter being associated with thermal desorption³¹.

Thermal mechanisms can better explain the negative ion desorption. An earlier idea has suggested that negative ions can form from neutral particles by ‘thermal’ electron capture [JJM95]. Such a mechanism appears possible after the positive ions leave the surface. ‘Thermal’ electrons can be trapped in the bulk by a positively charged surface region. The formation of negative ions would be a secondary effect and would imply neutral particles ejection from the surface, thus a thermal desorption. However, to prove this idea more experimental work is necessary.

³¹ Indeed, thermal effects were detected for a quartz target irradiated with femtosecond pulses of intensities greater than the damage threshold [LMG02].

3.2. EXTENSION OF ABLATION MECHANISMS TO SILICON

3.2.1. Charged particle desorption from silicon surfaces

To provide a comparison to fluoride materials, we carried out mass spectrometric measurements of charged particle yields from silicon surfaces, irradiated with femtosecond laser pulses. The experiments were carried out on pieces of Si(100) wafer, either p or n-doped. The native oxide layer was removed by a conventional etching in a 25% solution of HF. Neither the doping nature, nor the doping level did show any significant difference in the kinetics of ion emission.

The experiments were performed for intensities below the single-pulse damage threshold intensity for silicon Si(100), which is known to be around $\sim 2\text{TW}/\text{cm}^2$ [BBM04]. A typical positive ion mass spectrum displays atomic Si^+ ions and large clusters of up to at Si_{11}^+ (Figure 3.27 (a) at $\sim 1.5\text{ TW}/\text{cm}^2$). At the same incident intensities, the negative ion spectra reveal a lower number of products (Figure 3.27 (b)). In fact, the positive ion detection threshold intensity (at about $\sim 0.5\text{ TW}/\text{cm}^2$) is lower than the detection threshold for negatives (at about $\sim 1\text{ TW}/\text{cm}^2$).

We evaluated the ion kinetic energy (velocity) distribution by using the methods described in the preceding sections. Figure 3.28 (a) shows ToF ‘drift’ spectra from a Si (100) target, recorded for different incident intensities below and near the damage threshold. Similar to ion desorption from dielectric surfaces, both the ion density (i.e. the peak area) and ion velocity increase with the incident intensity. To fit the ‘drift’ ToF spectra, we used a superposition of two modified MB distribution of a Si^+ and Si_2^+ , respectively³² using Eq. 3.10. Following, the observations described in the preceding sections, here we considered different stream velocities $u(\text{Si}^+)$ and $u(\text{Si}_2^+)$ and a common distribution width (temperature) T_u . The results of the fits are presented in Table 3.3. The mean kinetic energy estimated from the fit parameter $u(\text{Si}^+)$ for Si^+ is plotted versus

³² Masses-to-charge ratios have been attributed to ‘drift’ ToF spectra by gradually increasing the extraction voltage (see Figure 3.22).

intensity in Figure 3.28 (b). These results are compared to mean kinetic energy estimates given by the retarding (stopping) potential analysis (see Figure 3.28 (c)).

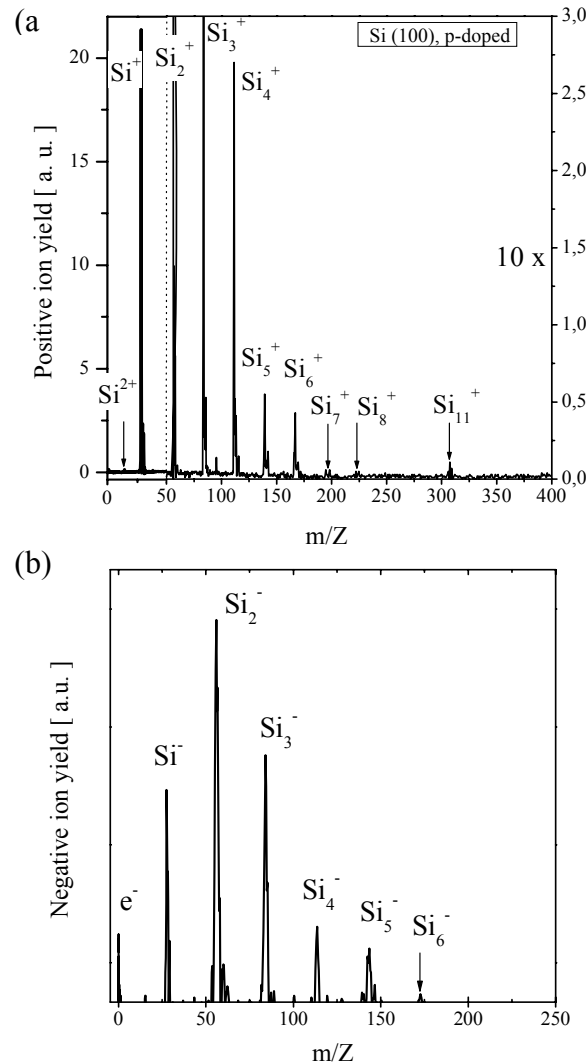


Figure 3.27. Positive ion mass spectrum (a) and negative ion mass spectrum (b) from Si(100) irradiated by 120-fs pulses at 1.5 TW/cm^2 .

The data reveal the following: (i) Both methods give a maximum kinetic energy for Si^+ and Si_2^+ ions at the order of $\sim 10 \text{ eV}$, i.e. fast ions with velocities of about 10 km/s . These values are evidently near the velocity estimates for the positive ion desorbed from fluoride targets. (ii) The ion velocity (kinetic energy) increases within this intensity range. (iii) T_u , if the surface temperature, corresponds to plasma temperature and increases with intensity.

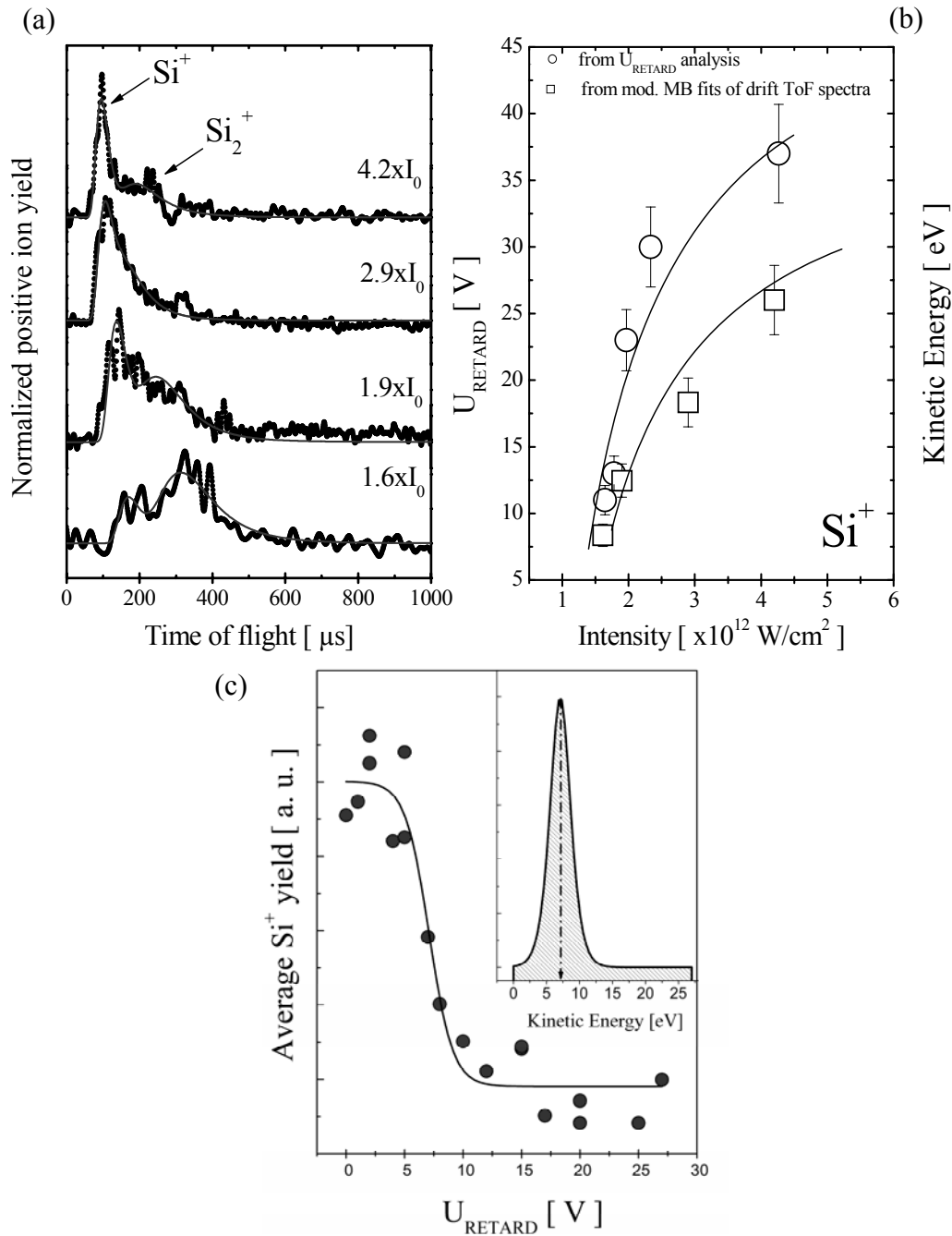


Figure 3.28. Kinetic energy distribution of positive ions desorbed from a Si target:

(a) ‘Drift’ ToF spectra recorded at different intensities ($I_0=1$ TW/cm²). The spectra were averaged over 1000 pulses. The spectra are fitted with a superposition of two modified MB distribution for a Si⁺ and Si₂⁺ ion, respectively, of different stream velocity $u(\text{Si})$ and $u(\text{Si}_2)$ and common temperature T . The fit parameters are listed in Table 3.3.

(b) Si⁺ kinetic energy resulted from the fits as a function of intensity in (a) and retard potential analysis with an example (c). The solid lines are drawn just to guide the eye.

(c) The effect of retarding voltage variation on Si⁺ yield obtained by integrating the corresponding peak from ToF spectra ($I_0=1.8$ TW/cm²).

The inset shows the kinetic energy distribution as derived from the sigmoid fit function.

Table 3.3. The results of fits with a modified Maxwell-Boltzmann distribution of the drift ToF spectra presented in Figure 3.28, for different intensities.

Intensity (TW/cm ²)	$u(\text{Si}^+)$, km/s	$u(\text{Si}_2^+)$, km/s	T , eV
1.6	≈7.5	≈3.6	≈0.6
1.9	≈9.2	≈4.3	≈1.3
2.9	≈11.2	≈5.1	≈2.6
4.2	≈13.4	≈5.5	≈2.8

3.2.2. Ion desorption from silicon: Coulomb explosion?

It is widely assumed that in semiconductors and metals, the holes produced by the laser ionization are immediately refilled, thus a quasi-neutrality of the target is preserved. Nanosecond and femtosecond laser ablation from silicon is mainly described using thermodynamical processes accompanied by fast phase transitions [YJM00, LMM02, SAP98, CSB99] usually involving high density of neutral particles, without an apparent consideration of charged particles ejection.

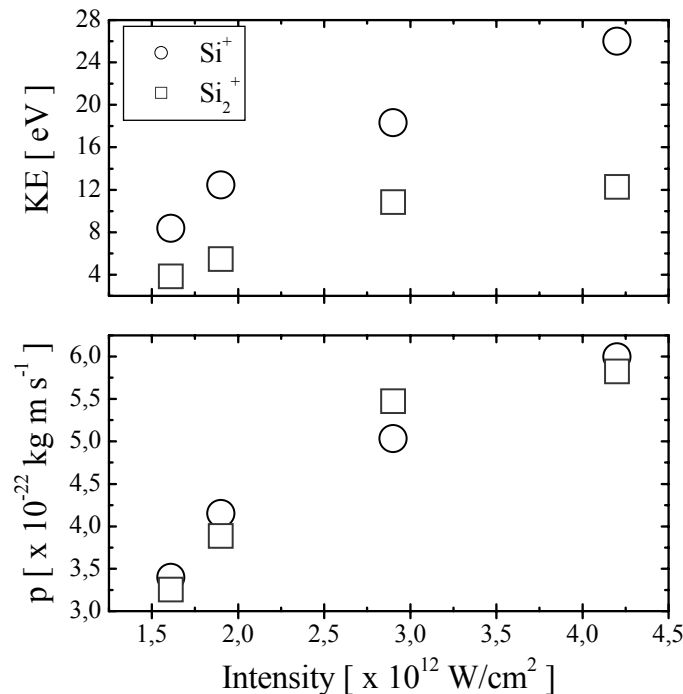


Figure 3.29. Kinetic energy and momentum of Si^+ and Si_2^+ , due to the most probable ion velocities extracted from fits to the ‘drift’ spectra as a function of incident intensity (see Table 3.3).

To our knowledge relatively recently, the fast positive ions emitted from silicon, both upon nanosecond [MBP04] and femtosecond laser irradiation [CKR04, RJV03, BOM04] are suggested to originate, unlike insulating materials, from an electrostatic repulsion mechanism. Estimates of charged carrier densities transported in and out of the target suggest the possibility of an electrostatic positive surface charging and decomposition for nanosecond and femtosecond laser ablation of silicon [BSR05].

Assuming that the electrons leave the surface rapidly and the remaining positive ions are accelerated in the electrostatic field built-up at the surface, *singly charged* fragments of a larger cluster would be ejected at the same momenta independent of mass. Figure 3.29 shows that Si^+ and Si_2^+ appear to be ejected at nearly the same momenta and high kinetic energy for this intensity range, i.e. near and above the damage threshold I_{th} (between $0.7I_{th} < I < 2.2 I_{th}$). These results are similar to observations on Coulomb explosion of clusters in high electric fields, which state that the emitted clusters have high kinetic energies [LSJ97].

Using also the experimental result of Sokolowski-Tinten et al. [SoL99], where a fluence of 4 TW/cm^2 would induce at the silicon surface a carrier density of over 10^{22} electrons/cm³, Roeterdink et al. [RJV03] estimated a surface charge density of 0.3 electron per silicon atom to be sufficient to overcome the binding energy and thus a Coulomb explosion of fast ions to be possible. The measured silicon momenta in their experiments were at the order of 10^{-22} kg m/s , therefore very similar to our estimates (see Figure 3.29).

However, it is likely that, for femtosecond laser pulse irradiated silicon, a phase explosion can be the dominant particle ejection mechanism, as also confirmed by the detection of a large amount of neutral particle emission [MBP04].

Our results, so far, give an experimental confirmation of similar kinetics of ion yield for fluorides and silicon as target materials.

3.3. CONCLUSIONS

In conclusion, the particularities of the femtosecond-laser induced electron and ion emission from BaF₂ and CaF₂, at intensities, below the estimated damage threshold and plasma onset, support the idea of desorption mechanisms triggered by the electronic excitation.

Thus, photo-electron emission could occur from a direct multiphoton ionization across the bandgap or via photo-excitation at intermediate defect states. Positive ions are ejected in a substantial amount, signaling a localized surface charging. Subsequently, a local electrostatic repulsion can give rise to ion desorption. This is confirmed by the ejection of ions at high mean velocities of a narrow distribution.

The pre-existing or radiation-induced defects greatly influence the excitation process, the emission characteristics and the macroscopic surface damage. The laser pulse can also generate defects with long relaxation times. These can contribute essentially to increasing the electronic excitation and indirectly the ion yields. Upon repetitive irradiation, the pulse-to-pulse accumulation of defect population may create the conditions (i.e. electron critical density) for both the ion emission and surface breakdown to happen even at low intensities.

With increasing intensity, the ions start to develop bimodal velocity distributions. For both CaF₂ and BaF₂, the estimates of most probable velocities indicate that the bimodal effect can be a superposition of two processes, both giving rise to ‘non-thermal’ velocities. It can also indicate that larger, slower clusters could be desorbed from regions deeper in the solid.

Negative ions are detected more significantly with increasing intensity for the intensity range used in our investigation. Their formation mechanism, although still unclear, may suggest a possible thermal desorption of neutral particles.

The kinetics of ion desorption from silicon targets reveal very similar features. This may suggest that either the mechanisms of ion desorption, i.e. the macroscopic Coulomb explosion which likely happen at around the damage threshold intensities in dielectrics, can take place also in silicon or that a particle emission analysis is *just* not sufficient to describe the desorption mechanisms.

CHAPTER 4

ULTRAFAST DYNAMICS OF FEMTOSECOND LASER ABLATION: TRANSIENT STATES OF MATTER

The dynamics induced on solid surfaces by femtosecond laser pulses are studied by pump-probe experiments.

Two-pulse correlation measurements using charged particle yields reveal processes that occur on a timescale comparable or much longer than the pulse duration. For all the dielectrics under investigation, an increased absorption response of the surface is detected at a characteristic timescale of around 1 ps. The dynamics of a perturbed lattice are shown to involve fast processes induced by electronic transitions such as the creation and decay of a defect state.

Further experiments reveal transient processes induced on silicon or aluminum long after one single pulse interaction. Apparently, the transient phases reflect the electron-lattice (phonon) coupling dynamics.

The transient (surface) effects seem to be related to the electron-lattice coupling strength of the various target materials.

The preceding chapters have shown that femtosecond laser interaction with dielectric targets leads to an electrostatic surface charging, locally enhanced by generation and accumulation of permanent intrinsic defects. Alternatively, fast processes which involve electron-lattice interaction and heat dissipation associated with phase transitions, can occur in all target materials upon femtosecond laser interaction.

In general, these different processes are supposed to change, at least transiently, the target optical properties. Thus, these processes can be studied by probing the transient optical reflectivity (or transmission) of the excited surface, the change in dielectric constant [GRL00], or the second harmonic generated (SHG) at the surface [TAB88, CBS88, HWG00]. This may involve the usage of pump-probe techniques combined with optical emission spectroscopy, frequency-domain interferometry [QGP01] or ellipsometry [YMU03]. Time-resolved measurements have shown that femtosecond laser pulses can induce lattice disorder on a time scale much shorter than the electron-phonon relaxation times [TAB88, SBB91]. Pump-probe measurements of the transient reflectivity or SHG at the surface of semiconducting targets suggest that, around the damage threshold, the type of excitation depends greatly on the incident fluence, leading to either lattice heating, lattice disorder or semiconductor-to-metal transitions [HCG98].

Although the ultrafast disordering of solids via phase transformations has been known for a long time, a theoretical description of the lattice instability as a result of photo-excitation has been provided much later [StB91, JGB02]. Calculation of energy absorption during ultrafast lattice deformation of graphite and silicon have revealed dramatic changes when the system undergoes phase transitions [JGB01].

In this chapter, the dynamics of charged particle desorption and matter transformation are studied in a pump-probe mode. The targets, i.e. dielectric semiconducting and metallic samples, were irradiated with 120-fs laser pulses at intensities below and near the damage threshold intensity. Basically, for all these materials, we observe a general trend for the temporal evolution of surface transient absorption induced by femtosecond laser pulses.

4.1. PUMP-PROBE EXPERIMENTS USING LASER DESORPTION PRODUCTS

Using ToF mass spectrometry, we study the temporal dynamics of the laser-desorbed particle yields, i.e. electrons, positive and negative ions.

4.1.1. Experimental details

The experiments were carried out in a typical pump-probe arrangement. Here, the laser pulse is divided into two equally intense pulses: a pump pulse, which induces a perturbation on the sample, and a probe pulse, which intensifies the effect produced by the pump pulse. The emitted ions are monitored with the help of the linear ToF mass spectrometer (Figure 4.1 (a)).

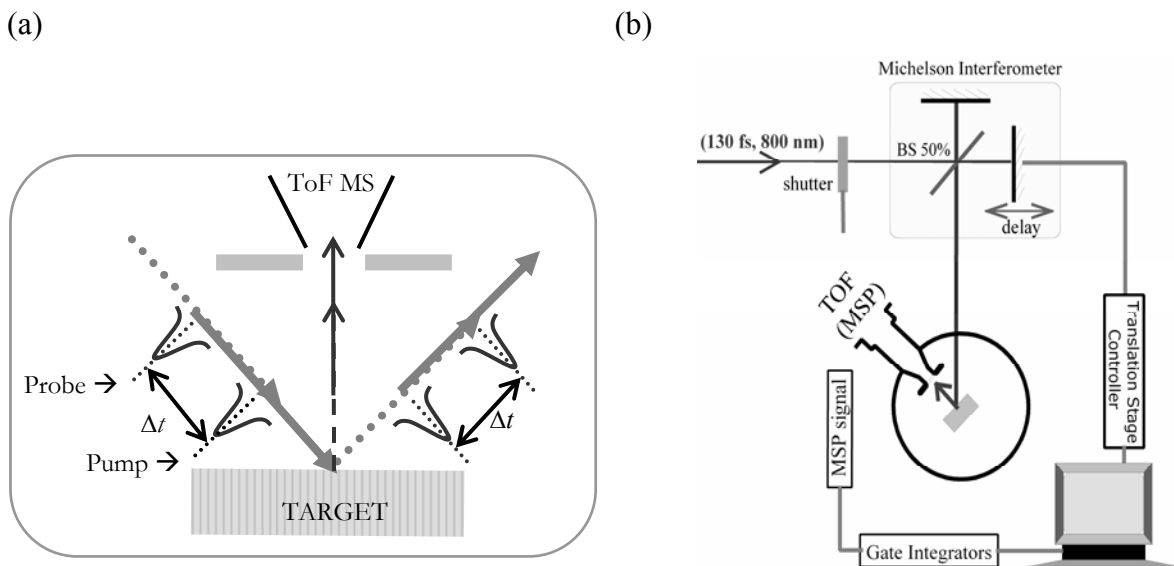


Figure 4.1. Principle of pump-probe mode used for the measurements (a) involve pump and probe pulses of nearly equal intensity delayed in time one against the other. The ejected ions are analyzed in a ToF spectrometer. (b) Pump-probe experimental set-up.

In a Michelson interferometer, the laser beam was divided into two p -polarized, nearly equally intense beams (Figure 4.1 (b)). The beam intensity was kept below or near the multi-shot damage threshold intensity for the dielectric targets investigated ($I_{pump} =$

$I_{probe} = I_b$, $2I_b = I_{sum}$, $2I_{sum} \leq I_{th}^{multi}$ ³³). Thus, the speed of the translation stage (scanning speed) was set to correspond to 10^4 pulses for 1.5 ps time (optical delay), in the experiments on dielectrics³⁴. To scan over longer delay times, as necessary in the case of aluminum and silicon, the scanning speed was increased to 10^4 pulses for 150 ps time (delay).

The path length variation in the Michelson interferometer was done with a motorized translation stage of 0.1 μm resolution³⁵. After being recombined in the interferometer, the two collinear beams were focused ($f = +300\text{mm}$) on the target at an incidence angle of 45° around the surface normal.

Ion peaks selected from ToF spectra could be synchronously monitored and integrated while continuously scanning over pulse separation times by controlling the optical delay stage.

We performed measurements on different samples such as freshly cleaved CaF_2 (111), BaF_2 (111), polished MgF_2 randomly cut, polished sapphire Al_2O_3 cut along the c-axes; low doped Si (100) wafers with a native oxide layer, and high purity Al foils.

In order to obtain stable signals, the dielectric surfaces had to be incubated (preconditioned) prior the measurement to reach the quasi-steady regime for ion emission (cf. Chapter 3).

In contrast to other similar experiments performed on dielectric materials³⁶, our experiments have concerned also the intensity range corresponding to ion desorption from individual sites. For silicon and aluminum, the intensity range ($2I_b$) is chosen near damage threshold conditions.

³³ Note also that, the intensity of the two pulses at a coherent overlap in the Michelson interferometer is four times the intensity of a single arm ($I = 4I_b$).

³⁴ In Chapter 3, Figure 3.9, the intensity versus the number of ‘incubative’ pulses was connected to multi-shot ablation threshold. Here 10^4 pulses correspond to $\sim 4 \text{ TW/cm}^2$. In the experiments using dielectric materials, the intensity for the interfering beams was set below or near this value.

For silicon and aluminum, the intensity was kept around the threshold.

³⁵ EPS6000, Newport Inc.

³⁶ Similar time-resolved studies of particles emission from dielectric materials irradiated at laser intensities above the optical breakdown combine pump-probe experiments with details of particles velocity [SRA02].

4.1.2. Dynamics of ions desorbed from a dielectric surface

As detailed in Chapter 3, femtosecond laser interaction with fluorides causes the desorption of a large number of positive atomic ions to large clusters. At intensities around $\sim 1 \text{ TW/cm}^2$ the ion emission may be sufficiently high to open additional desorption channels (cf. Chapter 3).

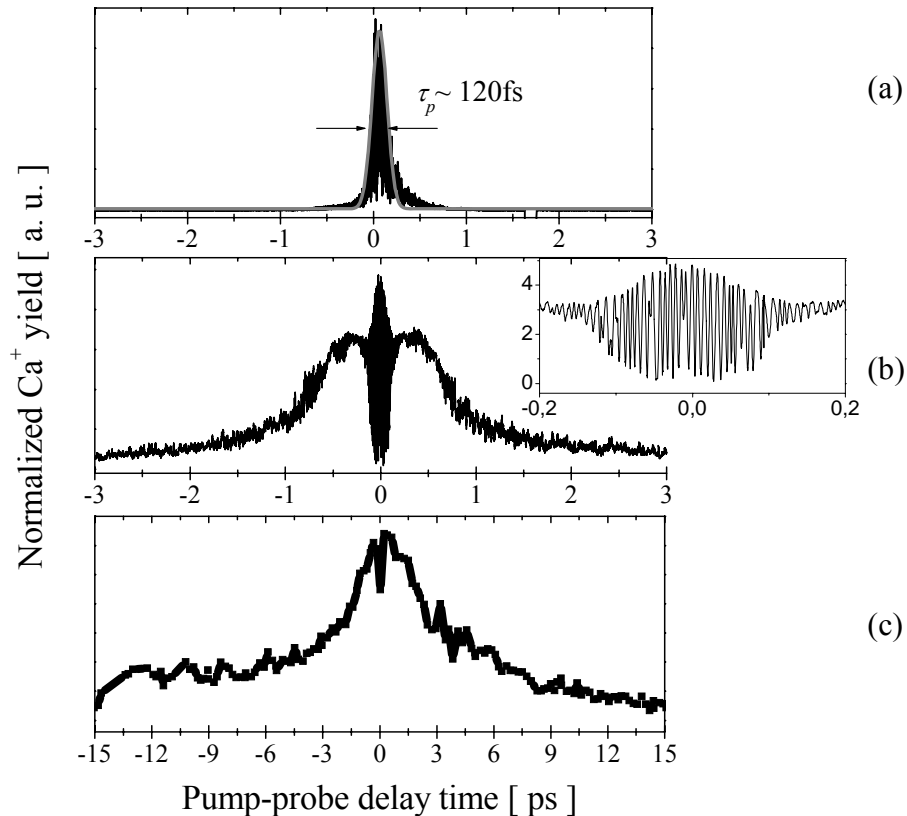


Figure 4.2. Ca^+ yield (CaF_2 target) as a function of the delay time between equally intense pump and probe pulses at different laser intensities $I_{\text{pump}} \cong I_{\text{probe}} = I_b$ (a) $I_b \sim 0.3 \text{ TW/cm}^2$. A Gaussian pulse of a $\sim 120 \text{ fs}$ width is overlapped on the ion yield around zero pump-probe delay time; (b) $I_b \sim 0.5 \text{ TW/cm}^2$; the insert represents a magnified segment of the measurement around zero delay. This shows the autocorrelation trace enlarged by an overlapped contribution from a transient phase; (c) $I_b \sim 1.4 \text{ TW/cm}^2$.

For measurements on a CaF_2 target the main positive ion products Ca^+ and F^+ were selected from the mass spectra and integrated.

At intensities below or near $I_b \sim 0.3 \text{ TW/cm}^2$, one single beam irradiation generates mainly random ion spikes. In the two-pulse correlation trace, the Ca^+ ion signal increases

significantly with the delay time $\Delta\tau$ around zero³⁷, i.e. at the pump-probe pulses temporal coincidence (Figure 4.2 (a)). As expected from using equally intense pump and probe pulses, the correlation trace is symmetrical around $\Delta\tau = 0$.

Interestingly, at slightly higher I_b intensity the ion emission revives again even when the pump and probe pulses are no longer temporally overlapped (Figure 4.2 (b) for longer Δt). This effect is observed for single beam intensities of about one order of magnitude below the damage threshold intensity. Here, the probe pulse sees apparently a target prepared by the pump beam in a transient manner, without a permanent surface change as indicated by the preserved symmetry in the ion yield around zero delay.

Further, Figure 4.2 (c) shows that the ion emission revival at an incident intensity of $I_b \sim 1.4 \text{ TW/cm}^2$ lasts *longer* than, for instance, at $I_b \sim 0.3 - 0.5 \text{ TW/cm}^2$ (Figures 4.2 (a, b)). Thus, an apparently higher I_b gives rise to an enhanced ion emission on a larger *time range*. Here, the ion signal returns to the corresponding single pulse desorption response at time delays around $\Delta\tau \geq 6 \text{ ps}$.

Similar effects are observed not only for Ca^+ but also for several positive and negative ion species ejected from a CaF_2 target. Figure 4.3 displays the F^+ , F^- and Ca^+ ion yields as a function of pump-probe delay time $\Delta\tau$. For all these ions, the measurements indicate the two-pulse correlation around $\Delta\tau = 0$ and the ion emission revival around a characteristic time delay in average of a $\Delta\tau_R(\text{CaF}_2) \sim 0.3 \text{ ps}$.

At low intensities, the two-pulse correlation indicates that the ion yield response to excitation is limited to the laser pulse width. Indeed, around zero delay a Gaussian pulse shape of $\sim 120 \text{ fs}$ width corresponds nearly to the two-beam correlation signal (Figures 4.2-4.3).

We obtained similar results when analyzing other dielectric targets such as BaF_2 , MgF_2 and Al_2O_3 .

³⁷ Also, the amplitude of the correlation trace is significantly reduced, when differently polarized (p and s) pump and probe pulses are employed, as this yields no interference [Eck06].

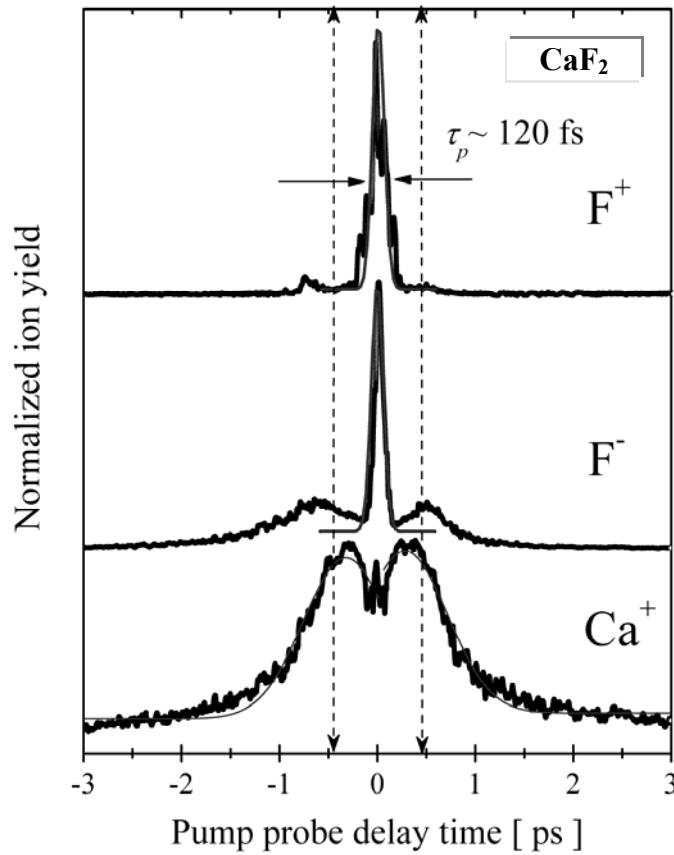


Figure 4.3. Positive F^+ and Ca^+ and negative F^- yields dependence on the delay time between two pump and probe pulses ($I_{pump} \cong I_{probe} = 0.5 \text{ TW/cm}^2$). The emission revival around $\Delta\tau_R \sim 300 \text{ fs}$ with regard to the laser pulse is indicated by dotted lines. The pump-probe correlation peaks distinguishable in the F^+ and F^- yields are fitted with Gaussian pulse shapes of $\tau_p \sim 120 \text{ fs}$ duration. In order to emphasize the symmetry in the negative and positive time delays, in the Ca^+ measurement, Gaussian functions are used to fit the delayed ion yields; here, the best fits are centered on $\pm 300 \text{ fs}$ and have about $\sim 900 \text{ ps}$ width.

From a BaF_2 target irradiated by laser beams of $I_b \sim 0.3 \text{ TW/cm}^2$, Ba^+ , F^+ , F^- and electron yields were recorded as a function of pump and probe delay time. As shown in Figure 4.4, all investigated ions, both positive and negative, respond similarly to the single pulse excitation. The ion emission increases significantly not only in a two-pulse correlation around zero delay, but also around a delay $\Delta\tau_R$ of a few hundreds of femtoseconds ($\Delta\tau_R(BaF_2) \sim 0.9 \text{ ps}$). Moreover, Figure 4.4 indicates that both electron and ion signals respond similarly to the pump-probe delay time variation.

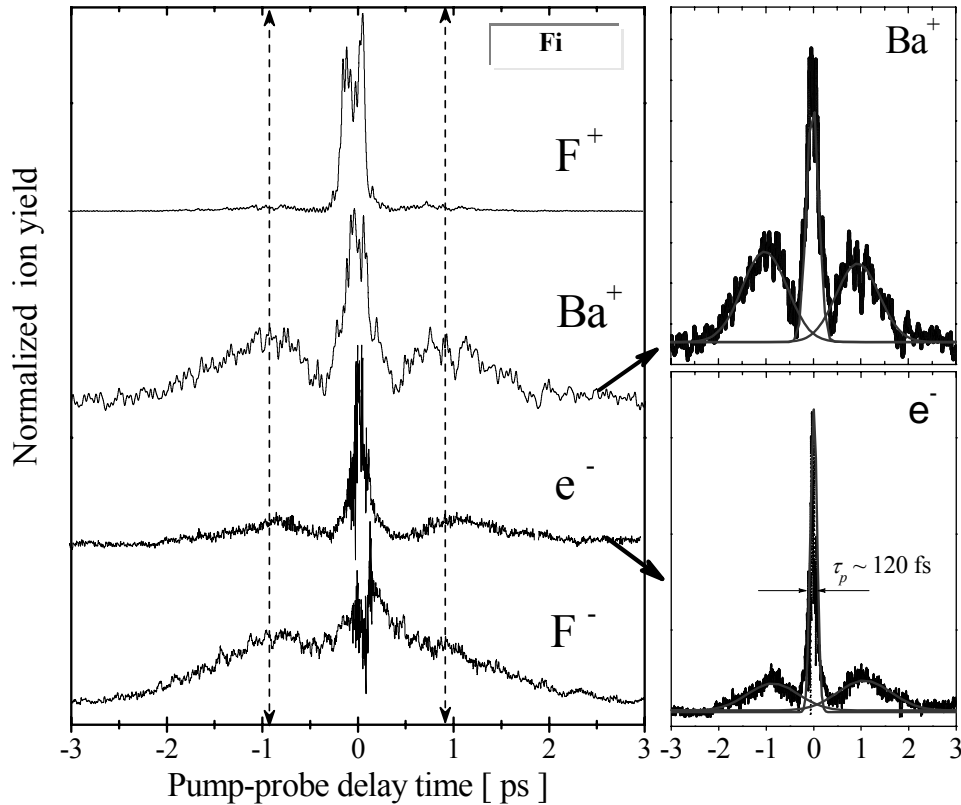


Figure 4.4. Ba^+ , F^+ , F^- and electron yields as a function of delay time between pump and probe pulses ($I_{\text{pump}} \cong I_{\text{probe}} = 0.5 \text{ TW/cm}^2$). Note, in all measurements, the symmetry of the two pulse correlation around zero delay³⁸. The dotted lines indicate the time delay $\Delta\tau_R = \pm 900 \text{ fs}$ where the ion emission increases again. For e^- and Ba^+ measurements, in the right side panels, Gaussian pulse shapes of about $\sim 120\text{-}150 \text{ fs}$ width are overlapped on the two-pulse correlation around zero delay (the dashed-dotted red lines). In order to emphasize the symmetry as well as the comparable time response in the negative and positive time delays, Gaussian functions centered at $\Delta\tau_R = \pm 900 \text{ fs}$ of width $\sim 1 \text{ ps}$ were applied on both peaks.

We represent in detail in Figure 4.5, the two-pulse correlation for two of the positive species, Ba^+ and BaF^+ , respectively. We can easily see the interference effect in the Michelson set-up. Here, it is worth to recall from the previous chapter that because electrons and ions are lost in transmission along the drift tube (a more critical condition for the lighter electrons than for the heavier ions) their absolute yields could greatly differ.

Furthermore, another fluoride single crystal i.e. *magnesium fluoride*, MgF_2 has been investigated. Magnesium fluoride has a wide bandgap of 12.3 eV. The radiation damage mechanism in magnesium fluoride is excitonic in nature, being similar to that in alkali

³⁸ Note also the modulation in intensity around the pump-probe coincidence, which is due to destructive interference in the Michelson set-up.

halides. Previous studies [DCD93] on ion bombarded MgF_2 , in the near UV and visible regions of the spectrum, identified the presence of F and several F_2 centers consistent with the rutile structure. Interestingly, at incident intensities below the damage threshold for a single pulse ($\sim 15 \text{ TW/cm}^2$ as indicated in [LiS95]), femtosecond laser interaction with MgF_2 targets gives rise to desorption of singly, *doubly* and *triply* charged positive Mg^+ ions and clusters (Figure 4.6).

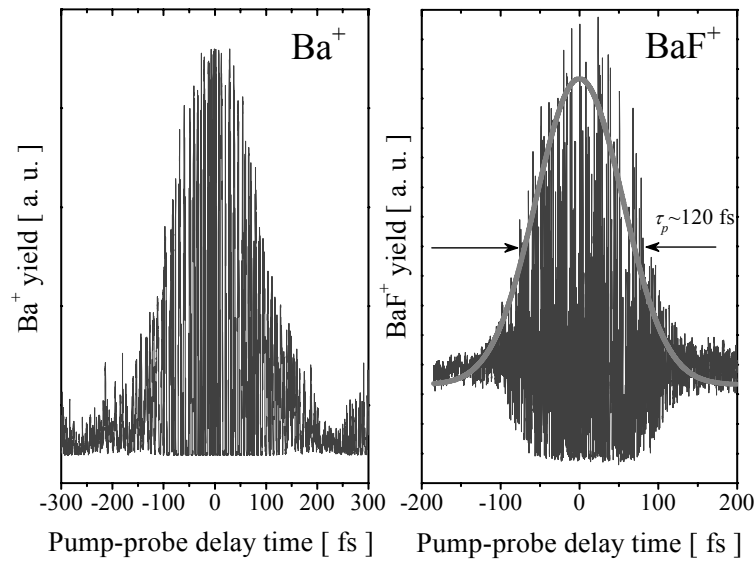


Figure 4.5. Ba^+ yield (left) and BaF^+ yield (right) at delay time corresponding to the pump-probe coincidence in a two-pulse correlation trace.

Mg^+ and MgF^+ ion yields were measured in the pump-probe mode employing again single beam intensities below the damage threshold (Figure 4.7 (a)). Similar to the observations shown above, the ion yield becomes important around zero delay and a characteristic time $\Delta\tau_R$ ($\Delta\tau_R(\text{MgF}_2) \sim 0.4\text{ps}$). It is evident that the dynamics of ion desorption by femtosecond laser pulse from these three alkaline-earth fluorides reveal similar temporal characteristics.

Fluoride materials exhibit strong electron-phonon ($e-ph$) coupling strength, thus for a comparison, we also investigated a material of an intermediate $e-ph$ coupling strength such as the crystalline sapphire (Al_2O_3). The femtosecond laser desorption from this material has been already intensively studied [HWR00, SAR00].

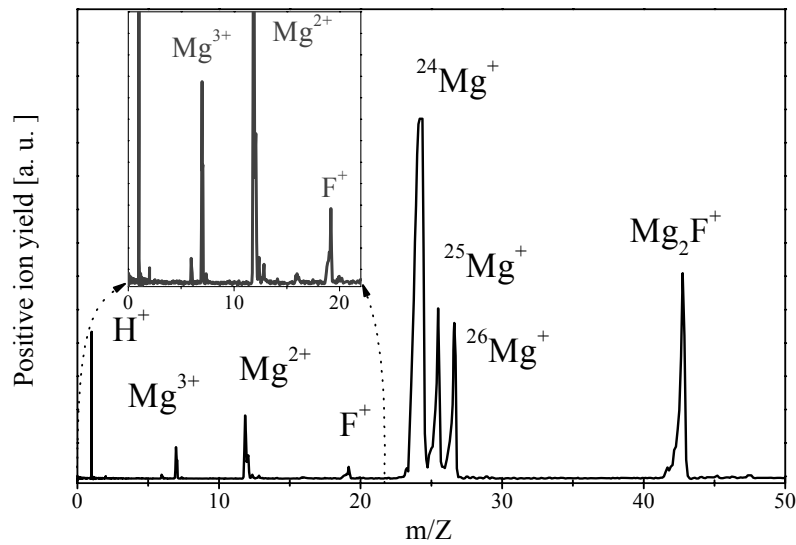


Figure 4.6. Positive ions desorbed from a MgF_2 target. The inset represents a magnified section of the mass spectrum.

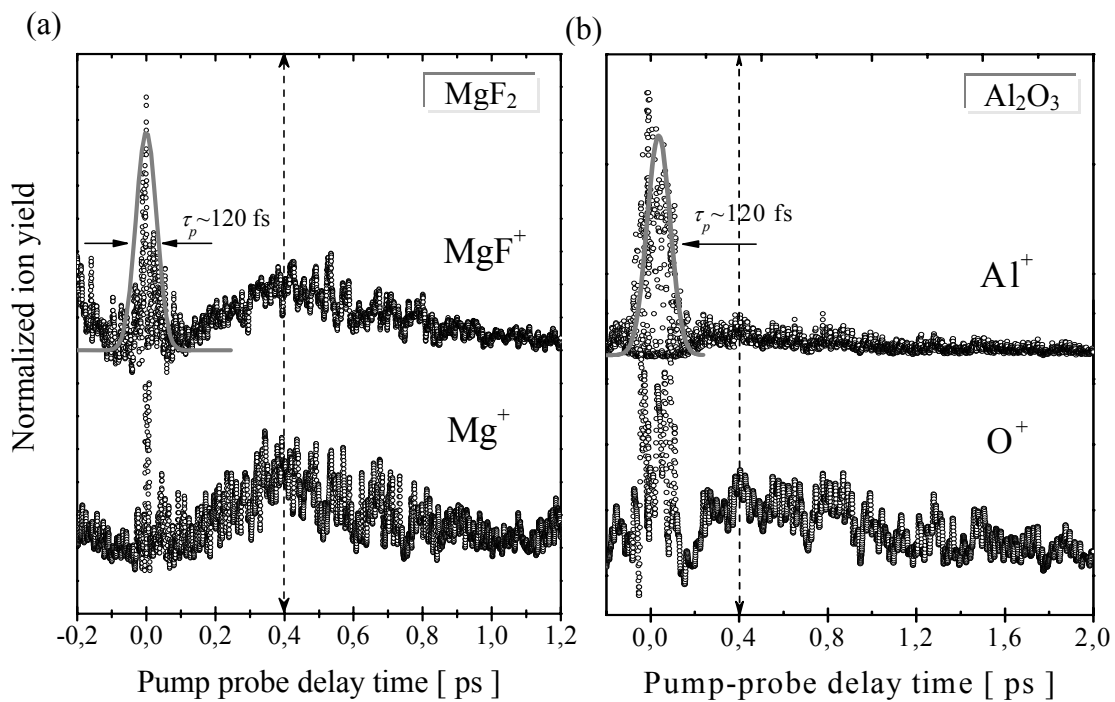


Figure 4.7. (a) Positive Mg^+ and MgF^+ yields dependence on delay time between two sub-damage threshold pulses ($I_{\text{pump}} \cong I_{\text{probe}} = I_b$; $I_b \sim 0.7 \text{ TW/cm}^2$). The dotted lines indicate the ion emission revival at a larger pump-probe time separation, characteristic for all the measurements. (b) Positive Al^+ and O^+ yields from an Al_2O_3 target as a function of the delay time between pump and probe pulses ($I_{\text{pump}} \cong I_{\text{probe}} = I_b$; $I_b \sim 2 \text{ TW/cm}^2$). Gaussian pulse shapes of $\sim 120 \text{ fs}$ width are applied in the two-pulse correlation region.

Figure 4.7 (b) displays the yields of Al^+ and O^+ as a function of the pump-probe delay time, measured in similar conditions as the fluoride targets. Again, the ion yield increases around zero delay and a characteristic $\Delta\tau_R$ time ($\Delta\tau_R(\text{Al}_2\text{O}_3) \sim 0.4\text{ps}$).

To summarize, time-resolved studies using ion desorption from dielectric materials, at intensities still below the (multi-shot) damage threshold, reveal as follows: the ion emission increases significantly not only in the two-pulse time overlap region but also for a *material characteristic time* (around a delay $\Delta\tau_R$). This time evidently indicates a regime where the surface prepared by the pump pulse has reached a phase of increased ionization response to the probe pulse. Additionally, the relaxation time of this phase becomes longer with increasing intensity.

In the following, we present results of experiments carried out in the same pump-probe mode on crystalline silicon and aluminum. Although the results will point toward similar temporal details, in the discussion that follows we will take into account that the prevailing desorption mechanisms are basically different.

4.1.3. Dynamics of ions desorbed from silicon and aluminum

Pump-probe studies on *Silicon (100)* were carried out at intensities around the damage threshold ($\sim 0.5 \text{ TW/cm}^2$, cf. Chapter 3). Figure 4.8 displays a Si^+ yield as a function of pump-probe delay time.

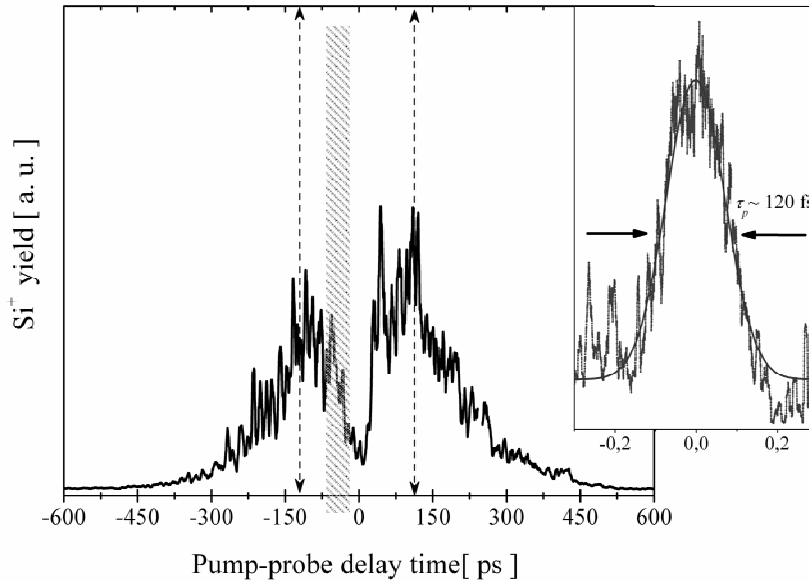


Figure 4.8. Si^+ yield as a function of delay time between pump and probe beams ($I_{\text{pump}} \cong I_{\text{probe}} = 0.2 \text{ TW/cm}^2$). The inset shows the correlation peak at a relevant time resolution together with a Gaussian pulse of $\sim 120 \text{ fs}$ width.

In the two-pulse correlation around zero delay, the ion yield response to excitation appears to be pulse-width limited (the inset in Figure 4.8). When the twin pulses are separated by a few picoseconds, the ion emission starts to increase again, reaches a maximum at around hundreds of picoseconds and dies out at a pulse separation of almost a nanosecond. This effect is also observed for the yields of larger clusters.

The ion desorption dynamics from *Aluminum* appear remarkably similar, although at a different timescale. Femtosecond laser pulses interaction with aluminum surfaces gives rise to desorption of positively and negatively charged particles. The mass spectrum of negative ions shows singly or doubly charged atomic ions and large clusters (larger than Al_{15} ; Figure 4.9). The positive mass spectrum indicates only a few number of species for the same incident intensity.

The ablation threshold intensity for a single pulse of was estimated by [AWA00] for similar irradiation conditions to be $I_{th} \sim 1 \text{ TW/cm}^2$. We employed laser intensities in the range of $I_{pump}=I_{probe}=I_b \sim 0.25 - 0.75 \text{ TW/cm}^2$, therefore around I_{th} . At this intensity, single beam irradiation gives rise to a rather low ion signal. Different species such as Al^+ , Al_2^+ , Al^- and electrons were recorded as a function of pump-probe delay time.

As shown in Figure 4.10, the two-pulse correlation signal around the zero delay can

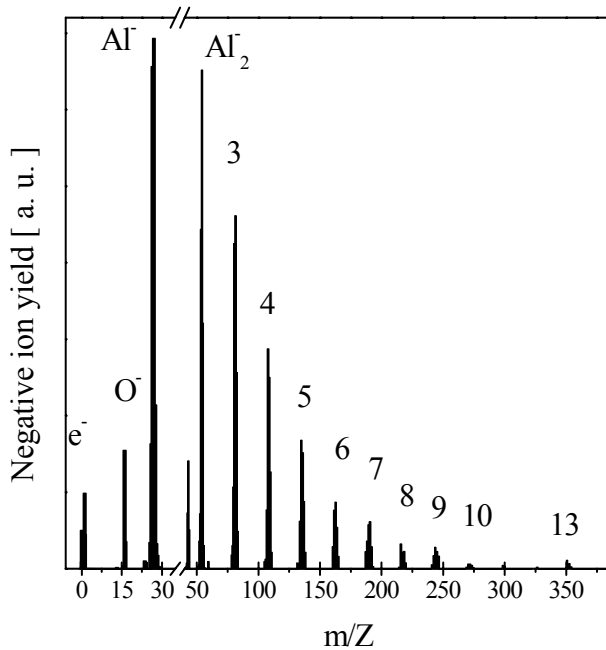


Figure 4.9. Typical negative ion mass spectrum from a femtosecond laser pulse irradiated Al target.

be already a combination of different ultrafast processes falling within the pulse width limit. At a time separation of several picoseconds the ion yield increases again, reaches a maximum around a characteristic time $\Delta\tau_R$ ($\Delta\tau_R(\text{Al}) \sim 17\text{ps}$), and then decreases down to a yield given by one pulse excitation. The evident symmetry in the measurement of Al_2^+ yield for negative and positive time delays suggests that the surface responds equally to each of the two pulses. Also, an apparent asymmetry in the correlation

signal is likely caused by the surface modification.

Figure 4.11 presents measurements of the electron, positive and negative ion yields dependence on the delay time recorded in the same conditions. It is evident that $\Delta\tau_R$ is a material characteristic time, since the ion yield evolution with the delay time is nearly the same for all the measurements.

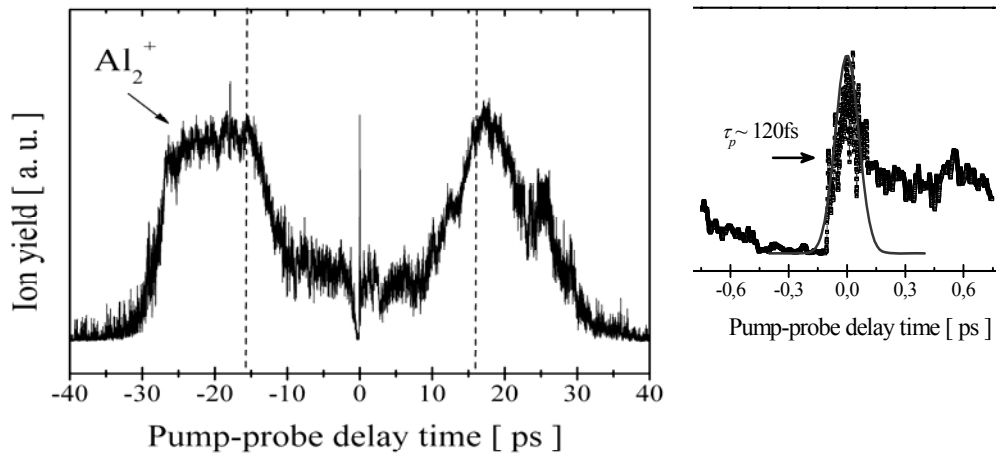


Figure 4.10. Al_2^+ (a) Al^+ , Al^- and electron yield (b) as a function of delay time between pump and probe pulses ($I_{\text{pump}} \cong I_{\text{probe}} = 0.7 \text{ TW/cm}^2$). The inset presents an asymmetrical two-pulse correlation likely induced by surface modification. The dotted lines indicate the characteristic $\Delta\tau_R$ (see text).

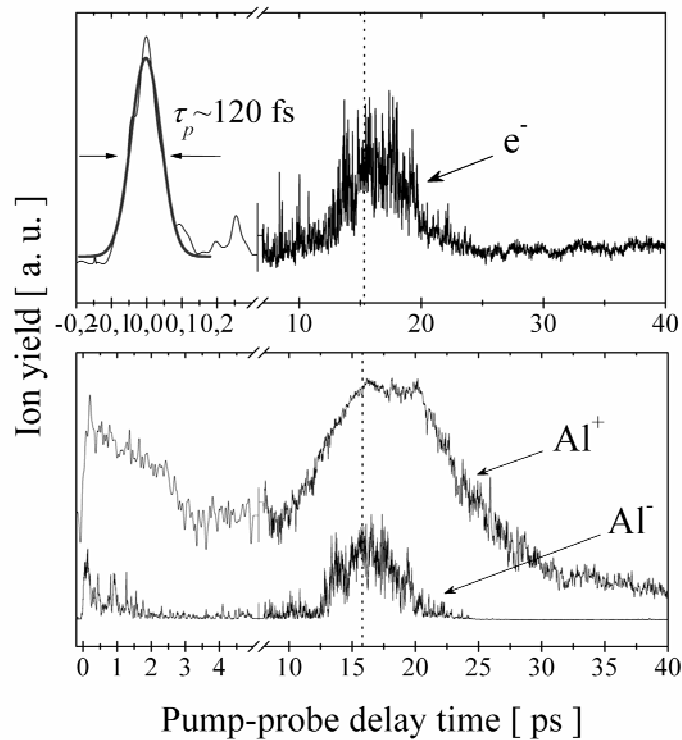


Figure 4.11. Al^+ , Al^- and electron yield as a function of delay time between pump and probe beams ($I_{\text{pump}} \cong I_{\text{probe}} = 0.7 \text{ TW/cm}^2$). For a better visibility of the increase in ion yield, the time-axis for the electron yield is broken to relevant scales. The two-pulse correlation around zero delay is compared with pulses of $\sim 120 \text{ fs}$ duration of a Gaussian shape. The dotted line indicates the characteristic $\Delta\tau_R$ (see text).

The regime (effect) taking place around $\Delta\tau_R$ time last longer with increasing intensity. This is, however, not surprising since the ion yield increases with intensity.

In a *conclusion* directed now to the variety of materials under study, the measurements indicate two main time regimes for ion desorption corresponding to:

(1) The two-pulse correlation around zero delay, most likely a convolution of ultrafast processes falling within the laser pulse width;

(2) The ion yield revival, i.e. absorption enhancement, related to a material characteristic $\Delta\tau_R$ ³⁹.

In the next subsections we suggest an origin for these time regimes. Accordingly, the results obtained on dielectric materials are analyzed and compared with the data from silicon and aluminum. We can associate our findings on temporal dynamics of ion desorption to the *e-ph* coupling strength of the studied materials.

³⁹ We have also previously indicated that these two time regimes can be well associated with fundamental relaxation times, namely phase relaxation (T_2) and energy relaxation (T_1) [CER04].

4.2. DISCUSSION ON CHARACTERISTIC TIMESCALES

In the experiments on dielectrics, by keeping the sum of pump and probe intensities below the damage threshold, no permanent surface modification is expected, once the sample is incubated. This situation is confirmed by the evident symmetry with respect to positive and negative pump-probe delays.

Intensity dependent or/and short timescale processes should occur within the two-pulse correlation timescale and be responsible of either an increase in signal amplitude or a temporal broadening of the correlation width.

As shown in the preceding chapters, the initial energy coupling between the incident light and the material is dominated, at this intensity range, by multi-photon generation of free electrons. This is a highly nonlinear process (order 7 and 8 for $h\nu = 1.55$ eV, where $7 h\nu > E_{g, \text{BaF}_2} \approx 10\text{eV}$ and $8 h\nu > E_{g, \text{CaF}_2} \approx 12$ eV) for our experimental conditions. The strong ion yield at the pump-probe coincidence, i.e. zero delay, already corresponding to four times the intensity of a single pulse, should be further enhanced by a nonlinear increase of the ion yield with intensity. In contrast, due to a lower order in the ionization process in silicon or aluminum (corresponding to 1-2 photon process) the amplitude of the correlation peaks should be comparatively smaller.

It is known that in solids scattering causes a fast dephasing of the coherence between the electronic excitation and the laser electromagnetic field. Coherent effects decay very fast (e.g. of about 10-100 fs for silicon [SuM02]). Basically, at pump-probe full coincidence the excited electrons are in phase, thus they act coherently at their combined intensity. For a decreasing pump-probe overlap, the electronic coherence is destroyed by electron-electron collisions. At complete separation, each of the pulses desorbs particles individually at a significantly lower rate. Since the correlation width is mainly limited by the pulse duration, no major conclusion could be derived from the data points around zero time delay, thus the coherent effects appear to be relatively un-important here.

4.2.1. Transient states of matter

In all measurements we found an increased ion desorption signal around $\Delta\tau_R$ (as listed in Table 4.1). This indicates that by gradually increasing the delay time between pulses, the lattice perturbation, as induced by the first pulse, is more and more amplified. The probe pulse adds more energy to the already perturbed system leading each time to higher ionization rates. Consequently, the ion yield increases again although the pump-probe pulses are completely temporally separated. In fact, when comparing the measurements from different target materials studied, we find that the starting time of the transient phase increases from fluorides to silicon and aluminum, hence corresponding to a decreasing *electron-phonon (e-ph)* coupling strength.

Table 4.1. The apparent starting and maximum time of the transient phase in different materials as extracted from pump-probe experiments.

Material	$\Delta\tau_R$ (ps)	<i>e-ph coupling</i>
CaF ₂	< 0.1÷0.3	strong
MgF ₂	< 0.1÷0.4	
BaF ₂	< 0.4÷0.9	
Si	< 3÷60	intermediate
Al	< 6÷17	weak

We attribute the apparent starting time of the transient phase to the primary significant lattice modification. This modification augments with larger pump-probe separation reaching a maximum. Its relaxation-like behavior is witnessed by a decreased coupling efficiency for the probe pulse.

As a possible explanation for this (transient) phase, in the following we explore the temporal dynamics of defect creation in dielectrics and lattice disorder or phase transitions in semiconductors and metals.

4.2.1.1. Probing transient states

We can immediately see that the ion desorption from dielectrics cannot be treated based on thermal equilibrium, since for cooling at equilibrium, the heat flow would require more than 10 ps and thus the correlation width would appear much broader.

On the other hand, the decomposition of an electrostatically unstable surface (Coulomb explosion mechanism) may already occur during the laser pulse [ChH95]. As

indicated by the experiments in dielectrics, the charge unbalance likely involves the creation of defects. Also, ion desorption originates predominantly from dynamics at the surface, as we suppose, for instance from excitation of defects, pre-existing or produced during the laser pulse.

We assume that the origin of the transient increase in ion emission in dielectrics (around $\Delta\tau_R$) indicates primary processes such as a free carrier localization/decay or the self-trapping of an exciton and its de-trapping time. Such processes can take place both at the surface and deeper in the bulk. Indeed, studies based on interferometry in a pump-probe mode indicate that rapidly exciton trapping – de-trapping in dielectric materials can occur within less than a picosecond [ADD94]. In particular for fluorides, self-trapped excitons could relax within up to tens of picoseconds as demonstrated by time-resolved optical absorption spectra [Tan01]. In fact, using a simple exponential function [$\exp(-t/\tau_d)$] for a decay of the ion yield transient phase (around $\Delta\tau_R$) we obtain a decay time of $\tau_d \sim 0.5$ ps for Ca^+ ; $\tau_d \sim 0.4$ ps for Mg^+ and $\tau_d \sim 1.1$ ps for Ba^+ (Figure 4.12 – blue lines). Additionally, the growth of ion emission is well described by a function of the form [$1 - \exp(-t/\tau_g)$], with a characteristic growth time of $\tau_g \sim 0.5$ ps in Ba^+ (Figure 4.12 – gray line).

Our results appear to be in line with previous time-resolved studies on ion desorption from other dielectric materials such as MgO and LiF [BJH00], which revealed an ion yield decaying in 2 ps respectively 20 ps after the laser pulse ended.

In the preceding chapters we showed that the conduction band electron density due to multiphoton and avalanche ionization develops rapidly during the laser pulse and can decay in a characteristic time for electron trapping or related processes.

Using Eq. 3.8 from Chapter 3, we evaluate the temporal evolution of electron density in CaF_2 irradiated with a single 120-fs pulse of intensity $I = 5 \text{ TW/cm}^2$ ($\sim 4I_b$ at the peak intensity at the pump-probe spatial overlap) and a trapping time $t_D = 0.5$ ps. The graphical representation displayed Figure 4.12 (a) follows closely our results on CaF_2 (Figure 4.12 (b)) for single-pulse excitation. At this intensity range, the electron density is still below the critical density usually associated with the damage threshold. However, it is evident when comparing panels (a) and (b) in Figure 4.12 that the growth of ion emission is delayed from the electron density relaxation curve.

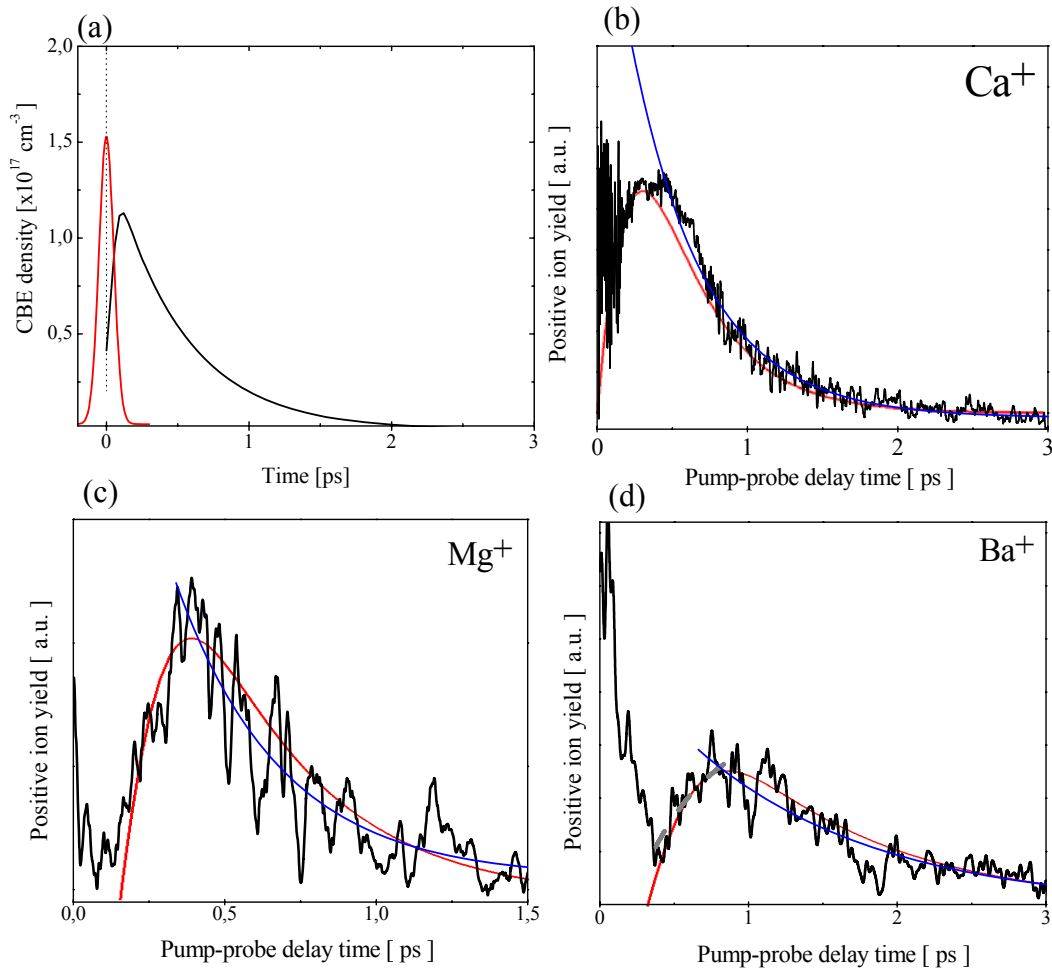


Figure 4.12. (a) The temporal evolution of electron density in CaF_2 irradiated with a single 120-fs pulse of $4I_b \sim 5 \text{ TW/cm}^2$ including an electron trapping term of 0.5 ps time decay. A Gaussian pulse (red line) of 120 fs was used in the calculation. (b-d) Positive ion yield as a function of pump-probe delay time in fluoride materials. Exponential fits to selected data with a time decay of 0.5 ps (Ca^+), 0.4 ps (Mg^+) and 1.1 ps (Ba^+) (blue lines) and a growth time of 0.5 ps (Ba^+) (dashed gray line). The solid red lines represent results from an analysis using a rate-equation model given by Eqs. 4.1-4.3 including temporal changes of surface states generation and decay; the results of the fits are listed in Table 4.2.

Table 4.2. Results of the fits with the rate-equation model given by Eqs. 4.1-4.3 on ion yield dependence on the pump-probe delay time in Figure 4.11.

Yield	t_0 , ps	w , ps	t_D , ps
Ca^+	0.02	0.5	0.5
Mg^+	0.15	0.3	0.4
Ba^+	0.3	0.6	1.1

Moreover, this delay appears more pronounced in the case of BaF₂ and MgF₂ (Figure 4.12 (c, d)). Thus, as compared to electron trapping on a defect state, the process responsible for the increase in ion yield should be more complex.

As already detailed in Chapter 1, the relaxation of electron-hole pairs is assumed to include several relaxed configurations of excitons, which occur due to the strong interplay between electron-phonon and hole-phonon interaction. Models for the formation of lattice defects as Frenkel pairs (*F-H*) pairs in alkali halides [SFS96, Tan01] included intermediate states attributed for instance to relaxation/cooling of a hole after having trapped an electron. Optical spectroscopy studies indicate that the formation of an STE can involve several transient states acting as precursors [SFS96].

We postulate that generation and relaxation processes of such transient states would account for a time delay between the electronic excitation and ion emission. Thus, we consider additional intermediate, transient states, as in the model proposed in [Tan01], to account for the generation of a defect (e.g. STE) which could account for the timescale where the ion yield varies (Figure 4.13).

Our model includes two steps: (1) ionization and ‘cooling’ of an intermediate state to form a relevant defect; (2) the defect relaxation to a more stable, lower energy configuration.

The transient intermediate state can be attributed to the primary electron-lattice interaction. This can be seen as a convolution of various lattice dephasing effects, electron-hole relaxation/cooling processes and hole localization. It is here represented by a generation function $G(t)$, which is taken to be a Gaussian of the form:

$$G(t) = A \cdot \exp\left(-\frac{(t-t_0)^2}{w^2}\right) \quad (4.1)$$

with an overall delay t_0 , a distribution width of $w/\sqrt{4\ln 2}$ and a scaling factor A .

The area under the generation curve represents the population density in this intermediate transient phase.

$$n_I = \int G(t)dt = \frac{1}{2} Aw\sqrt{\pi} \cdot \operatorname{erf}\left(\frac{t-t_0}{w}\right) \quad (4.2)$$

with $\text{erf}(x)$ the standard error function. We construct a simple rate equation including a gain provided by the generation function and a decay term with a time decay τ_D .

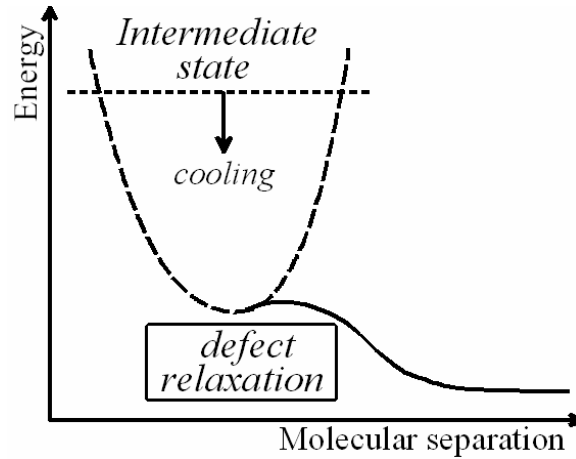


Figure 4.13. Schematic of a possible energy relaxation route for electron-hole pairs in fluoride crystals. The postulated, intermediate state ‘cools down’ on a defect state, which undergoes further relaxation to a more stable, lower energy configuration.

The rate equation giving the population of the defect state n_D reads:

$$\frac{dn_D}{dt} = G(t) - \frac{n_D}{\tau_D} \quad (4.3)$$

with a solution of $n_D \approx n_I \cdot \exp\left(-\frac{t}{t_D}\right)$. By using Eqs. 4.1-4.3, the data in Figure 4.12 can be fitted with $t_D = 0.5$ ps (Ca^+), $t_D = 0.4$ ps (Mg^+) and $t_D = 1.1$ ps (Ba^+), which would represent the decay time of the defect state excited in our conditions.

This model appears to explain reasonably well the transient phase observed the experiments on dielectrics.

In addition, such a defect state can account for a transient phase in laser ablation of silicon (recombination via surface states in silicon are well-determined; see for instance the local density calculations of Allan et al. [ADL96]). These states can be STEs in Si-Si dimers located near the surface. They are known to decay fast with increasing temperature (e.g. their decay time is in about microseconds at room temperature [KZW01]). To our knowledge, their behavior at the high temperature of laser ablation is so far unknown.

In the following, a different model is used to explain the origin of the transient phases found in aluminum and silicon.

4.2.1.2. Probing electron-lattice coupling dynamics: Thermal response of solids to the laser excitation

An increased electron yield at a longer pump-probe separation has been before indicated for a metallic target [WRL94]. Here, this contribution has been suggested to occur from a temporary suppression of electron emission due to screening induced by the formation of a space charged layer [WRL94]. This, however, cannot explain our observation of temporal correlation between electron and ion emission. More likely, we monitor here the lattice response to excitation in a characteristic electron-lattice coupling time. As the lattice heats up fast, it likely passes through a transient disordered phase (or a liquid phase as proposed in [SHB00]⁴⁰). This disordered phase absorbs better the incident radiation giving rise to an increased ion yield. The relaxation of this transient phase via heat diffusion should occur at a sufficient pump-probe separation.

As before indicated, femtosecond laser pulses induce changes in the material properties for time periods shorter than the electron-lattice energy transfer time $t < \tau_{ep}$. Here, the laser energy leads to electronic excitation while the lattice remains cold. The material phase change undergoes a non-equilibrium transition with a presumable electron temperature T_e of about several orders of magnitude higher than a lattice temperature T_i . For $t > \tau_{ep}$, the transition proceeds in ‘thermal’ conditions, for which the electron and lattice temperature are equilibrated $T_e \sim T_i$. The equilibration of the electronic subsystem with the lattice is dictated by electron-phonon relaxation mechanisms. Previous works distinguish between different regimes of heat propagation in metals, via electron heat transport, in a system of equations describing the spatial and temporal variation of the electron and lattice temperatures. The two temperature model (TTM) [AKP74], already mentioned in Chapter 1, considers that the electronic and lattice system are decoupled and being thermalized individually, but are linked by a finite electron-phonon coupling constant g , as following:

$$C_e \frac{\partial T_e}{\partial t} = \frac{\partial}{\partial z} \kappa(T_e) \frac{\partial T_e}{\partial z} - g \cdot (T_e - T_i) + S(z, t) \quad (4.4)$$

⁴⁰ It should be mentioned that also ultrafast melting [WaD92] could contribute to lattice deformation. This is attributed, however, to a higher intensity range than the one considered here.

$$C_i \frac{\partial T_i}{\partial t} = g \cdot (T_e - T_i) \quad (4.5)$$

where $S(t, z)$ is a source term accounting for the laser heating with intensity $I(t)$, C_e and C_i are the electron and cold lattice heat capacity respectively, and κ is the thermal conductivity. For $T_F > T_e \gg T_i$ where T_F is the Fermi temperature, the target surface region is in strong non-equilibrium conditions and the electron heat capacity is well approximated by a linear dependence on temperature $C_e \sim C_e' T_e$ with C_e' a constant [AsM76]. The dependence of κ on T_e is usually assumed to be of the form $\kappa = C_e v_F^2 \tau_e / 3 \sim T_e \tau_e$ for an incident fluence range around the damage threshold [CBS88, KSI98], where v_F is the Fermi velocity ($v_F = \sqrt{2E_F/m_e}$ with E_F the Fermi energy). The electron relaxation τ_e is determined by the electron-electron and electron-phonon collision times via $1/\tau_e = 1/\tau_{ee} + 1/\tau_{eph}$.

In the frame of the TTM, our data for aluminum suggest that the correlation trace at the pump-probe overlap could account for a fast increase of the *maximum (peak)* electron temperature. Also, it is possible that by measuring the electron (or ion) yield versus pump-probe time separation, we obtain an immediate evaluation of the hot-electron cooling curve for single-pulse excitation.

The TTM shows indeed that, in metals, the lattice heating occurs on a longer timescale (typically a few picoseconds), owing to its larger heat capacity as compared to the free electron heat capacity. In fact, when comparing the different target materials studied, we find that the starting time of the transient phase $\Delta \tau_R$ increases with decreasing *e-ph* coupling strength g . Taking in Eqs. 4.4 - 4.5 only the terms in g from the right side and $T_i \ll T_e$, we can obtain $\tau_{ee} \sim C_e/g$ and $\tau_{ep} \sim C_i/g$ with $\tau_{ee} \ll \tau_{ep}$ since $C_e \ll C_i$ [CBB89].

For a numerical evaluation of T_e and T_i in aluminum, we use known analytical solutions of Eqs. 3.4-3.5 [KSI98, ACI99]. Assuming that the laser pulse duration is small as compared to an electron-lattice relaxation time $\tau_p < \tau_{ep}$ and for a skin depth much smaller than the heat penetration depth, the source term can be neglected and Eqs. 4.4-4.5 become:

$$\frac{\partial T_e}{\partial t} = \frac{1}{C_e} \frac{\partial}{\partial z} \kappa(T_e) \frac{\partial T_e}{\partial z} - \frac{T_e - T_i}{\tau_{ee}}; \tau_{ee} = \frac{C_e}{g} \quad (4.6)$$

$$\frac{\partial T_i}{\partial t} = \frac{1}{C_i} \frac{T_e - T_i}{\tau_{ep}}; \tau_{ep} = \frac{C_i}{g} \quad (4.7)$$

$$\int_0^t \int_0^\infty C_e(T_e) \frac{\partial T_e}{\partial t} dt dz = F \quad (4.8)$$

with F being the laser fluence. Considering that at an initial stage of the process $T_i \ll T_e$ and mainly electron-electron collisions contribute to the electron relaxation, we can evaluate the time in which the temperatures equilibrate. According to [KSI98], the electron relaxation time can be taken here as $\tau_e = \tau_0 (T_F/T_e)^2$ with τ_0 a constant. Following these approximations, the second term in Eq. 4.6 can be neglected as compared to the diffusion term, this reducing the system of equations 4.6-4.8 to the case studied in [ACI99]. The system can be now evaluated analytically, yielding the following simplified solutions at the target surface ($z=0$), as follows:

$$\begin{aligned} T_e(t) &= c T_F \frac{F}{F_0} \sqrt{\frac{\tau_0}{t}} \\ T_i(t) &= 2c T_F \frac{F}{F_0} \frac{\sqrt{\tau_0 t}}{\tau_{ep}} \end{aligned} \quad (4.9)$$

with $F_0 = C_e' T_F^2 v_F \tau_0$ and c a constant.

In a numerical evaluation for Al, we used the following parameters: $C_i = 2.4 \times 10^6 \text{ Jm}^{-3} \text{K}^{-1}$ and $C_e' = 12.5 \text{ Jm}^{-3} \text{K}^{-1}$ [GRL00, EMS00], $T_F = 13.6 \times 10^4 \text{ K}$, $v_F = 10^8 \text{ m/s}$; $\tau_0 = 10^{-17} \text{ s}$ and $g = 2 \times 10^{17} \text{ Wm}^{-3} \text{K}^{-1}$ corresponding to a $\tau_{ep} = 12 \text{ ps}$. The TTM solutions for different fluence levels, given by Eq. 4.9 are represented in Figure 4.14. In Figure 4.14 (a), we can see the rapid decrease in time of T_e . The equalization time t_R for electron and ion temperatures turns out to be shorter than $\tau_{ep} \sim C_i/g$ because of the rapid decrease of T_e . This $t_R \sim 5 \text{ ps}$ agrees well with the apparent starting time for the transient phase in our pump-probe data on aluminum. Also note that, with increasing intensity, the calculated ion temperature at t_R can reach a few thousands Kelvin.

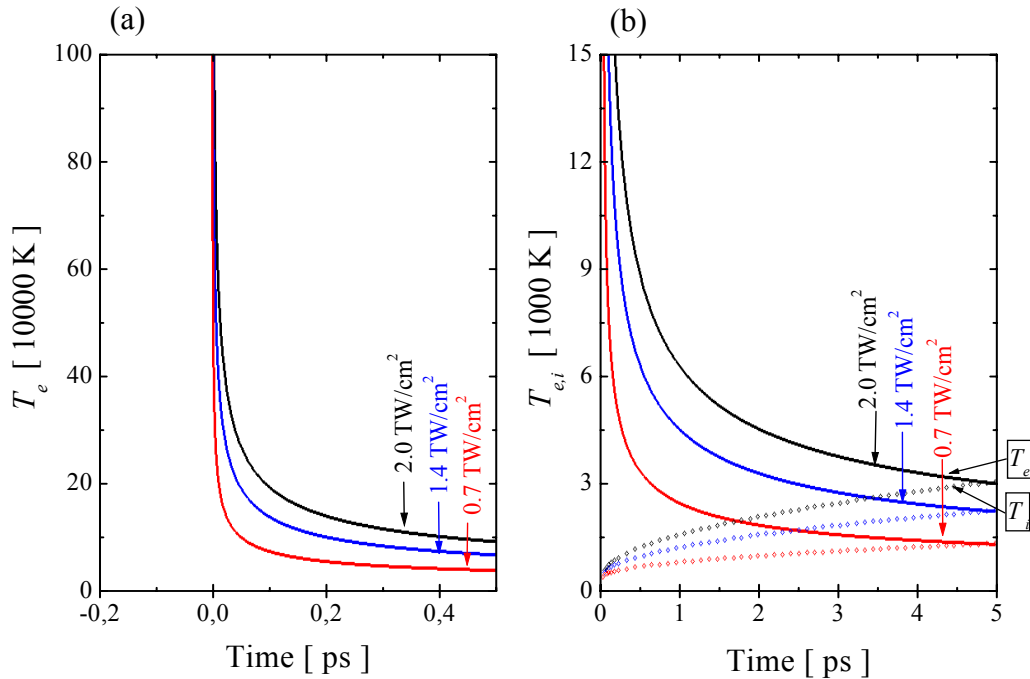


Figure 4.14. The temporal evolution of electron temperature T_e only (a) and T_e (solid lines) and lattice temperature T_i (diamonds) (b) at the surface of an aluminum target, estimated using Eq. 4.9, for different incident intensities. The initial T_i is taken to be 300 K.

Table 4.3. Electron-lattice coupling constant g and the characteristic τ_{ep} for the cold aluminum lattice at RT ($T_i \approx 300$ K) as indicated by different references.

g ($10^{17} \text{ Wm}^{-3}\text{K}^{-1}$)	τ_{ep} (ps)	Reference	Estimation from:
3.7 – 3.9	6 - 6.5	[FFH01]	Calculus
1.3 – 2.6	10 - 20	[EMS00]	Empiric
3.6	6.6	[WaD92]	Reflectivity measurements

On the other hand, for aluminum, the formation time of the transient phase extracted from the pump-probe data falls within the range of values for electron-lattice coupling strength (as well as the corresponding electron lattice relaxation time) reported in the literature⁴¹ (Table 4.3).

⁴¹ To our knowledge, the electron-lattice coupling in aluminum is to date not sufficiently researched. The literature provides only vague data (as the Table 4.2 suggests).

Thus, our data suggest a time when the transition to a new phase occurs, i.e. when the lattice becomes strongly perturbed (suggested by the high T_i). Subsequently, the incoming probe pulse is absorbed in the disordered (for instance a liquid) lattice at a higher rate, which in turn leads to an increased ion yield. Indeed, the crystalline lattice heated at high temperatures can cross an unstable state [LaL80] with thermal oscillations of atoms. The hot lattice allows the atoms to shift into positions, this leading to a new phase of higher disorder degree than the unperturbed solid, seeded by the unstable phase. Using the two-temperature model, Fisher et al. [FFH01] calculated for an aluminum target the time when the lattice (ions) temperature reaches the melting temperature t_{melt} , as a function of laser intensity (for 50-fs pulses at 800 nm). The results suggest a $t_{melt} > 1$ ps for about 1-2 TW/cm² intensity, which corresponds roughly to the single beam intensity in the results presented in Figure 4.10. The time t_{melt} is shown in [FFH01] to decrease with increasing the laser fluences.

We can use these conclusions to discuss the lattice temporal evolution of a silicon target (Figure 4.8). Accordingly, as compared to aluminum, considering the higher electron-phonon coupling strength of silicon, i.e. the shorter electron relaxation time, the transient phase should indeed occur earlier in silicon. This time is typically estimated in the range of a hundreds to a few picoseconds⁴², which is consistent to our findings. Previous molecular dynamics simulations showed that the fast excitation and thermalization of electrons and energy transfer to the silicon lattice rapidly results in a transient material modification [JGB01, JGL02]. Similar to aluminum, a primary lattice modification can be a softened phase (a disordered or a liquid phase). According to our measurements in silicon, the target relaxes via heat dissipation until this transient phase fades away in about hundreds of picoseconds.

⁴² In *silicon*, after initial excitation, each carrier has an average excess energy. This excess energy can become thermalized among the carriers already on a time scale of about ~ 100 -300 fs [GoP94]. The hot carriers equilibrate with the lattice with a time constant τ_{ep} - the electron-lattice energy relaxation time, which can be at the order of a few hundreds fs to a few picoseconds [GoP94, SCS99, SuM02]. Furthermore, studies on temporal dynamics of silicon ablation, using second harmonic generation (SHG) from the surface, show that the SHG signal vanishes in a few hundreds of femtoseconds [SBC98] while reflectivity still increases. The process is also attributed to an increase in disorder at the expense of a very rapid, ultrafast melting process [SAP98].

4.3. CONCLUSIONS

The temporal dynamics of femtosecond laser desorption from a variety of materials has been studied in pump-probe experiments by using equally intense pulses. In the measurements of charged particle yields versus pump-probe delay, one can distinguish two characteristic time regimes, which may correspond to:

- Ultrafast electronic processes taking place during the laser pulse (for instance electron coherence effects);
- Transient processes in the perturbed lattice.

Table 4.3. Timescales of the disordered phase and its possible origin for different materials as described in the text.

Material	$\Delta\tau_R$ (ps)	Possible origin
CaF ₂	< 0.1÷0.3	Electron-lattice coupling Transient defect state (e.g. STE)
MgF ₂	< 0.1÷0.4	
BaF ₂	< 0.4÷0.9	
Si	< 3÷60	Electron-lattice coupling Phase transition
Al	< 6÷17	

The second time regime is indicated by a revival of ion emission at full pump-probe time separation. This suggests the formation of a transient phase of higher absorptivity, linked to the material properties by a characteristic time $\Delta\tau_R$. This time regime seems to be strongly related with the material characteristic, i.e. electron-lattice coupling time. Table 4.3 summarizes, for the samples materials investigated, the observed time regimes as well as our suggestions for their possible origin. For dielectric materials, this time regime may imply the generation of transient species as precursors of the defect creation contributing to desorption of particles.

For silicon and aluminum the transient phases can be related with a transition from a cold solid lattice to a softened phase (disordered or liquid phase). The two temperature model can provide the description of a fast increase of electron temperature to very high values, electron relaxation and electron-lattice energy transfer. In this context the

formation of a transient phase of increased absorption response to a probe pulse would ease the ion desorption.

CHAPTER 5

SURFACE PATTERNING WITH ULTRASHORT LASER PULSES

Ultra-short, intense laser pulses can induce, at the surface region of the target, morphological features on the nanometer scale. The topographical investigation shows that surface structures build up on dielectric and silicon surfaces after single or multiple pulses irradiation. A variety of periodic structures (ripples) of a large range of spatial periods, including periods much smaller than the laser wavelength, are formed at the surface. Their characteristics may well differ from the 'classical' ripples previously believed to arise from an interference effect.

Single and double beam experiments reveal different parameters, which seem to influence and control the development of such 'non-classical' ripples. Various features concerning orientation, spatial periods or modulation depth are here presented. Thus, the ripple direction is dictated by the incident electric field. A positive gain in ripple growth rate is established with raising the irradiation dose.

Since ultra-short, highly intense laser pulses create instabilities at the target, a surface self-organization mechanism during the subsequent relaxation can contribute to structures formation mechanism. The interpretation of the ripples is based upon similarities with other structures originated from instabilities.

The experiments presented until here have shown that femtosecond laser ablation creates instabilities at the surface region, lasting possibly long after the laser pulse ends. This results in significant changes in the surface morphology and specific topographical features. Thus, the surface morphology after ablation can be used to trace back the fundamental transient ablation mechanisms. In particular, femtosecond laser pulses delivering high intensities onto the target have been recently shown to induce surface periodic structure with spacing much smaller than the laser wavelength [OMR99, HVD99, CHR02, RCH02].

In this chapter, the mechanism of *surface relaxation after ablation* is addressed, in particular considering processes which could possibly lead to the generation of *surface structures*. ‘Classical’ and ‘non-classical’ aspects of laser-induced surfaces structures, as revealed by experiments, are here used to identify influencing factors and understand the source mechanism of the structures. Yet, an objective of this study is to search for a connection, if any, between the femtosecond laser-induced surface instabilities and the origin of periodic surface structures formation.

5.1. LIPSS – EARLY EXPERIMENTAL RESULTS AND MODELS

Laser-induced periodic surface structures (LIPSS) have been reported since the early days of research in laser-matter interaction [Bir65, Wal74]. LIPSS (ripples) have been found on various metals [Ise77, KoS76], semiconductors [SAL94, GiS97], insulators [KrK99, TBL95], polymers [BoL93, CMB01], and composite materials [WiH85, WES98] after laser irradiation at wavelengths from ultraviolet to far infrared, from CW to picosecond pulse duration. They have been produced not only on bulk materials but also on thin films [TBL95, WES98].

One of the first interpretations called upon an inhomogeneous energy input due to an interference of the incident laser beam with waves resulting from scattering on different *macroscopic* surface defects or pre-existing particulates [Wal74]. Here, the resulting interference fringes have been supposed to give rise to surface ripples if the surface

melting threshold intensity is (periodically) exceeded. Thus, alternating regions of different crystallinity have been suggested to form on the surface [EBT82].

The most accepted interpretations introduce the concept of a surface-scattered wave (SSW) or surface plasma wave [GFS82, BrE82] *traveling* along the surface. Sipe et al. [SYP83] improved upon this picture by adding that, at normal incidence, the travelling SSW should be assisted by short range-fields resulting from scattering by surface microscopic defects contained within the *surface roughness*. This results in a travelling wave confined in an outer (selvedge) layer of thickness much smaller than the incident wavelength, λ (Figure 5.1).

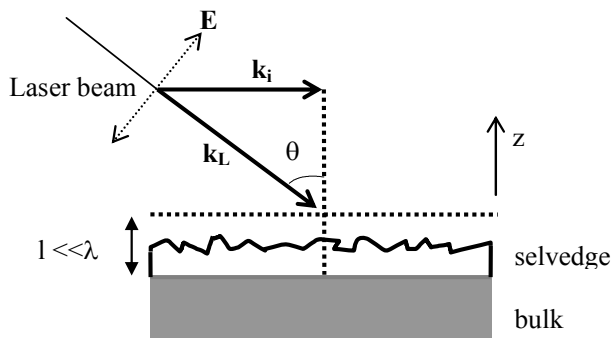


Figure 5.1. The geometry of a p-polarized laser beam incident on a rough surface.

To calculate the intensity of the interference pattern, $I(\mathbf{k})$ in \mathbf{k} space, Sipe et al. considered on one hand the wave vector of the laser beam \mathbf{k}_L with its components parallel to the surface \mathbf{k}_i and, on the other hand, the Fourier components of the random surface roughness at \mathbf{k}_L . The scattering of the incident beam on the surface roughness

results in a field that could propagate inside the bulk with the wave vector $\mathbf{k} = \mathbf{k}_i \pm \mathbf{k}_L$. Further, the corresponding electric field generated in the selvedge region (Figure 5.1) is obtained from the details of polarization \mathbf{P} induced in this region by the incident beam. This electric field is then added to the *refracted* electric field component of the incident beam to obtain the total field distribution just below the surface. The corresponding intensity distribution is, as described in [SYP83], strongly modulated and its spatial Fourier transform contains *strong peaks* which can reason an inhomogeneous absorption into the irradiated material.

The model has foreseen the formation of periodic structures with spatial periods given by:

$$\Lambda_{s^\pm} = \frac{\lambda}{1 \pm \sin \theta}$$

$$\Lambda_c = \frac{\lambda}{\cos \theta}$$
(5.1)

where Λ_{s^\pm} stands for the periods of the structure, θ being the angle of incidence of the beam on the target. Following the theoretical prediction, ripple patterns of spatial period Λ_{s^\pm} would form after irradiation with s- and p-polarized beams, as a result of forward and backward scattering, and be oriented *perpendicular* to the electric field of the incident beam \mathbf{E} . The third ripple pattern of spatial period Λ_c would occur after irradiation with p-polarized beams and be oriented *parallel* to \mathbf{E} . The theory has also predicted ripple periods scaling with λ for some materials, while with λ/n for others. The theoretical prediction for the periods of surface ripples has found excellent agreement with the experimental work at that time [YDP83, YPS83]. Also a prolonged or cumulative exposure to laser radiation has been shown to lead to the amplification of the modulation structure [YSD84], in i.e. a positive *feedback* mechanism. Despite these details, the model does not account for the energy absorption mechanisms or the formation timescales.

In order to explain the periodic fluctuation in energy *absorption* at the surface, the *generated surface wave* to interfere with the incident beam has been linked to various processes to account for the surface response such as: a resonant absorption of photons by plasmons at the surface and condensation of plasmons at the surface to yield high carrier density regions, generation of standing acoustic waves, or fields associated with surface polaritons [DSY82, BWJ82, CIE89]. Also structures indicating a transition from *order to disorder* have been reported, for instance after laser irradiation of silicon [PDS87, PDS89]. They have been attributed to capillary waves in a liquid layer at the surface, which, activated at higher fluences, rapidly re-solidify when the surface cools down.

In the following sections, we first present the experimental observation of a variety of surface structural features. This will show that the absorption mechanism and the formation timescales cannot be neglected anymore for femtosecond laser-induced ripples and the prediction for ripples period given by equation 5.1 is here not relevant.

5.2. FEMTOSECOND LIPSS ON DIELECTRICS

We examined the ablated crater morphology, produced on *freshly cleaved* surfaces⁴³ of single crystals of BaF₂ (111) and CaF₂ (111) by repetitive irradiation with up to several thousands of 120-fs laser pulses. The samples were placed in the UHV chamber, in the setup detailed in Chapter 2. The laser intensity was kept in the range of (1–20) TW/cm², thus below (or near) the damage threshold for the sample materials. As already mentioned in the preceding chapter, in this intensity range the ablation rate is rather moderate. For instance, an AFM investigation of the damage produced by 1000 pulses of 8 TW/cm² on a BaF₂ surface reveals a crater of only ~ 150 nm depth, while an estimate of the corresponding volume ablation rate gives only $\sim 0.5 \mu\text{m}^3/\text{pulse}$.

After laser excitation, the subsequent erosion of the surface leads to a variety of morphological features. Typically, surface structures ordered in periodic lines can occur (Figure 5.2), of very different characteristics as far as the spatial period and orientation are concerned.

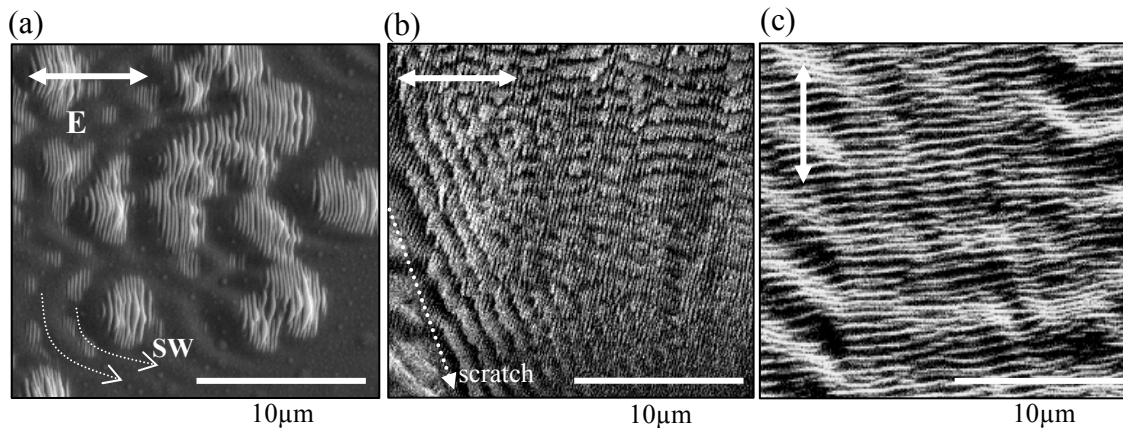


Figure 5.2. Details from laser ablated spots on a cleaved BaF₂ (111) surface revealing the coexistence of multiple patterns (after 6×10^3 pulses at $I_L = 15 \text{ TW/cm}^2$; 45° incidence): (a) waves scattered (SW) at surface defect sites and fine ripples; (b) larger period ripples. A pre-existing scratch on the surface changes the ripple orientation; (c) SW and short period, well-developed ripples. The beam polarization is indicated by double arrows.

⁴³ As compared to polished surfaces, cleaved surfaces influence the surface morphology upon ablation since additional topographical features can form next to steps and kinks.

Accounting for the various spatial orientations found for the periodic structure, the following nomenclature will be used throughout this chapter:

- ‘Scattered waves’ (SW) formed at surface structural defect sites;
- Short range order of fine (short period) ripples; well-developed, thus dominant patterns. According to their recurrence, these are named D(I), D(II), etc.⁴⁴
- Long range order of thick (large period) ripples; less prevailing, thus secondary patterns. According to their recurrence, these are named S(I), S(II), etc.

These different types of surface structures can occur superimposed on each other. Large amplitude SW expand either radially from an apparent point defect (Figure 5.2 (a-c)) or parallel to an extended step defect (Figure 5.2 (b)). Long and short ordering of S(I) and D(I), respectively, can arise simultaneously (Figure 5.2 (b-c)) when the irradiation conditions are adjusted correspondingly. The characteristic features of the various surface structures, the conditions as well as the factors that influence their formation are detailed in the following subsections.

5.2.1. ‘Scattered-surface waves’

As indicated in Figure 5.2, ‘scattered waves’ (SW) structures are produced on the dielectric surface after repetitive irradiation with femtosecond laser pulses. The SW seem to start from localized defect sites and extend radially toward the edge of the spot. Different aspects such as the shape and size of typical SW are indicated in Figure 5.3 from details of a crater inspected with white light interference microscopy (WLM) and scanning electron microscopy (SEM). The analysis indicates that the SW’s period is about few microns and its modulation depth is also of a few micrometers depending on the incident intensity.

In the literature, such SW have been typically observed upon irradiation with CW lasers or long laser pulses. They have been usually attributed to an inhomogeneous energy input on the surface due to interference between the incident beam and waves resulting from scattering in the vicinity of surface defects [Wal74].

⁴⁴ Also, if found, D(I) and D(II) denote structures comparable in period but differently oriented; D(III) and D(IV), if found, are structures of a different period than D(I) and D(II) etc. For the S type of structure, we follow the same nomenclature.

In fact, the SW in Figure 5.3, remind of confocal elliptical waves. They expand radially away from the surface defect sites (Figure 5.3 (d)), which, in this context, seem to serve both as epicenters and as scattering centers.

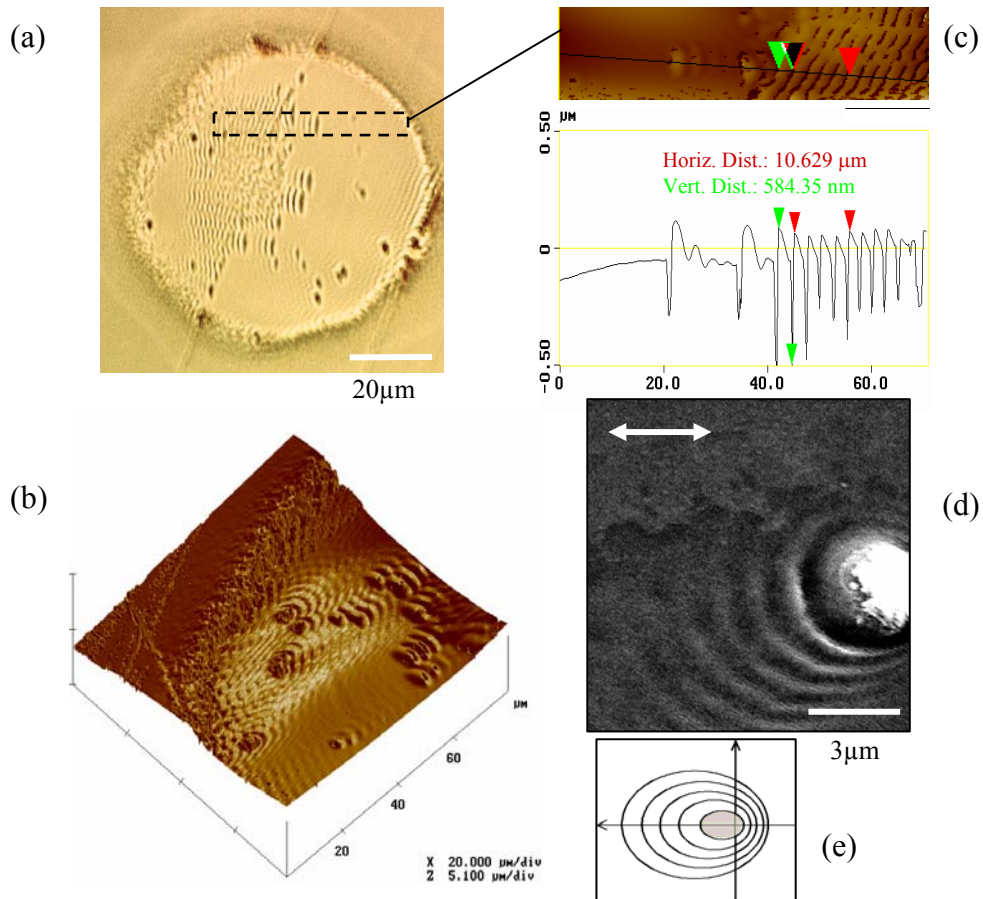


Figure 5.3. Crater morphology of a cleaved surface of $\text{CaF}_2(111)$. An ablated crater (a), produced after irradiation with 6×10^3 pulses; 8 TW/cm^2 ; 45° incidence, reveals ‘scattered wave’ (SW) structures. (b) A 3D image of a detail of the spot in (a). (c) A depth profile on a line as indicated. (d) SW at a defect sites; (e) Representation of SW as elliptical fringes propagating from a scattering center (SC).

These pictures are SEM micrographs (a, d) and white light interference microscopy images (c, b).

Alternatively, one can consider that the strong recoil resulting from the explosion of an outer unstable layer, reaching a pressure at the order of GPa [ChG97], can also provoke large amplitude surface waves, which ‘cool down’ rapidly from a *softened* lattice.

5.2.2. Periodic surface structures

As stated above, a closer surface inspection at increased SEM magnification reveals

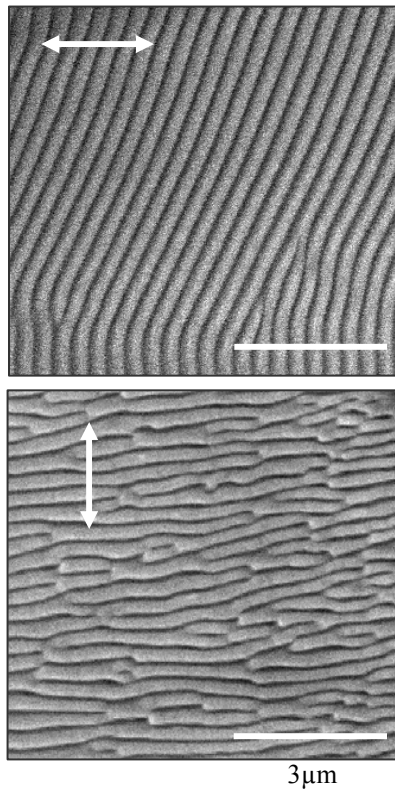


Figure 5.4. Linear, regular (a) and interlaced (b) lines obtained on a BaF₂ target by:
 - 10^3 pulses at $I_L = 11 \text{ TW/cm}^2$;
 - 45° incidence.
 The ripple structure has an average period of $\Lambda_D \cong 350 \text{ nm}$. The beam polarization is indicated by double arrows.

(a) different periodic surface structures (ripples) on the ablated surface. Similar to the structures generated by long laser pulses, here the dominant ripple structure is represented by fine, long and nearly parallel lines (Figure 5.4), aligned *almost perpendicular* to the beam polarization direction. However, in contrast to the ‘classical’ ripples, the period of these structure (the distance between adjacent crests or valleys) appears to be at least by a factor of two smaller than the laser wavelength λ . For instance, the ripple period of the dominant structures (D) in Figure 5.4 has $\Lambda_{D(I)} \sim 350 \text{ nm}$. This subchapter will show that periodic structures develop on the surface after single pulse or repetitive laser pulse irradiation. They can align in parallel structures of either highly regular (Figure 5.4. (a)) or segmented, interlaced lines (Figure 5.4. (b)). At a later stage of growing, a weaker ripple pattern (S(I)) develops oriented parallel to the laser polarization (as shown for instance in Figure 5.2, b).

5.2.2.1. Ripples generated by multiple pulses irradiation

Ripples are typically generated on various dielectric surfaces by multiple pulses irradiation. This analysis on ripple patterns is directed to discuss different issues as follows: (I) the conditions for generation of various structures; structures contrast; (II) structures orientation; (III) structures period.

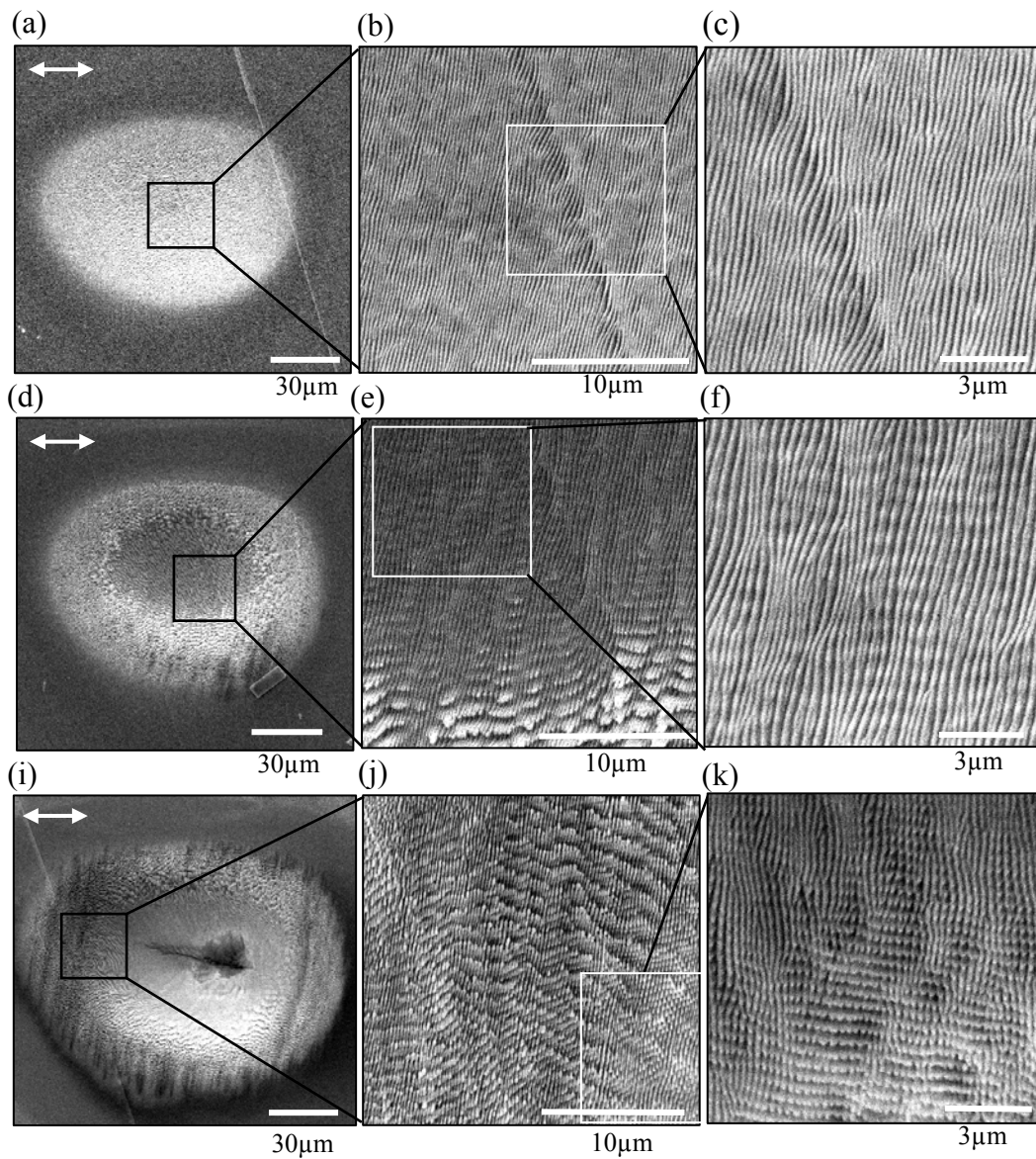
(I) *Multiple ripple patterns. Structures contrast.*

Figure 5.5. SEM micrographs of ablated spots obtained after multiple laser pulse ablation ($\text{BaF}_2(111)$ surface, 800 nm; 0° incidence). Development of patterns at constant $I_L = 14 \text{ TW/cm}^2$ when increasing the number of pulses: (a-c) 5×10^3 pulses; (d-f) 10^4 pulses; (i-k) 6×10^4 pulses. Magnified sections of the ablated spots reveal: (b) a dominant, fine pattern of type D(I); (c) the change in ripples orientation next to a surface scratch; (e, f) interlaced S(I) and D(I) structures; (j) well-developed larger period S(I) type of structure and a **magnified region with double crossed fine D(I)s** (k). The double arrows indicate the orientation of the incident beam polarization.

With increasing the intensity (level) and/or the number of pulses, one to several ripple structures can form on the surface, superimposing on each other.

Figure 5.5 summarizes typical surface structures formed on a BaF₂ (111) surface. Our investigation indicates important differences in the multi-shot intensity thresholds for the generation of the various types of structures. The conditions for the structures formation can be evaluated in terms of an *irradiation dose*, a parameter defined as a function of a product between the laser intensity and the number of pulses as follows: $I_D \propto f(I \cdot N)$ [CHR03].

Typically, upon irradiation at moderate laser intensities (of about 14 TW/cm²) with thousands of laser pulses one singular D(I) structure occurs, perpendicular to the beam polarization, and distributes uniformly across the ablated spot (Figure 5.5 (a), with details in (b-c)); after increasing the number of pulses, a second larger pattern (type S(I)) may emerge, superimposed on the first one and oriented perpendicular to it (Figure 5.5 (d), with details in (e-f)), thus parallel to the beam polarization; with even higher number of laser pulses, the number of structures increases even more (Figure 5.5 (i), with details in (j-k)). Thus, in Figure 5.5 (k), another fine structure, similar to a D(I) type, thus called here D(II), becomes observable. As the D(II) structure is oriented parallel to the beam polarization, the combination of D(I) and D(II) gives an interlaced-like surface morphology.

In the AFM analysis of an ablated spot from Figure 5.6, we present the shape and size of a typical D(I) pattern. A spot, irradiated with 10³ pulses at 10 TW/cm² has about 150 nm depth. A 2D Fourier transform of the AFM image reveals the spatial frequency of the ripples. The surface structure of period $\Lambda_{D(I)} \sim 200$ nm has in average a modulation depth of about 30 nm.

In addition, at constant intensity, we observe that the *modulation depth* increases slightly with the number of pulses.

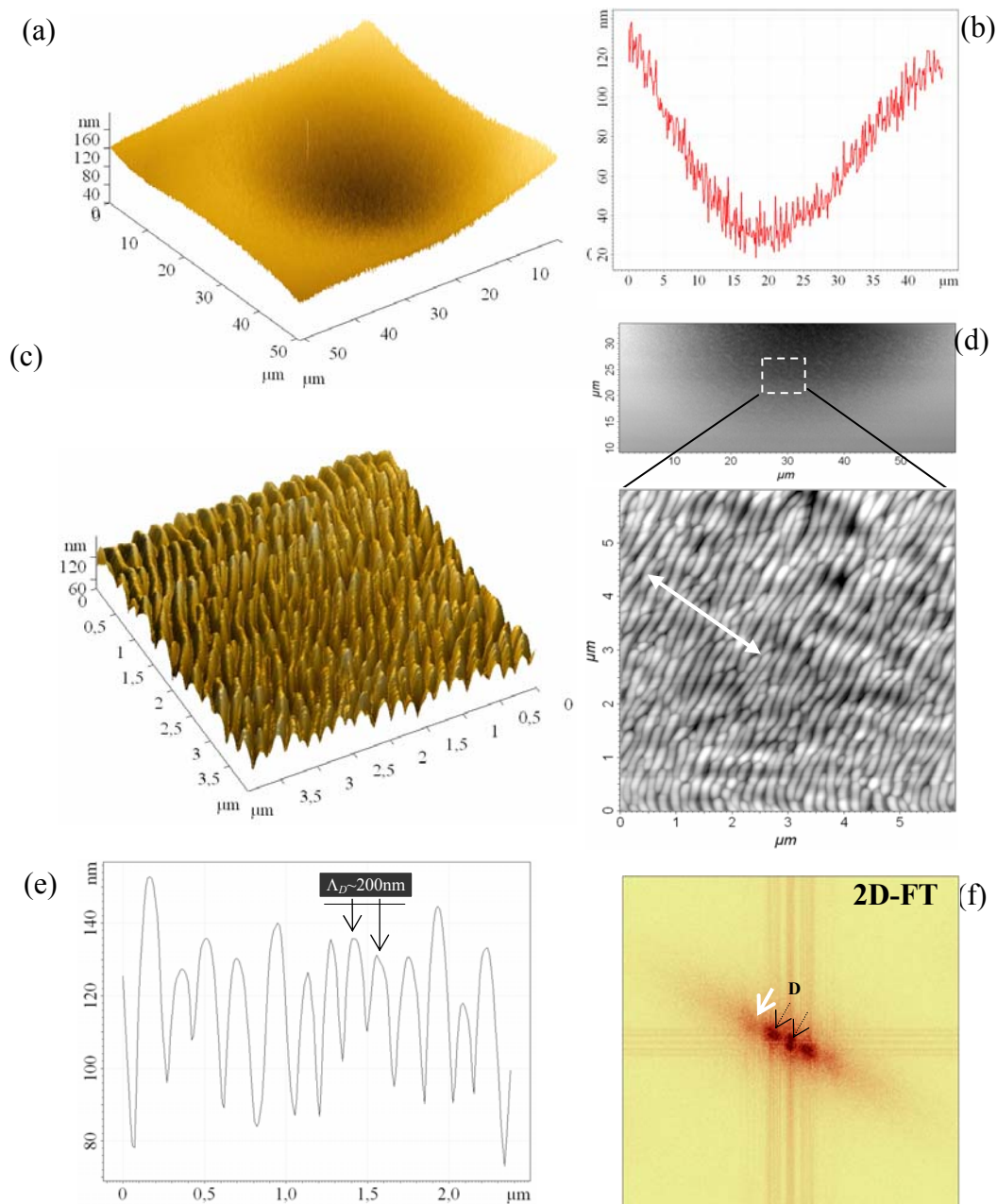


Figure 5.6. AFM images of an ablated spot on BaF₂ (120-fs; 800 nm; 1000 pulses; 10 TW/cm²; 0° incidence); (a) 3D image of the ablated spot; (b) depth profile of (a); (c) 3D image of a detail of (a) revealing ripples; (d) 2D image of a detail of (a); (e) depth profile on a line (the position is marked with a double arrow on (d)). (f) 2D Fourier transform of (c) with one dominant frequency $\Lambda_{D(1)} \sim 200$ nm. The additional (weaker) larger frequency, marked with a white arrow, has a period of about 100 nm.

(II) Ripples orientation

A rotation of the polarization direction results in a corresponding rotation of the ripple patterns.

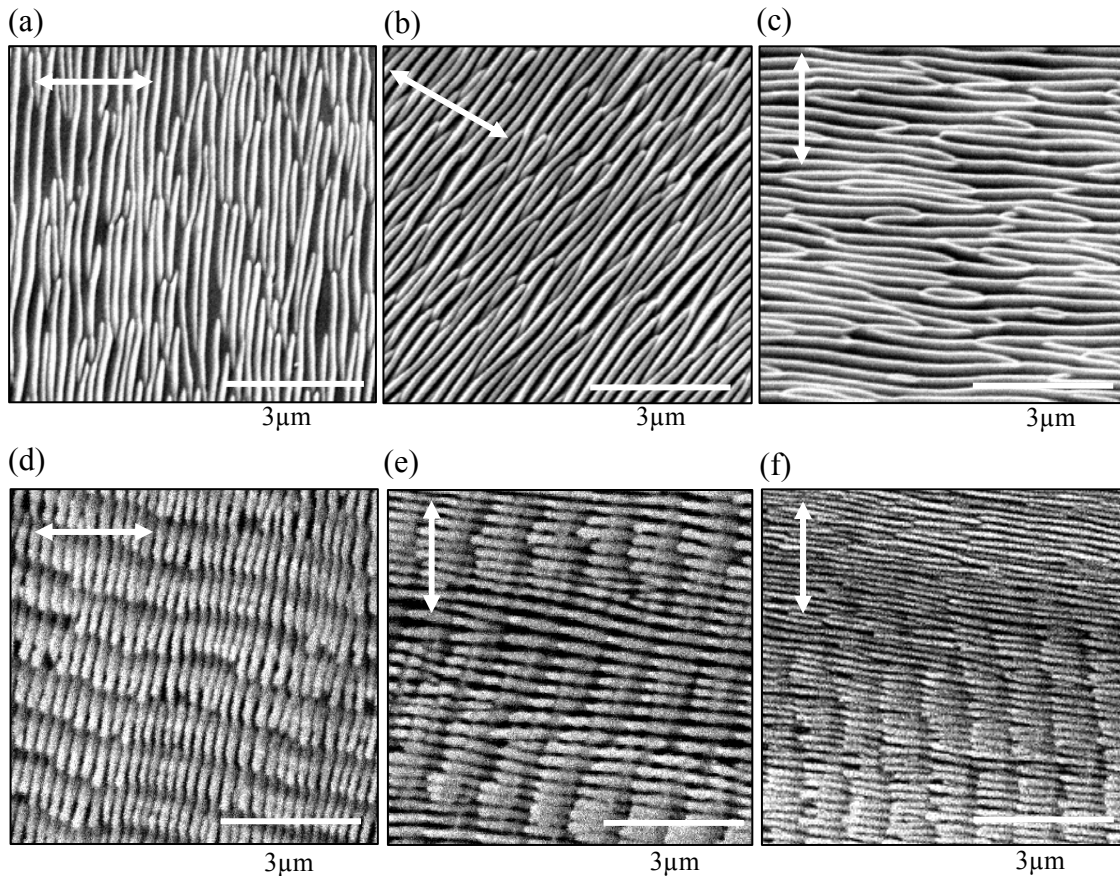


Figure 5.7. Influence of laser beam polarization on the ripples orientation (CaF_2 ; 800 nm; 0° incidence). (a-c) SEM micrographs of details from spots obtained after irradiation with 5×10^3 pulses at 12 TW/cm^2 ; (d-e) 5×10^3 pulses at 14 TW/cm^2 . Both types of ripples D(I) and S(I) rotate with polarization (the double arrows indicate the orientation of the incident beam polarization). Note the apparent bifurcations in the structure from picture (c).

As indicated in Figure 5.7 (a-f), the fine D(I) type aligns always perpendicular to the electric field of the incident beam \mathbf{E} , while the S(I) type of larger period aligns always parallel to \mathbf{E} (i.e. the thicker pattern from the interlaced structures in Figure 5.7 (d-f)). The fine, parallel lines of the dominant structure can locally intersect and also apparent *bifurcations* can be observed (Figure 5.7 (c)).

In addition, both D(I) and S(I) structures are typically *reinforced and reoriented*⁴⁵ near a pre-existing macroscopic surface defect.

(III) Ripples period

To test the dependence of the period of femtosecond laser-induced ripples on the laser wavelength and angle of incidence, we irradiated the dielectric samples as follows: at different laser wavelengths (800 nm and the double frequency of 400 nm) and different angles of incidence of the laser beam on the target (0° , 45° to the surface normal).

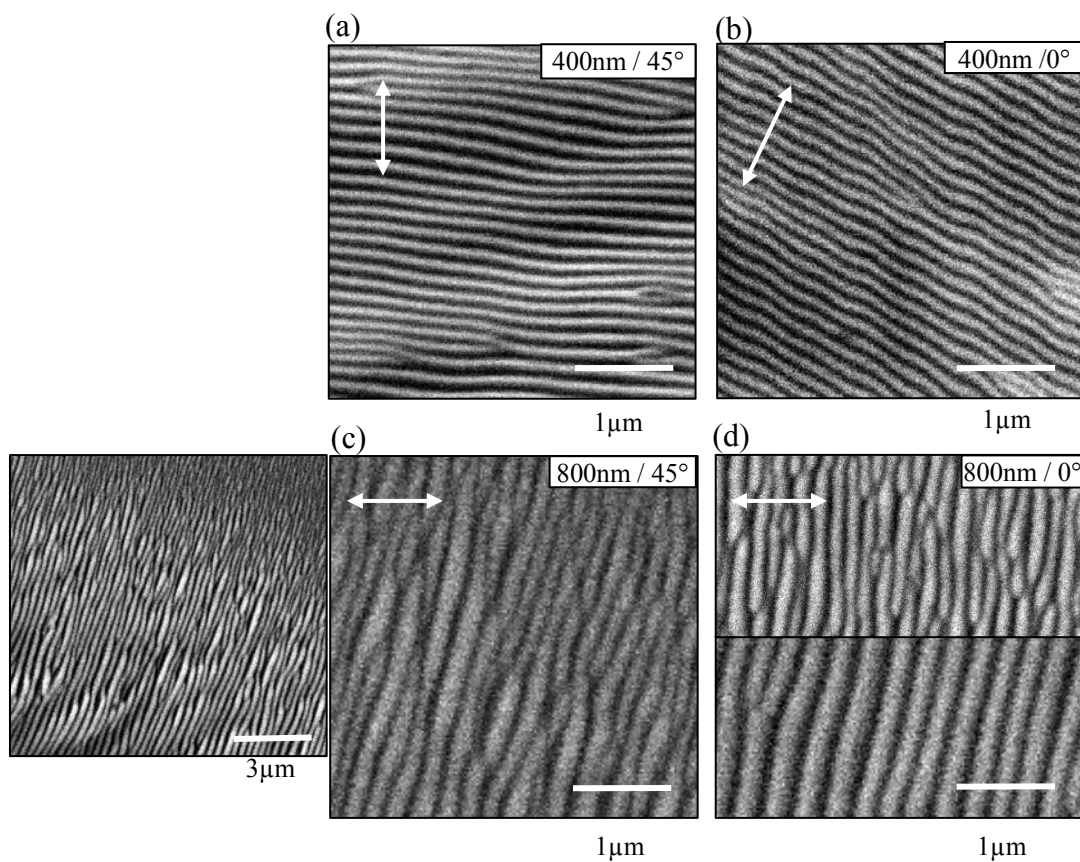


Figure 5.8. SEM micrographs of details from ablated areas (BaF_2) indicating a D(I) type formed upon irradiation with 400 nm, 4×10^4 pulses of 4 TW/cm^2 (a, b) and 800 nm, at 3×10^4 pulses at 10 TW/cm^2 (c, d) for different angles of incidence (0° and 45°). The periods of D(I) are in average: (a) $\sim 160 \text{ nm}$; (b) $\sim 155 \text{ nm}$; (c) between 200-290 nm (the overview picture from left side shows an apparent decrease of ripple period toward the spot edge); (d) $\sim 285 \text{ nm}$ (lower panel) and $\sim 210 \text{ nm}$ (upper panel) in details from different region of the same spot. The double arrows indicate the beam polarization direction.

⁴⁵ Refer to Figures 5.2 (b); 5.3 (d); 5.5 (a-c); 5.9 (a-c).

Figure 5.8 shows typical structures produced on a BaF_2 surface by multiple laser pulses of different laser wavelength and at different angles of incidence on the sample. The D(I) structure period seems to be nearly insensitive to the angle of incidence variation and increases only slightly with the incident wavelength. Also it is much smaller than the laser wavelength. At 400 nm wavelength and constant irradiation dose, the ripples period is in average ~ 150 nm for both angles of incidence (Figure 5.8 (a, b)). On the other hand, at 800 nm and constant irradiation dose, the period varies between 200-290 nm for both angles of incidence (Figure 5.8 (c, d)). In fact, the period of the D(I) structure can vary between different regions in the same spot (Figure 5.8 (c, d)). This last aspect is also supported by the pictures in Figure 5.9.

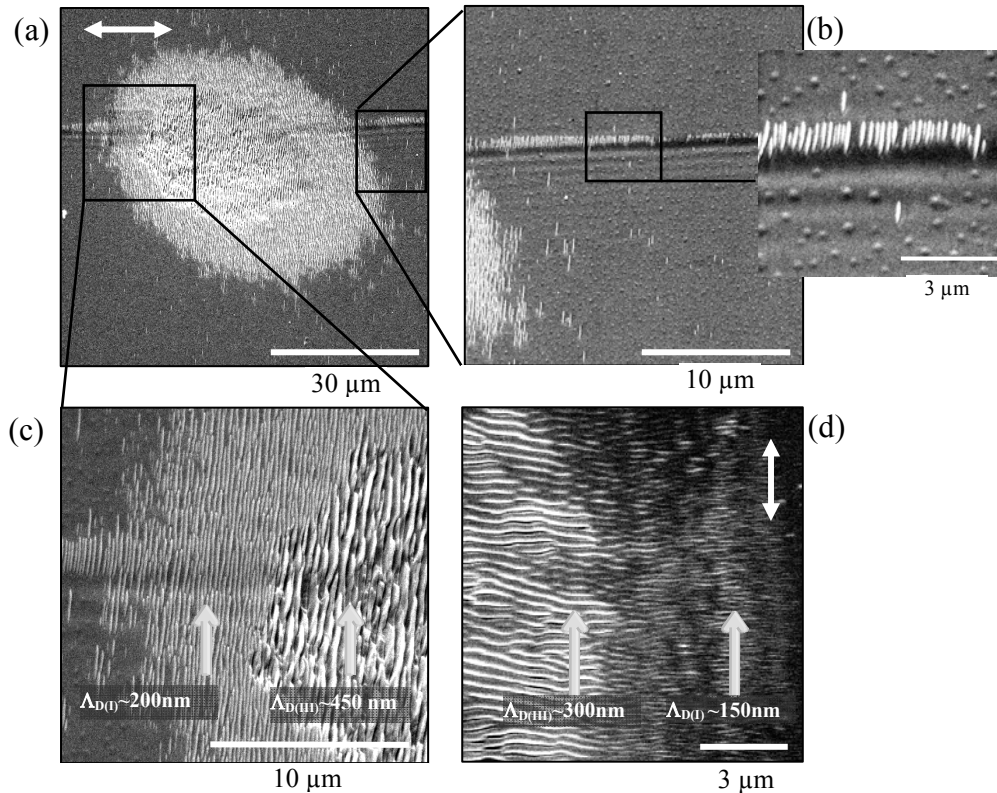


Figure 5.9. SEM micrographs of various sub-wavelength ripples on CaF_2 (111): (a) ablated spot (800 nm; 9200 pulses; 8 TW/cm^2 ; 45° incidence) revealing two dominant structures (D) of different periods as indicated in the magnified regions of selected areas in (a). In average the ripple periods are: (b, c) $\Lambda_{D(I)} \sim 200$ nm at the spot edge; (c) $\Lambda_{D(III)} \sim 450$ nm in the spot center. In (b), a D(I) type is aligned on a step defect. (d) Rippled area with a decreasing ripple period from the center where $\Lambda_{D(I)} \sim 150$ nm (right side of the picture) toward the edge of the spot where $\Lambda_{D(III)} \sim 300$ nm (left side of the picture). The arrows indicate the orientation of the incident beam polarization.

In Figure 5.9, ripples of a short range order type (D(I)) align perpendicular to the laser polarization and extend radially toward the spot edge. We observed a dependence of the ripple period on the local intensity. As shown in Figure 5.9 (b, c, d), ripples of different spatial period can develop in the same spot, namely of a larger period at the spot center and of a smaller period at the spot edge. In the central region of the spot, where the intensity of the Gaussian profile is higher, a larger period pattern forms called here D(III). The period $\Lambda_{D(III)}$ is about 300-400 nm, almost twice the ripples period on the edges ($\Lambda_{D(I)} \sim 150-200$ nm).

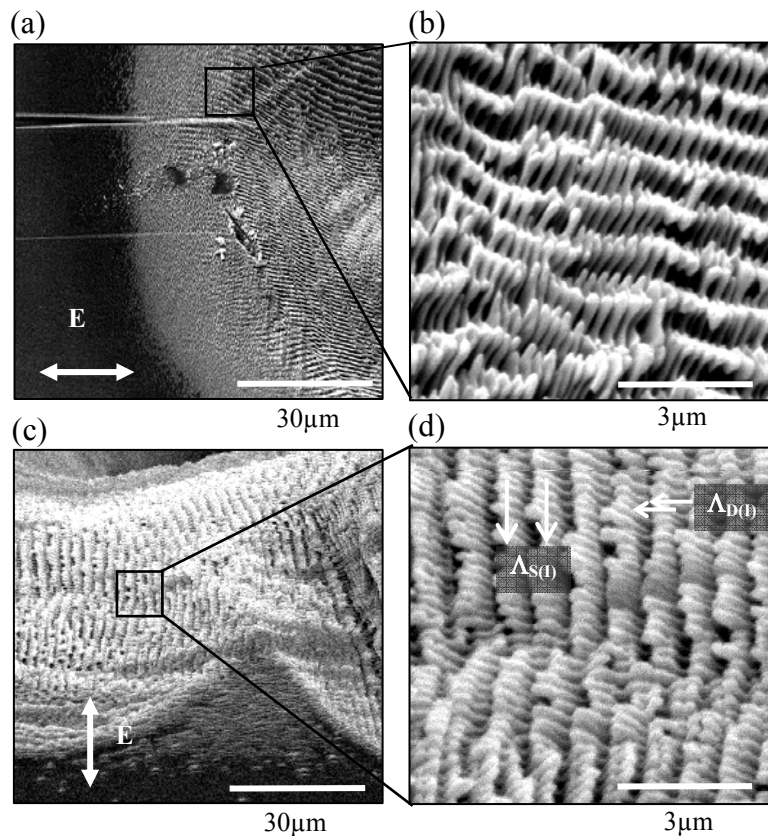


Figure 5.10. SEM micrographs taken on a detail from the edge of a deep crater (a); well-developed, interlaced D(I) and S(I) types (b) in CaF_2 (3×10^4 pulses; 18 TW/cm^2 , p-pol beam; 800 nm; 45° incidence). The ripples period are in average: $\Lambda_{D(I)} \sim 200$ nm, $\Lambda_{S(I)} \sim 900$ nm. Detail from the edge of a deep crater (c) with superimposed D(I) and S(I) types (d) in BaF_2 in the same irradiation conditions as (a, b) but s-pol beam. The ripples period are in average: $\Lambda_{D(I)} \sim 200$ nm, $\Lambda_{S(I)} \sim 900$ nm. The double arrows indicate the orientation of the incident beam polarization.

The dominant D(I) type forms clearly near to step defects (resulting from cleavage). As an increased absorption at the defect site is known to reduce the damage (or ripple

generation) threshold intensity, it is expected that even the low intensity in the wings of the laser beam be sufficient for ripples generation (Figure 5.9 (b)).

The D(I) and S(I) types of structure also occur at the edges of deep craters and their general aspect *does not depend neither on the type of dielectric material nor the orientation on the crystalline lattice*. On both BaF₂ and CaF₂ target surfaces, we found similar structures of *high contrast* (depth modulation) as shown in Figure 5.10. The finer lines of the D(I) structure seem to be interrupted by a superimposed S(I) structure. Also small *columns* appear to grow on top of the individual segments.

5.2.2.2. Effects of single pulse ablation interaction

So far, we discussed the surface morphology after ablation with thousands of laser pulses. We also investigated the surface morphology after ablation with a single to a few laser pulses. For this, we used the Ti: sapphire laser system of higher energy output⁴⁶ (800 nm; 50-120 fs pulse duration; 100 mJ/pulse; 20 Hz repetition rate). Figure 5.11 presents a schematic of the experimental set-up.

The sample was mounted in vacuum (with a base pressure $\sim 10^{-6}$ mbar). A shutter was used to select a known number of pulses from the 20 Hz pulse train. For a better control of the laser-induced damage, the irradiated surface was imaged with a CCD camera (after being magnified, in the beam transmission, with a +350 mm lens, as illustrated in to Figure 5.11). For instance in Figure 5.11, the (CCD) image in the left side presents a damaged spot produced after ablation with a single laser pulse (a dark disk positioned in the center of an illuminated surface area). We used a fluence range between 4-50 J/cm², therefore higher than the single pulse ablation threshold for fluoride materials. The surface morphology after ablation with one to several laser pulses was investigated ex-situ with SEM and AFM, searching for, in particular, laser-generated surface structures.

⁴⁶ LUCA laser system from CÉA, Saclay, France.

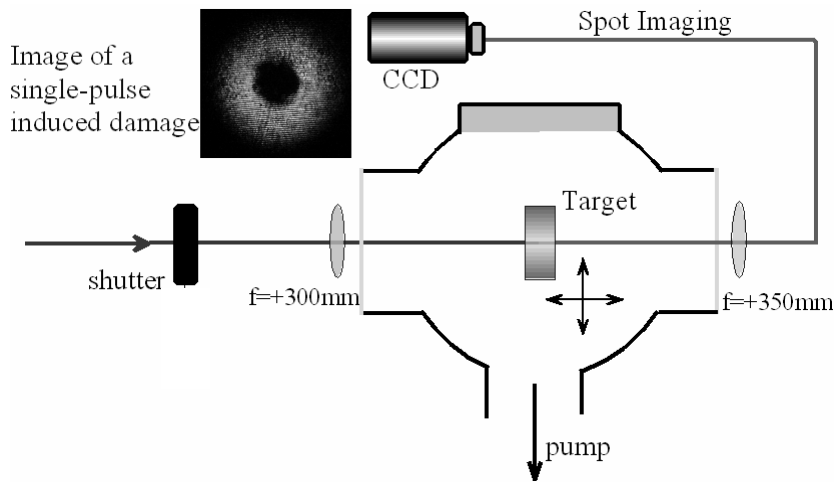


Figure 5.11. Experimental set-up for single pulse ablation. The interaction region is monitored by a CCD camera. The photo from left side represents the illuminated target surface, with a damaged crater produce by a single laser pulse in the center.

The topographical investigation revealed ripple patterns even after single pulse ablation. Figure 5.12 ((a), with a detail in (b)) presents a weak, fine pattern reminiscent of a D(I) structure, developed next to a step defect in the annular region of the ablated spot. An AFM inspection of a spot ablated with 3 pulses reveals, in the central region, nanoparticles uniformly distributed over the entire spot, of 10-300 nm in diameter (Figure 5.12 (c)). With increasing the number of pulses, at the same intensity, the nanoparticles seem to align in lines perpendicular to the \mathbf{E} -field of the incident beam (Figure 5.12 (d)). Thus, the first laser pulses seem to erode an initially flat surface and generate nanoparticles, which, at further irradiation, can increase in size and also align in lines. By exposing the surface to an increased number of laser pulses, the amplification in the local damage can also lead to an amplification of an initial surface modulation.

This result suggests that the development of a surface corrugation of high contrast would be favored by an increased number of pulses (a positive feedback⁴⁷).

⁴⁷ Note that the positive feedback has been earlier observed in the development of ‘classical’ ripples induced by CW and long pulse ablation [SYP83]. The similar result, to some extent, obtained here for non-classical ripples may only point out a general feature for periodic structure formation in nonlinear systems.

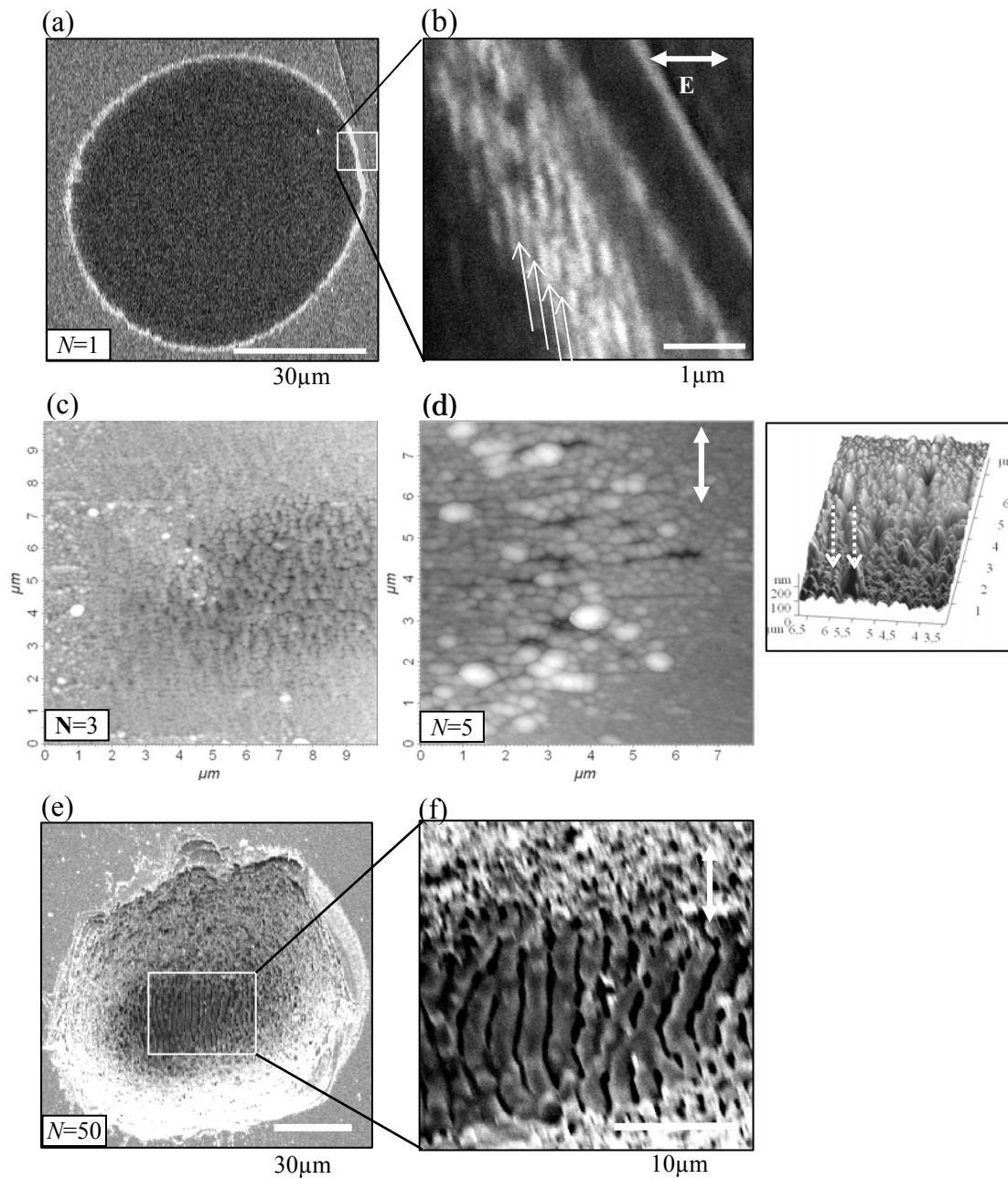


Figure 5.12. (a-d) Ablated spots on a BaF_2 (111) target with (120-fs) laser pulses (800 nm; 50 TW/cm^2 ; 0° incidence) for a number of laser pulses as indicated in the panels. Different features can be observed such as:

(a, b) SEM micrographs of a ripple pattern in the annular region of a single laser pulse ablated spot (b).

(c, d) AFM images of details from spots irradiated by (c) 3 pulses; (d) 5 pulses indicating nanoparticles (10-300 nm size). The insert displays a 3D image of a detail from (c) where apparent lines of nanoparticles are indicated by dotted lines.

(f) Details of an S(III) type of $\Lambda_{\text{S(III)}} \sim 2 \mu\text{m}$ period (50 pulses; $160 \text{ TW}/\text{cm}^2$; 800nm 0° incidence) found at the bottom of a deep basin (e).

The beam polarization is indicated by double arrows.

With increasing the intensity, at the bottom of deep craters, another particular structure was found by SEM analysis: a ripple structure, parallel to the beam polarization, of a large $\sim 2\mu\text{m}$ period (Figure 5.12 e, f), called here S(III).

The different ripples D/S types as observed on femtosecond laser irradiated dielectric surfaces, are summarized in Table 5.1, together with their spatial periods and their orientation on the incident electric field.

Table 5.1. The spatial periods, Λ and orientation on beam polarization (\mathbf{E}) of the different structures found on ablated dielectric surfaces. D(I), D(II), and D(III), denote fine, well-developed dominant patterns, and S(I), S(II), and S(III) are thick, less sharp secondary patterns.

	λ (nm)	θ	$\Lambda_{D(I)}$, nm ($\perp \mathbf{E}$)	$\Lambda_{D(II)}$, nm ($\parallel \mathbf{E}$)	$\Lambda_{D(III)}$, nm ($\perp \mathbf{E}$)	$\Lambda_{S(I)}$, nm ($\parallel \mathbf{E}$)	$\Lambda_{S(III)}$, nm ($\parallel \mathbf{E}$)
BaF₂	800	0°	$\sim 200 \div 300$	$\sim 200 \div 300$	-	700 \div 900	2000 \div 2900
		45°	$\sim 250 \div 350$	$\sim 250 \div 350$	~ 450	700 \div 900	-
	400	0°	$\sim 100 \div 200$	-	-	-	-
CaF₂	800	0°	$\sim 250 \div 350$	$\sim 250 \div 350$	-	700 \div 900	2000 \div 2800
		45°	$\sim 250 \div 350$	$\sim 250 \div 350$	$\sim 300-450$	700 \div 900	-
	400	0°	$\sim 100 \div 200$	-	-	-	-

Our investigation has shown so far that the femtosecond laser induced surface patterns do not comply with the ‘classical’ ripple features described in section 5.1. These ripples particularly reveal spatial periods much smaller (or much larger) than the laser wavelength for normal incidence irradiation and are apparently insensitive to both the incident wavelength and angle of incidence variation. A further intriguing feature is the occurrence of multiple bifurcations. In these regions the structures remind of similar structures observed in the sandy ground under shallow, wavy water [HEH01], or ion beam sputtered surfaces both attributed to *processes of self-organization from a state of extreme non-equilibrium*.

5.2.2.3. Control factors for ripples generation

The main factors that influence the ripples patterns features, as resumed in the preceding section, are likely the laser beam polarization and the irradiation dose. Here, we attempt to evaluate the limits of these factors on (sub-wavelength) ripple formation and control.

(I) Laser beam polarization

In femtosecond laser-matter interaction, the laser pulse finishes long before its energy is transferred to the lattice. Our topographical analysis indicates that, however, the preferential direction of the periodic ripples is independent on both the crystallographic structure of the sample and the orientation of its lattice. Instead, the ripple's orientation appears to be strongly influenced by the beam polarization.

However, as previously indicated, the periodic structures are *typically reoriented* near a pre-existing macroscopic surface defect.

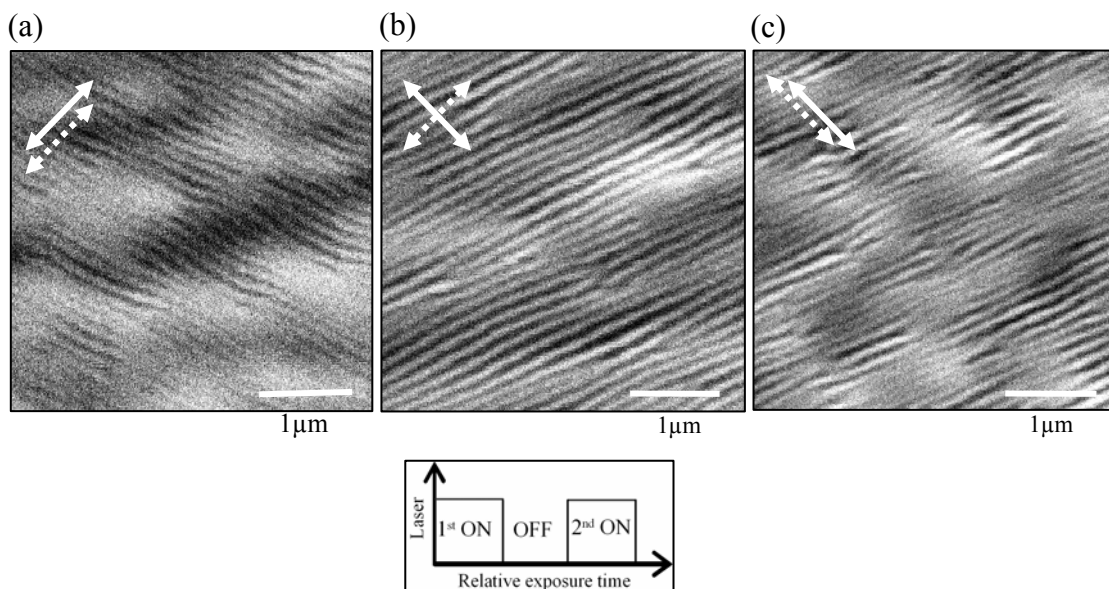


Figure 5.13. Structure's orientation after surface irradiation in a sequence as indicated in the sketch: **laser on - 1st irradiation / laser off - no irradiation / laser on - 2nd irradiation** (N pulses / laser off / N pulses; $N = 4 \times 10^4$ pulses at 3.5 TW/cm^2 ; 400 nm ; 45° incidence). For the 1st / 2nd irradiations the beam polarization on the target was set, respectively: (a) p-pol. / p-pol.; (b) p-pol. / s-pol.; (c) s-pol. / s-pol. In all pictures the ripples period is in average $\Lambda_{D(f)} \sim 140 \text{ nm}$. The orientation of the incident beam polarization is indicated by dotted arrows for the 1st irradiation and solid arrows for the 2nd irradiation.

It is possible that the beam polarization influences the ripple orientation if the pre-existing surface irregularities are smaller or comparable in size to the ripple period. Such an effect is presented Figure 5.13. Here, we double exposed the surface to a known number of pulses in a sequence as follows: a first surface exposure to $N = 4 \times 10^4$ pulses, a pause without irradiation and a second exposure to the same N . (In this example, we used the double frequency of 400 nm). The first irradiation gives rise to a D(I) structure oriented perpendicular to the beam polarization. By stopping the irradiation, we provide a time for the surface to cool down. If for the *second* irradiation the beam polarization remains unchanged the ripple orientation is not affected (Figure 5.13 (a, c)). However, if for the second irradiation the beam polarization is changed, the D(I) structure reorients correspondingly (Figure 5.13 (b)). Thus, the irradiation with linearly polarized beams of a surface both free of defects or with preexisting (nano)structures will essentially produce structures comparable in size and oriented on the beam polarization, as described in Section 5.2.2.1. The new generated structure apparently does not depend on the initial morphology of the surface. We note here that the earlier observations on ripples orientation on beam polarization have essentially indicated similar features. The beam polarization is a linking factor between the ‘classical’ and the sub-wavelength ripples.

(II) Irradiation dose

The initial conditions for the formation of the various types of structures can be discussed in terms of an irradiation *dose*, I_D , a parameter defined in the previous section.

Figure 5.14 displays several typical morphological features of a CaF_2 surface ablated with very different irradiation doses. At a low intensity of 3 TW/cm^2 , just at the threshold for a noticeably material removal and crater formation, and a large number of laser pulses (2×10^6), we observe a first indication of a D(I) structure. This is an ordered array of initial prominences oriented perpendicular to the laser beam polarization (Figure 5.14 (a)). At three times higher intensity (9 TW/cm^2) already for thousands laser shots (5×10^3), a pattern of very fine periodic ripples is observed, resembling a coalescence of multiple bumps into long lines (Figure 5.14 (b)). A superimposed, wider structure oriented parallel to the beam polarization forms on the spot center (Figure 5.14 (c)). The modulation amplitude increases with increasing fluence. This suggests that a positive feedback reinforces the ripple structure formation.

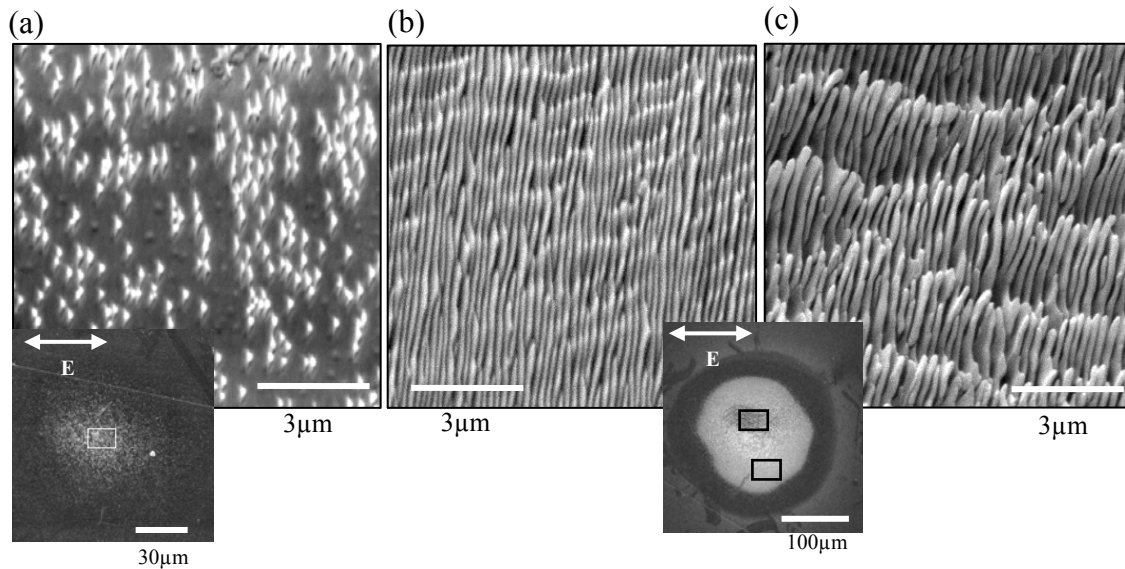


Figure 5.14. Ablated spots with details of different surface features (CaF_2 (111)). (a) Initial surface prominences (2×10^6 pulses; 3 TW/cm^2 ; 800 nm ; 45° incidence); (b) well-developed D(I) and weaker S(I) structures (5×10^3 pulses; 9 TW/cm^2 ; 800 nm ; 45° incidence) in a detail from the spot edge. (c) well-developed D(I) and S(I) structures in a detail from the spot center in a region shown in the spot overview. The double arrows indicate the orientation of the incident beam polarization.

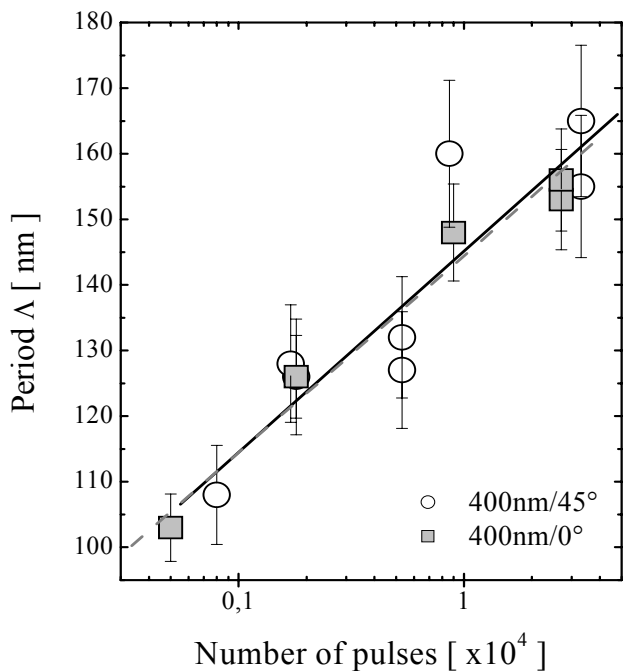


Figure 5.15. Semi-log plot of the ripple period dependence on the number of pulses at different angles of incidence as indicated. A p-polarized beam (respectively, horizontal polarized) was used and the laser intensity was kept constant at $I_L = 3 \text{ TW/cm}^2$. The solid and dashed lines are linear fits on the experimental data.

Although the D(I) structure covers a relatively narrow period range, there is an apparent *growth of the period with the number of pulses* accumulated on the surface as presented in Figure 5.15. This figure also indicates the *insensitivity* of the ripple period *to the variation of angle of incidence*.

As extensively shown so far, periodic ripples form on surfaces irradiated with trains of femtosecond laser pulses, in a small window of laser intensities. Figure 5.16 (a) presents the qualitative estimate of the intensity range for a given number of pulses, corresponding to surface structures formation, on a BaF₂ target. The lower limit of the shaded region in Figure 5.16 (a) can be regarded as a multi-shot threshold intensity for the generation of a ripple structure. Thus, the threshold intensity the ripple formation decreases with increasing the number of pulses, in a similar way as our estimates on multi-shot damage threshold intensity presented in Figure 5.16 (c).

From this empirical observation, the threshold intensity for ripple formation $I_{th,N}$, for N laser pulses, can be represented by an exponential decrease as:

$$I_{th,N} = I_{th,1} \cdot \exp(-k \cdot N) + I_{th,N \rightarrow \infty} \quad (5.2)$$

where k is a fit parameter. $I_{th,1}$ gives an estimate of the threshold intensity for ripple formation at single pulse irradiation, $I_{th,N \rightarrow \infty}$, i.e. the function offset, is a supposed threshold intensity for irradiation with an infinite number of pulses. This function is used in Figure 5.16 (a, b) to fit the data for fine ripples (D(I)).

Phenomenologically, this effect follows the same tendency as the damage threshold intensity reduction upon multi-shot ablation or incubation via defect accumulation on the surface as described in Chapter 3. In Figure 5.16, we compare the results for $I_{th,N}$ and the intensity dependence of the number of pulses necessary to overcome the incubation effect. The intensity ranges differ by almost a factor of 3, but the general trend is similar and can be represented by Eq. 5.2. Although the approach is somewhat speculative, since the two sets of data are results of measurements by using different techniques, apparently the ripple formation can be *correlated with the defect accumulation on the surface*.

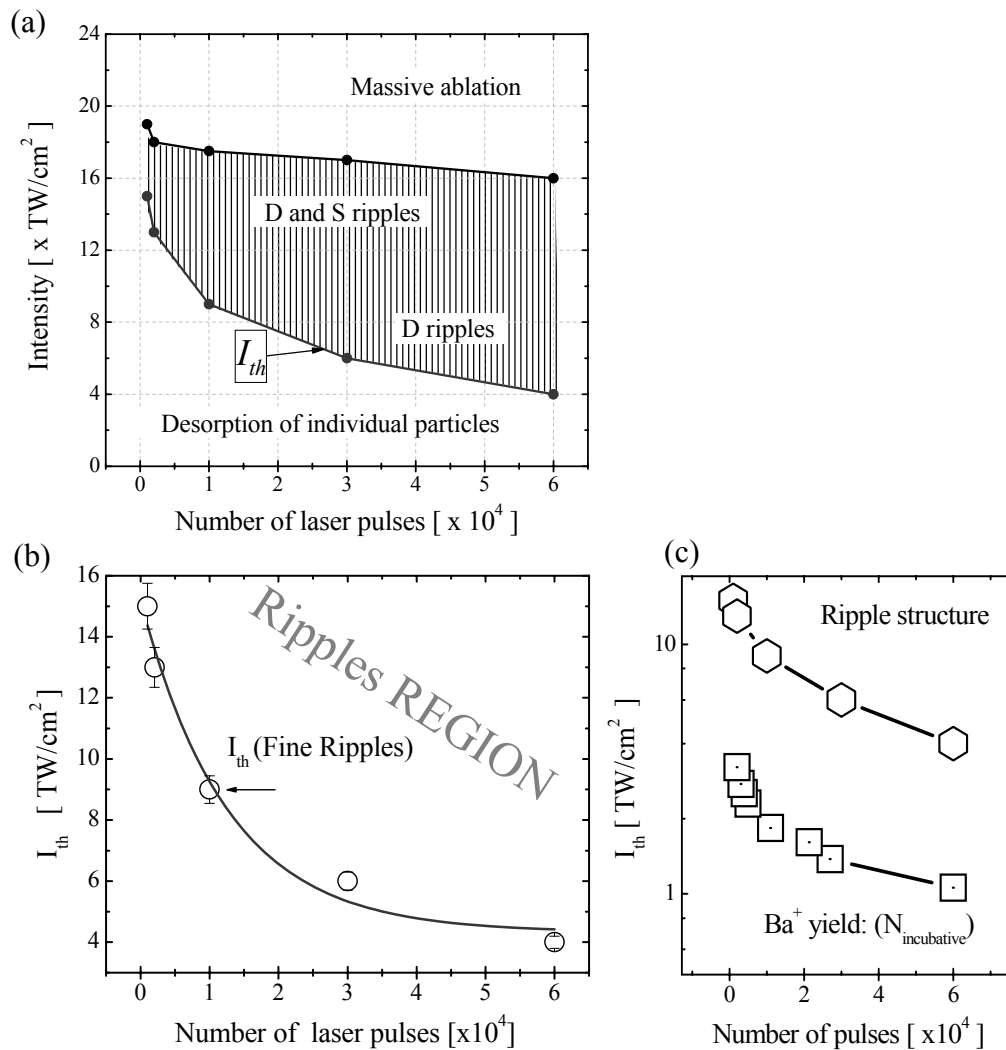


Figure 5.16. (a) Intensity vs. number of laser pulses corresponding to the generation of ripples as qualitatively indicated by the SEM investigation of surface morphology after ablation (BaF₂ target). Ripples are only observed in the shaded region. (b) The data for the lower limit of the intensity window in (a) are fitted with Eq. 5.2. (c) A comparison between these data and the results of incubation in Ba⁺ yield from Figure 3.7.

To briefly conclude this subchapter, several factors seem to influence the ripples characteristics: the surface structural defects and the beam polarization, which appear to dictate the structure orientation, and the irradiation dose, which apparently influences the ripples period and the generation of the different patterns. A possible correlation seems to exist between the irradiation dose for the incubation effect and the (sub-wavelength) ripple formation.

5.2.3. Two-beam experiment

Up to now we have shown that the dielectric surface morphology after femtosecond laser pulse irradiation exhibits *sub-wavelength* ripple patterns. These ripples are aligned with respect to the beam polarization direction, an indication that the surface retains the memory of the incident electric field after the laser pulse ends.

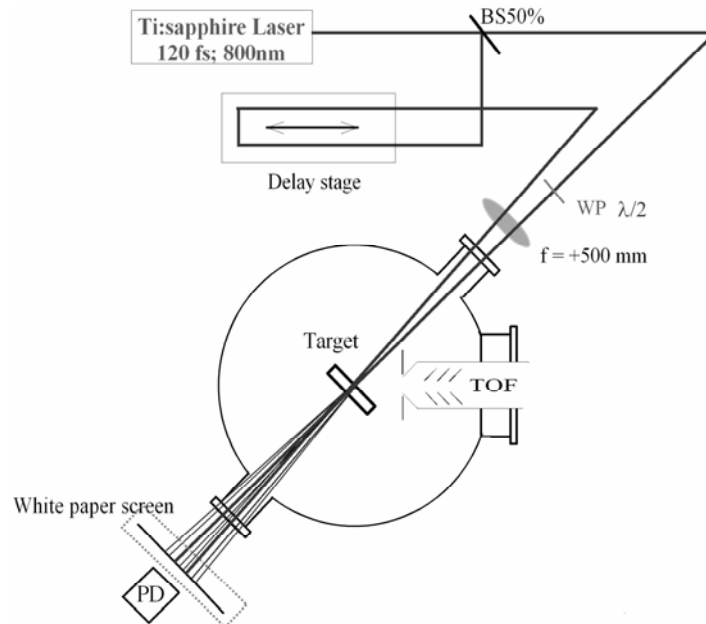


Figure 5.17. Experimental set-up for femtosecond ablation with two non-collinear beams of temporally and spatially overlapped 120-fs laser pulses. (The target is placed in the UHV chamber.) A spatio-temporal overlap of both beams interference results in the generation of a transient index grating [SSR01]. The self-diffraction pattern of the beams on this index grating⁴⁸ is easily visible on a white paper screen.

To test whether the femtosecond laser induced patterns result from an inhomogeneous energy input, a controlled transient interference pattern was produced on the target in a non-collinear two-beam experiment (Figure 5.17). The corresponding interference pattern should lead to, in addition to ripples, a modulation of ablation rate across the surface.

Spatially (temporally) overlapped pulses were produced in a set-up similar to a pump-probe experiment. The laser beam was split in two almost equally intense beams,

⁴⁸ As a consequence of a wave mixing effect, the self-diffraction pattern of the fundamental beam is accompanied by generation of the third harmonic (266nm) [SWM99, SSR01]. Thus the resulting UV light give rise to a blue fluorescence on the white paper screen. The self-diffraction pattern is easier visible, this facilitating the beams alignment.

and then recombined. The beams were focused onto the target with a small angle θ_b in between of about 6-10° (the bisection of this angle coincides with the surface normal). As a result, the two beams interfere forming a transient grating along the sample (Figure 5.18) [EGP85].

The grating constant (spatial distance between two interference maxima) results from Bragg's condition for interference maxima:

$$X = \frac{\lambda}{2 \sin(\theta_b/2)} \quad (5.3)$$

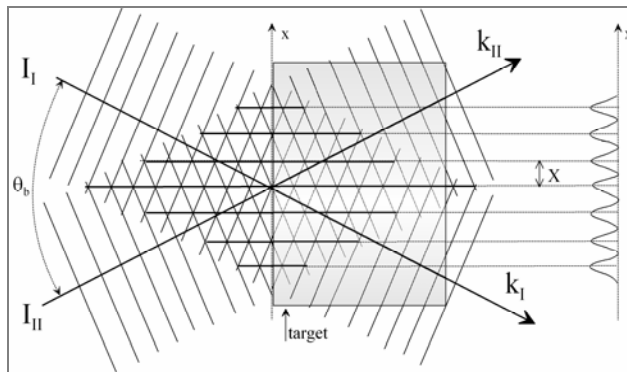


Figure 5.18. Grating induced by interference of two beams of intensity I_I and I_{II} and wave vectors \mathbf{k}_I and \mathbf{k}_{II} .

In our experiment, the two-beam overlap in space (time) was controlled by observing the self-diffraction from this transient grating [EGP85, SWM99].

The laser-induced *grating* generates an inhomogeneous energy distribution on the surface. For an incident wavelength of $\lambda = 800\text{nm}$, and $\theta_b = 6\text{-}10^\circ$, the grating constant X

varies between 4.5-7.6 μm . The grating thickness is $\sim 36 \mu\text{m}$, i.e. roughly the length in vacuum of a $\sim 120 \text{fs}$ pulse.

Figure 5.19 presents an ablated spot obtained with two interfering non-collinear beams, both p-polarized, at a best spatial overlap. Here, the laser beams were nearly equal in intensity of $\sim 12 \text{TW}/\text{cm}^2$ and $\sim 13 \text{TW}/\text{cm}^2$, respectively. The only detected structure is of D(I) type. This does not significantly differ from the one produced by single beam ablation, both as spatial period and orientation.

The ablated spot appears to be divided into areas of different morphology. A web-like structure occurs in the center of the crater with a peculiar transition from to a more regular pattern at the spot edge (Figure 5.19 (b, c)).

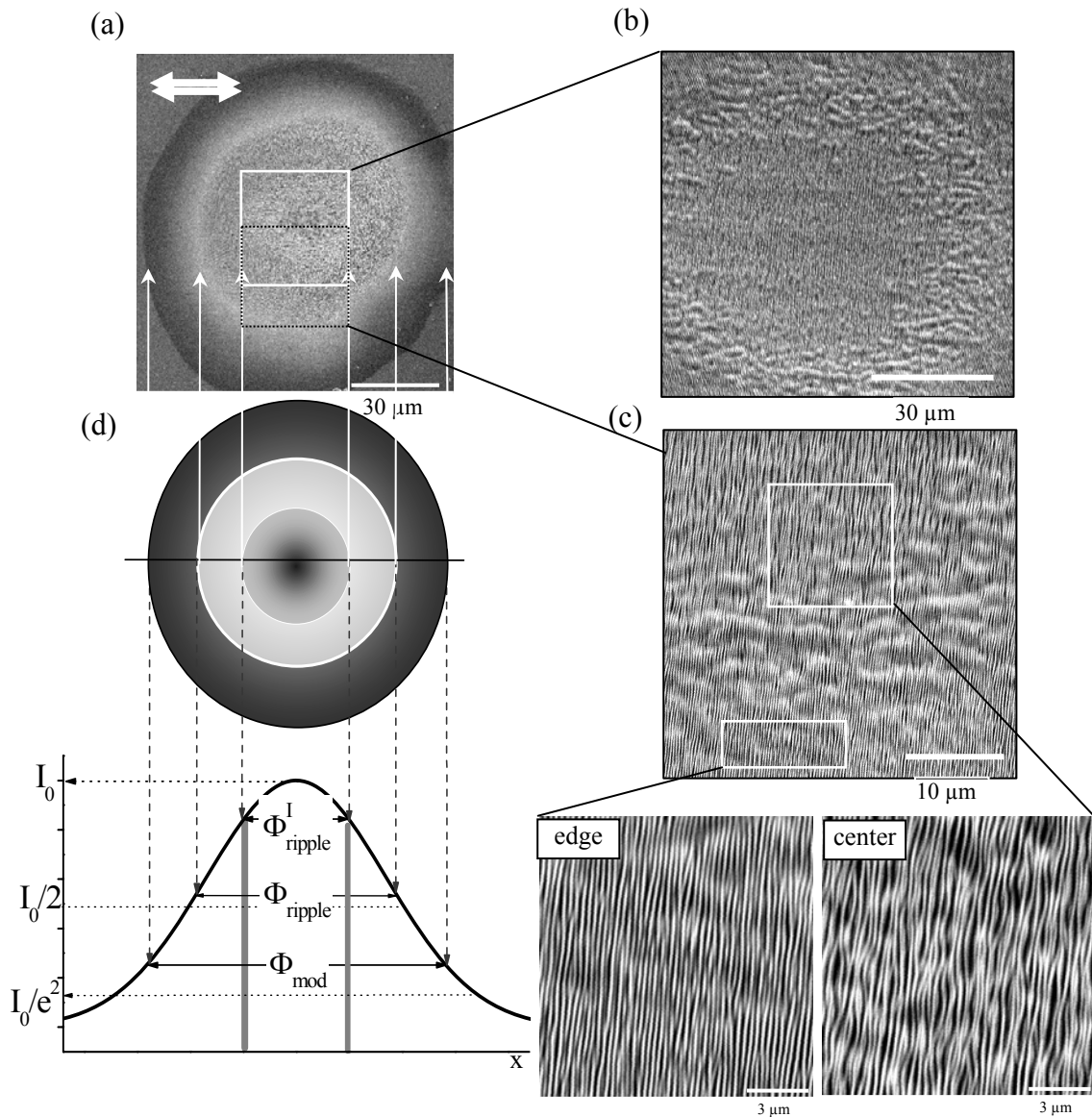


Figure 5.19. (a) Ablated spot obtained with two non-collinear beams, both p-polarized, of almost equal intensity 12 TW/cm^2 and 13 TW/cm^2 , respectively. (b) Detail of the central ripple zone; (c) Magnified area from the edge of central ripple zone with details presenting the relevant ripple structures;

(d) The areas in (a) of different morphology are compared to a spot of $\sim 70 \mu\text{m}$ (FWHM) diameter with a Gaussian intensity profile; the central ripple zone Φ_{ripple}^I ; the entire ripple zone Φ_{ripple} and the entire modified area Φ_{mod} are therefore delimited.

The polarization direction of the two beams is given by the double white arrows.

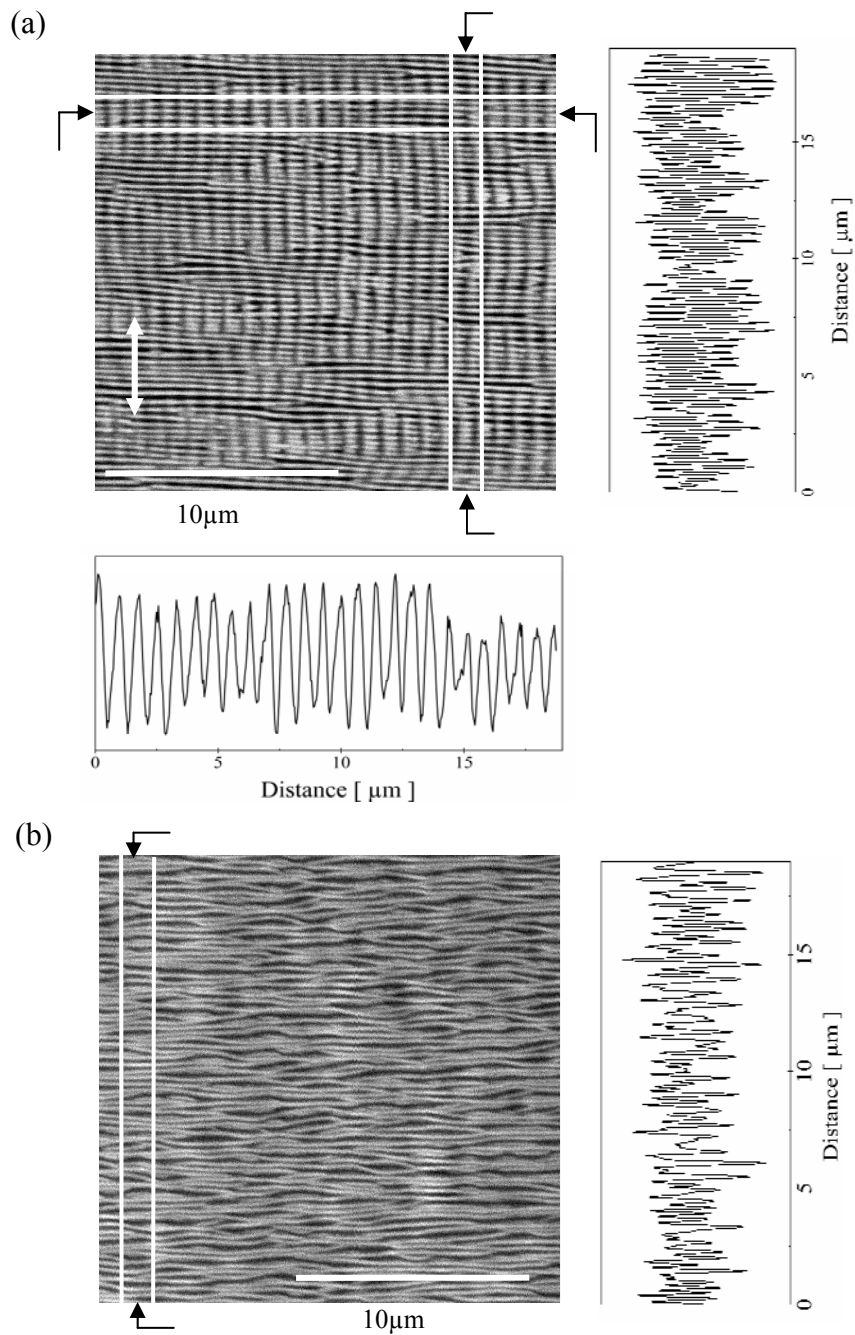


Figure 5.20. (a) Ripple structures produced after single pulse irradiation with surface modulation profiles of a fine modulation (right graph) and thick modulation (bottom graph) obtained after 4.3×10^4 laser pulses of 13 TW/cm^2 laser intensity (here modulation profiles are derived from the SEM image contrast). (b) Ripple structure produced by two temporally overlapped beams of the same polarization (4.3×10^4 laser pulses of 12 TW/cm^2 and 13 TW/cm^2 , respectively).

The regions of different surface morphological features, which extend radially across the spot, are qualitatively delimited in a graphical representation in Figure 5.19 (d). In a comparison with a Gaussian intensity profile, we distinguish the central disc of a Φ_{ripple}^I width as the zone modified by web-like ripples. The ‘cloudy’ over-structure from its annulus (its position is marked in Figure 5.19 (d)) seems to be *specific* for the two-beam ablation. The ripple zone covers a disk of a Φ_{ripple} width, which is an important part of the modified area of Φ_{mod} width. This last observation is also valid for surface morphology after ablation with a single beam.

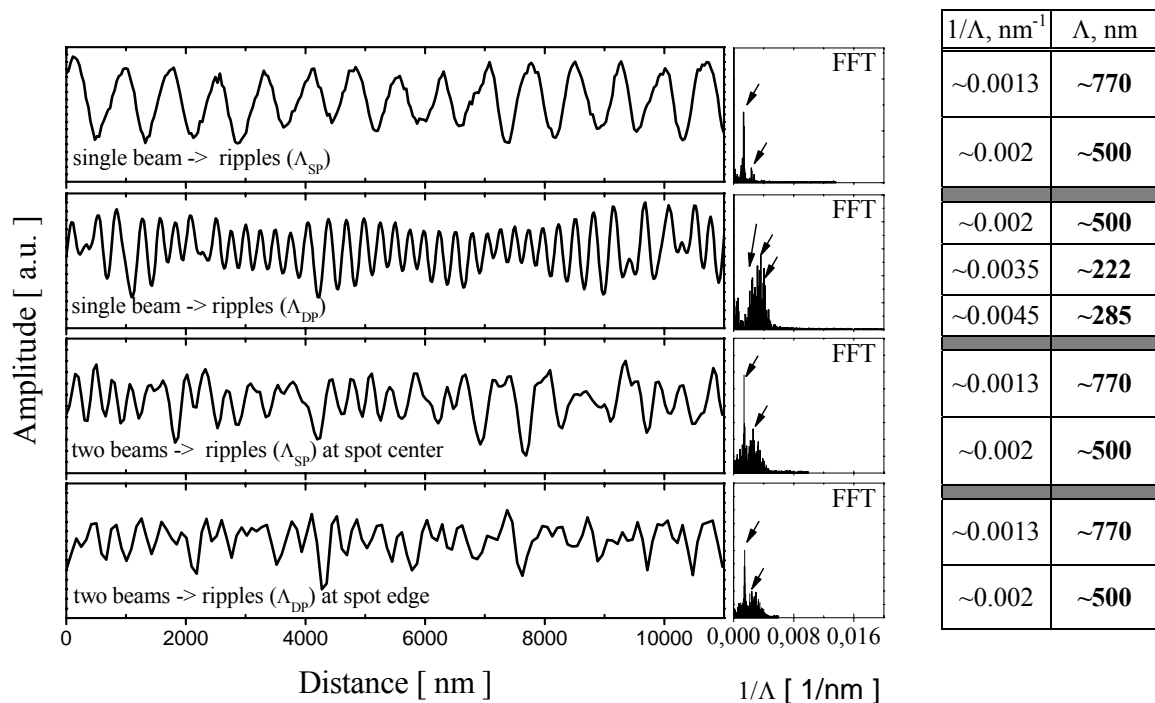


Figure 5.21. Fast Fourier transforms along lines of periodic ripples produced by single beam ablation as compared with two beam ablation (for clarity see also Figure 5.21); ripple frequencies / spatial periods can occur around $\Lambda_{S(I)} \sim 770\text{nm}$; $\Lambda_{D(I)} \sim 500\text{nm} / 222 \text{ nm} / 285 \text{ nm}$.

Figure 5.20 shows a comparison between ripple patterns produced with a single beam

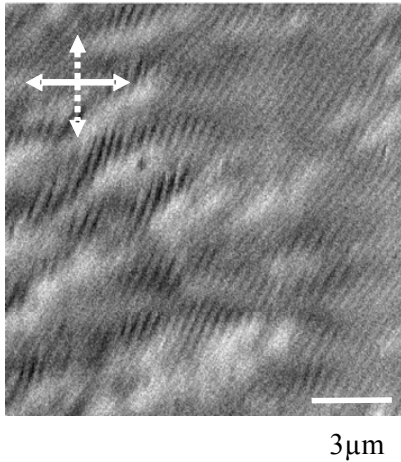


Figure 5.22. Detail from the center of a spot produced by two spatially (temporally) overlapped beams: 4.3×10^4 laser pulses of 13 TW/cm^2 laser intensity, p-pol (beam I); and 12 TW/cm^2 laser intensity, s-pol (beam II). The double arrows indicate the beams polarization: solid line - beam I; dotted line - beam II.

and two-beams. After single beam ablation, ordered, interwoven ripples grow perpendicular or parallel to the electric field of the incident beam. The profiles of the ripples' contrast (Figure 5.20 (a)) indicate a well-developed finer corrugation perpendicular to the beam polarization with a period of $\sim 230 \text{ nm}$ and a larger one of period about 700 nm . In contrast, the two-beam ablation generates a more irregular structure of $\sim 230 \text{ nm}$ period in average.

That single beam ablation gives rise to highly regular uniform structures is also revealed by the Fourier transform spectra in Figure 5.21. Here, several dominant frequencies can be distinguished as listed in the table from the right side of Figure 5.21. They correspond to periodic patterns of spatial periods of about $225\text{-}285 \text{ nm}$, 500 nm and 700 nm . These frequencies are better resolved for ripples produced with a single beam. The two beams ablation apparently causes a higher dispersion around the various frequencies, thus apparently a loss of symmetry.

The higher intensity obtained at the two beam interference⁴⁹ should play an important role in ripples contrast. For comparison, we also used beams of different polarization, thus no interference effect, and similar conditions of number of pulses and intensity. Indeed, the resulting ripple pattern (type D(I)) is much weaker (Figure 5.22) in this case and appears to align on the polarization of the more intense beam.

Finally, let us discuss the issue of the induced transient grating of a $4.5\text{-}7.6 \mu\text{m}$ period. Although the self-diffraction pattern, which indicates of the transient grating formation, was *clearly visible* in the beams transmission through the sample, a structure of such period has not been observed in the surface morphology after ablation. In the

⁴⁹ For equally intense beams, at constructive interference, the obtained pattern must correspond to four times the intensity of one single beam.

conditions presented here, *no evidence* of an inhomogeneous energy input due to the transient grating could be found at the two-beam overlap region. The ripple pattern is apparently not correlated to the intensity variation induced by this transient grating. Our results suggest that the ripples' origin is other than just an inhomogeneous energy distribution at the surface as a result of an interference related to the incident beam.

To briefly summarize, so far this chapter has shown that after femtosecond laser interaction, the dielectric surface appears modified with features in the nanometer scale. Periodic patterns of periods *much shorter* than the incident wavelength can form at the surface.

They relate to the initial excitation by keeping the memory of the incident beam polarization. A two-beam experiment indicates that their origin mechanism cannot simply be an effect of an inhomogeneous energy input. Thus these structures can be formed during a surface relaxation process after ablation.

5.3. SURFACE MODIFICATION AFTER LASER ABLATION OF SILICON

Regular periodic structures of nanometer size have also been reported upon laser ablation of silicon such as columnar, conical spikes [HFW98] or cluster arrays [PFG03]. In the following subsection, the surface morphology of silicon after femtosecond laser ablation is discussed, in particular the surface periodic patterns. Different ripples, such as those found on dielectric surfaces and their characteristics, will be presented and evaluated here for silicon.

In these experiments low doped silicon (100) samples were used, conventionally cleaned and then exposed to repetitive irradiation to multiple laser pulses (120-fs; 800 nm) at fluences below or near the ablation threshold of $\sim 2 \text{ TW/cm}^2$ (as indicated in the preceding chapter). In contrast to other ‘patterning’ studies on laser ablated silicon [HFW98, PFL00, BBK02], these experiments were performed under ultra-high vacuum conditions, thus neither in air nor using any reactive or buffer atmospheres. Scanning electron and atomic force microscopy were applied to investigate the morphology of the ablated spot, in particular the laser generated structures, and Raman spectroscopy to study phase changes in the interaction region.

5.3.1. From periodic to irregular surface patterns

The silicon surface morphology after ablation reveals typically multiple structures from the micro- to the nanometer scale. They can be either irregular or ordered in lines, randomly oriented or aligned on the beam polarization. The ordered periodic structures are again of several types, distinguishable by their dominance (recurrence), spatial period and orientation. For these different structures, we adopt a nomenclature similar to that used to describe the structures formed on dielectric surfaces, although the experiments have revealed several differences. Accordingly, the dominant, well-developed ripples pattern are called here D(I) and the secondary, weaker, structures are called here S(I). Contrary to dielectrics, the periods of S(I) structure are here much shorter than the incident wavelength, while the D(I)’s periods are larger and much closer to λ .

In brief, a repetitive irradiation of silicon (100) at laser intensities below the single shot ablation threshold (2×10^4 pulses at 1.6 TW/cm^2 ; for $\lambda = 800 \text{ nm}$ at normal incidence) gives rise to several structures (Figure 5.23, (a)):

(i) A *D(I) pattern*: a system of well-developed ripples with a spatial period of $\Lambda_S \sim 700 \text{ nm}$, aligned either *perpendicular* to the laser polarization or even radially from the center toward the edge of the irradiated spot (Figure 5.23 (b));

(ii) An *S(I) pattern*: a weak, fine ripple pattern of $\sim 200 \text{ nm}$ spatial period, oriented *parallel* to the laser polarization (Figure 5.23 (c, e));

(iii) A *columnar*, coarser structure (in the spot center). This structure seems to indicate a deeply eroded surface (Figure 5.23 (d));

As far as the ripple's orientation is concerned, the periodic structures appear to be similar to those observed on dielectric surface, i.e. the dominant pattern aligns perpendicular to the beam polarization, while the secondary patterns parallel to it. As for the spatial period, however, the period of S(I) type is *much shorter* than λ , while the period of D(I) type, larger than S(I)'s period, is still narrower than λ .

Similar to the dielectric surface morphology, the periodic structures on silicon surface exhibit several general features: (i) they form independently on the sample's crystallographic structure; (ii) certain parameters such as the beam *polarization* and *irradiation dose* (the laser intensity and number of pulses) control the structure formation and orientation.

The sequence of SEM micrographs in Figure 5.24 presents several surface patterns generated after irradiation with a laser beam at normal incidence. Thus, for a moderate intensity of 0.4 TW/cm^2 (almost an order of magnitude below the damage threshold) yet very many ablating pulses (6×10^4 pulses), a shallow crater is produced. This is only a few microns deep and is covered with regular weak structures of S(I) type (Figure 5.24 (a)). Their typical period is $\approx 200 \text{ nm}$ and additional features like bifurcations are observed. They are very similar as period to the D(I) structure which built up on a dielectric surface and seem to align *parallel to the laser polarization*.

With increasing intensity (as shown for instance in Figure 5.23), a well-developed structure forms (the D type), superimposing the fine one and extending radially across the spot. At even higher intensity, toward the center of the spot, a more irregular structure occurs, which seems to be the precursor of a crater. Indeed, upon further irradiation (or increased laser intensity) a real crater is formed. The affected zone around the spot is covered with fine grains, which already arrange themselves in a D(I) structure as displayed in Figure 5.24 (b).

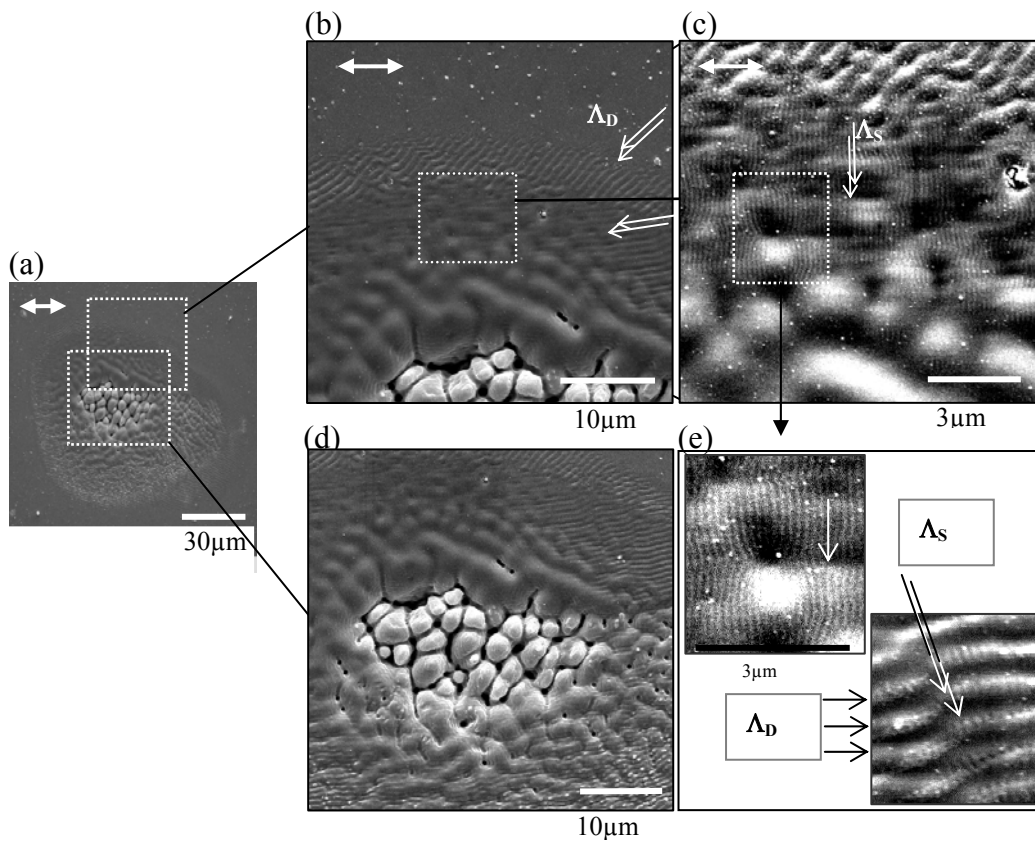


Figure 5.23. SEM micrographs of coexisting periodic structures at the bottom of an ablation crater produced after irradiation with 120 fs pulses at $\lambda = 800$ nm; 2×10^4 pulses of 1.6 TW/cm²; 0° incidence. (a) overview; the right panels are details of (a) revealing typical structures such as: ordered D(I) structures (b) coexisting D(I) of period $\Lambda_{D(I)} \sim 700$ nm and S(I) of $\Lambda_{S(I)} \sim 200$ nm (d) with details in (e); irregular, columnar area (c); The structures direction and laser polarization are indicated by (double) arrows.

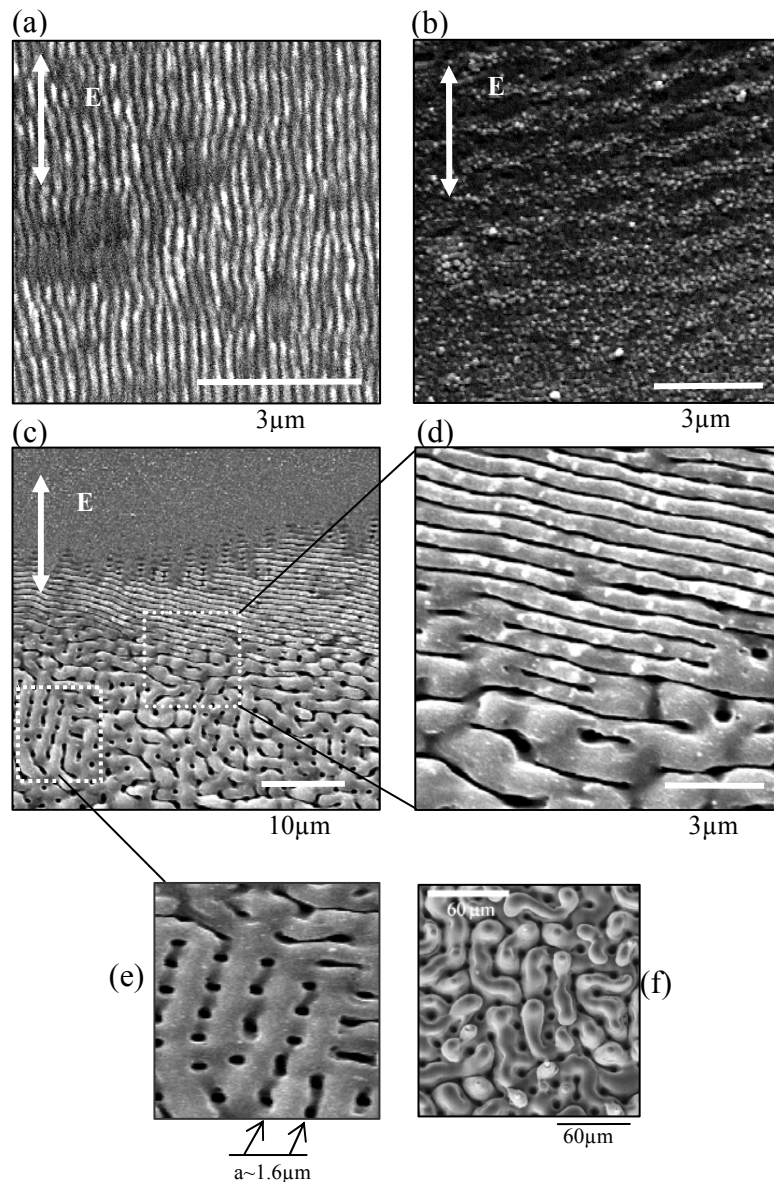


Figure 5.24. SEM micrographs of periodic structures after irradiation with 120-fs laser pulses ($\lambda=800$ nm; normal incidence):

- (a) Fine ripples of $\Lambda_S \sim 200$ nm (6×10^4 pulses at 0.4 TW/cm 2);
 - (b) Fine grains, on a detail from the edge of a spot, arranged in a dominant structure;
 - (c) Detail from a spot revealing a lamellar structure and a dominant type at the boundary (10^4 pulses at 1.6 TW/cm 2);
 - (d) Magnified region from (c) with ordered ripples of $\Lambda_D \sim 700$ nm; note that the gaps width appears to be only ~ 100 nm
 - (e) A region with ordered holes of < 1 μ m in diameter at an $a \sim 1.6$ μ m apart;
 - (f) A structure very similar, as aspect, to the lamellar structure in (c), but much different in size, found on a Si surface after nanosecond laser ablation (from [PFL00]; see text);
- The laser polarization is indicated by double arrows.

Thus, after repetitive irradiation with 10^4 pulses at 1.6 TW/cm^2 the D(I) structure is well-developed (Figure 5.24 (c, d)) at the spot edge but severely altered toward the spot center.

Also at the transition from a dominant type to the columnar structure in the spot center, an intermediate lamellar, randomly oriented structure of a $\sim 2 \mu\text{m}$ period occurs. This structure is accompanied by peculiar deep holes of about 700 nm in diameter, quite regularly arranged in a 2D matrix. The resulting arrangement resembles a lattice with a period of about $2 \mu\text{m}$ (Figure 5.24, in a magnified region from picture (c)). It is worth noting that a quite similar picture, at first sight, was reported by Pedraza et al. [PFL00] on silicon irradiated with nanosecond UV laser pulses, under oxygen-rich atmosphere (see Figure 5.24 (e)). These kinds of structures are, in the literature, often attributed to the initial stage of columns growing via a mechanism of surface self-organization. The two structures from Figure 5.24 (c and e) are quite similar as aspect, although they greatly differ in size.

A rather peculiar observation on ripples period variation in the same spot is presented in Figure 5.25.

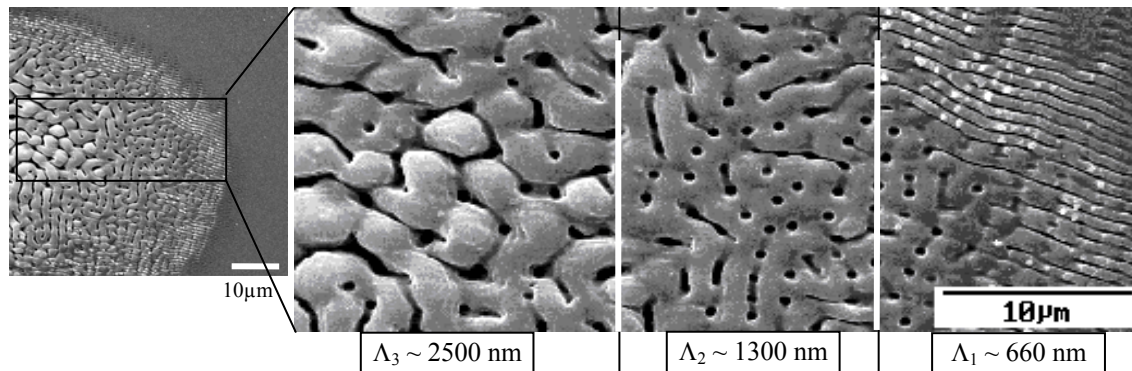


Figure 5.25. Spatial periods from an ablated spot on a silicon surface: from the spot center (left) to the edge (right) 3 zones of different periodic structures could be distinguished (delimited by white vertical lines).

Across an ablated spot, a rather sharp *transition from order to disorder* occurs: from a uniform arrangement of lines of spatial period $\Lambda_1 \sim 660 \text{ nm}$ at the edge of the spot (right) to a more irregular pattern of $\Lambda_2 \sim 1300 \text{ nm}$ towards the spot center and an even greater irregularity of $\Lambda_3 \sim 2500 \text{ nm}$ in the very center (left). The structures formation and

evolution depends on the incident intensity. To a rough approximation, between the periods of these structures a relationship of the form $\Lambda_3 \sim 2\Lambda_2 \sim 4\Lambda_1$ can apply. This suggests a period doubling effect, which is a feature pointing toward a chaotic surface evolution [Pei92].

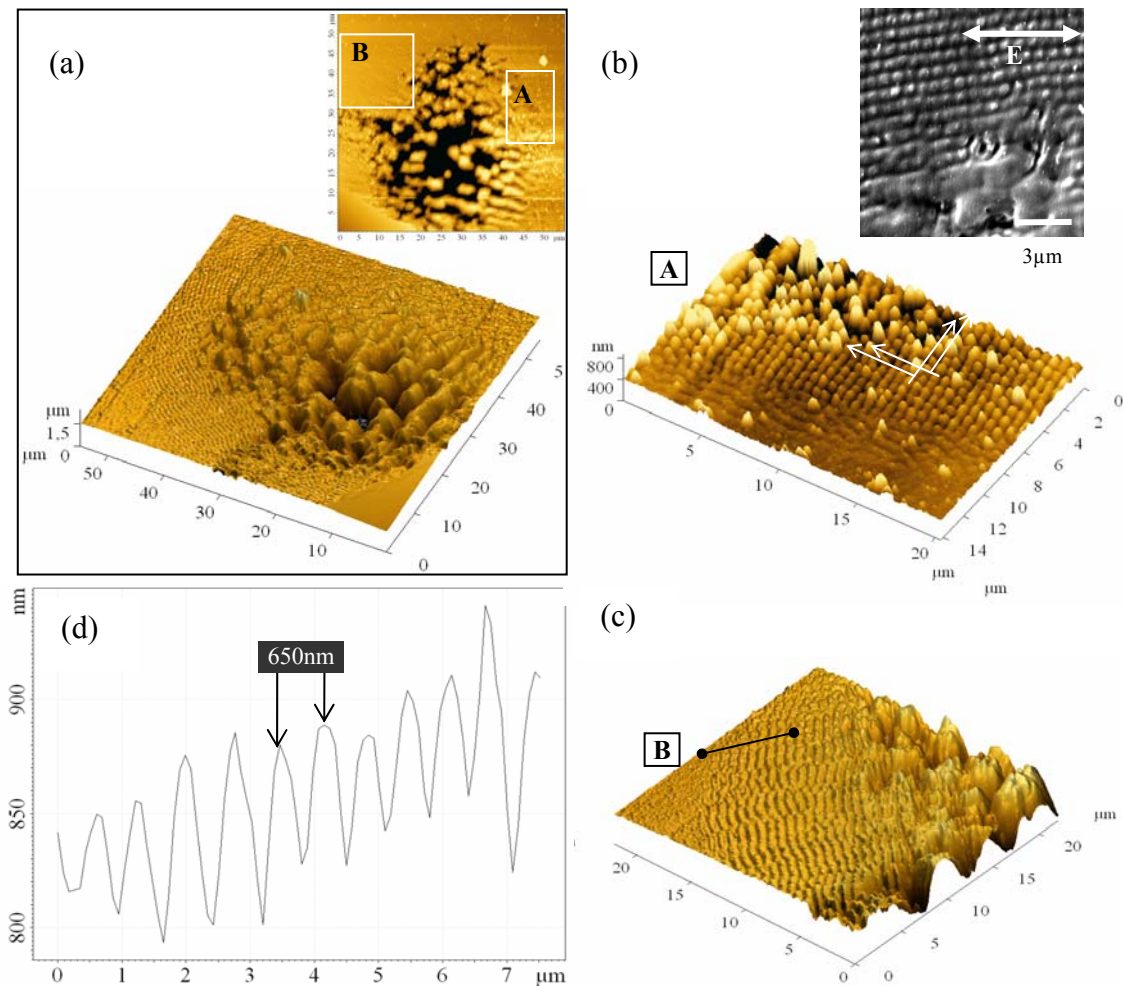


Figure 5.26. AFM images of periodic structures. (a) 3D image of a spot after irradiation with 12×10^4 pulses at 0.6 TW/cm^2 ; 800 nm , 0° incidence; (b) 3D image of a detail of region A. The two patterns, perpendicular to each other, are indicated by arrows. Also a SEM image of this detail is shown. (The laser polarization is indicated by double arrows) (c) 3D image of a detail of region B in (b) revealing an dominant structure of $\Lambda_D \sim 650\text{-}700 \text{ nm}$ as indicated in a depth profile in (d)

In addition, structures of a quite similar spatial period of ($\Lambda_D \sim 600 \text{ nm}$) can occur, apparently crossing each other in a net-like manner as revealed in Figure 5.26 after AFM and SEM investigation. Here, the ablated crater appears to be just several microns deep (Figure 5.26 (a)). Different structures occur across the spot: a columnar structure in Figure

5.26 (a), two crossed D-types of structures in Figure 5.26 (b) and a single D(I) structure in Figure 5.26 (c). The peculiar interlaced pattern in (b) may indicate that the D-types can align *both perpendicular and parallel to the polarization*⁵⁰. The ripples depth profile in (d) reveals a modulation depth of about 300 nm.

Typically at the spot center, micro-columns (or pillars) are noticeable. With increasing the number of pulses of certain laser intensity, the columnar area extends, until it covers the entire spot (see the sequence of SEM images in Figure 5.27). The columns extend laterally and vertically upon prolonged exposure and the erosion continues until a crater is formed (Figure 5.27).

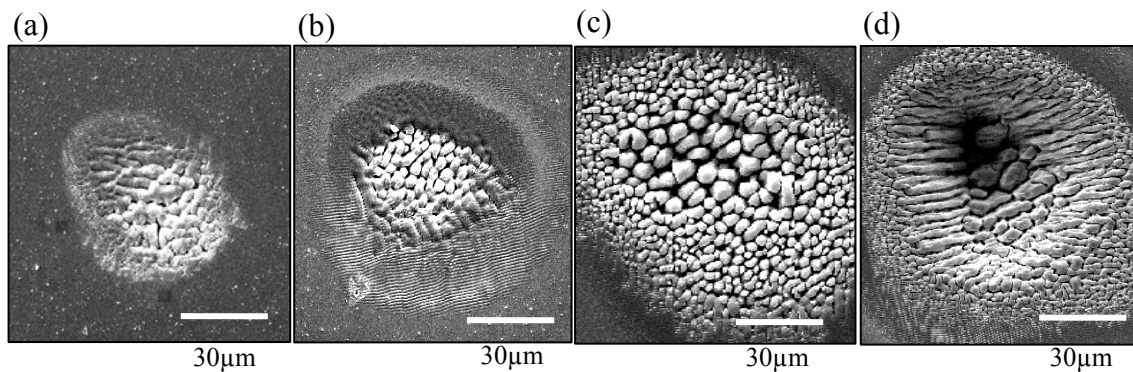


Figure 5.27. Evolution of the surface with increasing number of pulses: (a) 0.5×10^3 pulses; (b) 2×10^3 pulses; (c) 3×10^3 pulses; (d) 6×10^3 pulses at constant 10 TW/cm^2 intensity.

Similar columnar structures, generated at the center of femtosecond laser irradiated silicon, have been reported by Bonse et al. [BBK02], with the difference that the used fluence range was one order of magnitude higher than in the present work. These columns are believed to be an effect of surface self-organization, resulting from preferential erosion and material redeposition at the surface [LFP00]. Indeed, the perturbed silicon surface region of the silicon target can eventually reach the thermodynamic conditions of phase transitions (i.e. phase explosion). As an effect of homogeneous nucleation of gas bubbles, liquid droplets are ejected from the surface, which are, at a later stage, re-deposited on the surface.

⁵⁰ These peculiar structures were produced upon exposure to multiple pulses (12×10^4 pulses) at a low laser intensity (0.6 TW/cm^2). However, the exact conditions for the formation of these different structures are so far uncertain.

To summarize, so far, our analysis on fs-laser induced structures on silicon surfaces has shown as follows:

(I) Some of their characteristics are different from the structures generated on dielectric surfaces

Indeed, a general comparison of the patterns periods for BaF₂ and Si surfaces, as listed in Table 5.2, indicate that they *depend on the material*.

Table 5.2. Spatial periods for different laser induced structures on BaF₂ and Si surfaces (800 nm wavelength, at normal incidence). Λ_D and Λ_S denote the periods of dominant and secondary structures.

Material	Λ_D , nm (\perp E or \parallel E)	Λ_S , nm (\parallel E)	Λ_S , nm
Dielectric (BaF ₂)	270 – 350	~ 700 – 1200 (+ weak S \perp E)	~2000 (\perp E)
Semiconductor (Si)	600-700	~ 200	~2000 (random)

(II) All the structures presented here do not show the spatial periods, which, earlier, supported the idea of an inhomogeneous energy input.

A comparison between spatial periods of ripples obtained in our experiments and the prediction given by the classical interference model is displayed in Figure 5.28.

We present the ripples period dependence on the angle of incidence of the beam on the target and the incident wavelength as predicted by the classical interference model (given by Eq. 5.1) and compare it with ripples period (intervals) as obtained in our experiments on BaF₂ and Si.

It is evident that the (sub-wavelength) surface structures periods, as presented in this work, do not match the ‘classical’ prediction.

Instead, on the ablated silicon surface we found more features pointing toward a *chaotic surface evolution* such as an apparent order to disorder transition or a noticeable *period doubling effect and columnar structures*.

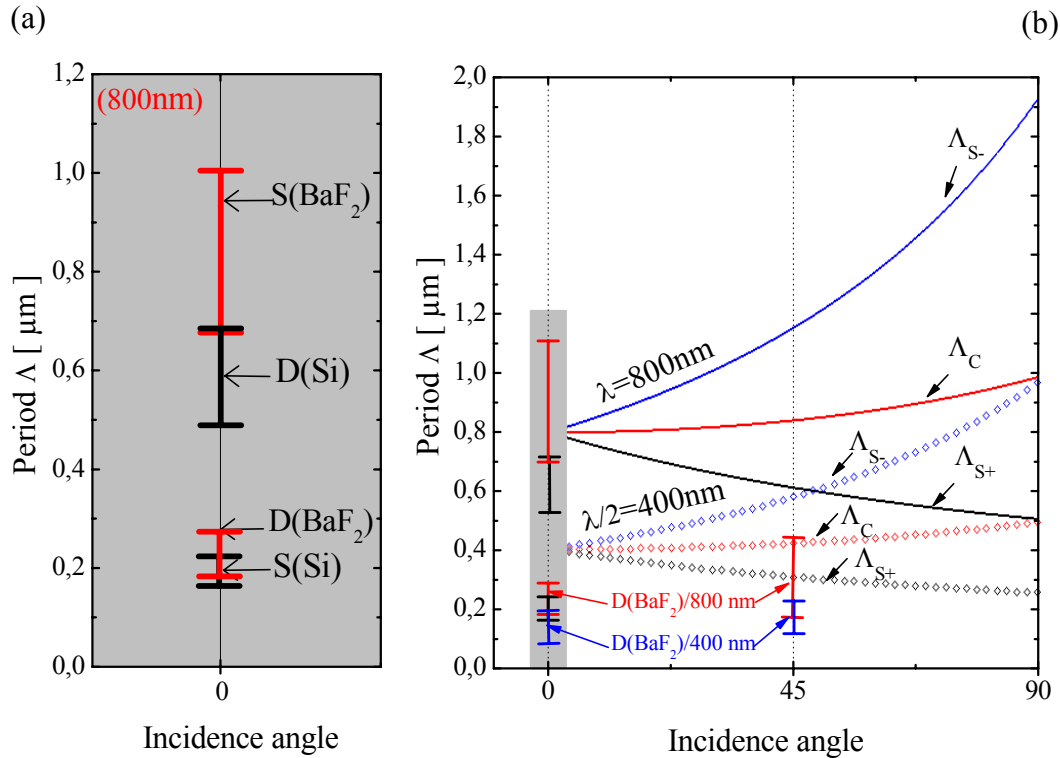


Figure 5.28. (a) Comparison between the dominant (D) and secondary (S) ripple period intervals from BaF₂ and Si irradiated by 120-fs pulses; 800 nm; 0° incidence. (b) ‘Classical’ versus ‘non-classical’ ripples period: dependence on the incidence angle and laser wavelength of the ‘classical’ ripple periods (from Eq. 5.1) for 800 nm (solid lines) and 400 nm (dotted lines), respectively, as compared to the ripple period intervals obtained in this work. The (a) graph is a magnification of the gray area in (b). The intervals marked with blue correspond to the period of ripples on BaF₂ surface irradiated by 400nm radiation.

5.3.2. Phase transformations after ablation

The silicon surface undergoes complex transformations after femtosecond laser ablation as it is indicated by the different features formed across the ablated spot. As discussed in the preceding chapters, ultra-short laser pulses can create *instabilities* at the silicon surface, which can be either fast phase transitions or a considerable surface charge unbalance. The different structures should appear from or be connected to the surface relaxation from such instabilities. The ejection of energetic particles from the surface gives rise to a corresponding recoil pressure, i.e. mechanical stress, in the interaction region. Thus, to additionally characterize the surface morphology upon ablation and the laser-induced instabilities on the silicon surface, we used Raman spectroscopy to analyze *the crystalline silicon transformation upon ablation*.

Subjecting *silicon* to high pressure results in phase transformations in the crystal lattice [KNG99, DoG02]. Because in the new phases the atoms are displaced from their equilibrium positions, they experience restoring forces and vibrate at characteristic phonon frequencies, which can be detected by Raman spectroscopy. This is today a common, non-invasive tool to reveal stress distributions and crystallographic changes of materials. Mono-crystals can be easily distinguished from polycrystalline or amorphous silicon as they give different Raman shifts.

Laser ablated spots were produced with multiple 120-fs laser pulses at different intensities on a piece of silicon Si (100) wafer. The spots were analyzed in a micro-Raman spectrometer (DILOR-X-Y). The ablated surface regions were excited using the emission line of 532 nm from a continuous wave, frequency doubled Nd:YVO4 laser (Coherent Verdi). The microscope optics allows focusing the incident laser beam to a 1 μm spot. The acquisition time for the Raman spectra was varied from 80 to 300 s depending on the modulation depth of the sample. In order to prevent artifacts due to laser heating during the exposure, the beam intensity was kept below the onset of a measurable heating (4mW) [KAW03].

In order to investigate the sample properties in different ablation regions, micro-Raman spectra were taken from several locations across an ablated spot (Figure 5.30). In fact, several crystalline phases of silicon are found. According to the structure of their primitive cell, they are labeled as follows: Si-I (*diamond*); Si-III (*bcc*); Si-IV (*hexagonal*); Si-XII (*rhomboidal*) and amorphous phase (*a-Si*) (see also Appendix A). In Figure 5.30, all spectra are dominated by the *c-Si*, TO-phonon peak at 521 cm^{-1} . This indicates that the newly formed Si-phases do not reach deep in the bulk (the penetration depth of the 532-nm Raman laser of $\approx 1 \mu\text{m}$ in silicon).

The different Raman spectra displayed in Figure 5.29 were taken in the locations correspondingly numbered across the SEM images of ablated spots. Inside the crater the detection is poor and other features may be hidden in the background. Here, for a better signal collection, we increased the irradiation time to 300 s (taking care to not alter the sample [KAW03, KOS03]).

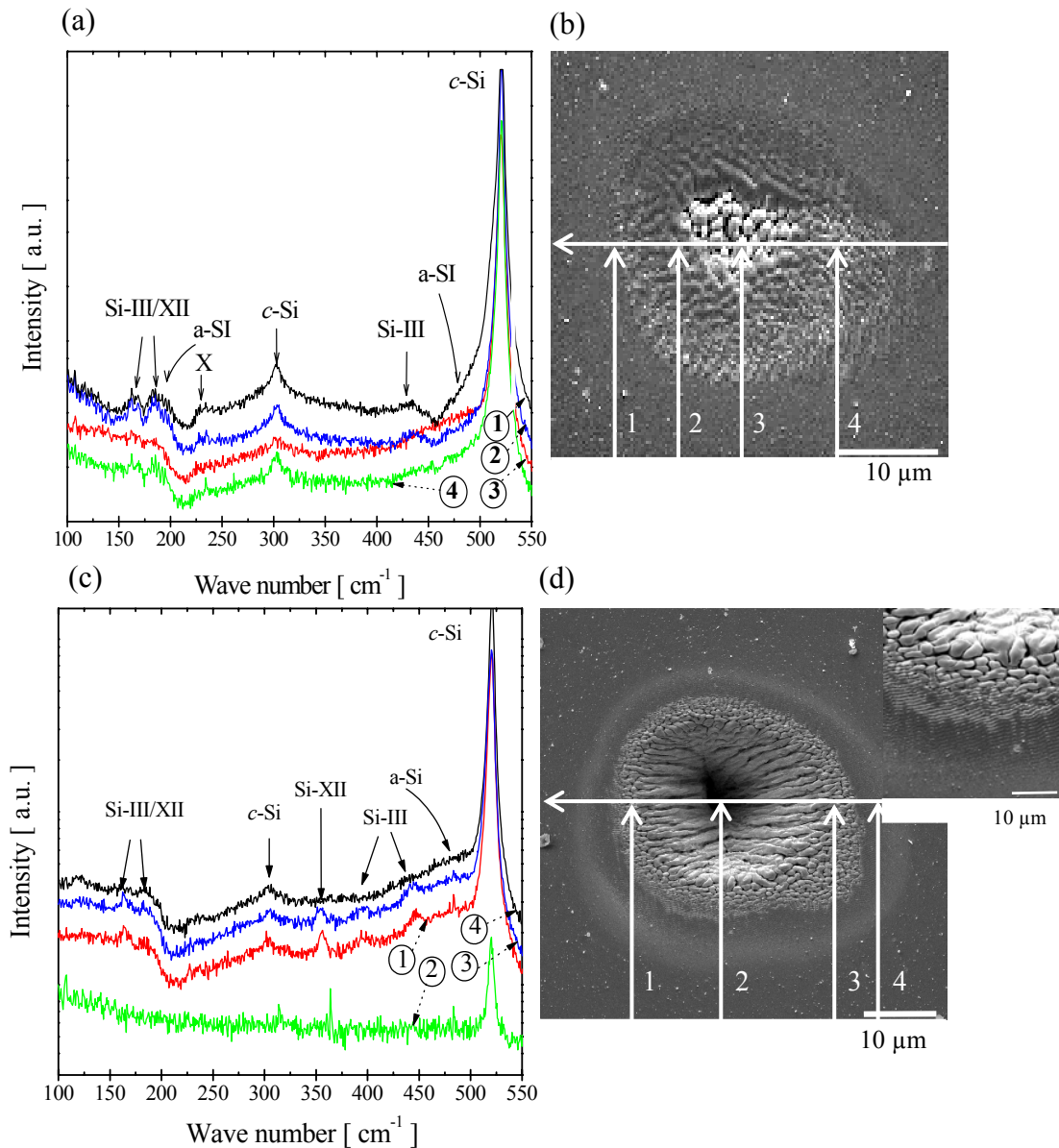


Figure 5.29. Raman spectra from the ablated area on p-doped Si(100), taken at different areas of a spot of a few μm depth as indicated in the SEM images. (a) Raman spectra from several locations across a ‘flat’ spot as indicated by the numbered arrows (b); (c) Raman spectra from locations across a ‘deep’ spot as indicated by the numbered arrows (d).

Figure 5.29 (a, b) displays Raman spectra obtained from a relatively shallow crater. In the $\sim 60\text{-nm}$ region covered with ripples (1, 2) the bcc and rhombohedral phases (Si-III and Si-XII) are very pronounced while the amorphous contribution is not significant. The origin of the sharp minimum at 220 cm^{-1} (labeled with X) is not yet clear but may result

from interference between the Si-I and Si-III signals. The columnar central area (3) is dominated by amorphous a -Si, although different other Si-phases may be just unresolved.

Figure 5.29 (c, d) shows Raman spectra obtained from different locations on a deep crater (several tens of microns deep). Deep inside the crater, the detection is poor, thus we only detected a low c -Si signal. Other features may eventually occur but they are too weak thus they could be lost in noise. At the crater wall, where columns align along, large contributions from Si-III and Si-XII phases are detected as well as amorphous Si. In the ripple area Si-III phase (bcc) is important, while in the heat affected zone around the spot the amorphous contribution seems to be strong.

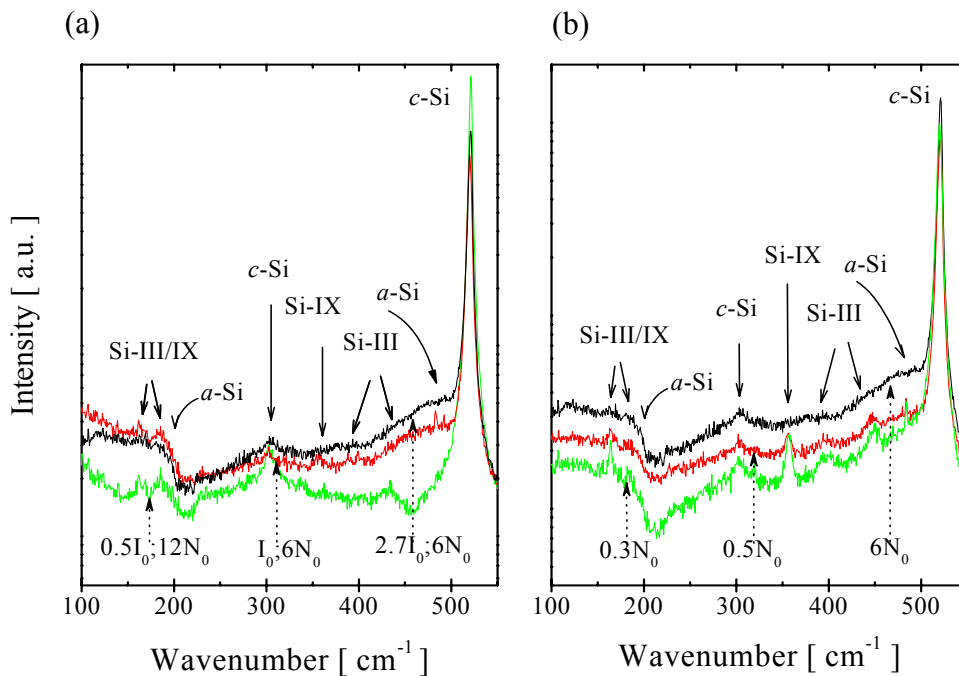


Figure 5.30. Si polymorphs formed at spots produced after irradiation with (a) a large number of pulses of different laser intensities; (b) different number of pulse at a constant $2.7 \times I_0$. Here, $I_0 = 1 \text{ TW/cm}^2$, $N_0 = 10^4$ pulses. The Raman spectra were collected in the ripple areas.

The transformation of different Si polymorphs in the ripple region with increasing the laser intensity and the number of pulses, respectively, as given by the Raman spectra, is represented in Figure 5.30. A general observation can be drawn both when increasing the intensity at a constant number of pulses, and increasing the number of pulses at constant laser intensity: at low intensities or for a low number of laser pulses, the crystalline Si phases are very well-represented. When increasing the dose, either the laser intensity or the

number of pulses, the phases seem to vanish under an overwhelming amorphous contribution. Indeed, as reported in [BMS05], the Raman spectroscopy investigation of silicon upon ablation with single pulses has revealed broadened *c*-Si peaks and a pronounced amorphous phase with no evidence of new crystalline phases.

To summarize, after femtosecond laser excitation, the silicon sample exhibits common *pressure-induced phase transformations*. The Raman spectra suggest that crystalline silicon (100) undergoes important structural changes leading to *amorphous silicon* and in different silicon *crystalline* phases. In the ripple region, all these crystalline phases are well-developed, suggesting an inhomogeneous surface of enhanced *disorder*. By increasing either the laser intensity or the number of pulses, the disorder becomes more evident, the surface transformation being dominated by amorphous Si.

5.4. RIPPLE FORMATION FROM INSTABILITIES

Recently, sub-wavelength ripples formed after femtosecond laser ablation have been attracted the experimentalists' attention quite intensely. In addition to the experimental findings presented in this work, similar sub-wavelength ripples have been reported on the surface of various materials irradiated with femtosecond laser of various wavelengths. For instance, under conditions similar to the present work (120-200 fs pulses at 800 nm), Varel et al. [VWR98] and Henyk et al. [HVW00] presented images of sub-wavelength ripples (200 nm) formed upon ablation of sapphire and Yasumaru et al. [YMK02] reported the formation of ripple patterns with 100-125 nm period on TiN and diamond-like carbon. Also Ozkan et al. [OMR99] found ripples of periods \sim 50-100 nm upon 248-nm femtosecond laser irradiation of thin diamond films, and later on Borowieck et al. [BoH03] reported sub-wavelength ripples in a series of compound semiconductors for laser wavelength of 800, 1300, and 2100 nm.

Despite the significant discrepancy between the experimental conditions, several works have tried to use the early model of an inhomogeneous energy input on the surface induced by interference, to explain ripples generated by femtosecond laser pulses [WMF03]. However, this theory, in the way that is developed so far, has turned up to not be able to explain the formation of sub-wavelength ripples [BMS05].

The experiments presented here have shown that the laser generated surface ripples appear to be rather insensitive both to the laser wavelength and the angle of incidence. Furthermore, these 'non-classical' ripples form independently on the crystallographic structure, although they seem to be dependent on the material. Their periods indicate a correlation with the laser intensity and number of pulses. Although they can form as long parallel regular lines, in many places the lines appear to be intersecting and bifurcating. Such bifurcations often indicate symmetry breaking in typical non-linear dynamics induced periodic structures. Therefore, we have proposed to connect ripple formation to self-organization mechanisms of surface relaxation upon ablation [HVW99, CHR02, RCH02].

With the goal of extending the interpretation for laser-induced ripples to a more general picture of structures formed from instabilities, in the following subsections we attempt to describe a possible origin mechanism of the femtosecond laser-induced surface structures considering: (I) a surface instability; (II) a beam polarization ‘memorizer’; (III) a possible scenario.

(I) Surface morphology after sputtering with laser and ion beams

To account for a surface periodic modulation, we observe other morphological features which are born as an effect of surface relaxation from instabilities. Such instabilities are invoked, for instance, to explain self-organized surface ripples produced by ion beam sputtering (IBS). Figure 5.35 illustrates, for comparison, ripples produced by IBS and femtosecond laser pulses on different crystalline surfaces. Indeed, the shapes and periods of these ripples appear to be very similar.

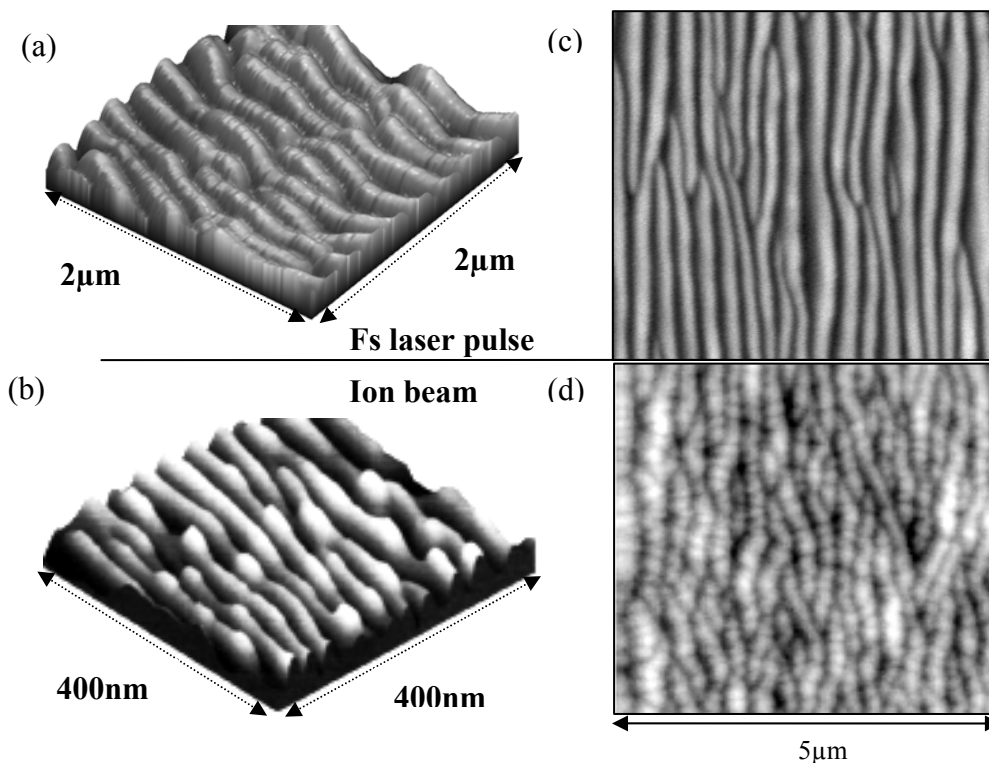


Figure 5.31. Shapes of surface ripples induced by fs-laser pulses on a $\text{BaF}_2(111)$ (a) and ion beam on a $\text{Ag}(001)$ [RCB99] (b). Periods comparable in size of ripples induced by fs-laser pulses on $\text{CaF}_2(111)$ and ion beam on $\text{Si}(001)$ [EAC00].

The mechanisms leading to particle ejection by laser pulses and energetic ion beams have often been connected [Sig92]. Also the appearance of the surface morphology subsequent to erosion has often been used to support this connection. The surface ripples formed by laser and ion beam sputtering (IBS) have many common characteristics (Table 5.3).

Table 5.3. The characteristics of surface ripples induced by (off-normal) ion beam sputtering, as reported in the literature, which resemble laser-induced ripples; the sections of this chapter where the corresponding laser-induced ripples characteristics have been discussed .

Ripples Characteristics: Similarities	Ion beam induced surface ripples	Reference	Laser induced ripples- in Section:
Period	~ 0.01-10 μm - depending on the sample temperature or the ion flux ⁵¹ ;	[UHC99]	5.2-5.5
Preferential direction	Align either parallel or perpendicular to the direction of the ion beam; also ripples change their orientation in the vicinity of a line defect.	[KHS97, HLK02, CMK94]	5.2.2/5.3.1
Irradiation dose	The ripples period depends on ions' energy and irradiation time.	[CMK94]	5.2.2.3/5.2.4
Positive feedback	Localized prominences at increased ion beam irradiation multiply and coalesce into stripes.	[EAC99]	5.2.2.3
Periodic modulation amplitude	It grows exponentially for short exposure times, but saturates after a typical crossover time has been reached.	[CEA01]	5.2.2.3
Additional morphological aspects	- eroded like shapes - bifurcations - dots and cones	[EAC99, GVC01, ErA97]	5.2-5.3

Here, we propose a similar mechanism at the origin of ripples formed by both processes. Thus, in the following we briefly describe the idea beneath the self-organized ripple formation by IBS.

Based on Sigmund's theoretical analysis of ion beam sputtering of solids [Sig73], Bradley and Harper [BrH88], and later on Cuerno et. al [CuB95], developed a model for the formation of self-organized surface periodic patterns induced by ion beams. The models are based on the assumption that the ion erosion rate depends on the surface initial

⁵¹ For instance, at high temperatures the ripple wavelength, l , depends on temperature following an Arrhenius law $l \sim (1/T)^2 \exp(\Delta E / kT)$ with ΔE being the activation energy.

morphology (curvature). If preferential surface erosion applies, then valleys and crests are expected to form⁵² [Sig73]. This instability increases exponentially in time and is counterbalanced by a competing smoothing effect provided by surface diffusion (or surface tension).

The microscopic picture of ion beam sputtering does not seem to apply to ripples generated by laser beams. However, it can be possible that the macroscopic picture is quite similar, since both are erosion processes.

(II) *Beam polarization ‘memorizer’*

Our experiments show that ripples orientation depends on the beam polarization. The processes responsible for ripples formation likely start during the laser pulse and last for a much longer time period until the surface relaxes. Therefore, it is crucial to search for a *beam polarization ‘memorizer’*. A possible candidate is a laser-excited surface electron plasma wave or surface plasmons.

As shown in the preceding chapters, intense femtosecond laser pulses induce ionization and free electron generation in the dielectric and semiconducting media. For laser intensities close to damage threshold (or many ablating pulses in dielectrics, cf. Chapter 3), the conduction band electron density can approach the plasma critical density, at least locally. The highly ionized dielectric or semiconducting material can exhibit metallic behavior, when the frequency of the laser field equalizes the plasma oscillation frequency.

A consequence of the Drude approximation is that, at the interaction with light, the free electron gas can sustain charge density oscillations. The charge density region can *propagate* inside the material like a wave (plasmon) oscillating at the plasma frequency.

⁵²In Sigmund’s theory, sputtering of random media results from a cascade of quasi-elastic collisions of moving target atoms. The general assumption is that the primary ion-target collision leads to further interaction involving the recoil target atoms. In its path through the target, the ion induces collisions with the target atoms, which may acquire enough energy to undergo further collisions or to leave the surface if they are located near it.

The energy distributed inside the bulk by an incident ion depends on the orientation of the surface. Here all its kinetic energy is released and spread out to the neighboring sites following a Gaussian distribution. The ion projectile delivers its energy upon impact within a superficial layer of thickness in the range of the ion penetration depth. From momentum consideration, a distribution of equidistant energy lines (contours) can be determined.

For an off-normal ion beam, depending on the surface curvature, different erosion rates should be expected at the valleys as compared to the crests.

Surface plasmon-polaritons (SPP) are electromagnetic modes that arise from the interaction between light and mobile *surface* charges, typically conduction band electrons. Since the SPP mode has a greater momentum than the light of the same frequency, it cannot propagate away from the surface, i.e. it is trapped within it. At an interface between two media, the SPP is bound to the surface and propagates until its energy is fully dissipated (in a metal, for instance, the SPP's energy is dissipated as heat). The SPP involves charges at the interface, which are sustained if the electric field at the interface changes signs. This implies that the relative dielectric constant ϵ (thus, the refractive index $n = \sqrt{\epsilon}$) of the two media should be opposite in sign. Figure 5.31 shows the oscillating nature of the surface charge distribution at the interface between two media. Also the SPP wavelength (period) λ_{SPP} , the separation between positions of equal charge on the surface, is indicated.

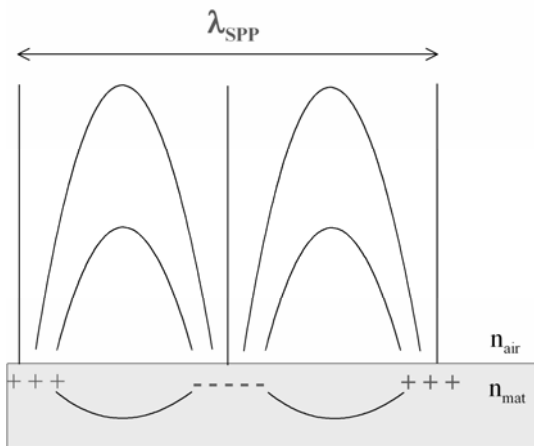


Figure 5.32. Surface charge distribution at an interface air-material associated with the SPP mode and indicating the SPP wavelength, λ_{SPP} [Bar06].

Usually SPP occurs at a dielectric-metal interface but also dielectric-semiconductor (silicon) interfaces have been reported to form SPP [BMB06]. The field strength of the SPP is shown to decay exponentially with the distance away from the surface [Bar06], reaching a maximum at the interface, a circumstance that makes SPP extremely sensitive to interface properties. The penetration depth depends on the wavelength of SPP. Also, it is known that the surface plasmons are excited by the femtosecond laser pulses at surface nano-

imperfections - nanoparticles or nanowires [CHT06]. The ripple pattern shown in Figure 5.3 (d) gives also an indication in this sense.

The laser excited surface plasma wave can propagate either parallel to the surface, in the direction of the projection of the laser electric field, or perpendicular to it.

The fact that a surface (electron) plasma wave can be excited by the laser impact and can contribute to ripple generation has been suggested from early times [BrE82, Kei83].

However, at those times only ripples of periods close to the laser wavelength could be observed. Then, the origin of these ripples was thought to be an interference of the plasma wave with the incident beam.

In a possible scenario, the plasma wave launched at the surface by the incident beam can contribute to the sub-wavelength ripple formation and dictate the ripples preferential direction with respect to the laser beam polarization. Thus, we can build, yet intuitively, a possible scenario.

(III) Possible scenario

Upon interaction of femtosecond laser pulses with non-metallic target, an electron surface

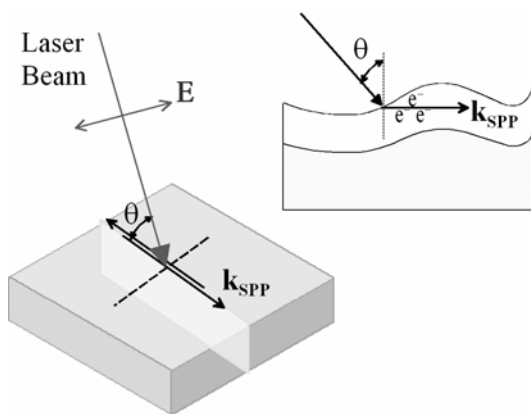


Figure 5.33. Schematic representation of the electric field component at the sample surface of the p-polarized beam; a surface plasma wave is launched at the surface. The interaction cross-section (in the right side) showing a local increase in the electron concentration on a corrugated surface layer.

plasma wave is launched parallel to the surface (see Figure 5.33). A fluctuation of electron density at the surface would trigger a fluctuation of laser-induced defect density.

Indeed, in [QKM00] it is shown that glass irradiated with femtosecond laser pulses develops a long-lifetime luminescence along the beam polarization direction. This was attributed to an anisotropic refractive index variation as an effect of an electron plasma wave.

In fact, this can appear from an anisotropic laser-induced surface defect distribution. As indicated in the preceding chapters, in fluoride materials, surface defects imply a local loss of charge. This can lead not

only to a local variation in the positive charge density but also to the formation of metallic bonds (colloids), the latter providing potentially a media suitable for surface plasmons generation.

Also, recently, an Auger spectroscopy analysis of sub-wavelength ripples on the surface of transparent materials [SKQ03], have revealed a modulated electron concentration variation, which was attributed to the formation of metallic bonds.

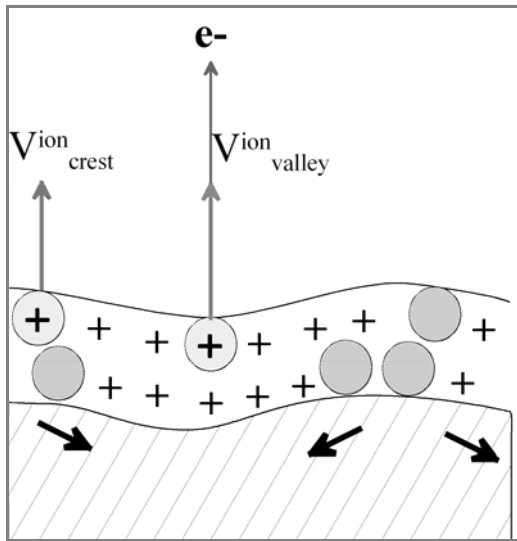


Figure 5.34. Sketch of a periodic surface this layer evolution after laser excitation and electron emission, with a distribution of positive charges and neutral particles. The thin arrows indicate the outward ion ejection, which is larger for the ions in the valleys than on the crests. The thick arrows indicate the counteracting effect of surface tension, which prevents the amplification of the corrugation.

If the electron plasma wave would, in effect, lead to a variation in the positive charge density along the laser polarization direction, we can envision that the ion desorption rate varies on the surface. Following the IBS macroscopic picture, we can draw a simple scenario as following:

1. An off-normal laser beam launches an electron plasma wave in the direction of its field; this would depend on the geometry of the surface asperities (Figure 5.33) and imply a local increase in absorption, thus a local variation in the electron density;
2. The electrons would be either trapped at defect sites or would be emitted out of the surface. In both cases, the positive ion formation would be favored.
3. Subsequently, assuming, e.g., surface ionization and Coulomb explosion as the possible ablation mechanism, each laser pulse contributes to building up a charge distribution at the surface (Figure 5.34).
4. Considering a corrugated surface, for positive ions sitting in a valley of a corrugation, the number of next neighbor positive charges is higher than for those on the crests. Thus, the ion desorption rate should be higher in the valleys as compared to the crests. This can lead potentially to a growing surface modulation.

Counteracting the emission of charged particles out of the surface, ions will diffuse from regions with higher density to lower density regions as in a smoothening effect.

Thus, at the surface, a competition between surface erosion due to the outward emission modulated by the electron plasma wave and ionic (surface) diffusion can well describe the unstable surface in IBS models.

Different attempts have been made so far to apply the IBS model to laser beam ablation. First results have been given by Georgescu et al. [Geo03]. A rate equation was used to describe the competition of the two processes: surface erosion due to particle emission and smoothing due to atomic self-diffusion.

An equation of a Kardar-Parisi-Zhang type [KPZ86] expresses the time evolution of the profile $h(x,y,t)$ of a growing surface by:

$$\frac{\partial h}{\partial t} = -v(h)\sqrt{1 + (\nabla h)^2} - D\Delta^2 h \quad (5.4)$$

The first term on the right-hand side describes the erosion velocity of a surface, $v(h)$, which depends on the surface curvature. The second term is the thermal self-diffusion. D depends on the surface diffusivity, the activation energy for surface self-diffusion, the surface density of diffusing atoms and temperature. In Georgescu's model, the Fresnel equations have been used to account for preferential orientation of the ripple pattern on the beam polarization. They were included in an equation similar to Eq. 5.4 to describe a local variation in the average energy deposited along the surface and erosion velocity.

So far, this model is very promising as it can potentially provide a large variety of ripple periods including those found in this work.

5.5. CONCLUSIONS

Plane polarized femtosecond laser beams can give rise to a self-assembly of coexisting periodic patterns on ablated dielectric and silicon surface. Ripples of period much smaller or much larger than the incident wavelength are generated after single or multiple pulses irradiation. Their characteristics deviate from the classical interference picture.

The beam polarization appears to act as a control parameter for ripple formation. A positive growth rate of ripples is assured by varying control parameters such as the laser intensity and the number of pulses. Also an evolution from order to disorder is identified, through coarsening or period doubling effects. After laser excitation the remaining unstable surface undergoes complex transformation as indicated by the observation of phase transformation of silicon. Morphological order to disorder transitions point to a growing instability at the origin of ripples formation.

From the complexity of mechanisms we selected those that might be responsible for the structures orientation on the beam polarization and surface relaxation phenomena. Our interpretation tries to connect the laser-induced ripples with periodic structures formed from instabilities. In a possible scenario, in an outer layer a modulated charge or defect density may contribute to preferential erosion counterbalanced by atomic surface diffusion. This picture, if holds, may lead to the formation of structures of periods much smaller than the incident laser wavelength.

CHAPTER 6

GENERAL CONCLUSIONS AND OUTLOOK

This thesis addresses a whole range of phenomena which occur at the interaction of femtosecond laser pulses with different materials, by employing various experimental techniques. Different experiments are designed to explain fundamental processes of laser absorption and electronic excitation, transient modification of the lattice, charged particle desorption and surface morphological changes at the nanometer scale. This work was directed to the investigation of such effects at the interaction of laser radiation with wide bandgap dielectrics. Further, for comparison, the research was extended to different other materials.

The experiments on the kinetics of emitted charged particles from dielectric targets have indicated that the lattice response to the initial laser excitation greatly depends on the irradiation dose (intensity and number of pulses). We studied the surface change after the repetitive laser pulse interaction, employing intensities below the damage threshold for a single pulse.

Under these irradiation conditions, the ionization processes can be described at best by multiphoton ionization and ionization at defects sites.

The structural defects play a crucial role in providing the means for an increased positive ion desorption rate. The incubation effect in the ion yield can be well-coupled to the effect of reduction of the multi-shot damage threshold with increasing intensity. We have advanced a possible explanation of the sudden increase and ‘saturation’ of the ion yield with the number of pulses, by suggesting that defects with lifetime of about 1ms can provide, in our irradiation conditions, a pulse-by-pulse increase in the free electron density.

By using this assumption, a threshold-like behavior for the incubation effect could be derived.

The kinetics of the charged particle emission is dependent of the irradiation dose. Thus, at intensities below the damage threshold, following the initial electron excitation and emission, positive ions are released from the surface in a substantial amount. Their ion velocities are high, with a narrow distribution, indicative of a localized microscopic electrostatic expulsion. With increasing intensity, the amount of ions gets larger and larger and their velocity distribution exhibit bimodal structure. Also, in these conditions, negative ions are better distinguishable. To elucidate the microscopic mechanisms of desorption, we suggest that a combination of localized electrostatic repulsion, macroscopic Coulomb explosion and also a thermal ‘explosive’ mechanism can concur. This is also based on the observation that the kinetics of ion emission from silicon is very similar, indicating also that energetic ions could be emitted in quite similar conditions. Further work is necessary to clearly separate these mechanisms and identify their connection.

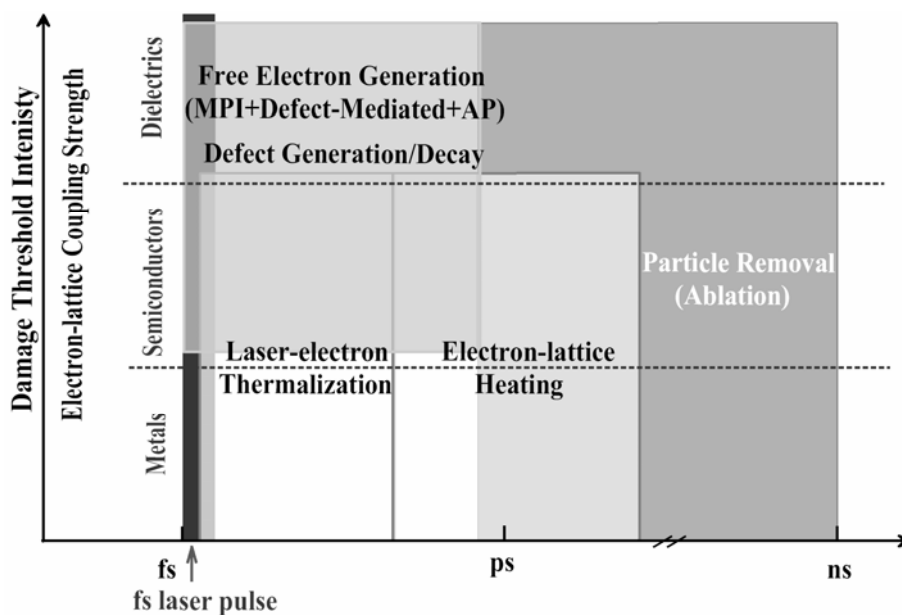


Figure 6.1. Timescales of femtosecond laser ablation dynamics indicated from results of the pump-probe experiments included in this work.

The temporal evolution of lattice dynamics upon single pulse excitation was analyzed by pump-probe experiments using the ion emission. Employing this technique on many

different target materials, we could study the timescale for the lattice deformation in response to the excitation. This deformation is indicated to be a material characteristic, manifesting itself as a generation of transient defects in dielectrics or fast phase transitions in silicon and aluminum. Thus, our results propose a sensitive method for measurements of the lifetime of transient defect states or electron-phonon relaxation times. Figure 6.21 brings together, processes induced by femtosecond laser pulse in different materials at the timescales provided by the results included in this work.

Further, we investigated the surface morphology after ablation, in particular, surface periodic patterns. The patterns observed seem to be very different from the ripples found ‘classically’ upon long pulse ablation. Dependent on the material (here fluorides on one hand and silicon on the other hand), several patterns were found on the irradiated surface. They can reach periods much smaller than the incident wavelength and are rather insensitive to the variation of the laser wavelength and angle of incidence. We show that control factors are laser beam polarization and irradiation dose (i.e. a concurrence of intensity and number of pulses). For silicon we also show that there is a close connection with the disorder induced by transformation into new crystalline phases. The reason for the formation of these sub-wavelength structure remains still to be elucidated, whether there is an inhomogeneous energy input on the surface (e.g. connected with a surface electron plasma wave), or an effect of surface self-organization upon relaxation from the non-equilibrium conditions of ablation, or both.

An investigation of the timescales for the formation of these structures is required to identify the mechanism responsible for the ripple formation. Also a better knowledge of the underlying mechanisms could help to control the formation and characteristics of such patterns and thus provide a complementary method to lithography for obtaining sub-100-nm (sub-wavelength) surface structures.

APPENDIX A

At atmospheric pressure silicon has a cubic diamond structure (labeled Si-I) up to its melting point. Compression and de-compression of silicon is known to lead to a transition to different crystalline phases. At elevated pressures, 11 other crystalline phases of Si have been identified from pressure cell experiments (see [DoG02] and references therein).

The crystalline phases of silicon found in laser ablation experiments are labeled as follows: Si-III (*bc8*: body-centered cubic structure with 8 atoms per cubic cell); Si-IV (*hd*: hexagonal diamond structure); Si-XII (*r8*, rhombohedral structure with 8 atoms per unit cell), and the amorphous phase [DoG02].

Si-XII is known to occur under a pressure load of 10-12 GPa is required and transform into Si(III) phase [KGN97].

It is evident that the occurrence of such phases, would imply a high local pressure induce by the laser pulse in the silicon material.

Table A.1 Wavenumber of Raman bands preliminarily assigned to different phases of silicon [KGN97].

Wavenumber (cm ⁻³)	Si-phase	Crystalline structure
150 (broad)	-	amorphous
161; 180	Si III/Si XII	bc8 / r8
300	Si I (2TA)	cubic diamond
350	Si XII	r8
382	Si III (TA)	bc8
394	Si XII	r8
412	Si III	bc8
430	Si III	bc8
470 (broad)	-	amorphous
505-515	Si IV or Si I	hexagonal(wurtzite) or nano-crystalline cubic diamond
521	Si I (TO)	cubic diamond

REFERENCES

- [ACD92] D. Arnold, E. Cartier, and D.J. DiMaria, Phys. Rev. B **49**, 10278 (1994).
- [ACI99] Y.U. Afanasiev, B.N.Chichkov, V.A. Isanov, A.P. Kanavin, and S.A. Uryupin, J. of Russ. Laser Res. **20**, 189 (1999).
- [ADD94] P. Audebert, Ph. Daguzan, A. Dos Santos, J.C. Gauthier, J.P. Geindre, S. Guizard, G. Hamoniaux, K. Krastev, P. Martin, G. Petite, and A. Antonetti, Phys. Rev. Lett. **73**, 1990 (1994).
- [ADL96] G. Allan, S. Delerue, and M. Lannoo, Phys. Rev. Lett. **76**, 2961 (1996).
- [AFP79] P. Agostini, F. Fabre, G. Manfray, G. Petite, and N. Rahman, Phys. Rev. Lett. **42**, 1127 (1979).
- [AgP88] P. Agostini and G. Petite, Comtemp. Phys. **29**, 57 (1988).
- [AKL87] P. Agostini, J. Kuperszytch, L.A. Lompre, G. Petite, and F. Yergeau, Phys. Rev. A **36**, 4111 (1987).
- [AKP74] S. I. Anisimov, B. L. Kapeliovich, T. L. Perel'man, Sov. Phys. JETP **39**, 375 (1974).
- [ALR99] D. Ashkenasi, A. Rosenfeld, H. Varel, M. Wahmer, and E.E.B. Campbell; Appl. Surf. Sci. **120**, 65 (1997); D. Ashkensi, M. Lorenz, R. Stoian, and A. Rosenfeld, Appl. Surf. Sci. **101-106**, 150 (1999).
- [ApH00] T. Apostolova and Y. Hahn, J. Appl. Phys. **88**, 1024 (2000).
- [AsM76] N. Ashcroft and N. Mermin, *Solid State Physics*, Saunders College Publishing, 1976.
- [ASR00] D. Ashkenasi, R. Stoian, and A. Rosenfeld, Appl. Surf. Sci. **154-155**, 40 (2000).
- [AWA00] S. Amoruso, X. Wang, C. Altucci, C. de Lisio, M. Armenante, R. Bruzesse, and R. Velotta, Appl. Phys. Lett. **77**, 3728 (2000).
- [Bar06] W.L.Barnes, J. Appl. Opt. A: Pure Appl. **8**, S87 (2006).
- [BBK02] J. Bonse, S. Baudach, J. Krüger, W. Kautek, and M. Lenzner, Appl. Phys. A **74**, 19 (2002).
- [BBM04] J. Bonse, K.-W. Brzezinka, and A.J. Meixner, Appl. Surf. Sci. **221**, 215 (2004).
- [Bir65] M. Birnbaum, J. Appl. Phys. **36**, 3688 (1965).
- [BJH00] K.M. Beck, A.G. Joly, W.P. Hess, Surf. Sci. **451**, 166 (2000).
- [Blo74] N. Bloembergen, IEEE J. Quantum Electron. **QE-10**, 375 (1974).
- [BMB06] M.I.Bakunov, A.V.Maslov, and V. Bodrov, J. Appl. Phys. **100**, 026106 (2006).
- [BMS05] J. Bonse, M. Munz, and H. Sturm, J. Appl. Phys. **97**, 013538 (2005).
- [BMT94] A. Barborica, I.N. Mihailescu, V.S. Teodorescu, Phys. Rev. B **49**, 8385 (1994).
- [BoH03] A. Borowiec and H.K. Haugen, Appl. Phys. Lett. **82**, 4462 (2003).
- [BoL92] M. Bolle and S. Lazare, J. Appl. Phys. **73**, 3516 (1993).
- [BOM04] A.V. Bulgakov, I. Ozerov, W. Marine, Appl. Phys. A **79**, 1591 (2004).
- [BrE82] S.R.J. Brueck and D.J. Ehrlich, Phys. Rev. Lett. **48**, 1678 (1982).
- [BrH88] R. M. Bradley and J.M.E. Harper, J. Vac. Sci. Technol. **A6**, 2390 (1988).
- [BrK00] T. Brabec and F. Krausz, Rev. Mod. Phys. **72**, 545 (2000).
- [BSR04] N.M. Bulgakova, R. Stoian, A. Rosenfeld, I.V. Hertel, and E.E.B. Campbell, Phys. Rev. B **69**, 054102 (2004).
- [BSR05] N.M. Bulgakova, R. Stoian, A. Rosenfeld, I.V. Hertel, W. Marine, E.E.B. Campbell, Appl. Phys. A **81**, 345 (2005).
- [BSR99] R. Bennowitz, D. Smith, and M. Reichling, Phys. Rev. B **59**, 8237 (1999).
- [BWJ82] M.F. Becker, R.M. Walser, J.K. Jhee, and D.Y. Sheng, Proc. Soc. Photo-Opt. Instrum. Eng. **322**, 93 (1982)
- [CBB89] P.B. Corkum, N.H. Burnet, and F. Brunel, Phys. Rev. Lett. **62**, 1259 (1989).
- [CBS88] P. B. Corkum, F. Brunel, N.K. Sherman, and T. Srinivasan-Rao, Phys. Rev. Lett **61**, 2886 (1988).
- [CCL05] L. P. Cramer, T.D. Cumby, J.A. Leraas, S.C. Langford, and J.T. Dickinson, J. Appl. Phys. **97**, 103533 (2005).
- [CER06] F. Costache, S. Eckert, and J. Reif, Appl. Surf. Sci. **252**, 4416 (2006).

- [ChG02] T. Choi and C.P. Grigoropoulos, *J. Appl. Phys.* **92**, 4918 (2002).
- [ChG97] H. Cheng and J.D. Gillaspay, *Phys. Rev. B.* **55**, 2628 (1997).
- [CHK75] P.J. Call, W. Hayes, and M.N. Kabler, *J. Phys. C* **8**, L60 (1975).
- [CHR02] F. Costache, M. Henyk, and J. Reif, *Appl. Surf. Sci.* **186**, 352 (2002);
- [CHR03] F. Costache, M. Henyk, and J. Reif, *Appl. Surf. Sci.* **208-209**, 486 (2003).
- [CHT06] L.I. Chelaru, M. Horn-von Hoegen, D. Thien, and F.-J Meyer zu Heringdorf, *Phys. Rev. B* **73**, 115416 (2006).
- [CKR04] F. Costache, S. Kouteva-Arguirova, and J. Reif, *Appl. Phys. A* **79**, 1429 (2004).
- [CKM97] E. E. B. Campbell, R. Kelly, G. Marleta, and M. Tuolemond, *Nucl. Instr. Meth. B* **122**, 65 (1997).
- [CIE89] S. E. Clark and D. C. Emmony, *Phys. Rev. B* **40**, 2031 (1989).
- [CMB01] M. Csete, O. Marti, and Zs. Bor, *Appl. Phys. A* **73**, 521 (2001).
- [CMK94] E. Chason, T. M. Mayer, B. K. Kellerman, D. T. McIlroy, and A. J. Howard, *Phys. Rev.* **72**, 3040 (1994).
- [CMT95] R. Cuerno, H.A. Makse, S. Tomassone, S.T. Harrington, and H. Eugene Stanley, *Phys. Rev.* **24**, 4464 (1995).
- [Cor93] P.B. Corkum, *Phys. Rev. Lett.* **71**, 1994 (1993).
- [CSB99] A. Cavalleri, K. Sokolowski-Tinten, J. Bialkowski, M. Schreiner, and D. Von der Linde, *J. App. Phys.* **85**, 3301 (1999).
- [CuB95] R. Cuerno and A.-L. Barabási, *Phys. Rev. Lett.* **74**, 4746 (1995).
- [DCD93] A.T. Davidson, J.D. Comins, T.E. Derry and A.M. J. Raphuthi, *Phys. Rev. B* **48**, 782 (1993).
- [DLK94] D. Du, X.Liu, G. Korn, J. Squier, and G. Mourou, *Appl. Phys. Lett.* **64**, 3071 (1994).
- [DJW93] J.T. Dickinson, L.C. Jensen, R.L. Webb, M.L. Dawes, and S.C. Langford, *J. Appl. Phys.* **74**, 3758 (1993).
- [DLS94] J.T. Dickinson, S.C. Langford, and J.J. Shin, *Phys. Rev. Lett.* **73**, 2630 (1994); J.T. Dickinson, J.J. Shin, and S.C. Langford, *Appl. Surf. Sci.* **96-98**, 316 (1996).
- [DoG02] V. Domnich and Y. Gogotsi, *Rev. Adv. Mater. Sci.* **3**, 1 (2002).
- [DSY82] H.M. van Driel, J.E. Sipe, and J.F. Young, *Phys. Rev. Lett.* **49**, 1955 (1982).
- [EAC99] J. Erlebacher, M.J. Aziz, E. Chason, M.B. Sinclair, and J. A. Floro, *Phys. Rev. Lett.* **82**, 2330 (1999).
- [Eck06] S. Eckert, ‘*Dynamics of femtosecond laser ablation from dielectrics*’, Diploma Thesis, Cottbus, 2006.
- [EGP85] H.J. Eichler, P. Günter, and D.W. Pohl, *Laser-Induced Dynamic Gratings*, Springer-Verlag, Berlin, 1985.
- [EIL97] J. W. Elam and D.H. Levy, *J. Appl. Phys.* **81**, 539 (1997).
- [EMS00] K. Eidmann, J. Meyer-ter-Vehn, and T. Schlegel, *Phys. Rev. E* **62**, 1202 (2000).
- [ErA97] J.D. Erlebacher and M.J. Aziz, *Mat. Res. Soc. Symp. Proc.* **440**, 461 (1997).
- [EBT82] D.J. Ehrlich, S.R.J. Brueck, and J.Y. Tsao, *Appl. Phys. Lett.* **41**, 630 (1982).
- [FaS83] P.M. Fauchet and A. E. Siegman, *Appl. Phys. A* **32**, 135 (1983).
- [FFH01] D. Fisher, M. Fraenkel, Z. Henis, E. Moshe, and S. Eliezer, *Phys. Rev. E* **65**, 016409 (2001).
- [FMB86] R.R. Freeman, T.J. McIlrath, P.H. Bucksbaum, and M. Bashkansky, *Phys. Rev. Lett.* **57**, 3156 (1986).
- [GDD96] S. Guizard, P. D'Oliveira, P. Daguzan, P. Martin, P. Meynardier, and G. Petite, *Nucl. Instr. Meth. Phys. B* **116**, 43 (1996).
- [Gen03] F. Génin (ed.); Special Issue *Femtosecond Techniques for Materials Processing*, *Appl. Phys. A* **76**, 299 (2003).
- [Geo03] I. Georgescu ‘*Pattern formation upon femtosecond laser ablation of transparent dielectrics*’, Diploma Thesis, BTU Cottbus, 2003.
- [GFS82] Z. Guosheng, P.M. Fauchet, and A.E. Siegman, *Phys. Rev. B* **26**, 5366 (1982).
- [GiG95] J.P. Girardeau-Montaut and C. Girardeau-Montaut, *Phys. Rev. B* **51**, 13560 (1995).
- [GiS97] G.K. Giust and T.W. Sigmon, *Appl. Phys. Lett.* **70**, 3552 (1997).

- [GNA02] L. Gallais, J.Y. Natoli, and C. Amra, *Opt. Exp.* **10**, 1465 (2002).
- [GoP94] J.R. Goldman and J.A. Prybyla, *Phys. Rev. Lett.* **72**, 1364 (1994).
- [GRL00] C. Guo, G. Rodriguez, A. Lobad, and A.J. Taylor, *Phys. Rev. Lett.* **84**, 4493 (2000).
- [GRT02] E.G. Gamaly, A.V. Rode, V.T. Tikhonchuk, and B. Luther-Davies, *Phys. Plasmas* **9**, 949 (2002).
- [GVC01] R. Gago, L. Vazquez, R. Cuerno, M. Varela, C. Ballestreros, and J. M. Albella, *Appl. Phys. Lett.* **78**, 3316 (2001).
- [HaK92] R. F. Haglund and R. Kelly in: *Fundamental processes in sputtering of atoms and molecules*, Ed. P. Sigmund, Vol. 43, *Math. Fys. Medd. Dan. Vid. Selsk. Copenhagen*, p. 527, 1992.
- [HaL02] S. Habenicht and K. P. Lieb, *Phys. Rev. B.* **65**, 2002, 115327.
- [HCR02] M. Henyk, F. Costache, and J. Reif, *Appl. Surf. Sci.* **186**, 357 (2002); M. Henyk, F. Costache, and J. Reif, *Appl. Surf. Sci.* **197-198**, 90 (2002).
- [Hen03] M. Henyk, *Partikelemission bei der Ablation dielektrischer Materialien mit ultrakurzen Laserpulsen*, PhD Thesis, Cottbus, 2003.
- [HEH01] J.L. Hansen, M. van Ecke, A. Haaning, C. Ellegard, K.H. Andersen, T. Bohr, and T. Sahms., *Nature* **410** (2001) 324.
- [HeR03] M. Henyk and J. Reif, *Appl. Surf. Sci.* **208-209**, 71 (2003).
- [HFW98] Tsing-Hua Her, R. J. Finlay, C. Wu, S. Deliwala, *Appl. Phys. Lett.* **73**, 1673 (1998).
- [HJB99] W.P. Hess, A.G. Jolly, K.M. Beck, R.M. Williams, and J.T. Dickinson, *Appl. Phys. A* **69**, S389 (1999).
- [HKG98] L. Huang, J.P. Callan, E.N. Glezer, and E. Mazur, *Phys. Rev. Lett.* **80**, 185 (1998).
- [HLK02] S. Habenicht, K.P. Lieb, J. Koch, and A.D. Wieck; *Phys. Rev. B.* **65**, 115327 (2002).
- [HLM92] A. L-Huillier, L.A. Lompré, G- Mainfray, and C. Manus in: *Atoms in Intense laser Fields*, Ed. M. Gavrilu, Academic, New York, p. 139, 1992.
- [HMW00] M. Henyk, R. Mitzner, D. Wolframm, and J. Reif, *Appl. Surf. Sci.* **154-155**, 249 (2000).
- [HoF74] L.H. Holway, Jr. and D.W. Fradin, *J. Appl. Phys.* **46**, 279 (1974).
- [HON92] K. Hattori, A. Okano, Y. Nakai, and N. Itoh, *Phys. Rev. B* **45**, 8424 (1992).
- [HRM97] M. Huisinga, M.Reichling, and E. Matthias, *Phys. Rev. B* **55**, 7600 (1997).
- [HuK97] S. Hughes and T. Kobayashi, *Semicond. Sci. Technol.* **12**, 733 (1997).
- [HVD99] M. Henyk, N. Vogel, D. Wolframm, A. Tempel, and J. Reif, *Appl. Phys. A* **69**, 355 (1999).
- [HWG00] J. Hohlfeld, S.-S. Wellershoff, J. Güdde, U. Conrad, V. Jähnke, and E. Matthias, *Chem. Phys.* **251**, 237 (2000).
- [HWR00] M. Henyk, D. Wolframm, and J. Reif, *Appl. Surf. Sci.* **168**, 263 (2000); M. Henyk, D. Wolframm, and J. Reif, *Nucl. Instr. Meth. B* **166-167**, 716 (2000).
- [Ise77] N.R. Isenor, *Appl. Phys. Lett.* **31**, 148 (1977).
- [Ito95] N. Itoh, *Pure and Appl. Chem.* **67**, 419 (1995).
- [ItT86] N. Itoh and K. Tanimura, *Rad. Eff.* **98**, 269 (1986).
- [JBC89] S. C. Jones, B. Braunlich, T. R. Casper, X. Shen, P. Kelly, *Opt. Eng.* **28**, 1039 (1989).
- [JBW88] Y. Jee, M.F. Becker, R.M. Walser, *J. Opt. Am. B.* **5**, 648 (1988).
- [JCH06] T.Q. Jia, H.X. Chen, M. Huang, F.L. Zhao, X.X. Li, S.Z. Xu, H.Y. Sun, D.H. Feng, C.B. Li, X.F. Wang, R.X. Li, Z.Z. Xu, X.K. He, and H. Kuroda, *Phys. Rev. B* **73**, 054105 (2006).
- [JCZ00] T. Jia, H. Chen, and Y. Zhang, *Phys. Rev. B* **61**, 16522 (2000).
- [JGB01] H. O. Jeschke, M.E. Garcia, and K. H. Benemann, *Phys. Rev. Lett.* **87**, 015003 (2001); H.O. Jeschke, M.E. Garcia, and K.H. Bennemann, *J. Appl. Phys.* **91**, 18 (2002); H.O. Jeschke, M.E.Garcia, and K.H. Bennemann, *Appl. Phys. A* **69**, S49-S53 (1999)
- [JGL02] H. O. Jeschke, M. E. Garcia, M. Lenzner, J. Bonse, J. Krüger, W. Kautek, *Appl. Surf. Sci.* **197-198**, 839 (2002).
- [JGS95] H. Johansen, S. Gogoll, E. Stenzel, M. Reichling, and E. Matthias, *Rad. Eff. and Def. in Solids* **136**, 151 (1995).

- [JHB02] A.G. Joly, W.P. Hess, K.M. Beck, and J.T. Dickinson, *Appl. Surf. Sci.* **186**, 339 (2002).
- [JJM95] A.L. Johnson, S.A. Joyce, and T.E. Madey, *Phys. Rev. Lett.* **61**, 19 (1988); M. Pertavic and J.S. Williams, *J. Vac. Sci. Technol. A* **13**, 26 (1995).
- [JXL03] T.Q. Jia, Z.Z. Xu, X.X. Li, R.X. Li, B. Shuai, and F.L. Zhao, *Appl. Phys. Lett.* **82**, 4382 (2003).
- [KAE00] F. Korte, S. Adams, A. Egbert, C. Fallnich, A. Ostendorf, S. Nolte, M. Will, J.-P. Ruske, B.N. Chichkov, and A. Tünnermann, *Optics Express* **7**, 41 (2000).
- [KAW03] S. Kouteva-Arguirova, Tz. Arguirov, D. Wolframm, and J. Reif, *J. Appl. Phys.* **94**, 4946 (2003).
- [KeB82] F. Keilmann and Y. H. Bai, *Appl. Phys. A* **29**, 9 (1982).
- [KeD88] R. Kelly and R.W. Dreyfus, *Nucl. Instr. and Meth. in Phys. Res.* **B32**, 341 (1988).
- [Kei83] F. Keilmann, *Phys. Rev. Lett.* **51**, 2097(1983).
- [Kel65] L.V. Keldysh, *Sov. Phys. JETP* **20**, 1307 (1965).
- [KeM96] R. Kelly and A. Miotello, *Appl. Surf. Sci.* **96-08**, 205 (1996).
- [KeM97] R. Kelly and A. Miotello, *Nucl. Instr. and Meth.* **122**, 374 (1997).
- [KGN97] A. Kailer, Y.G. Gogotsi, and K.G. Nickel, *J. Appl. Phys.* **81**, 3057 (1997)
- [KHM86] U.O. Karlsson, F.J. Himpsel, J. F. Mora, F.R. McFeely, D. Rieger, and J. A. Yarmoff, *Phys. Rev. Lett.* **57**, 1247 (1986).
- [KHS97] I. Koponen, M. Hautala, and O.-P. Sievänen, *Phys. Rev. Lett.* **78**, 2612 (1997).
- [Kit56] C. Kittel, *Introduction to Solid State Physics*, Wiley, New York, 1956.
- [KJR79] M.L. Knotek, V.O. Jones, and V. Rehn, *Phys. Rev. Lett.* **43**, 300 (1979).
- [KKL96] W. Kautek, J. Krüger, M. Lenzner, S. Sartania, C. Spielmann, and F. Krausz, *Appl. Phys. Lett.* **69**, 3146 (1996).
- [KMM 98] R. Kelly, A. Miotello, A. Melle, and A.G. Guidoni in: *Laser ablation and desorption* Eds. J.C. Miller and R.F. Haglund, Vol 30, Academic Press, San Diego, p. 225, 1998.
- [KnF78] M.L. Knotek and P.J. Feibelman, *Phys. Rev. Lett.* **40**, 964 (1978).
- [KoS76] J.C. Koo and R.E. Slusher, *Appl. Phys. Lett.* **28**, 614 (1976).
- [KOS03] S. Kouteva-Arguirova, V. Orlov, W. Seifert, H. Richter, and J. Reif, *Solid State Phenomena* **95-96**, 513 (2003); S. Kouteva-Arguirova, V. Orlov, W. Seifert, H. Richter, and J. Reif, *Solid State Phenomena* **95-96**, 513-518 (2004).
- [KrK99] J. Krüger and W. Kautek, *Appl. Surf. Sci.* **96-98**, 430 (1999).
- [KRV00] A. Kaiser, B. Rethfeld, M. Vicanek, and G. Simon, *Phys. Rev. B* **61**, 11437 (2000).
- [KSI98] A.P. Kanavin, I.V. Smetanin, V.A. Isakov, Yu. V. Afanasiev, B. N. Chichkov, B. Wellegehausen, S. Nolte, C. Momma, and A. Tünnermann, *Phys. Rev. B* **57**, 14698 (1998).
- [KPZ86] M. Kardar, G. Parisi, J.C. Zahng, , *Phys. Rev. Lett.* **56**, 889 (1986).
- [KZW01] A. Yu. Kobitski, K.S. Zhuravlev, H.P. Wagner, and D.R.T. Zahn, *Phys. Rev. B* **63**, 115423 (2001).
- [LaL80] L.D. Landau and L.M. Lifshitz, *Statistical Physics*, Pergamon Press, Oxford, 1980.
- [LeG85] K.-T. Lee and T. F. George, *Phys. Rev. B* **31**, 5106 (1985).
- [LFG98] H. Loesel, J.P. Fischer, M.H. Götz, C. Horvath, T. Juhasz, F. Noack, N. Suhm, and J.F. Bille, *Appl. Phys. B* **66**, 121 (1998).
- [LFP00] D.H. Lowdnes, J.D. Fowles, and A.J. Pedraza, *Appl. Surf. Sci.* **154-155**, 647 (2000).
- [LKS98] M. Lenzner, J. Krüger, S. Sartania, Z. Cheng, Ch. Spielmann, G. Mourou, W. Kautek, and F. Krausz, *Phys. Rev. Lett.* **80**, 4076 (1998).
- [LLM03] P. Lorazo, L.J. Lewis, and M. Meunier, *Phys. Rev. Lett.* **91**, 225502 (2003).
- [LMG02] F. Ladieu, Ph. Martin, and S. Guizard, *Appl. Phys. Lett.* **81**, 957 (2002).
- [LMM02] Q. Lu, S.S. Mao, X. Mao, and R.E. Russo, *Appl. Phys. Lett.* **80**, 3072 (2002).
- [LMN99] M. Li, S. Menon, J.P. Nibarger, and G.N. Gibson, *Phys. Rev. Lett.* **82**, 2394 (1999).
- [LSJ97] I. Last, I. Schek, and J. Jortner, *J. Chem. Phys.* **107**, 6685 (1997).
- [LWR01] R. Lindner, R.T. Williams, M. Reichling, *Phys. Rev. B* **63**, 0751108 (2001).
- [Mar83] M.M. Martynyuk, *Russ. J. Phys. Chem.* **57**, 494 (1983).

- [MBP04] W. Marine, N.M. Bulgakova, L. Patrone, and I. Ozerov, *Appl. Phys. A* **79**, 771 (2004).
- [MeG64] D. Menzel and R. Gomer, *J. Chem. Phys.* **41**, 3311 (1964).
- [MHL03] S. Martin, A. Hertwig, M. Lenzner, J. Krüger, and W. Kautek, *Appl. Phys. A* **77**, 883 (2003).
- [MiK99] A. Miotello and R. Kelly, *Appl. Phys. A* **69**, S67 (1999).
- [MJG00] M.E. Garcia, H.O. Jeschke, I. Grigorenko, and K.H. Benemann *Appl. Phys. B.* **71**, 361 (2000).
- [MTA92] P. Martin, R. Trainham, P. Agostini, and G. Petite, *Phys. Rev. B.* **45**, 69 (1992).
- [MTT03] Ch. Mühling, W. Triebel, G. Töpfer, A. Jordanov, *Proc. of SPIE* **4932**, 458-466 (2003).
- [Nie95] M.H. Niemz, *Appl. Phys. Lett.* **66**, 1181 (1995).
- [NMJ97] S. Nolte, C. Momma, H. Jacobs, A. Tünnermann, B.N. Chichkov, B. Wellegehausen, and H. Welling, *J. Opt. Soc. Am. B* **14**, 2716 (1997).
- [NoL88] I. NoorBatcha, R.R. Lucchese, and Y. Zeiri, *J. Chem. Phys.* **86**, 5251 (1988).
- [OEK03] H. Ono, A. Emoto, N. Kawatsuki, T. Hasegawa, *Appl. Phys. Lett.* **82**, 1359 (2003).
- [OMR99] A.M. Ozkan, A.P. Malshe, T.A. Ralihar, W.D. Brown, M.D. Shirk, and P.A. Molian, *Appl. Phys. Lett.* **75**, 3716 (1999).
- [OSN92] T. Okada, N. Shibamaru, Y. Nakayama, and M. Maeda, *Appl. Phys. Lett.* **60**, 941 (1992).
- [OtG93] C.E. Otis and P.M. Goodwin, *J. Appl. Phys.* **73**, 1957 (1993).
- [Pei92] H.O. Peitgen, H. Jürgens, and D. Saupe, *Chaos and fractals*, Springer-Verlag New York, 1992.
- [PER89] S. Petzoldt, A.P. Elg, J. Reif, and E. Matthias, *Proc. of SPIE* **1438**, 180 (1989); S. Petzoldt, A.P. Elg, J. Reif, and E. Matthias, in: H.E. Bennett, A.H. Guenther, B.E. Newnam, M.J. Soileau (Eds.), *Laser Induced Damage in Optical Materials*, NIST Special Publication **775**, 133 (1989).
- [PFG03] A.J. Pedraza, J.D. Fowlkes, Y.-F. Guan, *Appl. Phys. A* **77**, 2 (2003).
- [PFL00] A.J. Pedraza, J.D. Fowlkes, and D.H. Lowndes, *Appl. Phys. Lett.* **77**, 3018 (2000).
- [PGH99] A.A. Puretzky, D.B. Geohegan, G.B. Hurst, M.V. Buchanan, and B.S. Luk'yanchuk, *Phys. Rev. Lett.* **83**, 444 (1999).
- [PGM99] G. Petite, S. Guizard, P. Martin, and F. Quéré, *Phys. Rev. Lett.* **83**, 2189 (1999)
- [PoC98] L. Poth and A.W. Castleman Jr., *J. Phys. Chem. A* **102**, 4075 (1998).
- [Pou72] G.M. Pound, *J. Phys. Chem. Ref. Data* **1**, 135 (1972).
- [PuM96] A. Pukhov and J. Meyer-ter-Vehn, *Phys. Rev. Lett.* **76**, 3975 (1996).
- [PVH98] P.P. Pronko, P.A. VanRompay, C. Horvath, F. Loesel, T. Juhasz, X. Liu, and G. Mourou, *Phys. Rev. B* **58**, 2387 (1998).
- [QGP01] F. Quéré, S. Guizard, and P. Martin, *Europhys. Lett.* **56**, 138 (2001).
- [QKM00] J. Qiu, P.G. Kasannski, J. Si, K. Miura, and T. Mitsuyu, *Appl. Phys. Lett.* **77**, 1940 (2000).
- [RCE04] J. Reif, F. Costache, S. Eckert, S. Kouteva-Arguirova, M. Bestehorn, I. Georgescu, A.F. Semerok, P. Martin, O. Gobert, W. Seifert: *Proc. SPIE* **5662**, 737 (2004).
- [RCH02] J. Reif, F. Costache, M. Henyk, S.V. Pandelov, *Appl. Surf. Sci.* **197-198**, 891 (2002).
- [Red64] P.A. Redhead, *Can. J. Phys.* **42**, 886 (1964).
- [Rei89] J. Reif, *Opt. Eng.* **28**, 1122 (1989).
- [RHO98] M. Reichling, M. Huisinga, D. Ochs, and V. Kempter, *Surf. Sci.* **402-404**, 145 (1998).
- [RJV03] W.G. Roeterdink, L.B.F. Juurlink, O.P.H. Vaughan, J.Dura Diez, M. Bonn, and A.W. Kleyn, *Appl. Phys. Lett.* **82**, 4190 (2003).
- [Rub72] G.W. Rubloff, *Phys. Rev. B* **5**, 662 (1972).
- [Rus99] S. Rusponi, et.al. *Appl. Phys. Lett.* **75**, (1999) 3318.
- [RWM88] A. Rosen, E. Westin, E. Matthias, H. B. Nielsen, and J. Reif, *Physica Scripta* **T23**, 184 (1988).
- [SAP94] R. Serna, C.N. Alfonso, A.K. Petford-Long, and N.J. Long, *Appl. Phys. A* **58**, 197 (1994).

- [SAR00] R. Stoian, D. Ashkenasi, A. Rosenfeld, and E.E.B. Campbell, *Phys. Rev. B* **62**, 13167 (2000).
- [SAP98] P.L. Silvestrelli, A. Alavi, M. Parrinello, and D. Frenkel, *Phys. Rev. Lett.* **77**, 3149 (1998)].
- [SBC98] K. Sokolowski-Tinten, J. Bialkowski, and D. von der Linde, *Phys. Rev. B* **51**, 14186 (1995); K. Sokolowski-Tinten, J. Bialkowski, A. Cavalleri, D. von der Linde, J. Mejerter-Vehn, A. Oparin, and S. I. Anisimov, *Phys. Rev. Lett.* **81**, 224 (1998).
- [SBD87] R. Srinivasan, B. Braren, and R.W. Dreyfus, *J. Appl. Phys.* **61**, 372 (1987)
- [SBM01] C.B. Schaffer, A. Brodeur, and E. Mazur, *Meas. Sci. Technol.* **12**, 1784 (2001).
- [Sch55] L. Schiff, *Quantum Mechanics*, McGraw-Hill, New York, 1955.
- [SCP02] L. Sudrie, A. Couairon, M. Franco, B. Lamouroux, B. Prade, and A. Mysyrowicz, *Phys. Rev. Lett.* **89**, 186601 (2002).
- [SCS99] C.W. Siders, A. Cavalleri, K. Sokolowski-Tinten, Cs. Tóth, T. Guo, M. Kammler, M. Horn von Hoegen, K.R. Wilson, D. von der Linde, and C.P.J. Barty, *Science* **286**, 1340 (1999).
- [SCS99] C.W. Siders, A. Cavalleri, K. Sokolowski-Tinten, Cs. Tóth, T. Guo, M. Kammler, M. Horn von Hoegen, K.R. Wilson, D. von der Linde, and C.P.J. Barty, *Science* **286**, 1340 (1999).
- [SFH96] B.C. Stuart, M.D. Feit, S. Herman, A.M. Rubenchik, B.W. Shore, and M.D. Perry, *Phys. Rev. B* **53**, 1749 (1996).
- [SFR95] B. C. Stuart, M.D. Feit, A.M. Rubenchik, B.W. Shore, and M.D. Perry, *Phys. Rev. Lett.* **74**, 2248 (1995).
- [SFS96] T. Sugiyama, H. Fujiwara, T. Suzuki, and K. Tanimura, *Phys. Rev. B* **54**, 15109 (1996).
- [SGS97] E. Stenzel, S. Gogoll, J. Sils, M. Huisinga, H. Johansen, G. Kästner, and M. Reichling, *Appl. Surf. Sci.* **109-110**, 162 (1997).
- [SHB00] V. Schmidt, W. Husinsky, and G. Betz, *Phys. Rev. Lett.* **85**, 3516 (2000).
- [Sig73] P. Sigmund, *J. Mat. Sci.* **8**, 1545 (1973).
- [Sig92] P. Sigmund (Ed.) of *Fundamental processes in sputtering of atoms and molecules*, Vol. 43, *Math. Fys. Medd. Dan. Vid. Selsk. Copenhagen*, 1992.
- [SiI95] P. Simon and J. Ihlemann, *Appl. Phys. B.* **63**, 505 (1995).
- [SKB98] Ch. Spielman, C. Kan, N.H. Burnet, T. Brabec, M. Geissler, A. Scrinzi, M. Schnürer, and F. Krausz, *IEEE J. Sel. Top Quantum Electron.* **4**, 249 (1998).
- [SKQ03] Y. Shimotsuma, P. Kazansky, J. Qiu, and K. Hirao, *Phys. Rev.* **91**, 247405 (2003).
- [SoL99] K. Sokolowski-Tinten and D. von der Linde, *Phys. Rev. B* **61**, 2643 (1999).
- [SRA02] R. Stoian, A. Rosenfeld, D. Ashkenasi, I.V. Hertel, N.M. Bulgakova, and E.E.B. Campbell, *Phys. Rev. Lett.* **88**, 097603 (2002).
- [SSR01] R.P. Schmid, T. Schneider, and J. Reif, in *Ultrafast Electronics and Optoelectronics*, eds. Y.-K. Chen, W. Knox, and M. Rodwell, *OSA trends in Optics and Photonics* **49**, *Opt. Soc. Am.*, p. 111 (2001)..
- [SuM02] S.K. Sundaram and E. Mazur, *Nature Materials* **1**, 217 (2002).
- [SYP83] J.E. Sipe, J.F. Young, J.S. Preston, and H.M. van Driel, *Phys. Rev. B* **27**, 1141 (1983).
- [TAB88] H.W.K. Tom, G.D. Aumiller, and C.H. Brito-Cruz, *Phys. Rev. Lett.* **60**, 1438 (1988).
- [Tan01] K. Tanimura, *Phys. Rev. B* **63**, 184303 (2001).
- [TaO80] K. Tanimura and T. Okada, *Phys. Rev. B* **21**, 1690 (1980).
- [TBK99] A.C. Tien, S. Backus, H. Kapteyn, M. Murnane, and G. Mourou, *Phys. Rev. Lett.* **82**, 3883 (1999).
- [TBL95] P. Tosin, A. Blatter, and W. Luethy, *J. Appl. Phys.* **78**, 3797 (1995).
- [TeS91] P.A. Temple and M.J. Soileau, *IEEE J. QE-17*, 2067 (1981).
- [TKI89] K. Tanimura, T. Katoh, and N. Itoh, *Phys. Rev. B* **40**, 1282 (1989).
- [ToL83] P.D. Townsend, F. Lama: in *Desorption Induced by Electronic Transitions-DIET I*, eds. N.H. Tolk, M.M. Traum, J.C. Tully, and T.E. Madey, *Springer Ser. Chem. Phys.* Vol. 24, Berlin, p. 220, 1983.

- [TWM99] T. Schneider, D. Wolfframm, R. Mitzner, and J. Reif, *Appl. Phys. B* **794**, 68 (1999).
- [UHC99] C.C. Umbach, R.L. Headrick, B.H. Cooper, J.M. Balkely, and E. Chason, *Bull. Am. Phys. Soc.* **44**, 706 (1999).
- [VaN02] S.R. Vatsya and S.K. Nikumb, *J. Appl. Phys.* **91**, 344 (2002).
- [VAR96] H. Varel, D. Ashkenasi, A. Rosenfeld, R. Hermann, F. Noack, and E.E.B. Campbell, *Appl. Phys. A* **62**, 293 (1996).
- [VFM99] A.N. Vasil'ev, Y. Fang, and V.V. Mikhailin, *Phys. Rev. B* **60**, 5340 (1999)
- [VJL01] F. Vidal, T.W. Johnston, S. Laville, O. Barthelemy, M. Chaker, B. Le Drogoff, J. Margit, and M. Sabsabi, *Phys. Rev. Lett.* **86**, 2573 (2001).
- [VPM99] J. Viernow, D. Y. Petrovych, F. K. Men, A. Kirokasian, J.-L. Lin, F. J. Himpsel, *Appl. Phys. Lett.* **74**, 2125 (1999).
- [WaD92] X.Y. Wang and M.C. Downer, *Opt. Lett.* **17**, 1450 (1992).
- [Wal74] C. T. Walters, *Appl. Phys. Lett.* **25**, 696 (1974).
- [WES98] A. Wanknerl, D.T. Emerson, and J.R. Shealy, *Appl. Phys. Lett.* **72**, 1614 (1998).
- [WHG99] S.S. Wellershoff, J. Hohlfeld, G. Gdde, and E. Matthias, *Appl. Phys. A* **69**, 99 (1999).
- [WiH85] R. J. Wilson and F. A. Houle, *Phys. Rev. Lett.* **55**, 2184 (1985).
- [WMF03] Q. Wu, Y. Ma, R. Fang, Y. Liao, Q. Yu, X. Chen, and K. Wang, *Appl. Phys. Lett.* **82**, 1703 (2003).
- [WRL94] X.Y. Wang, D.M. Riffe, Y.-S. Lee, and M.C. Downer, *Phys. Rev. B* **50**, 8016 (1994).
- [WRM89] E. Westin, A. Rosn, and E. Matthias: in G. Betz, P. Varga, eds. *Desorption induced by electronic transitions DIET IV*, Springer Series in Surface Science 19, p. 316, Springer, Berlin, 1989.
- [WSF86] R.T. Williams, K.S. Song, W.L. Faust, and C.W. Leung, *Phys. Rev. B* **33**, 7232 (1986).
- [YeG01] M. Ye and C.P. Grigoropoulos, *J. Appl. Phys.* **89**, 5183 (2001).
- [YJM00] J.H. Yoo, S.H. Jeong, X.L. Mao, R. Grief, and R.E. Russo, *Appl. Phys. Lett.* **76**, 783 (2000).
- [YMU03] H.Yoneda, H. Morikami, Ken-ichi Ueda, and R.M. Moore, *Phys. Rev. Lett.* **91**, 075004 (2003).
- [YPD83] J.F. Young, J.S. Preston, H.M. van Driel, and J.E. Sipe, *Phys. Rev. B* **27**, 1155 (1983).
- [YPS83] J.F. Young, J.S. Preston, J.E. Sipe, and H.M. van Driel, *Phys. Rev. B* **27**, 1424 (1983). J.S. Preston, H.M. van Driel, and J.E. Sipe, *Phys. Rev. Lett.* **58**, 69 (1987); J.S. Preston, H.M. van Driel, and J.E. Sipe, *Phys. Rev. B* **40**, 3942 (1989).
- [YSD84] J.F. Young, J.E. Sipe, and H.M. van Driel, *Phys. Rev. B* **30**, 2001 (1984).
- [ZFG82] G. Zhousheng, P.M. Fauchet, and A.E. Siegman, *Phys. Rev. B* **26**, 5366 (1982).
- [ZhC97] W. Zhang and B.T. Chait, *Int. J. Mass Spectrom. Ion Processes* **160**, 259 (1997).
- [ZhG97] L.V. Zhigilei, P.B.S. Kodali, and B.J. Garrison, *Chem. Phys. Lett.* **276**, 269 (1997); L.V. Zhigilei and B. Garrison, *Appl. Phys. Lett.* **71**, 551 (1997).
- [ZhG00] L.V. Zhigilei and B.J. Garrison, *J. Appl. Phys.* **88**, 1281 (2000).
- [ZHS89] J.P. Zheng, Z.Q. Huang, D.T. Shaw, and H.S. Kwok, *Appl. Phys. Lett.* **54**, 280 (1989).
- [ZIV99] Y. Zhang, Z. Iqbal, S. Vijayalakshmi, and H. Grebel, *Appl. Phys. Lett.* **75**, 2758 (1999).

ACKNOWLEDGEMENTS

I would like to especially thank Prof. Dr. Jürgen Reif, my thesis supervisor, for giving me the opportunity to work on such an interesting topic and for his professional guidance, patience and direction throughout my efforts. It is because of his critical evaluation and tireless support that I am able to share my work with you now.

In addition, I would also like to thank my Dissertation referees Prof. Dr. Wolfgang Kautek and Dr. Philippe Martin for accepting my work and providing their expert evaluations. Their professional assistance and cooperation is greatly appreciated.

I would like to take this opportunity to express my sincerest thanks to my colleagues at the Chair of Experimental Physics II, who have helped me achieve this goal. I remain indebted to them for their input in the laboratory and participation in fruitful discussions as well as their friendship and understanding. I list their names alphabetically here, because it would be impossible for me to provide any ranking order to their support: Dipl.-Phys. Tzanimir Arguirov, Jürgen Bertram, Marion Borrmann, Dr. Matthias Henyk, Dipl.-Phys. Simona Kouteva-Arguirova, Prof. Dr. Reiner Schmid, Dipl.-Phys. Markus Ratzke, Dipl.-Phys. Olga Varlamova, and Dr. Dirk Wolfframm.

I would like to thank in particular to ‘my’ Diploma students Lei Zhu and Sebastian Eckert for their enthusiasm, involvement and contributions to our team work.

I am indebted to Dr. Winfried Seifert, Dipl.-Phys. Stanislav Pandelov and Dipl.-Phys. Jia Guobin for their assistance with the SEM, at the JointLab IHP/BTU Cottbus.

I gratefully acknowledge Dr. Philippe Martin, Dr. Alexandre Semerok, and Dr. Olivier Gobert for their assistance with the equipment and experiments within the SLIC project at CÉA, Saclay, France.

Finally, I would like to give my warmest thanks to my family and close friends for providing me with the emotional and physical strength needed to reach this aim. Words cannot convey my gratitude to them. At last I give my most heartfelt thanks to Frank Ritchie for being greatly supportive of me and incessantly caring for me in all these years.